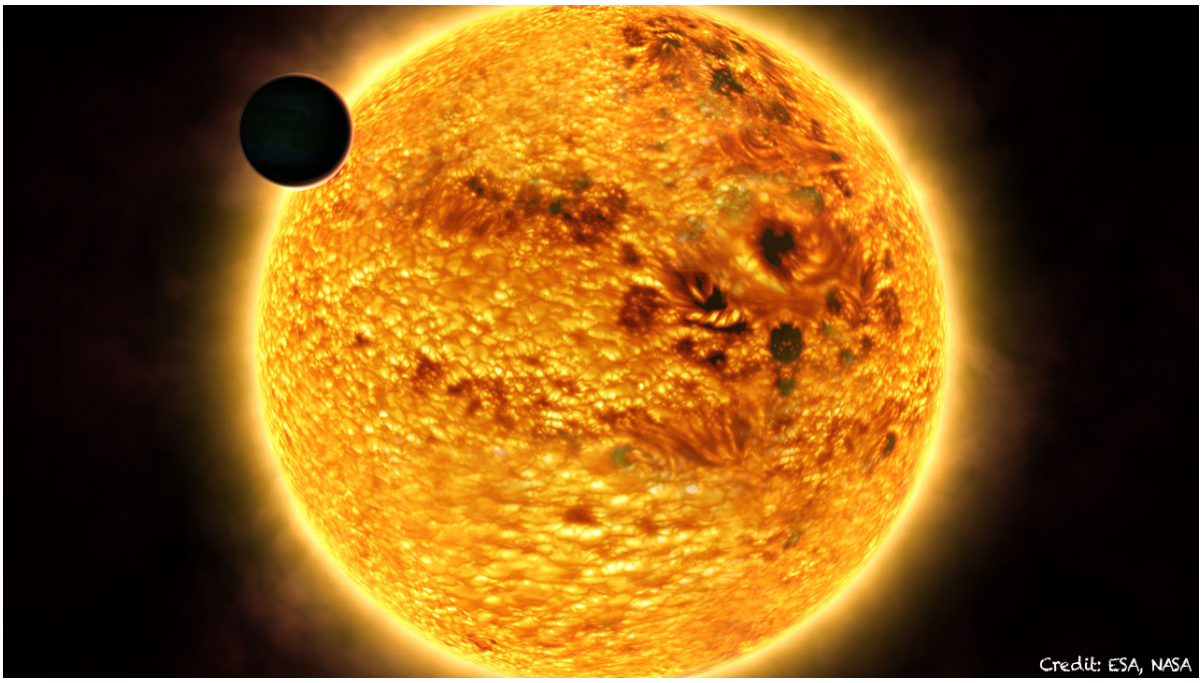


# Transiting exoplanets: characterisation in the presence of stellar activity

Aude Ekundayo Pauline ALAPINI ODUNLADE

Submitted by Mrs Aude Ekundayo Pauline Alapini Odunlade, to the University of Exeter as a thesis for the degree of Doctor of Philosophy in Physics, March 2010.



Mrs Aude E. P. Alapini Odunlade
March 2010

This thesis was supervised by Dr. Suzanne Aigrain – University of Exeter, University of Oxford

# Abstract

The combined observations of a planet's transits and the radial velocity variations of its host star allow the determination of the planet's orbital parameters, and most interestingly of its radius and mass, and hence its mean density. Observed densities provide important constraints to planet structure and evolution models. The uncertainties on the parameters of large exoplanets mainly arise from those on stellar masses and radii. For small exoplanets, the treatment of stellar variability limits the accuracy on the derived parameters. The goal of this PhD thesis was to reduce these sources of uncertainty by developing new techniques for stellar variability filtering and for the determination of stellar temperatures, and by robustly fitting the transits taking into account external constraints on the planet's host star.

To this end, I developed the Iterative Reconstruction Filter (IRF), a new post-detection stellar variability filter. By exploiting the prior knowledge of the planet's orbital period, it simultaneously estimates the transit signal and the stellar variability signal, using a combination of moving average and median filters. The IRF was tested on simulated CoRoT light curves, where it significantly improved the estimate of the transit signal, particulary in the case of light curves with strong stellar variability. It was then applied to the light curves of the first seven planets discovered by CoRoT, a space mission designed to search for planetary transits, to obtain refined estimates of their parameters. As the IRF preserves all signal at the planet's orbital period, t can also be used to search for secondary eclipses and orbital phase variations for the most promising cases. This enabled the detection of the secondary eclipses of CoRoT-1b and CoRoT-2b in the white (300–1000 nm) CoRoT bandpass, as well as a marginal detection of CoRoT-1b's orbital phase variations. The wide optical bandpass of CoRoT limits the distinction between thermal emission and reflected light contributions to the secondary eclipse.

I developed a method to derive precise stellar relative temperatures using equivalent width ratios and applied it to the host stars of the first eight CoRoT planets. For stars with temperature within the calibrated range, the derived temperatures are consistent with the literature, but have smaller formal uncertainties. I then used a Markov Chain Monte Carlo technique to explore the correlations between planet parameters derived from transits, and the impact of external constraints (e.g. the spectroscopically derived stellar temperature, which is linked to the stellar density).

Globally, this PhD thesis highlights, and in part addresses, the complexity of performing detailed characterisation of transit light curves. Many low amplitude effects must be taken into account: residual stellar activity and systematics, stellar limb darkening, and the interplay of all available constraints on transit fitting. Several promising areas for further improvements and applications were identified. Current and future high precision photometry missions will discover increasing numbers of small planets around relatively active stars, and the IRF is expected to be useful in characterising them.

# Contents

# List of Figures

# List of Tables

## Declaration

Most of the work described in this thesis has been published in scientific journals in the form of papers written cooperatively by myself, my supervisor Suzanne Aigrain, and other collaborators at the University of Exeter and in the CoRoT team.

The work presented on the Iterative Reconstruction Filter in Chapter 2 was published in Alapini & Aigrain (2009). This work was essentially my own but benefited from regular discussions and advice from S. Agrain and T. Naylor.

Parts of the work presented in Chapter 3 were carried out as part of the CoRoT collaboration and published in Fridlund et al. (2010) for CoRoT-6b and Léger et al. (2009) for CoRoT-7b. My contribution to these papers was to derive independent measurements of the planet parameters, using the IRF to process the light curve.

Some of the work presented in Chapter 4 was carried out as part of the CoRoT collaboration and published in Alonso et al. (2009a,b). Specifically, I used the method described in Chapter 4, as a method among other ones in the paper, to detect the secondary eclipses of CoRoT-1b and CoRoT-2b.

The work presented in Chapter 5 on building and testing equivalent width ratios as temperature sensors, benefited from several discussions and advice from G. Israelian, A. Ecuvillon, S. Aigrain and N.C. Santos. Based on the learning from this work, a more precise calibration using the same technique was built and published in Sousa et al. (2009). My additional contribution to this paper was in testing the robustness of this new calibration by comparing it to the old one. The temperature analysis of the host star of CoRoT-6b that I performed in Chapter 5 forms part of Fridlund et al. (2010).

Finally, the work performed in Chapter 6 benefited from regular discussion and advice from S. Aigrain and F. Pont. The MCMC was designed by S. Aigrain and F. Pont, but all the implementations presented in this chapter were my own work. My contribution to the overall MCMC was in developing our understanding of the impact the prior on the stellar temperature has on the probability distributions of the planet parameters.

# List of publications

*The secondary eclipse of the transiting exoplanet CoRoT-2b*. Alonso, R., Guillot, T., Mazeh, T., Aigrain, S., **Alapini, A.**, Barge, P., Hatzes, A., and Pont, F. – A&A 2009

*An iterative filter to reconstruct planetary transit signals in the presence of stellar variability*. **Alapini, A.** and Aigrain, S. – MNRAS, 2009

*Transiting exoplanets from the CoRoT space mission VIII. CoRoT-7b: the first Super-Earth with measured radius*. Léger, A., Rouan, D., Schneider, J., Barge, P., Fridlund, M., Samuel, B., Ollivier, M., Guenther, E., Deleuil, M., Deeg, H. J., and 151 coauthors of which **Alapini, A.** – A&A 2009

*Ground-based photometry of space-based transit detections: photometric follow-up of the CoRoT mission*. Deeg, H. J., Gillon, M., Shporer, A., Rouan, D., Stecklum, B., Aigrain, S., **Alapini, A.**, Almenara, J. M., Alonso, R., Barbieri, M., and 16 coauthors – A&A 2009

*The secondary eclipse of CoRoT-1b*. Alonso, R., **Alapini, A.**, Aigrain, S., Auvergne, M., Baglin, A., Barbieri, M., and 16 coauthors – A&A 2009

*Removing systematics from the CoRoT light curves. I. Magnitude-dependent zero point*. Mazeh, T., Guterman, P., Aigrain, S., Zucker, S., Grinberg, N., **Alapini, A.**, Alonso, R., Auvergne, M., Barbieri, M., Barge, P., and 24 coauthors – A&A 2009

*Noise properties of the CoRoT data. A planet-finding perspective*. Aigrain, S., Pont, F., Fressin, F., **Alapini, A.**, Alonso, R., Auvergne, M., Barbieri, M., Barge, P., Bordé, P., Bouchy, F., and 23 coauthors – A&A 2009

*Planetary transit candidates in CoRoT-LRc01 field*. Cabrera, J., Fridlund, M., Ollivier, M., Gandolfi, D., Csizmadia, Sz., Alonso, R., Aigrain, S., **Alapini, A.**, Almenara, J.-M., Barge, P., and 45 coauthors – A&A 2009

*An effective temperature calibration for solar type stars using equivalent width ratios. A fast and easy spectroscopic temperature estimation*. Sousa, S. G., **Alapini, A.**, Israelian, G., Santos, N. C. – A&A 2010

*Transiting exoplanets from the CoRoT space mission. IX. CoRoT-6b: a transiting "hot Jupiter" planet in an 8.9d orbit around a low-metallicity star*. Fridlund, M., Hébrard, G., Alonso, R., Deleuil, M., Gandolfi, D., Gillon, M., Bruntt, H., **Alapini, A.**, Csizmadia, Sz., Guillot, T., and 38 coauthors – A&A 2010

# Acknowlegments

I am grateful to a large number of people for having made my PhD a reality and a success.

My first thanks go to my supervisor, Suzanne Aigrain, for giving me the opportunity of doing my PhD in the fascinating field of exoplanets, for guiding my steps through moments of confusion, for her patience, and her good company.

My second thanks go to my better half, Dapo Odunlade, for his everlasting smile, support, and love. I thank him for his patience during my PhD, and for having proof-read more than half of my thesis in such a short time.

I thank my family, my mum, my dad, for having been so supportive throughout my education, and giving me the opportunity to satisfy my curiosity for science. I thank my sisters for being a great source of comfort and fun.

I thank my high school physics teacher, Antoine Guihal, for planting in me the seed of curiosity and passion for science.

I thank my work colleagues for having and still making my experience in Exeter an enjoyable one. I thank in particular Ben, Dave, Susie, Catia, Cameron and Farzana for their enthusiasm and caring.

I thank Didier Pelat, Tim Naylor, Frederic Pont, Matthew Bate, Suzanne Aigrain, and my family for supporting me in my enthusiasm for outreach in Benin. These trips were amazing experiences for everyone involved and especially for the Beninese people of all ages who had the opportunity of doing hands-on science.

To more exciting moments in science, in astrophysics, and in the search for exotic new worlds!

# Chapter 1

# Introduction

## 1.1 A brief history on the search for exoplanets

Pondering on the existence of worlds other than our own has always piqued human interest. There have been centuries of speculation on whether our planet, the Earth, and our planetary system, the Solar System, were ones of many. As early as the $3^{rd}$ century B.C., Epicurus (341-270 B.C.) said *"There are infinite worlds both like and unlike this world of ours. For the atoms being infinite in number, as was already proven, (...) there nowhere exists an obstacle to the infinite number of worlds"*. But his point of view was not commonly shared, as for instance by the philosopher Aristotle (384-322 B.C.) who claimed *"There cannot be more worlds than one"*. It was only in 1609 that Galileo Galilei (1564-1642) first observed with a telescope other planets in our Solar System, confirming the idea of Copernicus (1473-1543) that the sun is orbited by several planets, of which the earth is but one.

Our search for other worlds, need not to be limited to our Solar System. Indeed, the search for exoplanets, planets around other stars than the Sun, has already begun. However, unlike the planets in our Solar System which are close to us and thus appear very bright, exoplanets are very difficult to observe directly. The light of a planet is millions of times fainter than the light of its star. When seen from tens to thousands of light years[1] away, the planet appears very close to its star and its faint light is diluted in the glare of its star. Indirect methods designed to detect an exoplanet through its influence on its parent star or on other field stars, avoid these difficulties of contrast, and so have become successful and popular methods for detecting exoplanets. These methods by which exoplanets have been detected are briefly described in Section 1.2.1.

Several claims of exoplanet detections have been documented since the 19th century, but the first confirmed detections were made by Wolszczan & Frail (1992) who monitored the irregularities in the timing of pulsars. These exoplanets, PSR 1257+12 b and c, are a few Earth masses and orbit a pulsar[2] at radii similar to that at which Mer-

[1] A light year is the distance covered when travelling at the speed of light over one year.

[2] A pulsar is a very dense star, resulting from the collapse of the core a massive star during a supernovae,

cury orbits the Sun. The first discovery of an exoplanet around a star similar to the Sun was made by monitoring variations in the radial velocity of a star (Mayor & Queloz, 1995). This exoplanet, 51 Pegasi b, is classified as a Hot Jupiter as it is similar in mass to Jupiter (half the mass) and it orbits close to its star (about 8 times closer than Mercury orbits the Sun). The discovery of Hot Jupiters challenged our understanding of planet formation and evolution. Gas giant planets were originally expected to form beyond the snow line[3] and so were expected to be found at orbits similar to those of the giant planets in our Solar System (Pollack et al., 1996). But finding them so close to their stars prompted people to suggest that these planets may have undergone inward migration after their formation, due to interactions with their parent protoplanetary discs (Lin et al., 1996).

In the past two decades, the number of exoplanets discovered has gone from zero to more than 400. This progress is the result of several improvements in instrumentation and observing techniques, such as the development of CCD[4] cameras, the development of stable high resolution spectroscopy, and the introduction of computer-based image processing. It is also the result of an increased interest in the field of exoplanets and in the diversification of the techniques used to detect exoplanets.

In the 1950s, the first papers on the search for exoplanets using the transit method were published (e.g. Struve 1952), and the first detailed development of this detection method was carried out shortly after (Rosenblatt, 1971). The first observation of the transit of an exoplanet was published in Charbonneau et al. (2000). This planet, HD 209458b, was first discovered with the radial velocity technique (Mazeh et al., 2000). The combined detection of the planet's transit and radial velocity effect on its parent star opened a new area in the study of exoplanets, this combination of technique allows both the planet's radius and mass to be measured. These can then be compared to the predictions of planet evolution models with various compositions and heat deposition mechanisms (e.g. Guillot 2005, Baraffe et al. 2008) to infer the planet's bulk composition. These models are continuously challenged by new planet discoveries, the best known case of this being the small group of planets whose radii are larger than expected for their mass and irradiation level: HD 209458b (Charbonneau et al., 2000; Knutson et al., 2007b), HAT-P-1b (Bakos et al., 2007; Winn et al., 2007), WASP-1b (Collier Cameron et al., 2007; Charbonneau et al., 2007), TrES-4b (Mandushev et al., 2007), XO-3b (Winn et al., 2008), CoRoT-2b (Alonso et al., 2008), and WASP-12b (Hebb et al., 2009). To explain the inflated radii of these planets, most models require an additional heating mechanism that deposits energy deep into the atmosphere of the planet.

To date (March 2010), 431 exoplanets[5] have been discovered, more than 80 are

rotating around itself very rapidly and emitting very regular polar electromagnetic pulses.

[3]The snow line is the distance from the protostar where the temperature is low enough for the hydrogen compounds in the solar nebulae (e.g. water, ammonia, methane) to condense into ice grains.

[4]CCD stands for Charged Coupled Device

[5]http://exoplanet.eu/catalog.php

in multiple planet systems, more than 400 have been observed through radial velocity measurements, the transits of 70 of them have been observed, and at least 4 exoplanets[6] have been imaged directly.

## 1.2 The detection of exoplanets

### 1.2.1 The methods

There are several methods that have successfully detected exoplanets, and several other proposed methods which have not yet detected an exoplanet. Perryman (2000) and Lunine et al. (2008) review the different techniques and their performance and limitations. In this thesis, I focus on the science and usage of the transit method and use some information from the radial velocity method. I describe these two methods hereafter. For completeness I also describe in this section the other methods that have successfully detected one or more exoplanets to date. A summary of the different parameters measurable from the different methods is presented in Table 1.1.

#### The transit method

This method detects the passage of a planet in front of its host star. This event is called a $transit$. The passage of the planet behind its host star is called an $occultation$ or a secondary eclipse. Jupiter creates a transit of 1% depth in front of the Sun, and the Earth create a depth of 0.08%. The observation of the transit of a planet allows one to derive the dimensions of the planet relative to its host star, the planet to star separation, and the orientation of the planet's orbit relative to the plane of the sky, as described in Section 1.3.1. For a transiting object to be confirmed as a planet, its mass needs to be measured through the radial velocity follow-up of its parent star. For a transit to occur, the exoplanetary system needs to be seen nearly edge-on, which reduces the probability of a transit detection. The transit method is most sensitive to close-in planets as the probability of observing their transits is higher. The lower limit of detectable planet size depends on the photometric precision of the light curve. To increase the probability of transit detections within a survey, thousands of stars need to be monitored continuously with high precision photometry. The basic geometry and physics of transits is reviewed in Winn (2010).

#### The radial velocity method

This method detects the oscillating Doppler shift in the stellar spectrum due to the periodic radial velocity motion (motion along the line of sight) of a star gravitationally

[6]This number depends on the definition of an exoplanet. To date (March 2010), there are 4 exoplanets with $M_{\rm p}<13M_{\rm Jup}$ (above is the brown dwarf regime) orbiting a star (spectral class above M6; below is the brown dwarf regime).

tugged back and forth by an orbiting planet. For instance, Jupiter induces a radial velocity variation on the Sun of 12.5 $\mathrm{ms}^{-1}$, and the Earth a radial velocity variation of 0.1 $\mathrm{ms}^{-1}$. A close-in Jupiter-like exoplanet, such as 51 Pegasi b, induces a radial velocity variation on its host star of about 50 $\mathrm{ms}^{-1}$. The mass of a planet ($M_{\mathrm{p}} \sin i$, with $i$ the inclination of the planet orbital plane to the plane of the sky) can be measured from the amplitude of the radial velocity variation it causes on its host star (see Section 1.3.2 for formulae). For the true mass to be measured, the inclination angle, $i$ is needed, which can be obtained from transit observations if the planet transits its host star. The radial velocity method is most sensitive when the system is seen edge-on as the radial gravitational tug then appears stronger.

### The microlensing method

This method detects the magnification of the light of a background star due to the deflection of its light by the gravitational field of a foreground star and its planet acting as a gravitational lens. The foreground star acts as the main lens and the orbiting planet is a much more short lived lens that acts in addition to the lensing of its host star. The magnification of the background light lasts for $\sim$100 days for the host star, and the superimposed magnification due to the planet lasts for $\sim$2 h for a Jupiter-size planet. The microlensing technique is sensitive to exoplanets down to Earth-sizes. The detection of small planets depends on the time sampling as the smaller the planet, the shorter the microlensing event. The sensitivity of the microlensing technique peaks for planet to star separations equal to the Einstein radius, typically corresponding to a separation just beyond the snow line. This technique requires a crowed stellar background so microlensing surveys are performed along the Galactic disk. The theory of the microlensing method applied to exoplanets is reviewed in Gaudi (2010).

### The pulsar timing method

This method detects periodic anomalies in the frequency of the radio pulse of a neutron star, a remnant of super-novae. An Earth-like planet around a pulsar creates a detectable pulse delay of 1.2 miliseconds. This method is limited to pulsars.

### The direct imaging method

This method detects the light of a planet itself (emitted or reflected from the star), and works for those planets that are far enough from their parent stars such that the stellar glare can be suppressed. The suppression of the stellar light can be done using an occulter – a chronograph – to block the light from the star, or an interferometer to nullify it. In optical wavelenghts Jupiter is $10^9$ times less luminous than the Sun, and the Earth is ten times fainter than Jupiter. In the mid-infrared, the Earth is $10^6$ times fainter than the

Sun. The direct imaging technique uses adaptive optics to sharpen the image of the star which is then easier to suppress, and to sharpen the image of the planet which is then easier to detect.

### 1.2.2 Properties of the exoplanets discovered to date

Figure 1.1 displays the ranges in planet mass, radius and orbital distance of the exoplanets detected by Jan 26th 2010, for each of the detection methods mentioned in section 1.2.1.

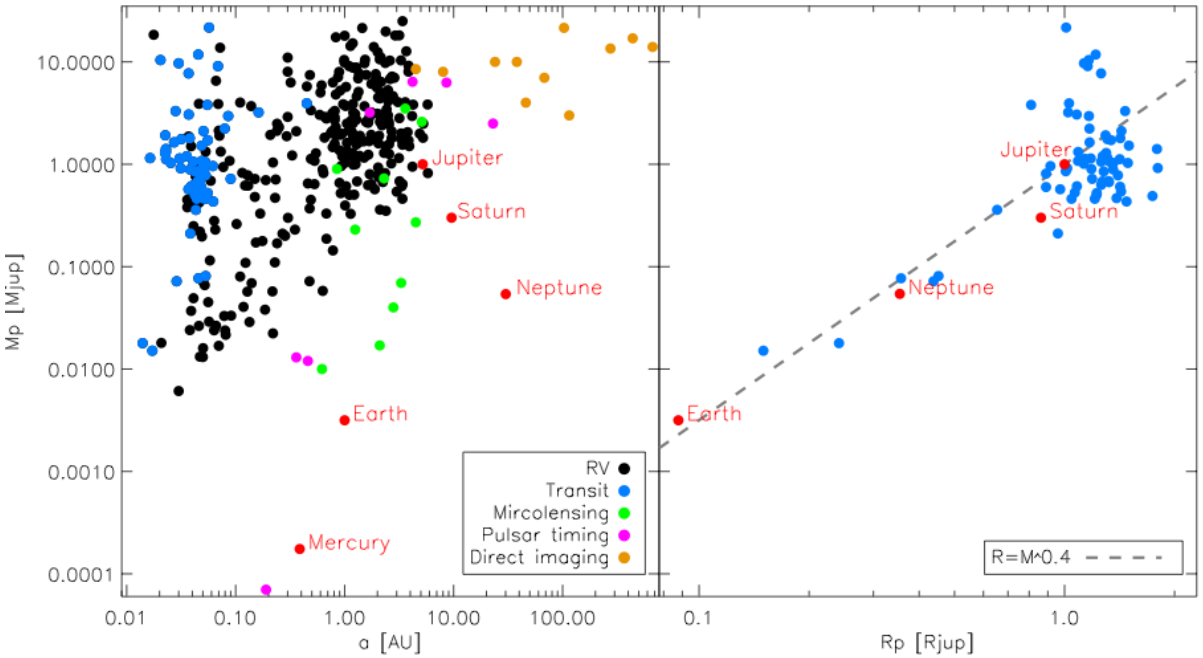


Figure 1.1: Graph of the masses, radii and orbital distances of the exoplanets detected by Jan 26th 2010, with the detection methods marked in different colours. The planet masses indicated for the radial velocity method (RV) are the lower limits of their $M_{\rm p}\sin i$ value. The grey dash line (right panel) shows the mass-radius relation for $R_{\rm p}$=$M_{\rm p}{}^{0.4}$.

Some features in the distribution of the detected exoplanets stand out in Figure 1.1. The transiting planets are detected at small orbital distances from their host stars ($\leq$0.5 AU so far); this is a bias of the transit method as close-in planets have a larger probability to transit. The planets detected by direct imaging have larger orbital distances ($\geq$4 AU so far); this is due to the current performance of the stellar nulling techniques which detect planets more easily when they are well outside the residual stellar glare. Most of the exoplanets detected by radial velocity measurements have masses and radii similar to, or larger than Jupiter; this is because the perturbations caused by massive planets on their host stars are larger, making these planets easier to detect. The pulsar timing method allows the detection of very small planets, smaller than Mercury. The

transit, radial velocity and microlensing techniques have so far allowed the detection of planets down to a few times the size or mass of the Earth. As the instrumental technology and the data analysis techniques evolve and as the on-going surveys monitor the stars for longer, these observational biases should reduce.

Exoplanets are found with eccentricities ranging from 0 to 0.97, while in our Solar System the maximum planet orbital eccentricity is 0.2 (Mercury). Planet-planet and planet-star interactions can induce larger orbital eccentricities and inclinations to the stellar rotation plane.

The sky-projected planet orbital inclination and the sky-projected inclination between the stellar spin and the planet's orbit rotation axis, have been measured for some exoplanets. With the latter, polar or retrograde planet orbits can be identified. However, as the inclinations are degenerate over the inclination to the plane of the sky, it is not possible to compare them to the values in the Solar System or in the planet formation and evolution models.

So far, the exoplanet search surveys have been focussed on solar-type stars (F,G,K stellar type) and small stars, especially the radial velocity and transit surveys for which planets give larger amplitude signatures on smaller stars. This is a bias that will be adjusted with surveys on massive stars (larger than a few solar masses).

Solar-type stars harbouring giant exoplanets have been found to have a higher metallicity than the Sun (e.g. Santos et al. 2004). However, the observed population of planets around different mass and different metallicity stars is too small to give robust statistics. Currently, it is not possible to obtain reliable trends in how the number of planets varies with these stellar properties.

Table 1.1: Table of the planet parameters and the stellar parameters relevant to deriving them, Plus the associated observable(s) and observing method(s) used to derive the physical parameters.

| Parameters | Observables | Method | Ref. |
|---|---|---|---|
| **Planet** | | | |
| Orbital period $P$ | time of transits | light curve - transit | (1) |
| Orbital inclination $i$ [1] | $t_F$, $t_T$, $\delta$, $P$ | light curve - transit | (1) |
| Planetary radius [2] ($R_{\rm p}/R_\star$) | $\delta$ | light curve - transit | (1) |
| Planetary mass [3] (($M_{\rm p}\sin i$)/($M_{\rm p}$+$M_\star$)$^{2/3}$) | $K_\star$ | radial velocity curve | (2) |
| ($M_p/M_\star$) | shape of magn. | mircolensing | (3) |
| ($M_p \sin i$) | pulse delay | pulsar timing | (4) |
| Orbital semi-major axis ($a/R_\star$) | $t_F$, $t_T$, $\delta$, $P$ | light curve - transit | (1) |
| ($a \sin i$) | $K_\star$ | radial velocity curve | (2) |
| ($a \sin i$) | $t_m$ | microlensing | (3) |
| ($a \sin i$) | pulse delay | pulsar timing | (4) |
| ($a \sin i$) | $\alpha_p$, $d$ | direct imaging | (5) |
| Orbital eccentricity $e$ | $\phi_{sec}$ | light curve - occultation | (6) |
| | RV shape | radial velocity curve | (2) |
| Argument of periastron $\omega$ | RV shape | radial velocity curve | (2) |
| Absorption spectrum | $\delta$ at various $\lambda$ | light curve - transit | (1) |
| Emission spectrum | $\delta_{sec}$ at various $\lambda$ | light curve - occultation | (6) |
| | $L_{\rm p}/L_\star$ at various $\lambda$ | direct imaging | (5) |
| Thermal emission | $\delta_{sec}$ (large $\lambda$) | light curve - occultation | (6) |
| Albedo | $\delta_{sec}$ (small $\lambda$) | light curve - occultation | (6) |
| Phase function | flux ampl., $\phi_{max}$ | light curve - orbit | (7) |
| Planetary wind speed | $\phi_{max}$ | light curve - orbit | (7) |
| Spin-orbit angle $\lambda_p$ [4] | shape of rossiter | radial velocity - transit [5] | (8) |
| Stellar spin angle [6] | oscill. modes | asteroseismology | (9) |
| **Star** | | | |
| Stellar mass $M_\star$ | $T_{\rm eff}$, $\log g$, $[M/H]$ | stellar evolution models | (10) |
| Stellar radius $R_\star$ | $T_{\rm eff}$, $\log g$, $[M/H]$ | stellar evolution models | (10) |
| | oscill. modes | asteroseismology | (9) |
| Stellar density ($M_\star/R_\star^3$) | $t_F$, $t_T$, $\delta$, $P$ | light curve - transit | (1) |
| | oscill. modes | asteroseismology | (9) |
| Limb darkening | transit shape | light curve - transit | (1) |
| Stellar rotation period | period of spots | light curve - stellar spots | (11) |
| Stellar age | rotation period | light curve - stellar spots | (11) |
| | $T_{\rm eff}$, $\log g$, $[M/H]$ | stellar evolution models | (10) |

**Notations:** $t_F$ is the transit duration with the planet disk fully superimposed to the stellar disk, $t_T$ is the total transit duration, $\delta$ is the transit depth, $K_\star$ is the semi-amplitude of the stellar radial velocity variation due to the planet, magn. stands for magnification, $a$ is the planet orbital semi-major axis, $d$ is the distance of the star to the Sun, ampl. stands for amplitude of the deviation, $t_m$ is the time difference between the magnification maximum due to the star and the one due to the planet, $\alpha_p$ is the angular distance between the planet and the star, $\phi_{sec}$ is the phase in the planet orbit of the mid-occultation relative to the phase of the mid-transit, RV stands for radial velocity, $\lambda$ is the wavelength, $\delta_{sec}$ is the depth of the occultation, $L_p/L_\star$ is the planet-to-star luminosity ratio, $\phi_{max}$ is the phase of the maximum flux in the planet orbit, oscill. stands for stellar oscillation, $T_{\rm eff}$ is the stellar effective temperature, $g$ is the surface gravity, (M/H) is the metallicity of the star relative to the solar metallicity.
**Notes:** [1] projected onto the plane of the sky, [2] relative to the radius of the host star, [3] relative to the mass of the host star, [4] angle between the stellar spin axis and the perpendicular to the planet orbital plane, projected onto the plane of the sky, [5] Rossiter-McLaughlin effect, perturbation over the radial velocity curve during the planet transit, [6] angle between the stellar spin axis and the plane of the sky.
**Example of reference:** (1) Charbonneau et al. 2000, (2) Mazeh et al. 2000, (3) Bennett 2009, (4) Phillips & Thorsett 1994, (5) Marois et al. 2008, (6) Charbonneau et al. 2005, (7) Knutson et al. 2007a, (8) Gaudi & Winn 2007, (9) Kjeldsen et al. 2009, (10) Torres et al. 2009, (11) Aigrain et al. 2008.

## 1.3 Characterising exoplanets

The different detection methods allow the measurement of different planet parameters, as summarised in Table 1.1. The planet properties measurable from the planet transit light curve and from the stellar radial velocity curve are described in sections 1.3.1, 1.3.2 and 1.3.3. The main properties of the exoplanets detected to date, and of their host stars are listed in section 1.2.2. More detailed descriptions of the physical properties of the detected exoplanets and of their environment can be found in Perryman (2000) and Baraffe et al. (2010).

### 1.3.1 Analytic equations to derive the planet parameters from the transit light curve

#### Equations for a uniform intensity stellar disk and a planet in circular orbit

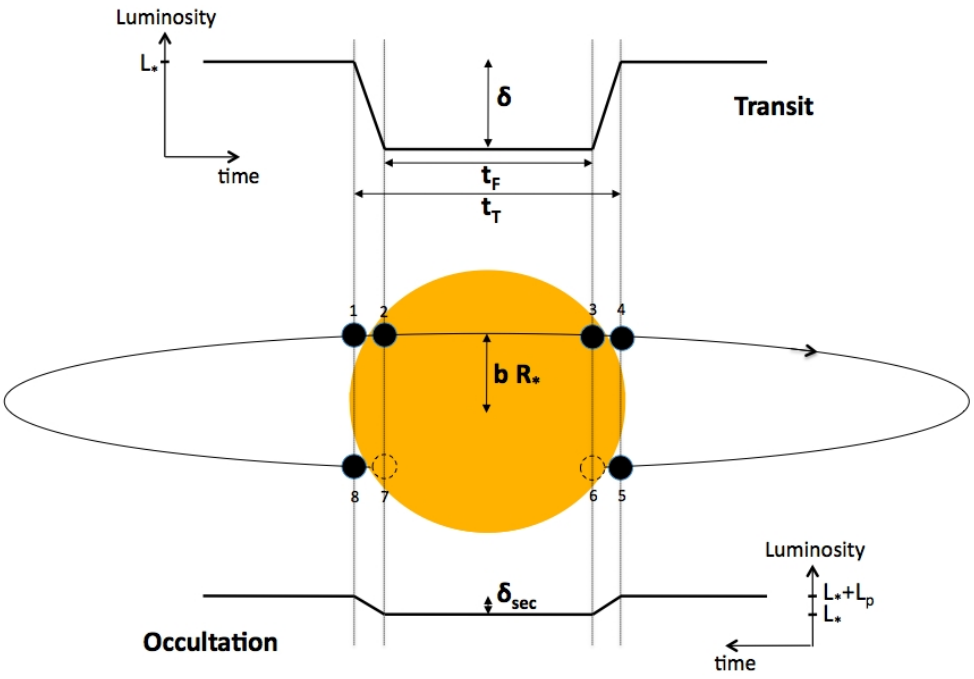


Figure 1.2: The schematic of a planet transiting its host star (middle) with the corresponding variation in brightness during the transit (top) and during the occultation (bottom). The impact parameters $b$ and the transit parameters ($\delta$, $t_F$, $t_T$) used in the equations here after are indicated on this figure.

Seager & Mallén-Ornelas (2003) give a set of simple analytical equations to derive the following planet parameters: $R_{\rm p}/R_\star$ the planet radius relative to the radius of the host star, $a/R_\star$ the orbital distance of the planet relative to the radius of the host star, $i$ the orbital inclination projected to the plane of the sky. Under the approximations listed herafter, these planet parameters can be derived from the following four observables of the transit light curve: $P$ the orbital period, $\delta$ the transit depth, $t_F$ the duration of the

transit when the planet disk is completely inside the stellar disk, and $t_T$ the total transit duration.

1. The planet is in a circular orbit. This is often true for planets close to their star as tidal interaction with the star acts to circularise the orbit of the planet.
2. The stellar intensity is uniform across the stellar disk, i.e. the stellar limb darkening is negligible. This is true at long wavelengths, e.g. the $I$ band (806$\pm$149 nm).
3. The planet is dark compared to the central star.
4. The light comes from a single star, i.e the light from the planet host star is not blended with the light from another star.

To gain a useful insight into the transit geometry, it is interesting to reproduce here the analytic equations given by Seager & Mallén-Ornelas (2003) for the planet-to-star radius ratio $R_{\rm p}/R_\star$ (equation 1.2), the planet impact parameter $b$ (equation 1.7), the planet orbital distance relative to the stellar radius $a/R_\star$ (equation 1.9), and the planet orbital inclination projected onto the plane of the sky $i$ (equation 1.12). The planet orbital period is measured from the time difference between successive transits, which requires a light curve with at least two transits. But under the above conditions, Seager & Mallén-Ornelas (2003) show that if the stellar mass and radius are know (e.g. from spectral type analysis), the transit period can be estimated from a single-transit light curve (equation 1.15). Under the approximation that $M_{\rm p}<<M_\star$, the stellar density ${M_\star}/{R_\star}^3$ can also be derived from the transit light curve (equation 1.13). Under the assumption that $a >> R_\star$, some of the equations can be simplified (see equations 1.8, 1.10, 1.14, 1.16).

The transit depth $\delta$ normalised by the stellar luminosity $L_\star$, assuming no stellar limb darkening, a dark planet, and no stellar blend, is

$$\delta = \frac{L_\star - L_{\star,\ with\ planet\ in\ transit}}{L_\star} \tag{1.1}$$

As $L_\star = \pi R_\star^2 F_\star$ and $L_{\star,\ with\ planet\ in\ transit} = L_\star - \pi R_{\rm p}^2 F_\star)$, where $R_\star$ and $F_\star$ are the stellar radius and stellar flux per unit surface area, and $R_{\rm p}$ is the planet radius, the transit depth is related to the planet-to-star radius ratio as follows

$$\delta = \left(\frac{R_{\rm p}}{R_\star}\right)^2 \tag{1.2}$$

The transit shape – equivalent to the transit duration inside the ingress and egress relative to the total transit duration – can be derived as follows

$$\left(\frac{\sin\left(t_F \pi/P\right)}{\sin\left(t_T \pi/P\right)}\right)^2 = \frac{[1 - R_p/R_\star]^2 - [a/R_\star\ \cos i]^2}{[1 + R_p/R_\star]^2 - [a/R_\star\ \cos i]^2} \tag{1.3}$$

Under the approximation that $a >> R_\star$, $t_T\pi/P << 1$, and as for small $x$, $\sin x \simeq x$, the equation 1.3 simplifies to

$$\left(\frac{t_F}{t_T}\right)^2 = \frac{[1 - R_p/R_\star]^2 - [a/R_\star \cos i]^2}{[1 + R_p/R_\star]^2 - [a/R_\star \cos i]^2} \tag{1.4}$$

The total transit duration $t_T$ can be derived as follows

$$t_T = \frac{P}{\pi} \sin^{-1}\left(\frac{R_\star}{a}\frac{\sqrt{[1 + R_p/R_\star]^2 - [a/R_\star \cos i]^2}}{\sin i}\right) \tag{1.5}$$

Under the approximation that $a >> R_\star$, $\cos i << 1$, and as for small $x$, $\arcsin x \simeq x$, and the equation 1.5 simplifies to

$$t_T = \frac{P\ R_\star}{\pi\ a}\sqrt{\left(1 + \frac{R_p}{R_\star}\right)^2 - \left(\frac{a}{R_\star}\ \cos i\right)^2} \tag{1.6}$$

From equations 1.5 and 1.2, the impact parameter $b$ – projected distance between the planet and star centres – can be derived from the light curve parameters as follows

$$b \equiv \frac{a}{R_\star}\cos i = \sqrt{\frac{(1 - \sqrt{\delta})^2 - [\sin^2(t_F\pi/P)/\sin^2(t_T\pi/P)](1 + \sqrt{\delta})^2}{1 - [\sin^2(t_F\pi/P)/\sin^2(t_T\pi/P)]}} \tag{1.7}$$

Under the approximation that $a >> R_\star$, $t_T\pi/P << 1$, and the equation 1.7 simplifies to

$$b = \sqrt{\frac{(1 - \sqrt{\delta})^2 - (t_F/t_T)^2](1 + \sqrt{\delta})^2}{1 - (t_F/t_T)^2}} \tag{1.8}$$

The planet orbital distance normalised by the stellar radius $a/R_\star$

$$\frac{a}{R_\star} = \sqrt{\frac{(1 + \sqrt{\delta})^2 - b^2[1 - \sin^2(t_T\pi/P)]}{\sin^2(t_T\pi/P)}} \tag{1.9}$$

Under the approximation that $a >> R_\star$, from equation 1.6 and 1.8, $a/R_\star$ can be expressed more simply as follows

$$\frac{a}{R_\star} = \frac{2P}{\pi}\frac{\delta^{1/4}}{\sqrt{t_T^2 - t_F^2}} \tag{1.10}$$

Using Kepler's $3^{rd}$ law[7] ($\frac{P^2}{4\pi^2} = \frac{a^3}{G(M_\star + M_p)}$), where $G$ is the gravitational constant, and under the approximation that $M_{\rm p} << M_\star$, the planet orbital distance $a$ can also be derived as

$$a = \left( \frac{P^2 G M_\star}{4\pi^2} \right)^{1/3} \tag{1.11}$$

From the definition of $b$ (equation 1.7), the planet orbital inclination projected onto the plane of the sky, $i$, can be derived as

$$i = \cos^{-1}\left(b \frac{R_\star}{a}\right) \tag{1.12}$$

Using Kepler's $3^{rd}$ law under the approximation that $M_{\rm p} << M_\star$, and equation 1.9, the stellar density $\rho_\star$ defined as follows, can be derived from the light curve parameters.

$$\rho_\star \equiv \frac{M_\star}{R_\star^3} = \frac{4\pi^2}{P^2 G} \left( \frac{a}{R_\star} \right)^3 = \frac{4\pi^2}{P^2 G} \left( \frac{(1+\sqrt{\delta})^2 - b^2[1 - \sin^2(t_T \pi / P)]}{\sin^2(t_T \pi / P)} \right)^{3/2} \tag{1.13}$$

Under the approximation that $a >> R_\star$ and that $M_{\rm p} << M_\star$, using Kepler's $3^{rd}$ law and equation 1.10, $\rho_\star$ can be expressed more simply as follows

$$\rho_\star = \frac{32P}{G\pi} \frac{\delta^{3/4}}{(t_T^2 - t_F^2)^{3/2}} \tag{1.14}$$

Under the approximation that $M_{\rm p} << M_\star$, reversing equation 1.13, if the stellar mass and radius are known, the planet orbital period can be derived from a single-transit light curve as follows

$$P = \sqrt{\frac{R_\star^3}{M_\star} \frac{4\pi^2}{G} \left( \frac{(1+\sqrt{\delta})^2 - b^2[1 - \sin^2(t_T \pi / P)]}{\sin^2(t_T \pi / P)} \right)^{3/2}} \tag{1.15}$$

The equation of $P$ simplifies to the following one, under the approximation that $a >> R_\star$, using Kepler's $3^{rd}$ law under the approximation that $M_{\rm p} << M_\star$ and equation 1.14.

$$P = \frac{M_\star}{R_\star^3} \frac{G\pi}{32} \frac{(t_T^2 - t_F^2)^{3/2}}{\delta^{3/4}} \tag{1.16}$$

#### Equations for an eccentric orbit

The equations presented above can be used to derive the planet parameters from the transit light curve of a planet in a circular orbit. The equation to derive the planet-

[7] Kepler's $3^{rd}$ law: "The square of the orbital period of a planet is directly proportional to the cube of the semi-major axis of its orbit."

to-star radius ratio $R_{\rm p}/R_\star$ is the same for a circular and for an eccentric orbit, as the equation is not dependent on the eccentricity $e$ and the argument of periastron $\omega$. The elements of an eccentric orbit used here after are as defined in Figure 1.3.

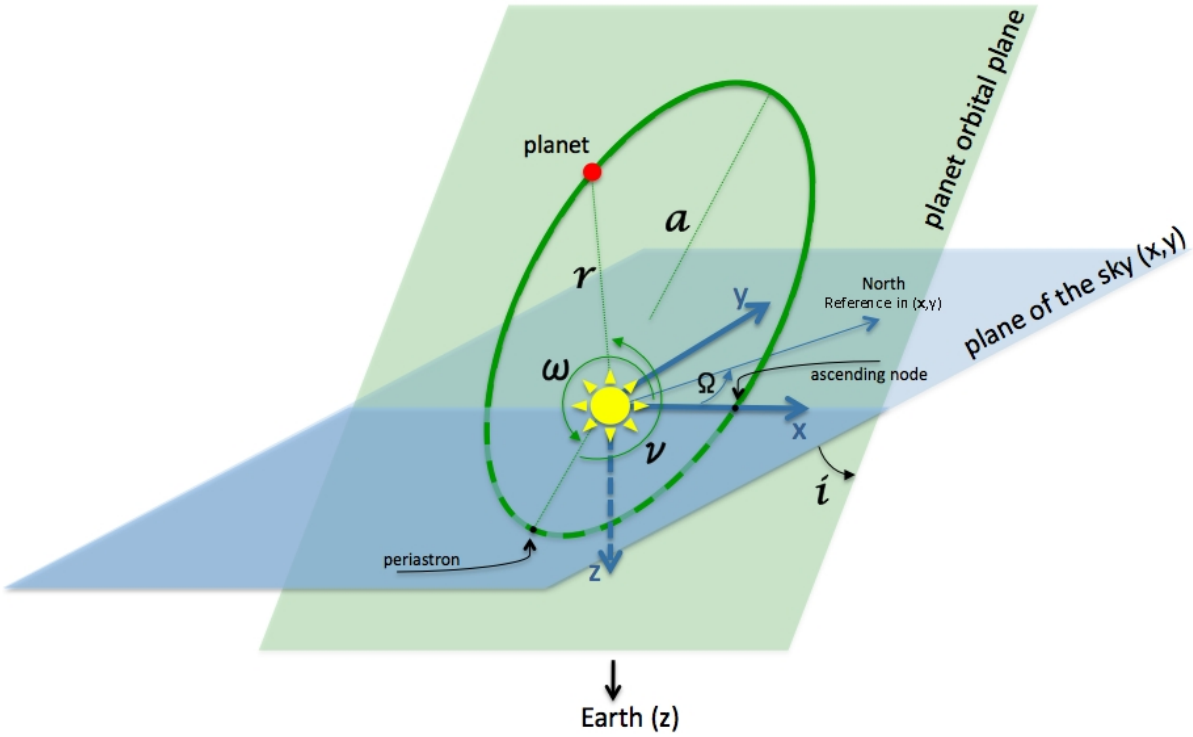


Figure 1.3: Sketch of a planet in an eccentric orbit around its host star. $a$ is the semi-major axis of the planet's orbit, $r$ is the planet to star distance, $i$ is the inclination of the planet's orbit with regards to the plane of the sky, $\nu$ is the true anomaly of the planet (i.e. the position angle from the periastron of the planet in its orbit), $\omega$ is the argument of periastron of the planet's orbit (i.e. the position angle of the periastron from the ascending node where the planet moves North through the plane of the sky) and $\Omega$ is the longitude of the ascending node (i.e. the angle in the plane of the sky between the North direction and the ascending node). The North is a reference direction in the plane of the sky corresponding to the direction of the North pole projected onto this plane.

Kepler's $1^{st}$ law[8] defines the equation of an ellipse. Applied to exoplanets, this gives the following relation for the star-planet distance $r$ in an eccentric orbit:

$$r = \frac{a(1-e^2)}{1+e\cos\nu} \tag{1.17}$$

where a is the semi-major axis of the orbit, $e$ is the eccentricity of the orbit ($e = \sqrt{1-\left(\frac{b}{a}\right)^2}$ with $b$ the semi-minor axis of the orbit), and $\nu$ is the true anomaly (the angle between the direction to the ascending node and the direction to the position of the planet in the orbit, see Figure 1.3).

[8]Kepler's $1^{st}$ law: "The orbit of every planet is an ellipse with the Sun at a focus"

If the planet transits its host star, the orbital inclination $i \approx 90^o$, and the true anomaly of the planet at mid-transit can be simplified to $\nu_c = \pm\frac{\pi}{2} - \omega$ ("+" for mid-transit and "-" for mid-occultation). As $\cos(\pm\frac{\pi}{2} - \omega) = \pm\sin\omega$, the star-planet distance at conjunction $r_c$ can be expressed as

$$r_c = \frac{a(1-e^2)}{1 \pm e\sin\omega} \tag{1.18}$$

The impact parameter is $b \equiv \frac{r_c}{R_\star}\cos i$ (same definition as in equation 1.7 but replacing $a$ by $r_c$). Using equation 1.18, $b$ can thus be expressed for an eccentric orbit as follows

$$b = \frac{a}{R_\star}\cos i\left(\frac{1-e^2}{1 \pm e\sin\omega}\right) \tag{1.19}$$

This equation compares to the definition of $b$ in a circular orbit (equation 1.7) by multiplying this expression by $\frac{1-e^2}{1\pm e\sin\omega}$ ("+" for mid-transit and "-" for mid-occultation).

$t_T$ and $t_F$ for an eccentric orbit should be solved numerically using Kepler's equations (Equation 1.27). Winn (2010) proposes, as a good approximation for eccentric orbits, to multiple $t_T$ and $t_F$ (calculated with the eccentric expression of $b$) by the following factor which accounts for the altered sky-projected speed of the planet at conjunction:

$$\frac{\dot{X}(\nu_c)\ [e=0]}{\dot{X}(\nu_c)} = \frac{\sqrt{1-e^2})}{1 \pm e\sin\omega} \tag{1.20}$$

where $X$ is the position of the planet in the plane of the sky along the axis towards the ascending node (see Figure 1.3), $\dot{X}(\nu_c)$ is the velocity of the planet along this axis at conjunction ("+" is for mid-transit and the "-" for mid-occultation), and $\dot{X}(\nu_c)\ [e=0]$ is the value of this velocity for a circular orbit.

### Limb darkening

In reality, the stellar luminosity is not constant across the stellar disk. The stellar disk is brighter at its centre than at its edge. The photons received from the centre of the stellar disk come from deeper into the stellar atmosphere than those received from the edge of the disk. A photon coming from deeper into the stellar atmosphere has a higher temperature and thus appears brighter at the associated wavelength. Thus, at the corresponding wavelength, the stellar centre appears brighter than the stellar limb, hence the expression "limb darkening".

Using a realistic model of stellar limb darkening is important when fitting transit light curves, as the shape of the limb darkening will influence the derived planet parameters (mainly the planet radius and impact parameter on the stellar disk).

There are different limb darkening laws proposed in the literature to model the varia-

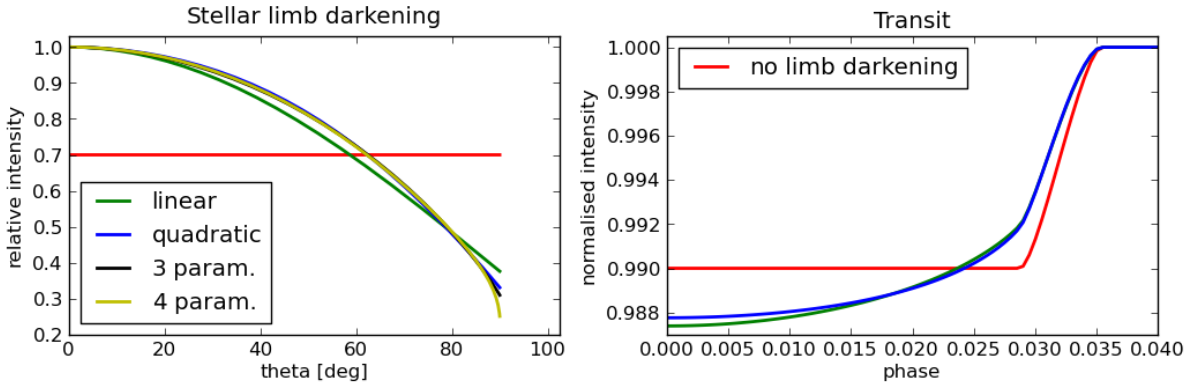


Figure 1.4: Left panel: Solar limb darkening in CoRoT bandpass with the linear law (green), the quadratic law (blue), the non-linear 3 parameter law (black), and the non-linear 4 parameter law (yellow). Right panel: The second half of the phase-folded transit of a Jupiter-size planet at $a/R_\star$=5 of a solar type star ($T_{\rm eff}$=5800K, $\log g$=4.5, (M/H)=0.0) seen in the CoRoT bandpass with no stellar limb darkening (red), a quadratic stellar limb darkening (blue) and a linear stellar limb darkening (green).

tion of intensity across the stellar disk: e.g. the linear law, the quadratic law, the square root law, the logarithmic law, the non-linear law (Claret 2000), and the 3-parameters non-linear law (Sing 2010). To date, the most commonly used when fitting transiting exoplanet light curves are the linear, the quadratic and the non-linear laws. In light curves with high precision photometry, the linear law is insufficient to correctly reproduce the intensity variation over the stellar disk (e.g. Brown et al. 2001). The quadratic law is valid in certain ranges of stellar effective temperatures; for main sequence stars this law is accurate within 3% of the transit depth (Mandel & Agol, 2002) which can become insufficient to model high precision photometry light curves (e.g. bright stars observed with HST, CoRoT or Kepler). The non-linear law is valid over a large range of stellar models. The 3-parameter non-linear law was introduced to better reproduce the limb darkening at small angles $\theta$ (angle between the line of sight and the emergent intensity). This law is very similar to the non-linear law but does not model a sharp drop in luminosity at small $\mu$.

This intensity variation across the stellar disk is calculated from stellar atmosphere models (e.g. ATLAS9[9], PHOENIX[10]) where the emergent intensity with regard to the line of sight is known. This intensity is then passed through different instrumental filters (e.g. the standard filters in Claret 2000 and Claret 2004, and the CoRoT and Kepler filters in Sing 2010), and fitted with different limb darkening laws to derive the associated limb darkening coefficients.

[9]http://kurucz.harvard.edu/grids.html
[10]http://www.hs.uni-hamburg.de/EN/For/ThA/phoenix/index.html

The linear law:

$$\frac{I(\mu)}{I(\mu=1)} = 1 - u(1-\mu) \tag{1.21}$$

The quadratic law:

$$\frac{I(\mu)}{I(\mu=1)} = 1 - u_a(1-\mu) - u_b(1-\mu)^2 \tag{1.22}$$

The non-linear law:

$$\frac{I(\mu)}{I(\mu=1)} = 1 - u_1(1-\mu^{1/2}) - u_2(1-\mu) - u_3(1-\mu^{3/2}) - u_4(1-\mu^2) \tag{1.23}$$

The 3-parameter non-linear law:

$$\frac{I(\mu)}{I(\mu=1)} = 1 - u_2(1-\mu) - u_3(1-\mu^{3/2}) - u_4(1-\mu^2) \tag{1.24}$$

where, $I(\mu=1)$ is the intensity at the centre of the stellar disk, $\mu = cos(\theta)$ with $\theta$ the angle between the line of sight and the emergent star light, $u$ is the linear limb darkening coefficients, $u_a$ and $u_b$ are the quadratic limb darkening coefficients, and $u_n$ are the limb darkening coefficients of the non-linear law.

In practice, the choice of which limb-darkening law to use depends on the signal-to-noise ratio ($S/N$) of the transit, the observational bandpass and the stellar type. High $S/N$ observations allow the shape of the limb darkening to be more accurately constrained, and so can justify the usage of a limb-darkening law with more coefficients.

#### Equations for a non-uniform intensity across the stellar disk

Mandel & Agol (2002) give a list of analytic functions to model transit light curves which include limb-darkening (quadratic and non-linear laws). The function to be used depends on the size (radius) of the planet relative to the star and on the position of the planet on the stellar disk. The exact analytic formulae are given in Mandel & Agol (2002), as well as a simpler version (less computing time) valid for small planets ($\frac{R_{\rm p}}{R_\star} \leq 0.1$) where the stellar brightness under the disk of the planet can be approximated as a constant.

Giménez (2006) also presents analytic functions to model the transit light curves. There is little difference between their formalism and that of Mandel & Agol (2002).

Throughout this thesis, I perform the modelling of transit light curves using the analytical equations of Mandel & Agol (2002) for transit light curves with quadratic limb darkening (or linear limb darkening by setting the second coefficient of the quadratic law to zero). Eric Agol kindly provides an IDL implementation of their formulae[11], which I made use of in Chapters 2 and 3.

[11] http://www.astro.washington.edu/users/agol

### 1.3.2 Analytic equations for the radial velocity variations of a star due to an orbiting planet

The equations listed in this subsection are based on those given in the Celestial Mechanics chapter of J. B. Tatum[12].

The equation for radial velocity variations $V$ of a star due to an orbiting planet is derived as:

$$V = V_0 + K_\star(\cos(\omega_\star + \nu_\star) + e\cos\omega_\star) \tag{1.25}$$

where $V_0$ is the mean radial velocity of the star-planet centre of mass with regards to the observer, $K_\star$ is the semi-amplitude of the radial velocity variations, $\omega_\star$ is the argument of periastron of the star's orbit around the star-planet centre of mass ($\omega_\star = \omega_p + \pi$), $\nu_\star$ is the true anomaly of the position of the star on its orbit around the star-planet centre of mass ($\nu_\star = \nu_p + \pi$), and $e$ is the eccentricity of the stellar orbit (same as that of the eccentricity of the planet's orbit).

Equation 1.25 is a function of the true anomaly which is itself a function of time. To solve this equation, the true anomaly needs to be known. This is done by using the mean anomaly $M$ (equation 1.26) to derive the eccentric anomaly $E$ (equation 1.27), which is then used to derive the true anomaly $\nu$ (equations 1.29 and 1.30).

The mean anomaly $M$ at a time $t$ (angle covered at the average angular speed $\frac{2\pi}{P}$ since the last passage at periastron) is defined as:

$$M = \frac{2\pi}{P}(t - T) \tag{1.26}$$

where $P$ is the orbital period of the planet and $T$ is the time at the last passage at the periastron.

The eccentric anomaly $E$ (projection of the true anomaly on a circle with radius equal to the orbital semi-major axis) can be derived from Kepler's equation:

$$M = E - e\sin E \tag{1.27}$$

where, $e$ is the eccentricity of the orbit.

This equation cannot be solved analytically and is solved numerically, e.g. using the Newton-Raphson method. This method consists of finding a better value at each iteration using the value found at the previous iteration, the expression of the function and its derivative: $x_{n+1} = x_n - \frac{f(x_n)}{f'(x_n)}$. In the present case of deriving the eccentric anomaly

[12]http://astrowww.phys.uvic.ca/~tatum/celmechs.html

$E$, $f(E_n) = E_n - e\sin E_n - M$ which becomes:

$$E_{n+1} = \frac{M - e(E_n \cos E_n - \sin E_n)}{1 - e\cos E_n} \tag{1.28}$$

The true anomaly is related to the eccentric anomaly through the following equations:

$$\cos\nu = \frac{\cos E - e}{1 - e\cos E} \tag{1.29}$$

$$\sin\nu = \frac{\sqrt{1-e^2}\sin E}{1 - e\cos E} \tag{1.30}$$

The mass of the planet $M_{\rm p}$ relative to the mass of its host star $M_\star$ can be derived as follows, using the $K_\star$ measured from the radial velocity curve of the star (see Figure 1.5):

$$\frac{M_p \sin i}{(M_\star + M_p)^{2/3}} = K_\star \left(\frac{P}{2\pi G}\right)^{1/3} \sqrt{1-e^2} \tag{1.31}$$

where $i$ is the orbital inclination and $G$ is the gravitational constant. If $M_p << M_\star$ then:

$$M_p \sin i = K_\star \left(\frac{P M_\star^2}{2\pi G}\right)^{1/3} \sqrt{1-e^2} \tag{1.32}$$

When a planet transits in front of its star, it creates during the transit a perturbation in the radial velocity (RV) variations of the host star (see Figure 1.5). This effect is called the Rossiter-McLaughlin (RM) effect. The shape of the perturbation depends on the inclination of the planet's orbital plane to the stellar spin axis. For transiting planets small in mass and/or with large orbits, the planet can create a larger amplitude RM effect than the RV variations of its star. Combined with the fact that the RM variation occurs on a shorter timescale than the RV variation, the RM effect will be a useful tool to confirm the planetary nature of small transiting planets orbiting in large orbits (Gaudi & Winn, 2007).

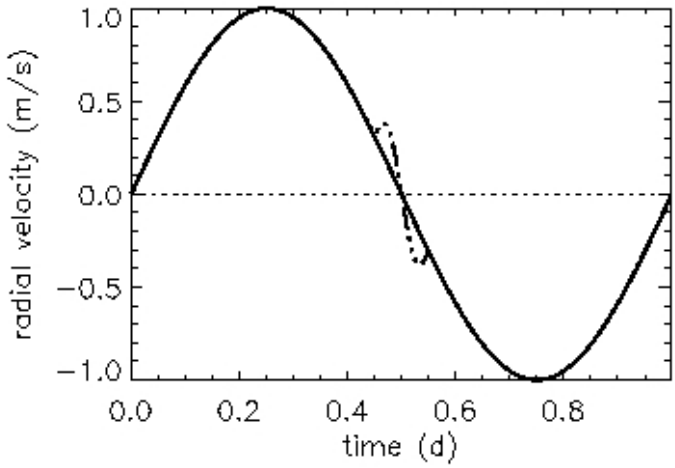


Figure 1.5: The radial velocity curve of a star orbited by a planet a few times more massive than the Earth, in a circular orbit (black line). The semi-amplitude of the radial velocity variation is called $K$, the period of the variation is the planet orbital period $P$. Here, $P = 1$, $K = 1$, and the mid-transit is at 0.5 d. The dashed-dotted blip is the spectroscopic transit of the planet, called the Rossiter-McLaughlin effect, which adds up to the star's radial velocity curve if the planet transits the stellar disk. Here, the sky-projected spin axis of the planet's orbit projected onto the sky is aligned with the sky-projected stellar rotation axis.

### 1.3.3 Planetary atmospheres

Transmission spectroscopy of a planet's atmosphere can be performed during its transit. Emission spectroscopy of a planet's disk can be performed during occultation, where light from the star and the planet can be separated. In addition the planet's orbital phase variations can be observed. The above techniques allow the study of some properties of the planet, such as the chemical composition of the planet's atmosphere, the planet's atmospheric circulation, the presence of clouds or hazes, the thermal emission of the planet, and the planet's albedo.

The transmitted spectrum of the upper atmosphere of an exoplanet is obtained by observing the transit of the planet in different wavelengths. Some chemical elements in the atmosphere will strongly absorb particular wavelengths of the starlight that pass through the planet's atmosphere, this makes the planet appear larger at these wavelengths. This type of observations has been performed from space using the Hubble Space Telescope (HST).

When planets are occulted by their star, the loss in received brightness is due to the planet's emission being obstructed by the star. The planet's emission has a component of stellar reflected light and a component of thermal emission. The thermal emission of the planet can be studied by measuring the depth of the occultation at long wavelengths (e.g. in the $I$ band and at redder wavelengths) where it dominates

over the stellar reflected light component. The first approximation made to derive the temperature of the planet, is to consider that the planet emits like a black body. In reality, if some of the planet's thermal flux is absorbed by molecules in its atmosphere, at this wavelength the depth of the occultation will appear smaller, thus giving a smaller temperature. Observing the occultation at multiple long wavelengths would allow the observation of the shape of the planet's black body due to thermal emission, and to derive a more realistic planet temperature. For instance, observations of the occultation of some transiting exoplanets have been made from space with the Spitzer Space Telescope (SST), and from the ground with the Very Large Telescopes (VLT) and soon the Gran Telescopio Canarias (GTC).

When observing the occultation of an exoplanet at shorter wavelength (e.g. in the optical), the dominant component of the planet emission is the stellar reflected light. The depth of the occultation due to the loss of the stellar light reflected by the planet, allows one to derive the albedo of the planet. However, if the planet's thermal emission is not negligible at the observed wavelength, the albedo cannot be uniquely calculated from the depth of the planet's occultation at only one wavelength. If multiple short and mid wavelength observations of the depth of the planet's occultation can be performed, then the wavelenght distribution of reflected stellar light and of the planet thermal emission can be obtained. These two components of the planet's flux can then be separated from each other, and both the albedo and the thermal emission can be extracted. For instance, observations of exoplanet occultations in the optical have been performed from space using CoRoT and Kepler, and from the ground using the VLT for instance.

Differential spectroscopy consists of taking the spectrum of the light received from the star-only during the planet's occultation, and from the star-and-planet when the planet emerges from the occultation. By comparing the two spectra, one can extract a low-signal emission spectrum of the planet.

When the photometric orbit of the exoplanet is followed from one transit to the next, the orbital phases of the planet – variation in flux due to the varying visible fraction of the planet's day-side – can be observed. At long wavelengths, if the phase of the maximum of this modulation is shifted from the phase of the planet's occultation, it indicates that strong winds in the planet's atmosphere are blowing the point of maximum heat on the planet away from the point directly facing the host star. This is a measurement of the planet's atmospheric circulation. At short wavelengths, the phase modulation of the planet depends on the properties of the particle reflecting the light. Ice has a uniform phase function as it has the same intensity seen from different angles, whilst water has a more complicated phase function, as for instance oceans appear darker seen from directly above than from an angle.

The amplitude of all the effects mentioned above can be two orders of magnitude smaller than the planet's transit signal (depending on the eccentricity of the orbit, the

size of the planet and its distance to the host star), and their observation requires high precision photometry (large collecting area, stable instruments).

## 1.4 Challenges for the detection and characterisation of exoplanets

Limitations in the detection and characterisation of an exoplanet can come from different sources, and depend on each planet, star and instrument used. For instance, the characterisation of CoRoT-7b is limited by stellar activity affecting the measure of the mass of the planet, whilst the characterisation of the OGLE planets is limited by the poor determination of the stellar parameters due to the star's faintness.

### 1.4.1 Stellar systems mimicking planetary transits

Stellar systems mimicking planetary transits create false alarms in the search for transiting exoplanets. The systems of stars that can create planetary-transit-like light curves are listed bellow.

Small stars, brown dwarfs and gas giant planets have similar sizes, so have similar transit depths in a light curve. However, as these objects have different masses, they can be differentiated using radial velocity measurements of their host stars to derive the mass of the transiting object. OGLE-TR-122 is an example of a planetary-like candidate discovered using the transit method and confirmed by radial velocity measurements to be a low mass star (Pont et al., 2005).

If the host star is a giant star, a Jupiter-like transit depth (1%) would be caused by a stellar companion and not a planet. This is due to the fact that the transit depth gives the radius of the companion relative to the radius its host star, so for the same transit depth, a larger star means a larger companion. This false detection can be ruled out from the transit light curve which allows one to derive an estimate of the stellar density $M_\star^{1/3}/R_\star$ (Seager & Mallén-Ornelas, 2003), giant stars being less dense than main sequence stars as they have a larger radius.

Grazing binaries are another source of false detections as only a fraction of the disk of the transiting star crosses the stellar disk, causing the transit to be shallower and thus more planetary-like. These events can be identified from the light curve by analysing the shape of the transit, as grazing binaries have V-shaped transits and planetary transits are more U-shaped (due to limb darkening and radius ratio).

An eclipsing binary pair blended with a third star physically associated (triple system) or aligned by chance in the line of sight (background or foreground eclipsing binaries), can mimic a planet transit light curve as the real depth of the eclipse is diluted by the light of the third star. A case of an eclipsing binary pair blended with a third

star can be identified by detecting a double peak when cross-correlating the spectra of the blended stars with model stellar spectra, or by resolving the blend with high spatial resolution imaging (e.g. WASP-9b was retracted from the list of planets as later, through spectroscopy, identified as the member of a stellar binary). For high precision photometry light curves, another method is to compare the stellar density derived from the light curve (equation 1.13) with the stellar density derived from the observed spectral type; if the two are very different it indicates that the transit is diluted by the light of another star (Seager & Mallén-Ornelas, 2003).

Colour photometry can also be used to differentiate between a planetary transit and an eclipsing binary (e.g Tingley 2004) as the transit depth of planets will be quasi colour independent (the planet is dark compared to its host star), while the transit of a star is colour dependent and will have different depths at different wavelengths.

### 1.4.2 Systematics

The noise in a light curve is not purely gaussian (white noise), but has a component of correlated noise (red noise, Pont et al. 2006) mainly due to atmospheric effects for ground observations (e.g. scintillation, transparency variations, over-flights of satellites and planes, moon), or to instrumental effects for space observations (e.g. hot pixels due to cosmic rays, telescope jitters due to thermal shocks or battery ignitions).

Systematics in the transit light curve reduce the detectability of planets and limit the characterisation of the planet. These systematics can be instrumental, and/or atmospheric when observing from the ground. For instance, in the detailed analysis of the CoRoT light curves in Chapter 4, hot pixels create systematic noise which are difficult to filter out in an automated way and which affect the detection of low amplitude signals such as secondary eclipses and planet orbital phases.

### 1.4.3 Stellar activity

Stellar variability is another source of correlated noise superimposed onto the planet signal in the stellar light curve and radial velocity curve.

Stellar variability is caused by physical processes which have different time scales. Stellar magnetic activity, i.e. variations in magnetic field lines over time, is the main cause of stellar variation. The magnetic field is created by the dynamo effect of moving charged particles in the stellar plasma, e.g. due to differential rotation between the stellar core and the stellar convective envelope for main sequence stars. The differential rotation also causes magnetic lines to twist and break allowing the material trapped in the field of the broken magnetic line to rise and emerge from the stellar surface carrying hot material out, and cooled material back into the stellar surface. The regions where the hot material emerges from the sub-surface, along the field lines, appear brighter (plages). The regions where the cooled material sinks back into the

stellar surface, along the field lines, appear darker (spots). As the star rotates, the stellar spots and plages appear and disappear on the visible side of the star, which changes the stellar brightness at the timescale of the stellar rotation. The number of spots and plages also evolve in time over longer timescales (e.g. the 11-years solar activity cycle). These magnetic-field-induced stellar variations produce photometric and spectroscopic stellar variability on time scales from days to weeks (stellar rotation) and from month to years (stellar activity cycles). The amplitudes of these variations are larger than the that of the two other processes described hereafter, and is comparable or larger than the amplitude of planetary transits.
Stellar granulations arise from the convection of hot material being brought from the stellar subsurface to the surface, due to thermal difference between the two surfaces. This process creates variations in stellar brightness at shorter time scales (hours).
Stellar oscillations are due to the displacement of stellar material under the convection which produces pressure and gravity waves on the material of the stellar surface. This process creates stellar variability at higher frequencies (minutes).

Stellar activity is dependent on stellar type/mass, and stellar age. This dependence comes from the internal structure of the star along with the presence, size, and position of a stellar convective envelope. Stars with smaller convection envelopes (e.g. massive stars emitting more flux), will show smaller level of activity.
The dependence on stellar age comes from the stellar rotation rate driving the differential rotation between the stellar core and the convective envelope, which is the magnetic field production mechanism for main sequence stars (stars with a hydrogen burning core). Stars rotating faster display a higher activity level. Young stars have larger rotation rates (i.e. are more active) as they have gained angular momentum through contraction under the gravity.
The dependence on mass also comes from the ability for the star to form a radiative core, as radiative pressure will halt the stellar contraction. The stars then stop gaining angular momentum, and the dissipation of its angular momentum (e.g. though disk locking) will force the star to spin down, thus reducing the activity level for older stars. Lower mass stars ($M_\star$<0.5$M_\odot$) will not start the hydrogen burning phase, will not develop a radiative core, and will maintain their activity level longer. As a comparison, the Sun (G-type on the main sequence) is a relatively aged star, it is a slow rotator and has a low level of activity.
Favata & Micela (2003), Schrijver & Zwaan (2000) and Aigrain et al. (2004) provide detailed information on the dependency of stellar activity with stellar type, mass and age, and on the physical processes behind the different timescales of the stellar activity.

The photometric and radial velocity amplitude of stellar variability can easily be larger than the amplitude of the signal of a planet, which can affect the detection of the later by creating false alarms and reducing the amplitude of the real signal, especially in the regime of small planets (see Jenkins 2002 for a study on the impact of

solar-like variability on the detectability of transiting exoplanets). Stellar variability also hinders the characterisation of the detected planets as it adds correlated noise to the planet signal, reducing the precision and altering the accuracy of the derived planet parameters.

As the star rotates, a stellar spot on its surface will hide a part of the stellar surface rotating towards us and then a part rotating away from us, creating red-shifted and blue-shifted perturbations respectively. To identify radial velocity variations due to stellar activity and remove it to some extent, several techniques are combined (see Boisse et al. 2009 for a detail explanation and application of these techniques). To average over the high frequencies of the stellar activity due to oscillations for instance, longer exposures ($\sim$1h) can be taken. To remove the stellar activity components due to granulation, a boxcar smoothening (few hours) can be applied. The stellar activity component due to spots and plages are more difficult to remove as their amplitude in radial velocity can be larger than that of the planet signal. Techniques to identify radial velocity variations due to stellar activity at long times scales include the photometric follow-up of the star simultaneous to the radial velocity measurements, the analysis of the correlation between the radial velocity variations and the variations in the bisector of the cross-correlation peak of the stellar spectra, or with the variations in CaII H&K lines, $H_\alpha$ line and HeI line (spectroscopic indices for stellar activity).

Different filters are used by different teams to remove the photometric stellar variability from the stellar light curves due to the flux variations intrinsic to the star. Unfortunately, these filters degrade the information on the transit shape, as the transit signal and the stellar activity frequency domains overlap. This results in the physical parameters of the planet being mis-estimated. This is discussed in the Chapter 2 and a new method to filter the stellar variability with minimum alteration to the transit signal is then presented.

The stellar variability can also affect the observation of the atmosphere of the exoplanet. The variation in stellar flux due to the activity is chromatic, so the multi-wavelength observations of the planet's transit and occultation need to be performed over an interval of time shorter than the timescale of the stellar variability.

### 1.4.4 Uncertainties on the planet parameters

The uncertainties in the mass, radius, and inclination of a planet depend on the uncertainties of the host star's mass and radius ($M_\star$, $R_\star$), on the uncertainties on the transit parameters ($\delta$, $t_F$, $t_T$), and on the uncertainties on the radial velocity measurements. For large planets (larger than Jupiter), the uncertainties on the planet mass and radius are mainly due to the uncertainties on the stellar parameters. For smaller planets (smaller than Uranus) around active stars, the uncertainties on the planet mass and radius can be dominated by the uncertainties on the transit parameters. Figure 1.6 shows the contribution to the uncertainties in a planet's mass and radius coming from

the stellar parameters (in blue) and from the transit parameters (in black).

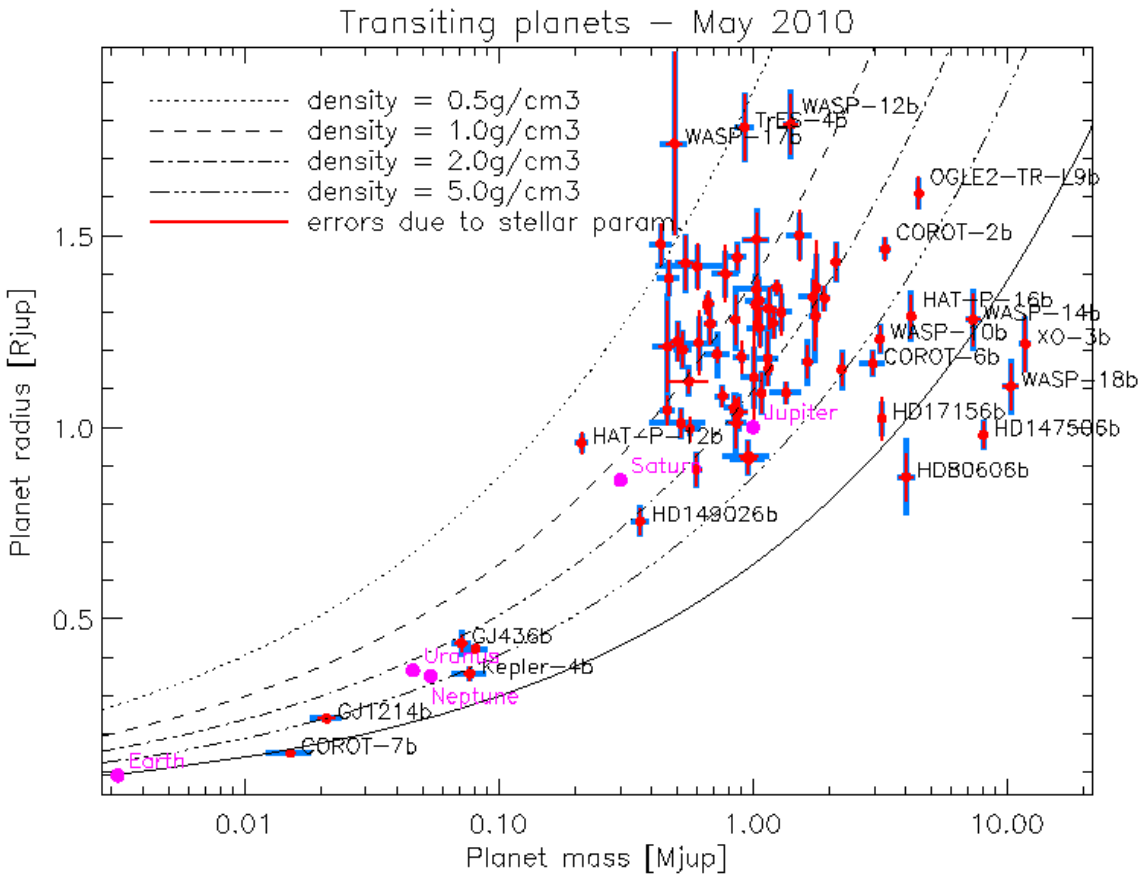


Figure 1.6: Mass-radius diagram of the transiting planets discovered to date (May 21th 2010) with the error bars on the planet's mass and radius with the contribution from the uncertainties in the transit parameters (black) and the contribution from the uncertainties in the stellar parameters (blue). The planet masses and radii are taken from http://www.inscience.ch/transits/, except for CoRoT-7b which is taken from http://exoplanet.eu/catalog-transit.php. The uncertainties in the planet parameters due to the stellar parameters are calculated by propagating the uncertainties in the stellar parameters assuming the measurements for the transit and radial velocity curves have no uncertainty.

## 1.5 Instruments for the detection and characterisation of transiting exoplanets

### 1.5.1 Current

CoRoT (COnvection ROtation and planetary Transits), is a French-ESA (European Space Agency) satellite with 27-cm diameter mirror and a 3x3$^o$ field of view. It has been in orbit around the Earth since December 2006 and searches for short period exoplanets with radii down to few times that of the Earth. CoRoT looks at stars with V magnitude in the range 11 to 16 V, in 4 different areas in the galactic plane each year (20 to 150 days on each field). In this thesis, the light curves of the CoRoT planets are studied.
Kepler is a NASA (National Aeronautics and Space Administration) satellite with a 95-cm diameter mirror and a 10$^o$ field of view. It has been in an Earth-trailing heliocentric orbit since March 2009 and searches for exoplanets similar to the Earth in terms of size, orbital distance and stellar host type. Kepler looks at stars with V magnitude in the range of 9 to 16, in a single area of the sky (continuously for 3.5 years).
In 2009, CoRoT found a close-in Earth-like planet around a solar type star, and Kepler is expected to detect several more of these. Follow-up observations of these objects, for mass measurement and atmosphere characterisation, are challenging as these planets are small compared to their host stars. For smaller stars, e.g. M-dwarfs ($\sim$0.1$M_\odot$, $\sim$0.1$R_\odot$, $\sim$3000 K), an Earth-size planet in the habitable zone[13] will have a larger radius ratio and mass ratio with its star and will be closer to the star, making its transit and gravitational tug easier to detect. The atmosphere of these Earth-size planets will also be easier to detect through transmission spectroscopy as the atmosphere can be thicker for lower mass, lower gravity planets. MEarth is a ground-based mission with a set of eight 40-cm telescopes searching for super-Earths around small stars. RoPACS (Rocky Planets Around Cool Stars) is a network using the UKIRT (United Kingdom Infrared Telescope) to search for transiting planets around cool stars.
SuperWASP (Wide Angle Search for Planets) and HATNet (Hungarian Automated Telescope Network) are ground based missions searching for transiting exoplanets around bright stars across the sky ($\sim$9 mag).
Precise radial velocity measurements are currently done with the HARPS spectrograph on the 3.6 m telescope at ESO-La Silla Observatory in Chile, and with the HIRES (High Resolution Echelle Spectrometer) spectrograph on the 10 m Keck-1 telescope at the Keck Observatory in Hawaii. With these current high-resolution spectrographs, stellar radial velocity variations down to 0.3 to 1 ms$^{-1}$ can be detected, which corresponds to the signal of a close-in Super-Earth planet.
Other spectrographs with precision down to 10 ms$^{-1}$ are used in the search and follow-up of exoplanets, such as SOPHIE at the Observatoire de Haute Provence in France

[13]The habitable zone around a star is defined as the range in distance from the star where water can be in its liquid state

which is optimised for the search for exoplanets.
Figure 1.7 shows the planet detection limits for different instruments with different photometry and radial velocity precisions, and different lengths of survey.

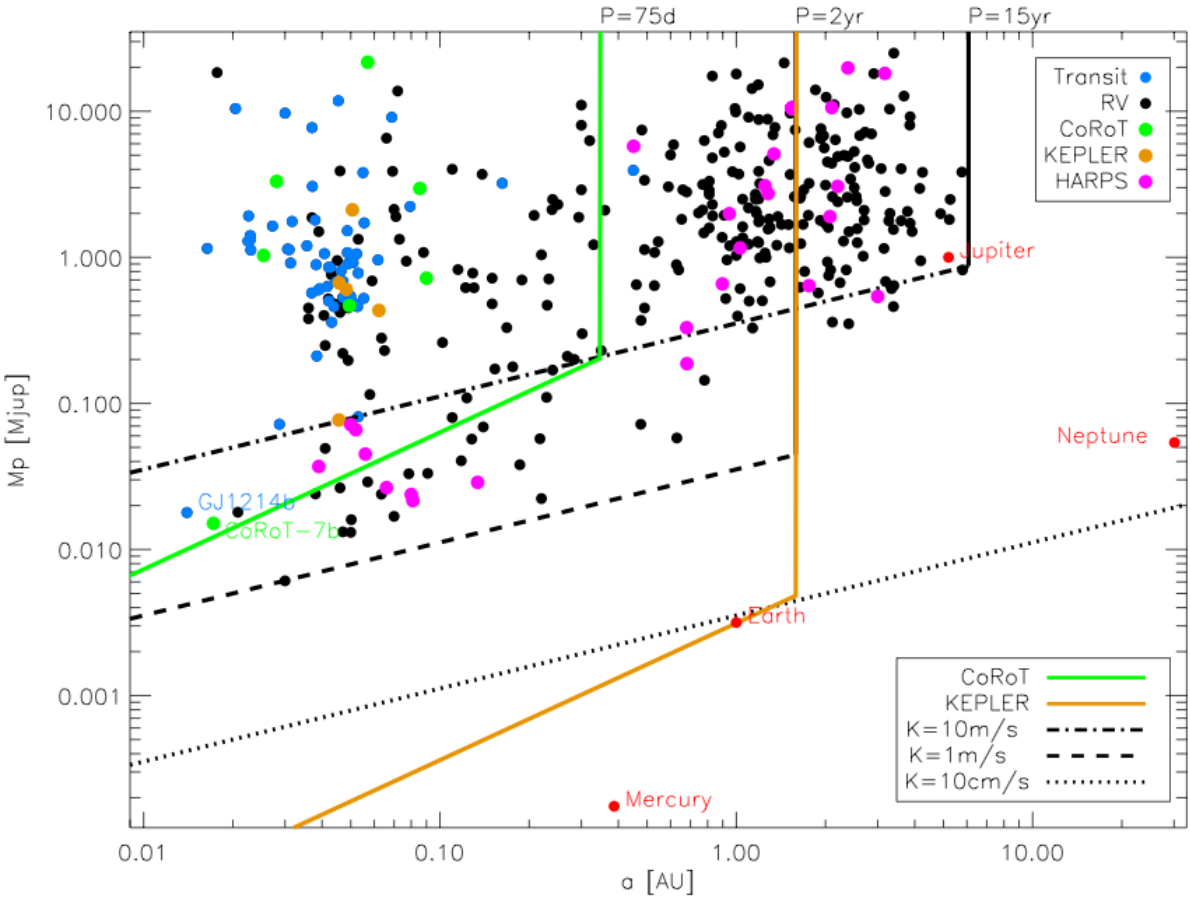


Figure 1.7: Diagram of the planet mass $M_{\rm p}$versus orbital semi-major axis $a$ of the exoplanets discovered by Jan 26th 2010 with the transit method (blue, green, and orange dots) and with the radial velocity method (black and pink dots). The diagonal black lines mark the detection limits in planet mass-separation for a planet around a ($M_{\odot}$,$R_{\odot}$) star using instruments with precision in radial velocity measurements of 10 ms$^{-1}$(dashed-dotted line), 1 ms$^{-1}$(dashed line), and 10 cms$^{-1}$. The diagonal green and orange lines mark the detection limits in planet mass-separation for a planet around a ($M_{\odot}$,$R_{\odot}$) star using CoRoT and Kepler respectively. These lines are drawn for an observation of at least two transits with combined signal-to-noise ratio of 20, in a light curve with a photometric precision of 200ppm for CoRoT (Aigrain et al., 2009) and 10ppm for Kepler (Jenkins et al., 2010) – ppm = parts per million, 100ppm = 0.1 mmag. The vertical lines mark the upper limits in planet to star separations – detection of at least two orbital periods to secure the periodicity of the signal – due to the finite duration of the surveys: 30 years of radial velocity data (black), 4 years of continuous Kepler observations (orange), and 150 days of continuous CoRoT observations (green).

### 1.5.2 Future of the transiting exoplanet search and characterisation

The future of the characterisation of exoplanets lies with bigger telescopes, as a larger collecting area means more photons and thus a lower level of photon noise. The future instruments will also need to be more stable to reduce the level of correlated noise. For instance a more stable wavelength calibration for a spectrograph will allow the detection of fainter radial velocity variations. The future in the detection of Super-Earth atmospheres using the transit method lies in the new target choice of near-by (brighter) small host stars (larger planet-to-star radius ratio).

**Near future:** The JWST (James Webb Space Telescope), estimated to be launched in 2014, is a cooled infrared telescope with a segmented 6-m diameter mirror which will observe the transits of known exoplanets at various infrared wavelengths to study the atmosphere of Super-Earths orbiting small stars. The ground-based ELTs (Extremely large Telescopes), include the E-ELT (European-Extremely Large Telescope) 42-m telescope, the GMT (Giant Magellan Telescope) equivalent to a 25-m telescope, and the TMT (Thirty Meter Telescope), and will allow follow-up study from the ground of even more of the detected exoplanets (atmosphere, albedo, etc). The building stage of the E-ELT is estimated to start in 2010 for a start of operations planned for 2018. Future spectrographs, such as CODEX on the E-ELT, are being designed to reach precision down to $0.01\,\mathrm{ms}^{-1}$ which will allow the detection of radial velocity signals of Earth-like planets. To improve the precision in radial velocity measurements, new wavelength calibration techniques are needed and are being developed, such as the Laser Comb.

**And after:** The next generation of space mission searching for transiting exoplanets are being designed to look for the nearest transiting planets, targeting the bright stars (9th to 11th magnitude) across the whole sky. These missions include the PLATO mission (PLAnetary Transits and Oscillations of stars) and the TESS mission (Transiting Exoplanet Survey Satellite). They will use an array of small cameras with large fields of view and high resolution CCDs to monitor large areas of the sky. If funded, they should be launched from 2015 onwards. In a more distant future, proposed missions include TPF (Terrestrial Planet Finder) and Darwin, which are space missions with telescopes and/or instruments flying in formation in space. These missions are designed to study the light from the exoplanets themselves, using infrared nulling interferometry or visible-light coronography to suppress the light from the planet host star without affecting the light from the planet, therefore increasing the planet-to-star light ratio. If funded, these missions should be launched after 2020.

**Foreseen challenges:** For next generation telescopes and instruments, the challenges of studying small exoplanets which will limit the precision of their measurements include, physical processes such as the level of stellar activity for transits and radial velocities studies, and the level of dust emission for direct imaging. The solution to these limiting factors, if any, will most likely be in the development of new data processing and analysis techniques. From an instrumental point of view, the challenges are in

the improvement of the precision of the radial velocity measurements in the optical (for Earth-size planets around solar-type stars) and in the infrared (for Earth-size planets around M-dwarfs), and in the improvement of the nullifying techniques to better suppress the stellar light for the direct imaging of exoplanets.

## 1.6 This thesis

### 1.6.1 Motivations

The radius $R_{\rm p}$ and the mass $M_{\rm p}$ of an exoplanet can be ascertained when measuring both the flux and the radial velocity variations of the parent star due to its orbiting planetary companion. Improving the precision of observational planet masses and radii is important for both planet structure and planet formation models. The internal structure of a planet can be studied by comparing its mass and radius to model predictions of planets with different composition. Determining planet structure is important to derive observational statistics on planet types, which can then be compared to the predictions of planet formation models. Seager et al. (2007) show that to determine the composition of planets smaller than Uranus, error bars of less than 2% on the planet parameters are required. The current uncertainties on planet masses and radii are of order 10%. Improving these measurements is thus vital to help confirm the models.

As mentioned in Section 1.4.3, a side effect of the current photometric variability filters is that optimal stellar variability filtering, changes the shape of a transiting planet's light curve, and so the planet's properties derived from that light curve. As for small planets, the major source of uncertainty comes from the transit light curve, improving the processing of the light curve before deriving the planet parameters is essential. The first motivation of the thesis is thus to design a stellar variability filter that filters out the stellar variability whilst reconstructing the original transit signal as much as possible. This should enable us to derive more precise planet parameters from the transit light curve.

As seen in Section 1.4.4, the major contributor to the uncertainties of the planet parameters for large planets, are the precision of the stellar mass and radius which are derived from the stellar parameters inputed into the stellar evolution models. Thus, the second motivation of this thesis is to reduce the uncertainty of the stellar atmospheric parameters, starting with the stellar effective temperature which is used to derive the other parameters.

### 1.6.2 Structure

In Chapter 2, I present a new stellar variability filter, the Iterative Reconstruction Filter (IRF), and discuss its performance on simulated data. In Chapter 3, I re-derive the planet parameters of the first seven CoRoT planets using the IRF-filtered light curves. A by-product of the IRF is the reconstruction of all signals at the orbital period of the

planet. In Chapter 4, I search for secondary eclipses and orbital phase variations in the IRF-filtered light curves of CoRoT-1b and CoRoT-2b. In Chapter 5, I present a new temperature calibration to derive stellar effective temperatures using ratios of equivalent width of spectral lines, and re-derive the effective temperatures of the first nine CoRoT planet host stars. In Chapter 6, I combine the outcomes of the two new techniques presented in this thesis, i.e light curve filtering using the IRF and $T_{\rm eff}$ determination using calibrated equivalent width line ratios, by re-deriving the planet parameters of CoRoT-2b using a Markov Chain Monte Carlo (MCMC) on the IRF-filtered light curve. This approach takes into account the prior knowledge on the stellar temperature, taken as the equivalent width $T_{\rm eff}$ derived in Chapter 5. In Chapter 7, I summarise what has been discovered in this thesis (techniques developed, results, comparison with the literature and implication to the physics of the planets) and I finish with a few words on future prospects.

# Chapter 2

# Transit signal reconstruction

This chapter focuses on improving the planet parameters by improving the accuracy of the transit signal.The motivation for a new stellar variability filter is presented in Section 2.1. The Iterative Reconstruction Filter, the new post-detection stellar variability filter developed during this PhD thesis, is presented in Section 2.4, and tested over simulated data. The performance of the filter is then discussed in Section 2.5.

The work presented in this chapter was published in Alapini & Aigrain (2009).

## 2.1 Motivation

As smaller and lower-mass planets become increasingly detectable, thanks to space-based transit searches and improvements in ground-based radial velocity instruments, the uncertainties arising from the transit and radial velocity fits are expected to become more important. A specific problem arises when the transits become comparable in depth with the amplitude of the intrinsic brightness fluctuations of the host star. The amplitude of these variations can be several orders of magnitude greater than the transit signal, particularly for terrestrial planets and/or active stars, and they can occur on timescales significantly shorter than the orbital period of the planet (Fig. 2.1, black curve). Stellar variability can thus hinder the detection of planetary transits (Aigrain et al., 2004). A number of 'pre-detection' filters have been developed to tackle this problem.

Pre-detection filters aim to remove stellar variability in light curves to improve the detectability of transits, without any prior knowledge of the transit signal except for the fact that stellar variability typically occurs on longer time scales (hours to days) than the transit signal (minutes to hours). All of the techniques tested in the first CoRoT blind test (Moutou et al., 2005), which range from simple Fourier-domain low-pass filters to slightly more sophisticated implementations involving simultaneous fitting of hundreds of low-frequency sinusoids, or time-domain nonlinear iterative filtering (Aigrain & Irwin, 2004), exploit this difference. These filters proved effective in removing stellar variability

to facilitate the detection of transits but, as pointed out in Moutou et al. (2005) and Bonomo & Lanza (2008), they deform the shape of the transits.

The performance of several of these filters in terms of transit detection was evaluated in the context of first CoRoT blind test, a hare-and-hounds exercise involving 1000 simulated CoRoT light curves containing various transit-like signals, stellar variability and instrumental noise. This test showed that the most successful filters recover a detection threshold close to that obtained in the presence of instrumental noise only, except for a few cases involving the most active and rapidly rotating stars simulated.

However, these filters also have the property of modifying the shape of the transit signal (Moutou et al., 2005; Bonomo & Lanza, 2008), and would destroy any signal at the period of the transit occuring on longer timescales than a few hours.

After introducing, in Sect. 2.2, the simulated data set used for test purposes throughout this chapter, in Sect. 2.3 the effect on the transit signal of a benchmark pre-detection filter, the nonlinear iterative filter of Aigrain & Irwin (2004), is quantified. Described in Sect. 2.4 is the iterative reconstruction filter designed in this thesis, evaluating its effect on the transit signal. The IRF is a post-detection filter that uses the knowledge of the transit period to reconstruct signals at that period while filtering out signals at other timescales. The impact of these two filters on the accuracy of planet parameter measurements are compared in Sect 2.5, and the main results are summarised in Sect 2.6.

## 2.2 Data set

### 2.2.1 BT2 light curves

The starting dataset used in this study is a sample of 236 simulated CoRoT light curves taken from the second CoRoT blind test (hereafter BT2; Moutou et al. 2007), which was carried out to compare methods for discriminating between planetary transits and grazing or diluted stellar eclipses. Twenty six (26) of these light curves have planetary transits and 210 have eclipsing binary signals. We selected for this study of transit deformation only the BT2 light curves with planetary transits.

The production of the light curves followed roughly the same steps as that for the first CoRoT blind test (BT1), described in detail in Moutou et al. (2005), incorporating transits simulated with the Universal Transit Modeler (UTM[1], Deeg 2009), instrumental noise simulated using the CoRoT instrument model (Auvergne et al., 2003), and stellar variability curve simulated using a combination of the methods of Lanza et al. (2004) and Aigrain et al. (2004). The stellar variability modelled in the BT2 light curve is pessimistically strong both in terms of amplitude and times scale. The CoRoT data show that most stars are not quite so variable (Aigrain et al., 2009). An updated version of the CoRoT instrument model was used in the BT2, incorporating more realistic satellite jitter

[1]See `http://www.iac.es/galeria/hdeeg/`.

and enabling the production of 3-colour light curves, though the 3 bandpasses were summed in the present study to construct a 'white' light curve. The two approaches, used in the BT1 to model stellar variability, were merged in the BT2 using the scaled spot model of Lanza et al. (2004) to simulate rotational modulation of active regions and the stochastic model of Aigrain et al. (2004) to simulate granulation. The simulated transits correspond to planet radii ranging from 0.2 to $1.1\,R_{\rm Jup}$, orbital periods from 2.6 to 11.0 d, and impact parameters from 0.25 to 0.88.

As in the BT1, the flux in each aperture was modelled as arising from two stars, only one of which contained a transit-like signal. This is to reflect the fact that there is almost always one or more background star in the CoRoT aperture. This has the effect of diluting the transit signal, and to account for it we subtract from each BT2 light curve a constant corresponding to the fraction of the median flux contributed by the star which is not eclipsed (see Tab. 2.1 for contaminant fluxes (percentages of total flux) corrected from each BT2 light curve studied).

An example of a light curve with transit from the BT2 is shown in Fig. 2.1. The full set of light curves is shown in Fig. 2.8.

Table 2.1: Table of flux percentages coming from a contaminant star, for each of the BT2 light curve studied. Each light curve was corrected from the contaminant flux, before deriving transit and planet parameters. The fraction of flux coming from a contaminant star in each colour channel (CoRoT red, green and blue) was given in the parameter file used to build the BT2 light curves. For each light curve, the total contaminant flux was computed as the median of the sum of the contaminant fluxes in each colour channel, normalised by the median of the total flux.

| BT2 LC $n^o$ | contaminant flux (%) | BT2 LC $n^o$ | contaminant flux (%) |
|---|---|---|---|
| 105 | 0.2 | 177 | 0.6 |
| 110 | 0.1 | 186 | 0.3 |
| 126 | 2.2 | 192 | 0.8 |
| 131 | 90.6 | 193 | 13.1 |
| 133 | 0.2 | 196 | 0.9 |
| 135 | 0.1 | 200 | 3.3 |
| 145 | 2.3 | 208 | 1.8 |
| 152 | 0.3 | 220 | 1.9 |
| 154 | 1.9 | 223 | 77.4 |
| 162 | 0.1 | 225 | 0.6 |
| 165 | 91.1 | 233 | 0.6 |
| 169 | 0.5 | 236 | 1.4 |

### 2.2.2 Reference light curve sample

As the data is simulated, each component of the signal is known and can be studied individually. Thus two sets of reference light curves were constructed, using only the transit signal (no noise, no stellar variability) and the transit signal with instrumental noise only (no variability). We use the first set to evaluate the reference values of

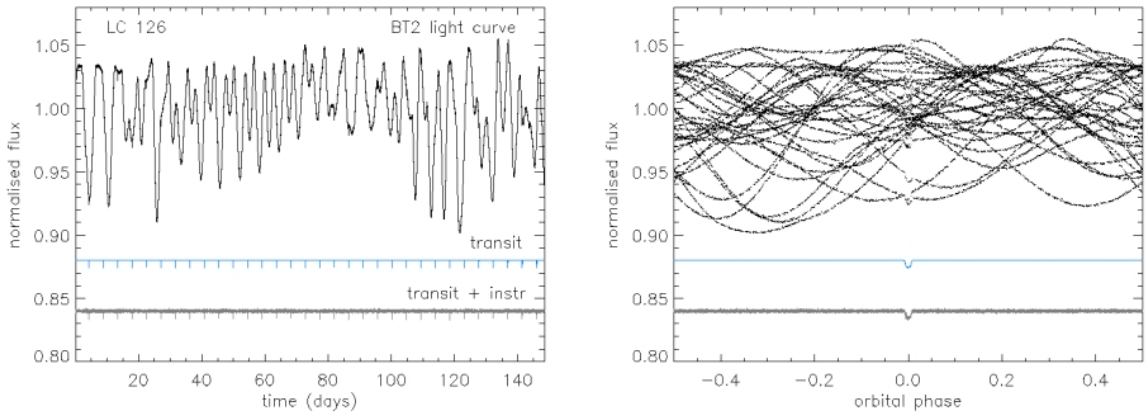


Figure 2.1: BT2 light curve (black), in which transit signal of a Saturn-like planet orbiting a particularly active Sun-like host star with an orbital period of 4.576 d. Transit signal only (blue) and with instrumental noise (grey) plotted underneath for comparison. Left: unfolded light curves. Right: phase-folded versions.

the parameters derived from transit fits. These could have simply been deduced from the input parameters given to the transit modelling software UTM when simulating the light curve. However, there can be differences between those and the parameters recovered from the transit fit due to the fitting process, rather than to the noise, and we wish to keep those effects, which are not specifically of interest here, separate from the effects of the stellar and instrumental noise. The second set was used to provide a benchmark for how well one can measure the parameters of interest in the presence of instrumental (white) noise, i.e. if the stellar variability was removed perfectly. These reference sets are shown in blue and grey respectively in Fig. 2.1.

After visual analysis of our two reference sets of light curves, we discarded two of the 26 light curves, where the transits were so small as to be undetectable even in the light curves with no stellar variability, as such cases would not realistically reach the post-detection stage.

## 2.3 Quantifying transit deformation with the Non-linear Iterative Filter

In this section, we quantify the impact of the deformation caused by the nonlinear iterative filter (NIF) of Aigrain & Irwin (2004) on the derived planet parameters. The NIF performance as a pre-detection filter was recently compared to a range of other published methods (Bonomo & Lanza, 2008), and it emerged as the method of choice among those compared, which makes it a suitable benchmark for the present work.

### 2.3.1 Definition of the NIF

The NIF has been extensively used at a pre-detetection / transit search level. Here we briefly describe the main steps of the NIF, we refer the reader to Aigrain & Irwin (2004) for further details.

The NIF separates stellar variability from the transit signal in the time domain, using an iterative procedure with the following steps:

1. apply a short base-line (here we use 7 data-points, $\sim$1 hour) moving median filter to smooth out the white noise and reduce the sharpness of any high-frequency features in the data;

2. apply a longer base-line moving median filter (here we use 24 hours, NIF trade of point to remove stellar variability while keeping away from the transit time domain in these light curves) to the output of the step (1), followed by a shorter base-line (here we use 2 data-points, $\sim$17 minutes) boxcar filter (moving average);

3. subtract the output of step (2) from that of step (1) and evaluate the scatter of the residuals as $\sigma = 1.48 \times \mathrm{MAD}$; [2]

4. flag all outliers differing by more than $n\sigma$ from the continuum;

5. return to step (2) and repeat the process, interpolating over any flagged data points before estimating the continuum and excluding them when estimating the scatter of the residuals, until convergence is reached (typically less than 3 iterations);

6. subtract the final continuum from the original light curve.

As the procedure converges, more and more of the in-transit points become flagged at step (4), so that the effect of the transits on the final continuum estimate is minimal. However, the choice of long base-line for the moving median filter in step (2) and of $n$ in step (4) must reflect a trade-off between appropriately following the stellar variations and incorporating too much of the transit signal when evaluating the continuum. This trade-off results in some of the transit signal been unavoidably filtered along with the variability. For the value of $n$ in step (4), one would normally use $n = 3$ to flag more in-transit points. In the case of the BT2, some light curves contain very strong and rapid variability. Thus, using a low $n$ would clip not only in-transit points but also out-of-transit points where the variability is too rapid to be well modelled by the continuum estimate (e.g. Fig. 2.2 left, green curve compared to black one). Hence, we used a large $n$

[2]The $\mathrm{MAD}$ is the median of the absolute deviation from the median of the points, in other words it is the median of the absolute value of the residuals from the median. 1.48*$\mathrm{MAD}$ is the equivalent of the standard deviation when using the median of the points rather than the mean. In this thesis, the use of the median and $\sigma$=1.48*$\mathrm{MAD}$ is preferred to the mean and the standard deviation, as the first combination is more resilient to outliers in the data due to the way it is calculated.

(150) in this study, which effectively means no points are clipped and convergence occurs at the first iteration.

### 2.3.2 NIF quantitative impact on transit parameters

We applied the NIF to our sample of 24 BT2 light curves. The post-NIF light curves are shown in green on Figs. 2.2 and 2.8. Clear variability residuals are visible in the unfolded post-NIF curves, corresponding to sections of the light curve where the variability is too rapid to be filtered adequately. The phase-folded light curves also show that the shape of the transits is affected by the filter. In practical terms, the transit appears both shorter and shallower than before filtering.

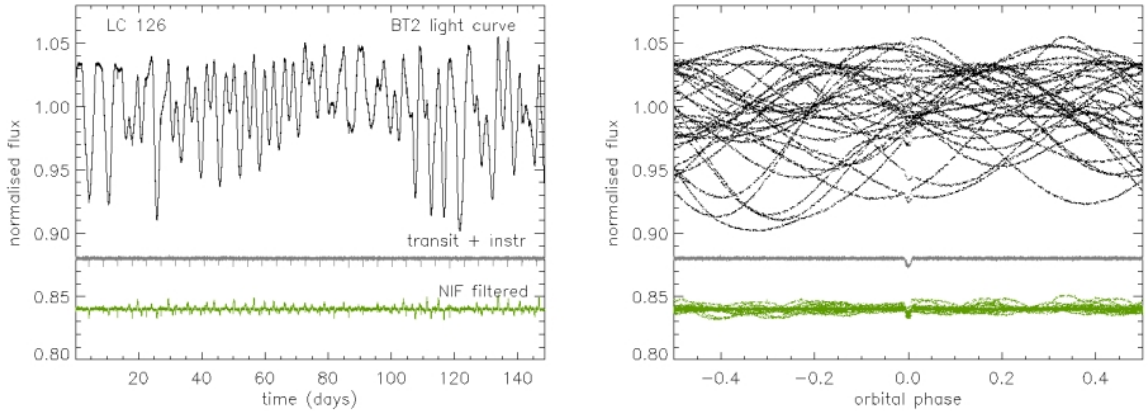


Figure 2.2: As in Figure 2.1 but the NIF-filtered light curve is now shown in green. The right panel shows that the NIF filtering reduces well the amplitude of the variability (green compared to black). The left panel shows that the NIF difficultly filters out fast stellar variability (spikes in green curve).

We then folded all light curves at the period of the injected transits and performed least-squares fits of trapezoidal models to the results to estimate the basic transit parameters: depth $\delta$, internal and external duration $d_{\rm i}$ and $d_{\rm e}$ (respectively excluding and including ingress and egress), and the phase $\phi$. The light curves were normalised such that the out-of-eclipse level is always 1. The same folding and trapeze fitting procedure was applied to the two reference sets described in Section 2.2.2.

In 4 of the BT2 light curves (Fig. 2.9), the stellar variability was so strong that, after applying the NIF, the phase-folded transits were barely detectable, and meaningful fits to these transits impossible. These 4 light curves were excluded from the comparison sample between the reference and filtered versions of the light curves.

We list the measured values of the transit parameters ($\delta$, $d_{\rm i}$, $d_{\rm e}$) of direct relevance to the determination of planet parameters for all 20 light curves in Fig. 2.8 (transit parameters in Tab. 2.2). We also show, in Fig. 2.3, cumulative histograms of the relative error $\sigma(\theta) = |\theta - \theta_0|/\theta_0$, where $\theta$ is the parameter of interest and the subscript $0$ refers to the

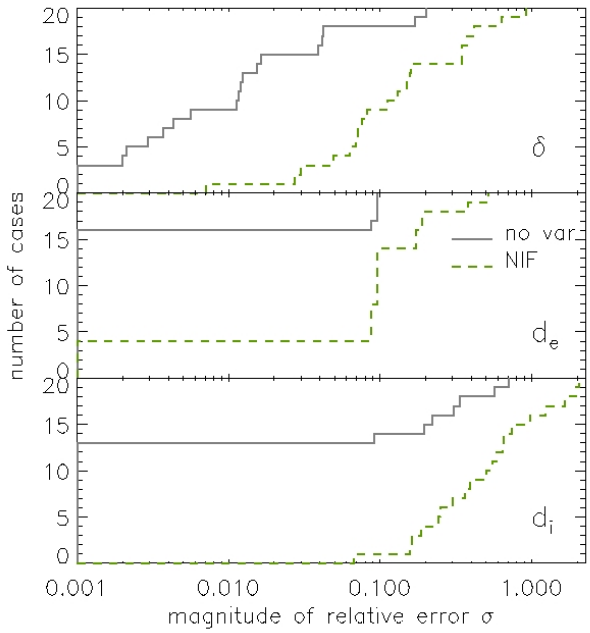


Figure 2.3: Cumulative histograms of the relative error $\sigma$ (see text for exact definition) on the transit parameters measured from trapezoidal fits to the light curves with no variability (grey), and to NIF-filtered light curves (green). Upper panel: transit depth $\delta$; middle panel: external duration $d_{\rm e}$ (total transit duration); lower panel: internal duration $d_{\rm i}$ (duration in full-transit). $\sigma > 1$ when a parameter is mis-estimated by more than its true value.

value measured from the reference light curve with transits only (no noise), contrasting the NIF case (green dashed line) to the case with no variability (black solid line). The median relative errors obtained with the NIF over our sample are $\sigma_{\rm NIF}(\delta) = 12\%$, $\sigma_{\rm NIF}(d_{\rm e}) = 10\%$ and $\sigma_{\rm NIF}(d_{\rm i}) = 52\%$, indicating that the planet parameters would be seriously affected if derived from NIF-filtered light curves. We note that the internal duration $d_{\rm i}$ tends to be systematically underestimated even for the reference set of light curves with no stellar variability. This bias is due to the white noise in the data smoothening the edges of the transit and making it appear more grazing, i.e with smaller orbital inclination so a shorter transit internal duration $d_{\rm i}$.

We therefore set out to develop a new post-detection filter: an alternative algorithm, hereafter referred to as 'reconstruction filter', designed to remove variability at other periods than that of the transit and preserve the transit signal, once the transit period has been determined.

## 2.4 A new stellar variability filter: the Iterative Reconstruction Filter

In an attempt to avoid the undesirable effects of the NIF on the transit shape, an iterative reconstruction filter (IRF, Alapini & Aigrain 2009) was develop to remove the stellar variability post transit detection whilst altering the transit signal as little as possible using the knowledge on the planet orbital period.

### 2.4.1 Definition of the IRF

The IRF is an iterative approximation of the full signal at the period of the transit. It uses the NIF to simultaneously estimate the continuum variation (i.e., stellar variability). Let $\{Y(i)\}$ (where $i = 1, \ldots, N$, $N$ being the number of data points in the light curve) represent the observed light curve (which is assumed to be normalised), $\{A(i)\}$ the detrended light curve and $\{F(i)\}$ the signal to be filtered out. We give the main steps of the IRF below:

1. Select an initial estimate for $\{F(i)\}$. $\{F(i)\} = 1$ is adopted as the initial estimate of the stellar variability, instead of a closer estimate using a median filter for instance. This is to avoid removing some transit signal before its first evaluation by the IRF, as this signal would never have been evaluated by the IRF as part of the transit signal and the IRF will not know that it has to be recovered.

2. Compute a corrected time-series $\hat{Y}(i) \equiv Y(i)/F(i)$.

3. Estimate $\{\hat{A}(i)\}$ by folding $\{\hat{Y}(i)\}$ at the transit period and boxcar averaging it in intervals of a fixed duration in phase units (binning is used to reduce high frequency noise). For the BT2 light curves, a duration of 0.09% of the phase was found to be suitable (this value was selected by trial and error, longer duration implying lower noise in the estimate of $\{\hat{A}(i)\}$ but more distortion of the transit signal).

4. Unfold $\{\hat{A}(i)\}$ to obtain $\{A(i)\}$. Compute a new estimate of $\{F(i)\}$ by applying the NIF (described in Section 2.3.1) to $\{Y(i)/A(i)\}$. The baseline for the median filter used in the NIF at this step can be chosen on a case-by-case basis, and can be significantly shorter than in the pre-detection case, because it is applied to a light curve from which most of the transit signal has been removed. In the present study, we adopt a baseline of 12 hours, the rest of the NIF parameters being the same as in Section 2.3.1.

5. Return to step (2) with the new estimate of $\{F(i)\}$, and iterate until the condition $|\mathcal{D}_{j-1} - \mathcal{D}_j| < 10^{-4}$ is satisfied for two consecutive iterations, where $j$ is the iteration

number (initialisation at $j = 0$), and

$$\mathcal{D}_j = \frac{\sum_{i=1}^{N} \left[Y(i)/A_j(i) - F_j(i)\right]^2}{N-1}.$$

In the case of the BT2 light curves, the convergence was reached after 4 iterations (i.e $D_j$ was calculated up to $j = 6$).

The final detrended light curve is given by $\{Y(i)/F(i)\}$, where $\{F(i)\}$ is the last (presumably best) estimate of the stellar variability. The steps of the IRF are sketched out in Figure 2.4.

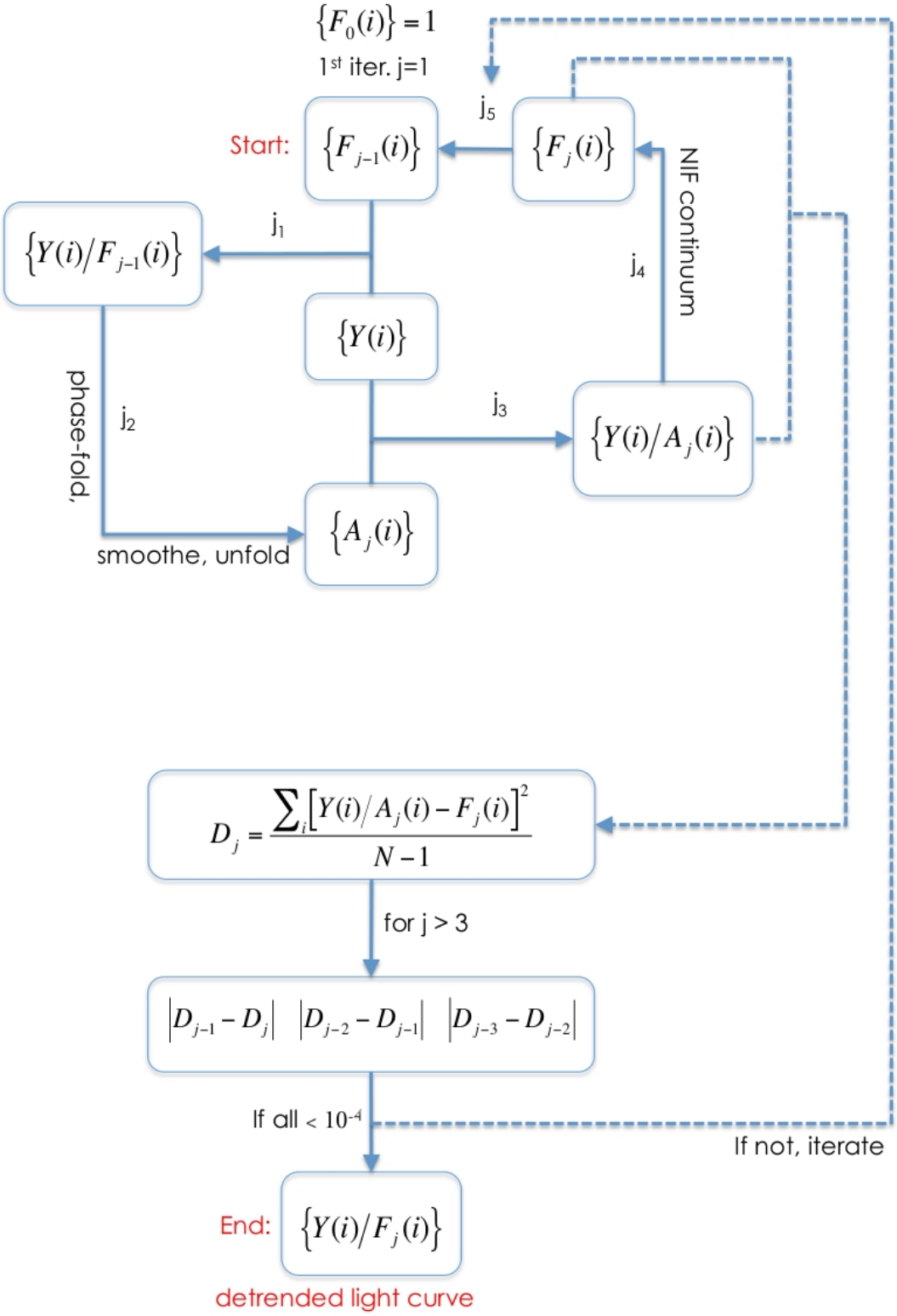


Figure 2.4: Flow chart of the IRF. $\{Y(i)\}$ represents the observed light curve, $\{A(i)\}$ the detrended light curve and $\{F(i)\}$ the signal to be filtered out. $i$ is the data points index (1 to $N$) and $j$ is the iteration index.

### 2.4.2 Comparison with the Trend Filtering Algorithm (TFA)

This algorithm is in some ways analogous to the TFA (Kovács et al., 2005) in post-detection mode. For clarity, we briefly list the main similarities and differences between the two algorithms.

- The TFA is designed to remove systematic trends which are common to large numbers of light curves in the transit surveys, rather than stellar variability which is individual to each object. Both algorithms work by decomposing each light curve into three components: the signal of interest $\{A(i)\}$ (the transits), the signal to be filtered out $\{F(i)\}$ (the systematics in the case of the TFA and the stellar variability in the case of the IRF), and the residuals. In the TFA, the signal to filter out (systematics) is modeled as a linear combination of a number of template light curves selected from the survey sample. In the IRF, the signal to filter out (stellar variability) is taken as the continuum of the light curve estimated with the NIF. In this analogy, the NIF would be equivalent to TFA in pre-transit-detection mode. When used in reconstruction mode (post-detection), both methods make use of the knowledge of the transit period to iteratively improve the evaluation of the transit signal and of the signal to be filtered out (which is assumed not to be periodic).

- Whereas $\{F(i)\}$ and $\{A(i)\}$ are treated additively in the TFA, they are treated multiplicatively here since the signal to be filtered out is intrinsic to the star, and the planet blocks out a certain fraction of the flux emitted by the star. This results in a different initialisation of $\{F(i)\}$. In Kovács et al. (2005), the first estimate of $\{F(i)\}$ is obtained from the pre-detection implementation of the TFA. In the IRF, it would be counter-productive to use the NIF-filtered light curve as the initial estimate of $\{F(i)\}$, since we have shown that the NIF affects the transit signal we are trying to reconstruct (see Section 2.3.2), so the initial estimate of $\{F(i)\}$ is taken to be constant at 1.

- Finally, the IRF treats high frequency effects by smoothing the phase-folded signal, while the TFA treats them by filtering out common outlier values.

### 2.4.3 Performance of the IRF on the BT2 transits

The IRF was applied to the 24 BT2 light curves described in Section 2.2, with the filtering parameters described in Section 2.4.1. The red curves in Fig. 2.5 and Figs. 2.8, show the light curves after applying the IRF.

As shown in Fig. 2.5, the IRF preserves any signal at the period of the transit. If the stellar variability contains power at this period, it is also preserved, inducing a flux gradient around the transit which must be removed before fitting the transits. This correction setting the out-of-transit level constant at 1, was done by fitting a $2^{\mathrm{nd}}$ order polynomial

fit – the lowest-order found to give satisfactory results – to the data about the phase-folded transit. The data used for the polynomial fit are two segments, each lasting 0.1 in phase, and offset by 0.15 in phase from the center of the transit on either side. This is a significant improvement over the common practice of performing a local polynomial fit to the vicinity of each transit, since the latter option has many more free parameters (one set of free polynomial parameters per transit, rather than one for the entire light curve). Fig 2.5 right panel gives an example of polynomial fit of the continuum about the transit (black segment superimposed to red curve) and of the resulting re-normalised transit (orange).

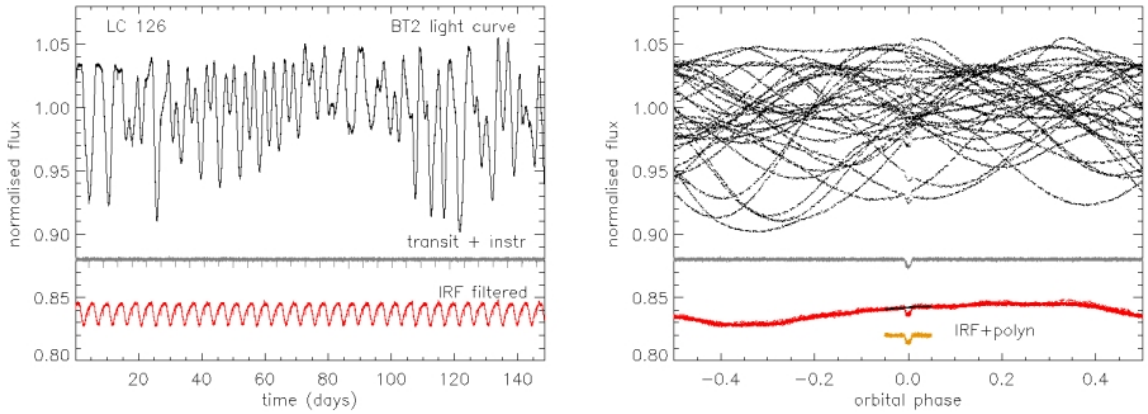


Figure 2.5: IRF-filtered light curve is red. Black and grey same as Fig. 2.1, plotted for comparison; the black curve is the starting point, the grey curve is the level of clean filtering we want to reach. These graphs show that the IRF conserves all variations at the period of the transit. The right panel shows that the IRF recovers the transit signal better than the NIF in Fig. 2.2. The IRF-filtered transit can be corrected from the non-constant local continuum by dividing it by a 2nd order polynomial fit about the transit (black line superimposed to the phase-folded IRF-filtered transit signal). The locally re-normalised transit is shown in orange.

The transit parameters were then estimated from a trapezoidal fit to the resulting phase-folded transit, in the same way as described in Section 2.3.1 for the NIF case. The results are listed in Tab. 2.2 and shown as the red dash-dot curves in Fig. 2.6. For the 20 BT2 transit light curves which were also used to evaluate the performance of the NIF, the IRF gives median relative errors of $\sigma_{\rm IRF}(\delta) = 3\%$, $\sigma_{\rm IRF}(d_{\rm e}) < 10^{-4}\%$ and $\sigma_{\rm IRF}(d_{\rm i}) = 42\%$, representing a significant improvement over the NIF case. Additionally after applying the IRF, in 2 of the 4 cases which are not included in the comparison sample as the transits were barely detectable after applying the NIF (Fig. 2.9), the transits are now clearly detectable and yield meaningful fits. In the two other light curves, the IRF-filtering gives a light curve closer to the reference version than the NIF, but the transits – already hidden in the instrumental noise in the reference set – stay barely detectable even in the IRF-filtered version.

Looking at Fig. 2.6, we see that while a relative error on the transit depth in excess of

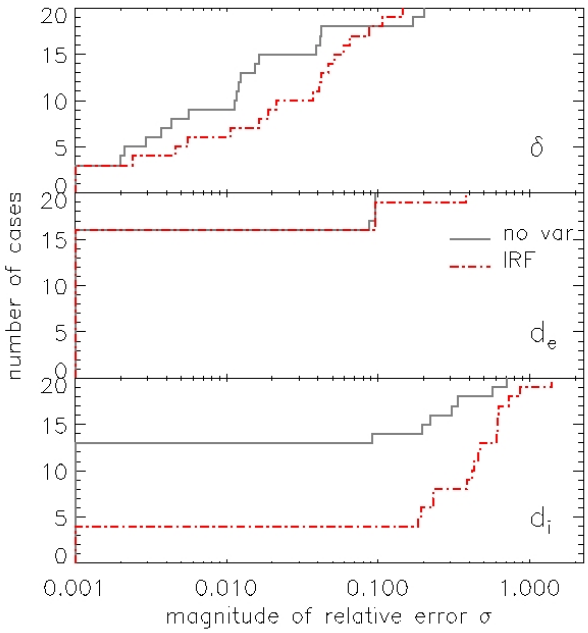


Figure 2.6: Same legend as Fig. 2.3 but for the IRF.

10% (essentially precluding any meaningful constraints on the planet structure) occurs in 60% of the cases studied with the NIF, it occurs in only 5% of the cases with the IRF. Similarly, the NIF yielded $\sigma(\delta) < 3\%$ (potentially allowing discrimination between different kinds of evolutionary models as well as a reliable basic structure determination) in only 15% of the cases, but the IRF did so in 50% of the cases.

It is also clear that the external transit duration is recovered near-optimally in the light curves treated with the IRF, with $\sigma(d_{\rm e}) < 0.1\%$ in 80% of the cases and $\sigma(d_{\rm e}) < 10\%$ in 95% of the cases, compared to a significantly decreased performance with the NIF. However, although the IRF also systematically improves the determination of the internal transit duration compared to the NIF, this improvement is much less significant, and the relative errors remain large (more than 10% for 80% of the cases studied). This implies that the IRF would probably not significantly increase the number of cases where both internal ($2^{nd}$ to $3^{rd}$ contact) and external ($1^{st}$ to $4^{th}$ contact) duration can be determined precisely enough to break the degeneracy between system scale and inclination, and thus to constrain the stellar density in a model-independent fashion.

## 2.5 Discussion on the IRF performance

### 2.5.1 Star-planet parameters

Although the basic trapezoidal fits performed in the previous two sections provide a quick estimate of the degree of deformation of the transit signal due to the variabil-

ity filtering process, one would in practice perform a full transit fit based on a physical model of the star-planet system. Mandel & Agol (2002) provided an analytical formulation which has become very widely used for such purposes, and was also used to generate the transits injected in the BT2 light curves.

We used the quadratic limb darkening prescription of Mandel & Agol (2002) to fit transit models to the 20 BT2 transit light curves where the transits were clearly detectable with both filters. We also performed these fits on both reference sets described in Section 2.2.2, as well as on the BT2 light curves themselves after applying the NIF on one hand, and the IRF – followed by a polynomial fit to the region around the transit (as described in Section 2.4.3) – on the other hand. The best transit fits were derived using MPFIT, an IDL implementation of the Levenberg-Marquardt algorithm[3]. The parameters of the model used are the transit epoch $T_0$, the period $P$, the system scale $a/R_{\rm s}$ (where $a$ is the semi-major axis), the star-to-planet radius ratio $R_{\rm p}/R_{\rm s}$, the orbital inclination $i$ (or impact parameter $b \equiv a\cos i/R_{\rm s}$), and the quadratic limb-darkening coefficients $u_a$ and $u_b$. In this study, we fixed the period and limb-darkening coefficients at the values used to build the light curves[4]. The initial epoch was taken directly from the trapezoidal fits. The initial value for $a/R_{\rm s}$ was derived from the period using Kepler's $3^{\rm rd}$ law, assuming $R_{\rm s} = R_{\odot}$ and $M_{\rm s} = M_{\odot}$. In order to ensure convergence in both grazing and full transits we selected, after some trial and error, an initial inclination corresponding to an impact parameter $b = 0.7$. We assumed zero eccentricity in all cases (all the transit light curves in our sample were simulated for circular orbits).

The results of the transit fits are listed in Table 2.3, while the fits themselves are shown in Figures 2.8 and 2.9. They are also compared in cumulative histogram form in Fig. 2.7. Instead of the relative error $\sigma$, we show the absolute error $\xi = |\theta - \theta_0| \equiv \sigma \times \theta_0$ with respect to the no noise case (subscript 0), for $\theta$ the key planet parameters $R_{\rm p}/R_{\rm s}$, $a/R_{\rm s}$ and $b$.

The IRF provides an overall improvement over the NIF in all three parameters, reducing the median of $\xi(R_{\rm p}/R_{\rm s})$ from 0.007 to 0.003, $\xi(a/R_{\rm s})$ from 1.7 to 1.0, and $\xi(b)$ from 0.07 to 0.04 for $b$. For comparison, the corresponding median values for the case with no variability are 0.003, 1.4 and 0.07 respectively. However, the situation is not as defined as when viewed in terms of transit parameters: there are a few cases where the NIF gives a better match with the parameters obtained from the noise-free light curves, and even cases where the largest error occurs in the light curves containing instrumental noise only. In an attempt to understand the reason for this, we examined all the light curves one by one (Figures 2.8 and 2.9). The light curves separate fairly

[3] MPFIT is kindly provided by C. Markwart on http://cow.physics.wisc.edu/∼craigm/idl/fitting.html

[4] Visual examination of the phase-folded light curves revealed that the folding was not perfect even in the no noise case, suggesting that the period values used may have been slightly inaccurate. We attempted to refine the periods but did not succeed. It seems that the observation dates in the light curve files themselves, rather than the periods, suffer from a small rounding error. It is not possible to remedy this problem without re-generating the entire light curve set, but it is not expected to affect the results strongly, and any effect would be common to all versions of a given light curve.

naturally into three broad classes:

1. cases where the IRF performed better than the NIF (transit shape and derived planet parameters closer to the shape and parameter obtained in the absence of stellar variability): light curves 126, 162, 169, 196, 200, and 223. These are cases where the original light curves contain large amplitude, short timescale stellar variability (active and rapidly rotating stars).

2. cases where the NIF performance was already satisfactory, and the IRF gives results similar to the NIF: light curves 145, 152, 186, 193, 208, 225, and 233.

3. cases where, while the transit reconstructed with the IRF appears closer to the original than the transit in the NIF-treated curve, the fitted parameters are not significantly improved or worsened: light curves 131, 133, 135, 154, 177, 192, 220. These are typically low signal-to-instrumental noise transits, where it becomes difficult to break the degeneracy between impact parameter and system scale. The radius ratio is typically less affected, except in the highest impact parameter cases (grazing transits).

Thus, we can see that where the limiting factor was stellar variability, the IRF is very successful in improving the errors on the planet parameters. As might be expected, the improvement is minor or non-existent where the limiting factor was the signal-to-white noise or the grazing nature of the transits.

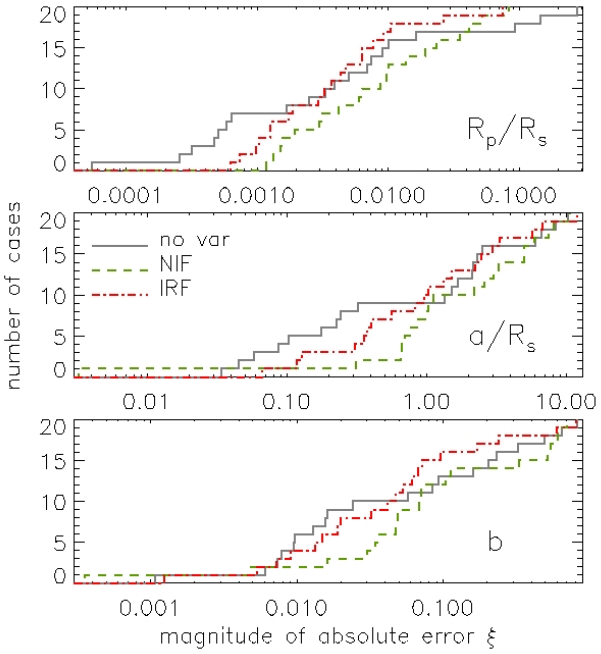


Figure 2.7: Cumulative histograms of the absolute error $\xi$ on the planet parameters derived from the light curves with no variability (grey), NIF-filtered (green) and IRF-filtered (red). The planet to star radius ratio $R_{\rm p}/R_\star$ is plotted in the upper panel, the planet orbit to stellar radius ratio $a/R_\star$ in the middle panel, and the impact parameter $b$ in the lower panel.

### 2.5.2 Application to orbital signal reconstruction

The fact that the IRF preserves any signal at the period of the transit has positive consequences: it implies that potentially interesting signals, such as secondary eclipses, reflected light variations, or thermal emission variations, are preserved. The IRF therefore presents itself as an interesting tool to detect these signals. However as the remaining variations at the period of the transit after IRF-filtering can also be due to stellar variability signal at the planet's orbital frequency, any detection of planet phase variations will need to be analysed carefully. The residual stellar variability at the orbital period of the planet is a worse problem for the detection of the phase curve than for the detection of the secondary eclipse as the latter happens on a shorter timescale.

As the BT2 light curves were not built with any of these orbital signals, the study of the IRF performance in detecting planet orbital signals will have to be done on another sample of light curves.

### 2.5.3 Potential application to transit detection

Another potential application of the IRF would be at the detection stage. Among the 24 light curves of our sample, there were 2 where the transit signal was larger than the instrumental noise but where the residual stellar variability after NIF-filtering was too

strong to perform any kind of meaningful fit. Naturally, these events were not detected in the NIF-filtered light curves during the original blind test for which the light curves were generated. There are two more cases which we did include in our 20-strong comparison sample, as their transits after NIF-filtering could still be fitted, but for which transits were not detected in the original exercise: light curves 192 and 200. After applying the IRF, two of these 4 cases became detectable[5] (light curves 165 and 200), the other 2 cases remained undetectable due to the level of instrumental noise. Using the IRF as part of the detection process might therefore enable the detection of transits which would otherwise be missed around particularly active stars. However, since the IRF would have to be run at each trial period, and is relatively computationally intensive, this would require a very large amount of CPU time unless the algorithm can be significantly optimised. However, as radial velocity measurements are also affected by stellar activity (which induces radial velocity jitter and line bisector variations at the rotation period of the star), the new photometry detections will be difficult to follow-up in radial velocity, so it is not clear at this stage if the above CPU investment would be justified.

## 2.6 Conclusion

In the absence of a prior knowledge of the planet's orbital period, the transit and the stellar signal cannot be separated effectively if they overlap too much in the frequency domain. Because of this, commonly used pre-detection stellar variability filters, such as the NIF, alter the transit signal, causing systematic errors in the resulting star and planet parameters. We have quantified this effect using 20 CoRoT BT2 simulated light curves including transits, instrumental noise and stellar variability. We found that the effect on the transit signal can be very significant, leading to errors on the star-planet radius ratio of up to 50%.

We thus developed the IRF to take advantage of the strictly periodic nature of planetary transits (in the absence of additional bodies in the system) to isolate the transit signal more effectively, following a method similar to the TFA algorithm previously developed for the reconstruction of transits in the presence of systematics. The IRF requires accurate knowledge of the transit period. We evaluated the performance of the IRF relative to the NIF and the no variability light curves by comparing a) the transit parameters from trapezoidal fits, b) the star-planet parameters from analytic transit fits, and c) the light curves themselves by visual examination. The results can be summarised as follows: the transits reconstructed with the IRF are systematically closer to the no variability case than the NIF-processed transits, and the improvement in the transit depth and duration can be very significant particularly in cases with large am-

[5]The detectability of the events was evaluated using the transit search algorithm of Aigrain & Irwin (2004), which was used in both CoRoT blind tests.

plitude and high frequency stellar variability. However, the full transit fits are affected by other factors including instrumental noise and the well known degeneracy between system scale and impact parameter, which dominate the final parameter estimates in approximately one third of the cases in our sample, or about half of the cases where the IRF provided a visual improvement over the NIF. The IRF will be most useful when applied to light curves which are strongly affected by stellar variability. The improvement in the planet parameters is likely to be better seen when the signal-to-noise ratio – for other noise than the stellar variability – of the light curve is high, as the noise allows degenerate solutions to the transit fit and thus keeps us from measuring the real impact of the IRF.

The IRF preserves any signal at the period of the transit, which implies that potentially interesting signals, such as secondary eclipses, reflected light variations, or thermal emission variations, are preserved.

Any power in the stellar variability signal at the frequency corresponding to the planet's orbital period is also preserved by the IRF. If required, this remaining variability can be removed locally using polynomial fits about the desired phase, but it is likely to limit the extent to which the IRF can be used to recover signals associated with the planet which vary continuously in phase.

# 2.7 Appendix

## 2.7.1 Best-fit parameters to BT2 transits

Table 2.2: Transit parameters (transit depth $\delta$, total transit duration $d_{\rm e}$, and internal transit duration $d_{\rm i}$) derived from trapezoidal fits to the light curves with transit signal only (`no noise'), transit signal and instrumental noise only (`no stvar'), the BT2 light curves filtered using the pre-detection nonlinear iterative filter (`NIF'), and the same light curves filtered using post-detection iterative reconstruction filter (`IRF').

| LC | period | $\delta$ | | | | $d_{\rm e}/P$ | | | | $d_{\rm i}$/P | | | |
|---|---|---|---|---|---|---|---|---|---|---|---|---|---|
| | (days) | no noise | no stvar | NIF | IRF | no noise | no stvar | NIF | IRF | no noise | no stvar | NIF | IRF |
| 126 | 4.576 | 0.00501 | 0.00495 | 0.00326 | 0.00504 | 0.0153 | 0.0153 | 0.0138 | 0.0153 | 0.0064 | 0.0064 | 0.0084 | 0.0079 |
| 131 | 6.880 | 0.00477 | 0.00469 | 0.00437 | 0.00448 | 0.0134 | 0.0121 | 0.0108 | 0.0121 | 0.0056 | 0.0017 | 0.0098 | 0.0098 |
| 133 | 8.128 | 0.00168 | 0.00161 | 0.00155 | 0.00160 | 0.0058 | 0.0058 | 0.0047 | 0.0057 | 0.0016 | 0.0010 | 0.0026 | 0.0015 |
| 135 | 3.733 | 0.00155 | 0.00148 | 0.00144 | 0.00152 | 0.0147 | 0.0147 | 0.0147 | 0.0147 | 0.0062 | 0.0062 | 0.0073 | 0.0090 |
| 145 | 5.557 | 0.00938 | 0.00949 | 0.00931 | 0.00923 | 0.0167 | 0.0153 | 0.0167 | 0.0167 | 0.0054 | 0.0064 | 0.0067 | 0.0086 |
| 152 | 7.360 | 0.00185 | 0.00185 | 0.00158 | 0.00176 | 0.0115 | 0.0125 | 0.0104 | 0.0115 | 0.0060 | 0.0065 | 0.0090 | 0.0071 |
| 154 | 10.987 | 0.00056 | 0.00065 | 0.00054 | 0.00061 | 0.0172 | 0.0172 | 0.0155 | 0.0237 | 0.0088 | 0.0038 | 0.0067 | 0.0051 |
| 162 | 4.171 | 0.00933 | 0.00922 | 0.00585 | 0.00894 | 0.0167 | 0.0167 | 0.0138 | 0.0167 | 0.0037 | 0.0037 | 0.0074 | 0.0070 |
| 169 | 5.195 | 0.00772 | 0.00770 | 0.00504 | 0.00769 | 0.0209 | 0.0209 | 0.0191 | 0.0209 | 0.0066 | 0.0066 | 0.0109 | 0.0107 |
| 177 | 7.339 | 0.00271 | 0.00267 | 0.00252 | 0.00260 | 0.0209 | 0.0209 | 0.0191 | 0.0209 | 0.0066 | 0.0046 | 0.0090 | 0.0107 |
| 186 | 4.373 | 0.00683 | 0.00679 | 0.00649 | 0.00690 | 0.0209 | 0.0209 | 0.0191 | 0.0209 | 0.0087 | 0.0087 | 0.0134 | 0.0127 |
| 192 | 3.915 | 0.00085 | 0.00102 | 0.00071 | 0.00076 | 0.0086 | 0.0094 | 0.0078 | 0.0078 | 0.0029 | 0.0023 | 0.0078 | 0.0070 |
| 193 | 6.763 | 0.00749 | 0.00747 | 0.00847 | 0.00858 | 0.0167 | 0.0167 | 0.0167 | 0.0167 | 0.0070 | 0.0070 | 0.0065 | 0.0086 |
| 196 | 4.608 | 0.01378 | 0.01384 | 0.00509 | 0.01288 | 0.0248 | 0.0248 | 0.0201 | 0.0248 | 0.0127 | 0.0127 | 0.0201 | 0.0175 |
| 200 | 5.995 | 0.00317 | 0.00313 | 0.00185 | 0.00311 | 0.0095 | 0.0095 | 0.0059 | 0.0086 | 0.0023 | 0.0023 | 0.0052 | 0.0038 |
| 208 | 4.064 | 0.00313 | 0.00301 | 0.00278 | 0.00302 | 0.0267 | 0.0267 | 0.0242 | 0.0267 | 0.0136 | 0.0136 | 0.0158 | 0.0162 |
| 220 | 7.253 | 0.00215 | 0.00212 | 0.00181 | 0.00216 | 0.0230 | 0.0250 | 0.0210 | 0.0230 | 0.0050 | 0.0030 | 0.0148 | 0.0140 |
| 223 | 5.237 | 0.00771 | 0.00736 | 0.00065 | 0.00761 | 0.0184 | 0.0184 | 0.0088 | 0.0200 | 0.0059 | 0.0059 | 0.0082 | 0.0102 |
| 225 | 2.613 | 0.01061 | 0.01053 | 0.01032 | 0.00998 | 0.0344 | 0.0344 | 0.0311 | 0.0344 | 0.0073 | 0.0073 | 0.0224 | 0.0174 |
| 233 | 3.083 | 0.00461 | 0.00460 | 0.00431 | 0.00459 | 0.0153 | 0.0153 | 0.0153 | 0.0153 | 0.0035 | 0.0035 | 0.0040 | 0.0049 |

Table 2.3: Star-planet parameters (planet to star radius ratio $R_p/R_\star$, system scale $a/R_\star$, and impact parameter $b$) derived from full transit fits. The columns corresponding to the 4 sets of light curves used in the fits are labelled as in Table 2.2.

| LC | period | $R_p/R_\star$ | | | | $a/R_\star$ | | | | $b$ | | | |
|---|---|---|---|---|---|---|---|---|---|---|---|---|---|
| | (days) | no noise | no stvar | NIF | IRF | no noise | no stvar | NIF | IRF | no noise | no stvar | NIF | IRF |
| 126 | 4.576 | 0.0799 | 0.0800 | 0.0698 | 0.0817 | 12.27 | 12.09 | 13.14 | 11.89 | 0.862 | 0.870 | 0.858 | 0.872 |
| 131 | 6.880 | 0.0760 | 0.1687 | 0.0779 | 0.0749 | 15.64 | 9.64 | 10.65 | 12.30 | 0.825 | 1.058 | 0.893 | 0.873 |
| 133 | 8.128 | 0.1389 | 0.2836 | 0.0557 | 0.0642 | 17.70 | 15.59 | 20.99 | 20.65 | 1.074 | 1.233 | 0.961 | 0.979 |
| 135 | 3.733 | 0.0469 | 0.0369 | 0.0372 | 0.0393 | 10.00 | 20.34 | 20.62 | 16.75 | 0.916 | 0.422 | 0.397 | 0.676 |
| 145 | 5.557 | 0.1050 | 0.1044 | 0.1080 | 0.1079 | 14.35 | 14.24 | 13.34 | 13.38 | 0.788 | 0.795 | 0.822 | 0.820 |
| 152 | 7.360 | 0.0481 | 0.0476 | 0.0495 | 0.0475 | 15.48 | 15.80 | 13.29 | 15.35 | 0.860 | 0.836 | 0.908 | 0.865 |
| 154 | 10.987 | 0.0263 | 0.0313 | 0.0323 | 0.0245 | 11.54 | 9.24 | 8.50 | 23.47 | 0.829 | 0.914 | 0.933 | 0.023 |
| 162 | 4.171 | 0.1335 | 0.1245 | 0.1102 | 0.1272 | 10.91 | 11.13 | 11.58 | 11.21 | 0.927 | 0.910 | 0.911 | 0.913 |
| 169 | 5.195 | 0.0918 | 0.0921 | 0.0781 | 0.0925 | 12.61 | 12.36 | 11.84 | 12.25 | 0.720 | 0.736 | 0.750 | 0.735 |
| 177 | 7.339 | 0.0486 | 0.0555 | 0.0549 | 0.0549 | 17.53 | 10.92 | 11.66 | 11.83 | 0.150 | 0.794 | 0.760 | 0.749 |
| 186 | 4.373 | 0.0839 | 0.0872 | 0.0869 | 0.0876 | 12.71 | 11.21 | 11.69 | 11.69 | 0.667 | 0.760 | 0.738 | 0.735 |
| 192 | 3.915 | 0.0504 | 0.0488 | 0.0152 | 0.0240 | 10.97 | 12.64 | 12.09 | 8.51 | 0.988 | 0.978 | 0.656 | 0.926 |
| 193 | 6.763 | 0.0904 | 0.0929 | 0.0990 | 0.0996 | 15.26 | 13.90 | 14.60 | 14.42 | 0.723 | 0.780 | 0.759 | 0.764 |
| 196 | 4.608 | 0.1162 | 0.1160 | 0.0970 | 0.1150 | 11.87 | 11.91 | 14.47 | 11.98 | 0.546 | 0.533 | 0.000 | 0.547 |
| 200 | 5.995 | 0.0860 | 0.3645 | 0.0444 | 0.0755 | 14.59 | 12.10 | 22.72 | 15.91 | 0.965 | 1.290 | 0.916 | 0.945 |
| 208 | 4.064 | 0.0582 | 0.0588 | 0.0597 | 0.0592 | 9.33 | 9.30 | 8.63 | 8.93 | 0.710 | 0.716 | 0.780 | 0.763 |
| 220 | 7.253 | 0.0475 | 0.0436 | 0.0433 | 0.0462 | 10.71 | 12.86 | 15.67 | 12.93 | 0.722 | 0.519 | 0.019 | 0.550 |
| 223 | 5.237 | 0.0976 | 0.0811 | 0.0452 | 0.1008 | 11.33 | 19.75 | 18.84 | 9.82 | 0.835 | 0.017 | 0.231 | 0.854 |
| 225 | 2.613 | 0.1033 | 0.1028 | 0.1017 | 0.0989 | 8.28 | 8.22 | 8.59 | 8.84 | 0.624 | 0.625 | 0.575 | 0.552 |
| 233 | 3.083 | 0.1426 | 0.1500 | 0.1414 | 0.1378 | 9.29 | 9.38 | 9.30 | 9.23 | 1.020 | 1.029 | 1.020 | 1.012 |

## 2.7.2 Full BT2 light curve sample

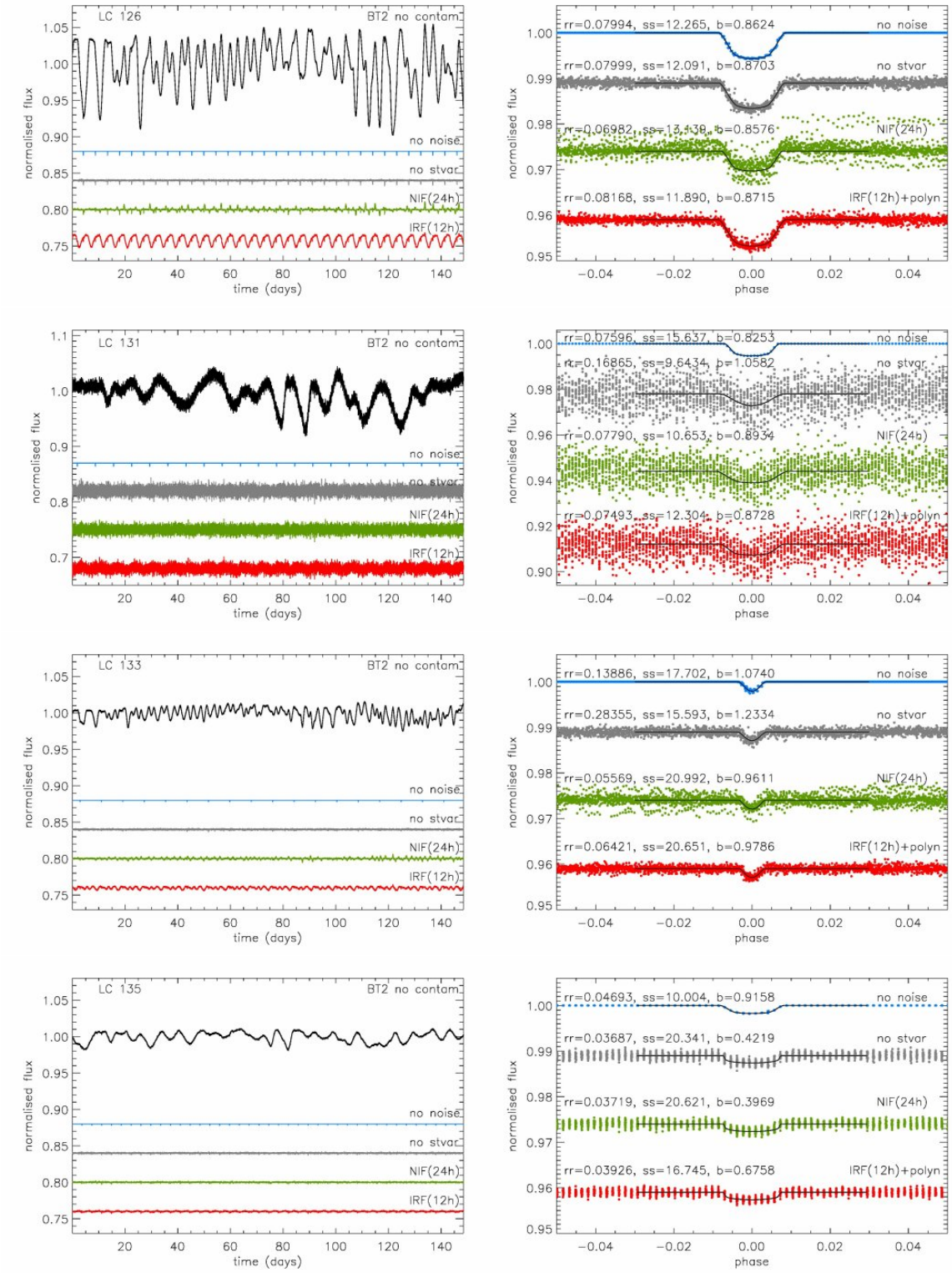


Figure 2.8: The 20 BT2 light curves in the comparison sample (left:unfolded; right : phase-folded section around the transit). The light curve number is shown on the plots in the left column (original BT2 numbering scheme) and the planet to star radius ratio (`rr`), system scale (`ss`), and impact parameter (`b`) in the right column.

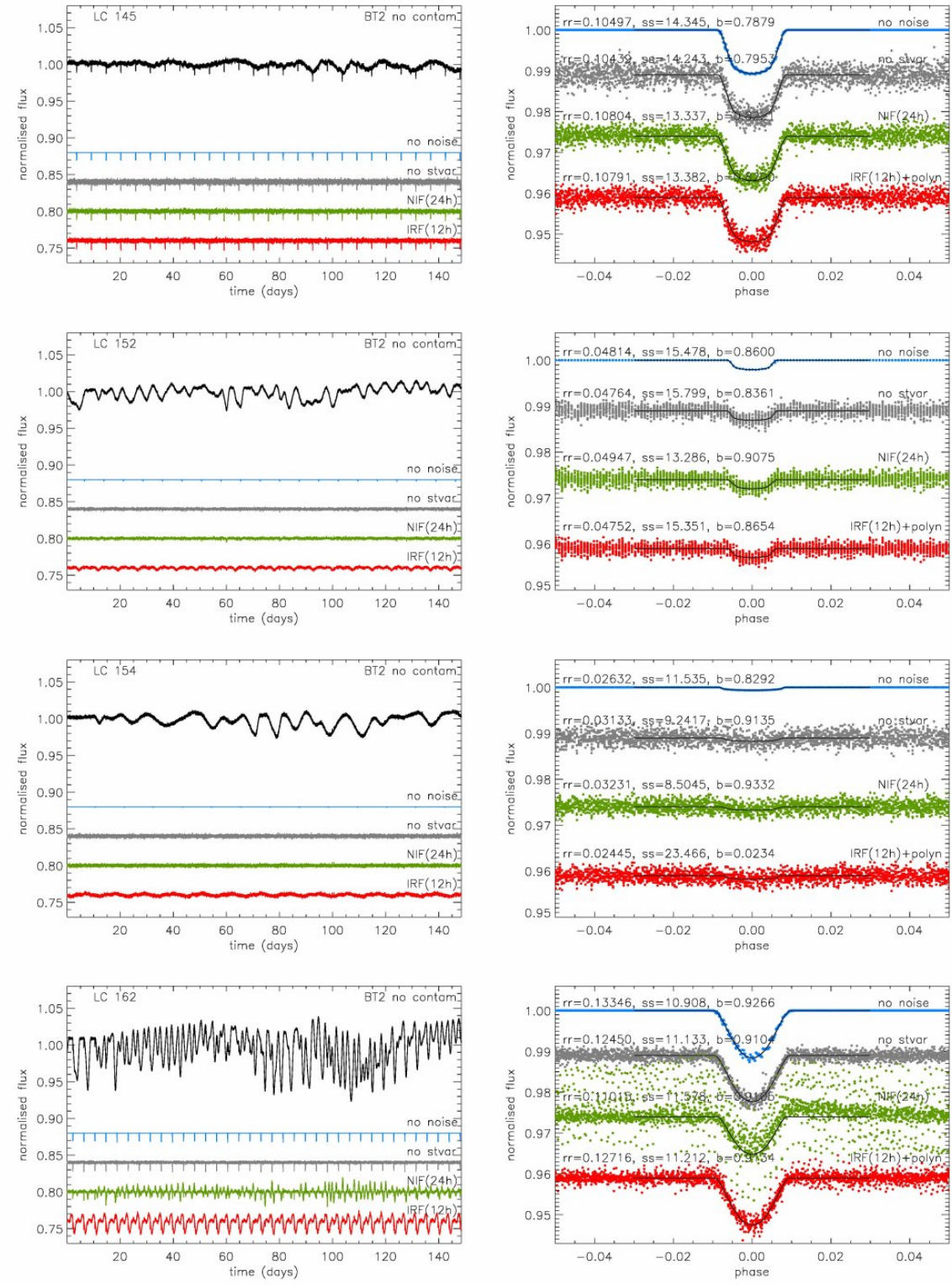


Figure 2.8: continued

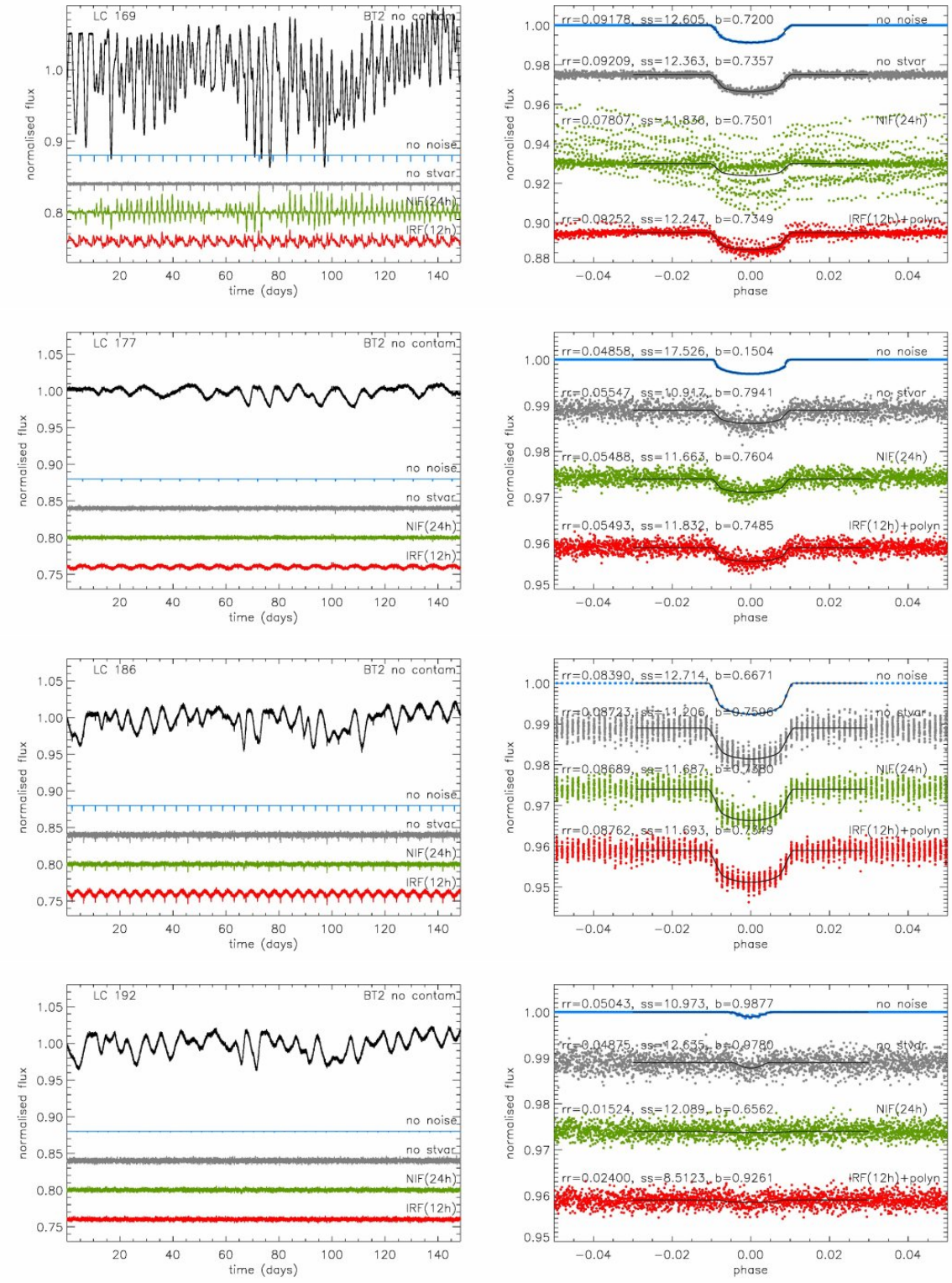


Figure 2.8: continued

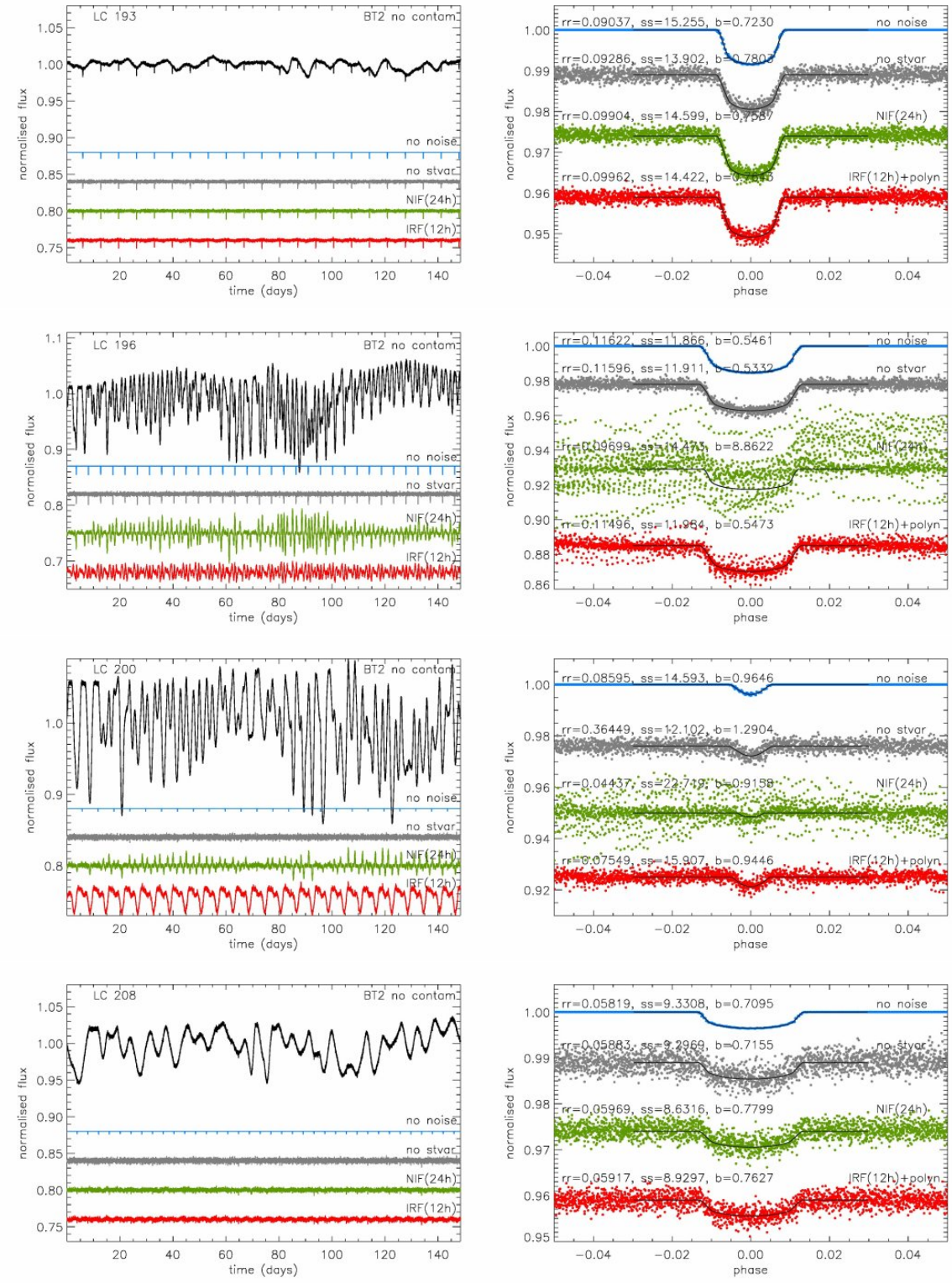


Figure 2.8: continued

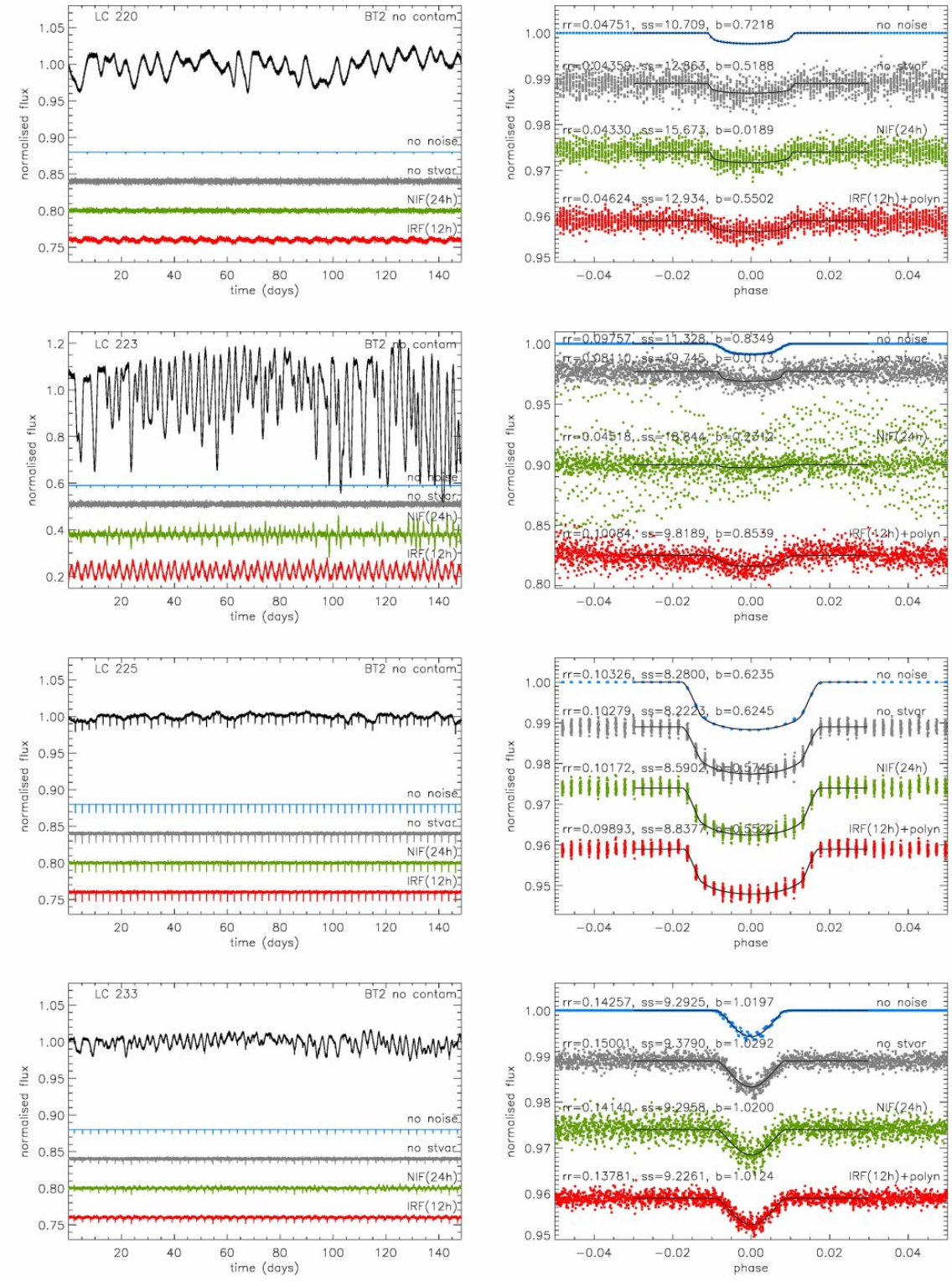


Figure 2.8: continued

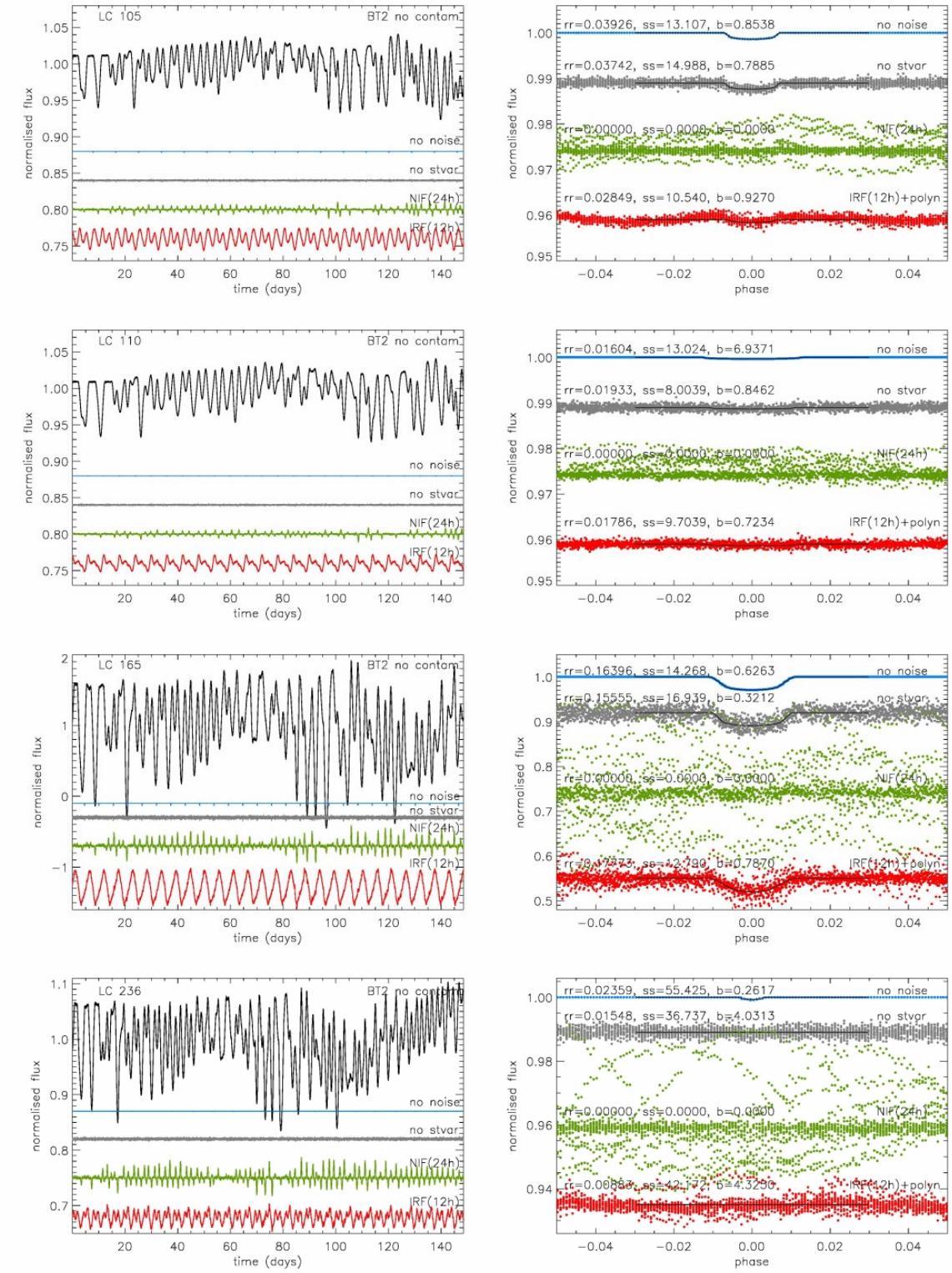


Figure 2.9: The 4 BT2 transit light curves where the transit was undetectable after applying the NIF and miningfull fits to the resulting transits were not possible. Same legend as Fig. 2.8. These transits became boarder-line detectable in the IRF-filtered light curves.

# Chapter 3

# IRF applied to the transit of CoRoT planets

In this chapter, the IRF is applied to the CoRoT light curves of the first seven planets and brown dwarf discovered by CoRoT. The phase folded transits of the IRF-filtered light curves are fitted to derive the planet parameters using a Levenberg-Marquardt algorithm and the analytical transit models of Mandel & Agol (2002). The results are compared to the parameters published in the planet/brown dwarf discovery papers.

Some of the work presented in this chapter has been published: in Fridlund et al. (2010) for the work on CoRoT-6b and in Léger et al. (2009) for the work on CoRoT-7b. The IRF was used as an independent analysis of the transit light curves. The method was optimised further since these publications, especially in the understanding (strengths and limitations) of the IRF and of the techniques used to find the best model to the transit.

## 3.1 Description of the CoRoT data

### 3.1.1 Instrument

CoRoT (Convection, Rotation and planetary Transits)[1] is a modest scale mission (626 kg satellite, 80 million euros in cost) primarily funded by the French space agency CNES (Centre National d'Etude Spaciale), with contributions from ESA (European Space Agency), Belgium, Austria, Germany, Spain and Brazil. The satellite was launched on December 27th 2006 into a polar orbit at $\sim$ 900 km of altitude.

CoRoT is the first space-based telescope designed for high precision photometry with long time coverage after MOST[2] (150 days for the long runs and 20-30 days for the short runs, with duty cycle greater than $93\%$). Aigrain et al. (2009) evaluated the noise

[1] Official CoRoT website: http://corot.oamp.fr

[2] The MOST (Microvariability and Oscillations of STars telescope) satellite, launched in 2003, has a diameter of 15cm and stares at each single field for about 30 days.

level of real CoRoT data on 2h timescale at 0.1 mmag and 1 mmag for R magnitude of 11.5 and 16 respectively. CoRoT is designed to perform two types of science: stellar seismology (to study stellar interiors), and exoplanet transits search. In this thesis, we are interested in the planet-finding channel of CoRoT. Over the nominal duration of the mission, in the exoplanet channel, CoRoT will have observed over 12000 stars (V $>$ 16.5) per run. CoRoT nominal duration is three years, and has been extended for another three years. CoRoT operates at half field of view since March 2009, due to a problem effecting two of its four CCDs.
The telescope is afocal and has a 27 cm diameter primary mirror and a baffle (to prevent reflected light from the Earth reaching the CCDs). CoRoT has two 6-month viewing zones each year, pointing from April to October towards the galactic anti-centre (RA $\sim 6^h50^m$, DEC $\sim 0°$) in the constellations of Aquila and Serpens Caput, and from October to April towards the Galactic centre (RA $\sim 18^h50^m$, DEC $\sim 0°$) in the constellation of Monoceros.
In the exoplanet channel, there are two 2048 x 2048 pixels CCDs with a combined field of view of $1.3°$ x $2.6°$. A bi-prism, placed in the optical path, disperses the light and provides a very low-resolution spectrum of each star (light divided into blue, green and red channels). This is intended to help identify transit like events caused by stellar binary systems or stellar activity, as stellar dependent effects are chromatic while planetary transits are not.
A general description of the CoRoT science objectives can be found in Baglin et al. (2006), and a technical description of CoRoT in Boisnard & Auvergne (2006) and in the CoRoT instrument handbook[3]. Auvergne et al. (2009) describe the CoRoT satellite in flight performance.

### 3.1.2 Light curve generation

The different levels of light curve generation are summarised in Baudin et al. (2006).

#### Treatment on board

Due to a limited telemetry rate (1.5 Gbit per day), aperture photometry is performed and co-added on board the satellite and then downloaded to Earth. The raw data (time stamped aperture photometry of each star) received on Earth are labelled N0 data.
As the image of each star (PSF, point spread function) is tear-shaped due to the diffraction through the bi-prism, the aperture photometry is done with a tear-shaped mask – chosen among 256 templates depending on the star magnitude, temperature and position on the CCD but fixed for each star during a given run. A mask has typically between 50 and 100 pixels. For most of the stars, all the light falling inside the mask

[3]CoRoT instrument handbook: http://corotsol.obspm.fr/web-instrum/payload.param/

(white light, 300 to 1000 nm) is integrated on board and downloaded to Earth. For a selection of up to 5000 stars with R magnitude less than 15, the mask is divided into three bands (blue, green and red channels), the light is integrated within each band and three colour stellar flux is computed on board and downloaded to Earth.
The integration time of each exposure is 32 s. The aperture photometry is co-added on board every 512 s. For 500 selected stars showing sharp flux variations (potential transit candidates), the 32 s rate is downloaded to Earth.

### Treatment on the ground

On the ground, the N0 photometry is pipeline-processed to correct (and/or flag) anticipated astrophysical and instrumental noise effects (e.g. background, high energy particles during the crossing of the South Atlantic Anomaly, satellite jitter, outliers e.g. images of debris or high energy particles). The pipeline also transform the CoRoT time stamps into HJD (Heliocentric Julian Date), and the electron counts into stellar flux. The flux-time series (the light curves) are then produced for each star, these data are labelled N1.
Information from preliminary observations (e.g. stellar magnitude) are added as keywords in the header of the N1 data. The resulting files are labelled N2. The N2 data are ready for scientific analysis and released to the CoRoT Co-Investigators a few months after the end of each run and to the public[4] a year later.
The steps of the N1 to N2 data was also intended to correct for common noise sources identified in all the N1 light curves (e.g. using $\mathrm{SysRem}$ described in Tamuz et al. 2005 and Mazeh et al. 2009), but this is in practice implemented on the N2 data by the CoRoT scientific team on a case to case basis.
With practice on the real CoRoT data, additional noise effects affecting all the light curves have been identified, such as:

- the temperature variation of the satellite when it passes through the Earth's shadow cone causing satellite pointing jitters and stellar flux drops as some flux falls outside the aperture mask. This effect can be corrected as it is a systematic effect affecting simultaneously all the stars and hence their light curve, with a method such as was described in Mazeh et al. (2009). Points in the light curve affected by this effect are flagged in the new N2 data (N2v2). The data used in this chapter are from the previous N2 data.

- hot pixels which are due to high energy particle hits on some pixels. These hits affect the electronic response of the pixels which translates into sharp flux jumps and flux decay in the light curve. This effect is more difficult to systematically correct from. Drummond et al. (2008) discuss methods to tackle this issue but none so far can be used in a fully automated way.

[4]CoRoT data archive: http://idoc-corot.ias.u-psud.fr

When solutions to correct these noise effects are kown and well tested, corrections to these effects are included to the pipeline producing the N2 level light curves.
The photometry used in this chapter was performed using the latest version of the CoRoT reduction pipeline. This new version of the pipeline uses the information about the instrument's PSF and the centroids of the stars measured in the asteroseismology channel to correct the effects of the satellite jitter in the white light curve.

### 3.1.3 Additional light curve pre-processing

The light curves used in this chapter are the N2 data. In these light curves, several common effects are present:

- upward outliers due to high energy particle hits (such as during the South Atlantic Anomaly crossing) causing an increase in the background level
- downward outliers due to the satellite entry and exit from the Earth's shadow causing a temporary loss of pointing accuracy resulting in a drop in flux
- long term downward trend due to instrumental performance decay or pointing drift
- variations on timescales of days to weeks caused by rotational modulation of active regions on the stellar surface
- sudden discontinuities called "hot pixels" caused by high energy particles hits on one or more pixels temporally affecting the sensitivity of these pixels. The decay of the pixel back to its original non-excited level can be smooth or sudden

The approach adopted here to correct for these effects is the following. The upward and downward outliers are identified by an iterative non-linear filter (Aigrain & Irwin, 2004), also described in Chap 2 Section 2.3.1) consisting of 5 iterations with a 5-points boxcar filter, a 1-hour median filter and a $3\sigma$ outliers identification. The downward outliers are flagged by the N2 pipeline. The flagged outliers are removed from the light curve.
The long term downward trend, the smooth decay after "hot pixels" and the stellar flux modulation are modelled and corrected using the iterative reconstruction filter (IRF, Alapini & Aigrain 2009, also described in Chap 2, Section 2.4.1), with the filtering timescales adapted to each stellar variability signal and transit signal. The IRF has the advantage of using only two free parameters which are the smoothing lengths used to estimate the signal at the planet's orbital period and the signals at other timescales – including the stellar variability. The former represents a compromise between reducing the noise and blurring out potential sharp features associated with the planet, and the latter between removing the stellar signal and affecting the planetary signal.
The iterative reconstruction filter works on uniformly sampled light curves so any part of

each light curve sampled at 32 s is resampled to 512 s before running this filter.
The iterative reconstruction filter cannot thoroughly remove very sharp flux variations such as those caused by "hot pixels" (the residuals of these hot pixels are visible at a $10^{-3}$ level in the phase-folded light curve), so the regions of light curve affected by sharp flux variations are clipped out before running the IRF.

### 3.1.4 Planetary transit detection and confirmation

The light curves from each run are systematically searched for planetary transits and priority-ranked by several teams (France: LAM, IAS, LESIA, LUTH; UK: Exeter; Germany: DLR, Köhln; Spain: IAC; ESA: ESTEC; Austria: Graz). Each detection team uses its own set of pre-processing, de-trending and transit search tools (Moutou et al. 2005 describes most of them). Each team ranks the detected planetary-transit-like events with the same criteria: transit depth (planet-candidate to star radii ratio), signs of binary nature (secondary eclipses, ellipsoidal variations, transit depth different in the three colours), transit shape ("U" for central transits, "V" for grazing transits). The rankings are automatically merged to extract a list of high quality candidates for follow-up.
The follow-up consists of: ground-based in and out of transit photometry at high spacial resolution to spatially resolve the stars falling in the CoRoT aperture mask and identify which star is being eclipsed, multiple radial velocity measurements to derive the planet-candidate to star mass ratio, and a high resolution, high signal to noise spectrum of the host star to derive precise stellar parameters and hence precise planet parameters.
The parameters measured for each CoRoT planet are the orbital period $P$, the epoch of the centre of the first transit observed $T_0$, the planet orbital to plane-of-view inclination $i$, the orbital distance to stellar radius ratio $a/R_\star$, and the planet to star radii ratio $R_\mathrm{p}/R_\star$. Some stellar parameters can also be derived from the light curve: the stellar mass to radius ratio ${M_\star}^{1/3}/R_\star$ (derived directly from $a/R_\star$ and $P$), the star rotation period $P_\mathrm{rot}$, and the stellar limb darkening coefficient $u_a$ (linear law) and $u_b$ (second coefficient in quadratic law).

## 3.2 Primary transit parameters with the IRF-filtering

The work in this section was performed on the CoRoT space-photometry of the stars harbouring the first six planets and the first brown dwarf discovered by the CoRoT mission.

### 3.2.1 Method

We filter the light curve with the IRF (definition in Chap. 2, Sec. 2.4.1) to remove the flux variation intrinsic to the star. By default, the IRF is run with a bin size of 0.0006 in

phase (IRF $\mathrm{binsize}$ parameter, which controls the smoothing length used to estimate the phase-folded transit signal), and with a convergence limit of $1\ 10^{-8}$. The $\mathrm{cvlim}$ parameter sets the convergence criterion. At each iteration, the residuals of the light curve with the last estimate of the stellar variability and the transit signals removed are compared with those of the previous iteration. $\mathrm{cvlim}$ is the maximum difference allowed between these two sets of residuals. To explore the performance of the IRF in evaluating the stellar variability signal with a given time scale (IRF $\mathrm{timescale}$ parameter, which controls the smoothing length used to estimate the stellar variability), two values of this parameters are tested systematically: 0.50 and 0.25. $\mathrm{timescale}$=0.10 days is also tested to see how the IRF behaves in the case of extreme filtering.

CoRoT has a large PSF due to the defocussing of the telescope and the prism in the optical path. It used different aperture masks (50 to 100 pixels each) to extract the photometric time series of the stars. Often in CoRoT photometry, a second star falls into the mask of the target star, contaminating the light of the latter. This is the case for the CoRoT light curves of the host stars of CoRoT-2b, CoRoT-3b, CoRoT-4b, CoRoT-5b and CoRoT-6b, with the following respective fractions of contaminant flux: 5.6±0.3 % (Alonso et al., 2008), 8.2±0.7 % (Deleuil et al., 2008), 0.3±0.1 % (Aigrain et al., 2008), 8.4% (Rauer et al., 2009), and 2.8±0.7 % (Fridlund et al., 2010). The transit of a planet in a light curve contaminated by the flux of another star, appears shallower. Thus, the flux from the contaminant star should be removed before deriving the planet parameters from the transit light curve. In this chapter, this is done by subtracting the fraction of the contaminant (e.g. -0.056 for 5.6%, the uncertainty on this flux is taken into account in the error estimate of the best transit model) from the normalised IRF-filtered light curve, and re-normalising the resulting light curve.

When an out-of-transit variation around the phase-folded IRF-filtered transit signal is observed, a $2^{nd}$ order polynomial ($y = a + b\,x + c\,x^2$) is fitted about the phase-folded IRF-filtered transit and divided into the transit. The phase range each side of the transit used to evaluate the polynomial fit is (0.015,0.025) for orbital period $P > 10$ d, (0.04,0.08) for $4 < P < 10$ d, and (0.1,0.2) for orbital period $P < 4$ d.
The transit signal (corrected from the polynomial slope about the phase-folded transit when necessary) is then fitted using the analytical formulation of Mandel & Agol (2002). The method used to find the best fit to the transit light curve is non-linear least squares method, the Levenberg-Marquardt algorithm.

#### Best fit with the Levenberg-Marquardt algorithm

The Levenberg-Marquardt algorithm is a method to efficiently find a local minimum in a nonlinear $\chi^2$ space, given a good first estimate.
This thesis makes use of an $\mathrm{IDL}$ implementation of the Levenberg-Marquardt algorithm called $\mathrm{MPFIT}$[5] and written by Craig Markwardt (Markwardt, 2009). $\mathrm{MPFIT}$ takes as in-

[5]http://www.physics.wisc.edu/ craigm/idl/fitting.html

put a model function and the list of parameter values to be tried, evaluates the model for each of these parameters, returns the residuals of the data, and moves in the parameter space to find the minimum in $\chi^2$ using a combination of Newton's method (adjusting search direction according to the curvature, i.e. the second derivative) and steepest-descent method (adjusting the steps according to the value of the gradient, i.e. the first derivative).
The limitation of the Levenberg-Marquardt method is that if the $\chi^2$ space has several local minima and the initial guess are not close the true minimum, the algorithm might find a local minimum in the $\chi^2$ space and not the true minimum. This is a problem when dealing with a complex $\chi^2$ space, in which case using a Markov Chain Monte Carlo (Section 6.1) to find the true minimum is a more robust approach.
The adjusted parameters are the epoch of the first transit in the CoRoT light curve $T_0$, the system scale $a/R_\star$, the inclination between the planet orbital plane and the plane-of-view $i$, and the planet-to-star radii ratio $R_\mathrm{p}/R_\star$. Also simultaneously adjusted are $u_+$ and $u_-$, combinations of limb darkening coefficients ($u_+ = u_a + u_b$ and $u_- = u_a - u_b$ where $u_a$ and $u_b$ are the quadratic limb darkening coefficients. The choice of the quadratic law was made as it follows the limb darkening of a star better than a linear law, without adding too many additional free parameters. The eccentricity and angle to periastron are fixed to 0. The transit period is fixed to the value in the discovery paper of the planet, or to a refined value when needed. If a refined value of the period is needed, it is determined using Aigrain & Irwin (2004) transit search algorithm with a small period search window around the value in the planet discovery paper.

#### Uncertainties on the parameters

Estimating the uncertainties on the derived parameters can be done in several ways:

- Alonso et al. (2008) evaluate the uncertainty on the planet parameters of CoRoT-1b using a bootstrap analysis. They randomly shuffle a fraction of the residuals, re-add the transit model and re-evaluate the planet parameters. They do this several thousand times and estimate the uncertainty on each planet parameter as the standard deviation of the values taken by this parameter. This method accounts for the white noise in the data.

- Aigrain et al. (2008) evaluate the uncertainties on the planet parameters of CoRoT-4b using a correlated bootstrap approach. They randomly shuffle intervals of the residuals of a chosen length (e.g. 1.12h avoiding aliases with periodic signals such as the satellite and Earth orbits), re-add the transit model and re-evaluate the planet parameters. They do this several hundred times and estimate the uncertainty on each planet parameter as the standard deviation of the values taken by this parameter. The fact that each interval is shuffled in its entirety preserves

the correlated noise on hourly timescales. This method thus accounts for both the white noise and the correlated noise in the data.

- Rauer et al. (2009) derive the planet parameters of CoRoT-5b using a Markov Chain Monte Carlo (MCMC) procedure. The uncertainty on a parameter is taken as the standard deviation of its posterior distribution. The uncertainties take into account the shape of parameter space around the best model.

Out of these three methods to derive the uncertainties, the later is the most robust. This approach is studied in Chapter 6. In the current chapter, the method adopted is similar to the second one. The uncertainties on the parameters of the best transit fit are evaluated by removing this fit from the IRF-filtered light curve, circularly permuting the residuals, re-inserting the best transit fit, re-fitting the resulting transit signal, doing the above 100 times, and evaluating the standard deviation of the parameters of the best fit for each parameter. Circularly permuting the residuals conserve the correlated features in the data and take them and the white noise into account when evaluating the uncertainties.

When the light curve was corrected from the light of a contaminant star, the uncertainty on the contaminant flux should be taken into account in the derivation of the uncertainties associated to the planet parameter. This is done by adding to each realisation of the noise (as described above) a constant drawn from a Gaussian distribution with zero mean and standard deviation equal to the uncertainty on the contaminant flux and re-normalising the resulting light curve. The uncertainties on the planet parameters are then derived from the different realisations as described previously.

### 3.2.2 CoRoT-1b

CoRoT-1b is a Jupiter-like planet orbiting its solar type host star in 1.5 days. This planet was observed with CoRoT for 55 days from February 6th 2007. The light curve was sampled every 512 s for the first 28 days, and then every 32 s for the remaining 24.7 d. The discovery of this planet was published in Barge et al. (2008). Radial velocity measurements were performed with SOPHIE[6] to confirm the planetary nature of the transiting companion. Further radial velocity measurements of the planet were performed with HARPS[7] to derive a precise mass for the planet. Table 3.1 lists the parameters derived for CoRoT-1b and its host star.

The period was refined using Aigrain & Irwin (2004) transit search algorithm. The new best period found is 1.5091897 days, this is the value that was used below for the IRF and the transit fits. The IRF cannot correct sharp flux variations, so before running the IRF, the points before HDJ-2451545=2594 and after HDJ-2451545=2638 were cut out. The IRF was run with the default values and the IRF-filtered transit signals were fitted, as described in Section 3.2.1. The resulting IRF-filtered light curves along with their transit fit are shown in Fig. 3.2, and the planet parameters in Table 3.1.

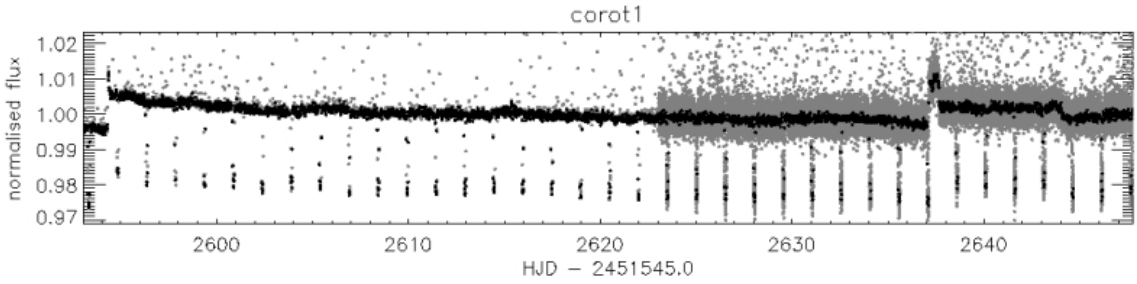


Figure 3.1: CoRoT-1's light curve (grey), re-binned with outliers clipped out (black).

[6]SOPHIE: 40000-resolution echelle spectrograph on the 1.93m telescope at the Observatoire de Haute Provence, France

[7]HARPS: 100000-resolution echelle spectrograph on the 3.6m telescope at ESO La Silla Observatory, Chile

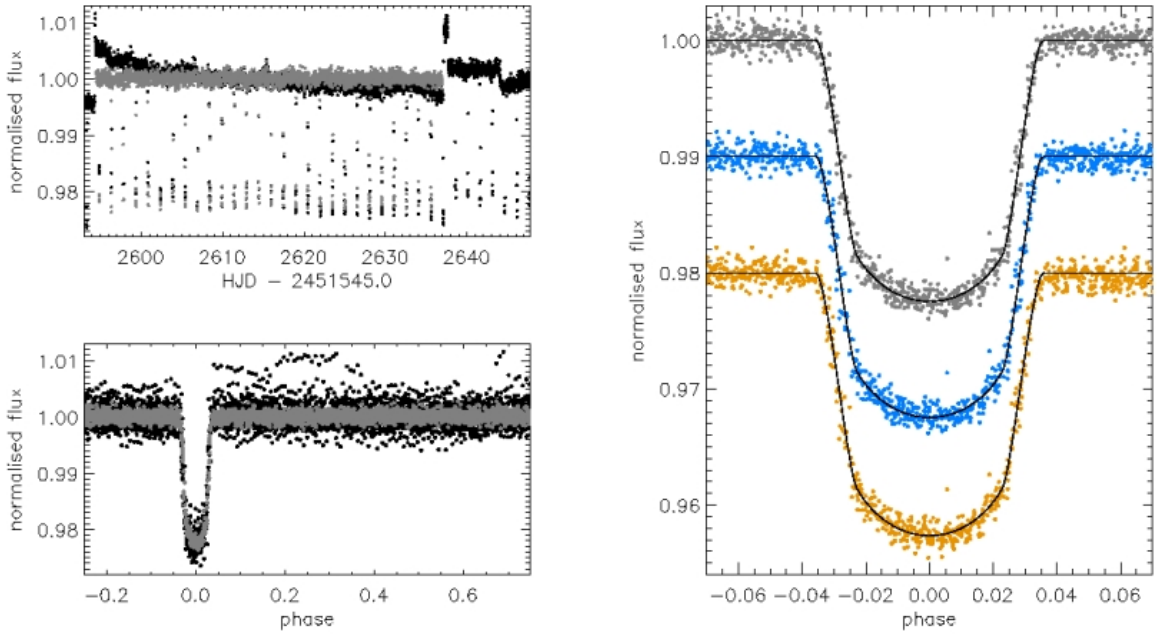


Figure 3.2: The IRF-filtered transit light curve of CoRoT-1b. Left panel: the IRF-filtered transit light curve with $\mathrm{timescale}$=0.5 d (grey) superimposed on the pre-processed light curve (black), unfolded (top panel) and phase-folded (bottom panel). Right panel: the IRF-filtered light curve with $\mathrm{timescale}$=0.5 d (grey), 0.25 d (blue) and 0.10 d (orange). The black lines are the best fits to each IRF-filtered transit, the planet parameters derived from these fits are shown in Table 3.1.

Table 3.1: Host star and planet parameters of CoRoT-1b.

| | Barge et al. (2008) | this study | | |
|---|---|---|---|---|
| **Star** | | IRF 0.5d | IRF 0.25d | IRF 0.1d |
| RA (J2000) | $06^{\mathrm{h}}\ 48^{\mathrm{m}}\ 19.17^{\mathrm{s}}$ | | | |
| Dec (J2000) | -03° 06′ 07.78″ | | | |
| $V_{\mathrm{mag}}$ | 13.6 | | | |
| $v \sin i$ (km s$^{-1}$) | 5.2 ± 1.0 | | | |
| $T_{\mathrm{eff}}$ (K) | 5950 ± 150 | | | |
| $\log g$ | 4.25 ± 0.30 | | | |
| [Fe/H] | -0.3 ± 0.25 | | | |
| $M_\star$ ($M_\odot$) | 0.95 ± 0.15 | | | |
| $R_\star$ ($R_\odot$) | 1.11 ± 0.05 | | | |
| **From light curve** | | | | |
| $P$ (d) | 1.5089557 ± 0.0000064 | 1.5091897 (fixed) | 1.5091897 (fixed) | 1.5091897 (fixed) |
| $T_0$-2454159 (d) | 0.4532 ± 0.0001 | 0.45265 ± 0.00007 | 0.45265 ± 0.00007 | 0.45269 ± 0.00008 |
| $R_{\mathrm{p}}/R_\star$ | 0.1388 ± 0.0021 | 0.1433 ± 0.0005 | 0.1432 ± 0.0006 | 0.1437 ± 0.0008 |
| $a/R_\star$ | 4.92 ± 0.08 | 4.56 ± 0.04 | 4.57 ± 0.04 | 4.54 ± 0.05 |
| $i$ (°) | 85.1 ± 0.5 | 83.1 ± 0.3 | 83.1 ± 0.3 | 83.0 ± 0.3 |
| $u_a$ | 0.42 ± 0.34 | 0.49 ± 0.02 | 0.49 ± 0.02 | 0.51 ± 0.02 |
| $u_b$ | 0.29 ± 0.34 | 0 | 0 | 0 |
| $e$ | 0 (fixed) | same (fixed) | same (fixed) | same (fixed) |
| $\frac{M_\star^{1/3}}{R_\star}$ ($M_\odot$,$R_\odot$) | 0.887 ± 0.014 | | | |
| $b$ | 0.42 ± 0.05 | 0.55 ± 0.03 | 0.55 ± 0.03 | 0.55 ± 0.03 |
| **Planet** | | | | |
| $M_{\mathrm{p}}$ ($M_{\mathrm{Jup}}$) | 1.03 ± 0.12 | | | |
| $R_{\mathrm{p}}$ ($R_{\mathrm{Jup}}$) | 1.49 ± 0.08 | | | |

### 3.2.3 CoRoT-2b

CoRoT-2 is an active solar-type star, its light curve is shown in Figure 3.3. CoRoT-2b is a Jupiter-like planet orbiting its host star in 1.7 days. This planet was observed with CoRoT nearly continuously for 152 days from May 16th 2007. The discovery of this planet was published in Alonso et al. (2008). Radial velocity measurements of the star were performed with SOPHIE, CORALIE[8] and HARPS to confirm the planetary nature of the transiting companion and derive the mass of the planet. Figure 3.3 shows CoRoT-2's light curve, and table 3.2 lists the parameters derived for CoRoT-2b and its host star.

The IRF was run with the default values and the IRF-filtered transit signals were fitted, as described in Section 3.2.1. The resulting IRF-filtered light curves along with their transit fit are shown in Fig. 3.4, and the best fit planet parameters in Table 3.2.

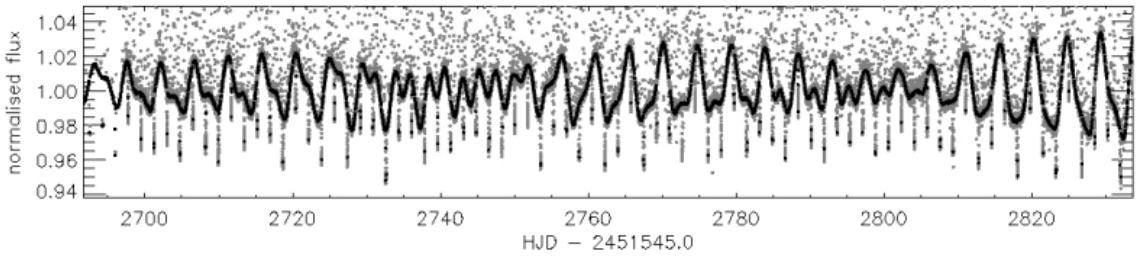


Figure 3.3: CoRoT-2's light curve. Same legend as Figure 3.1.

[8]CORALIE: 50000-resolution echelle spectrograph on the Euler 1.2m telescope at ESO La Silla Observatory, Chile

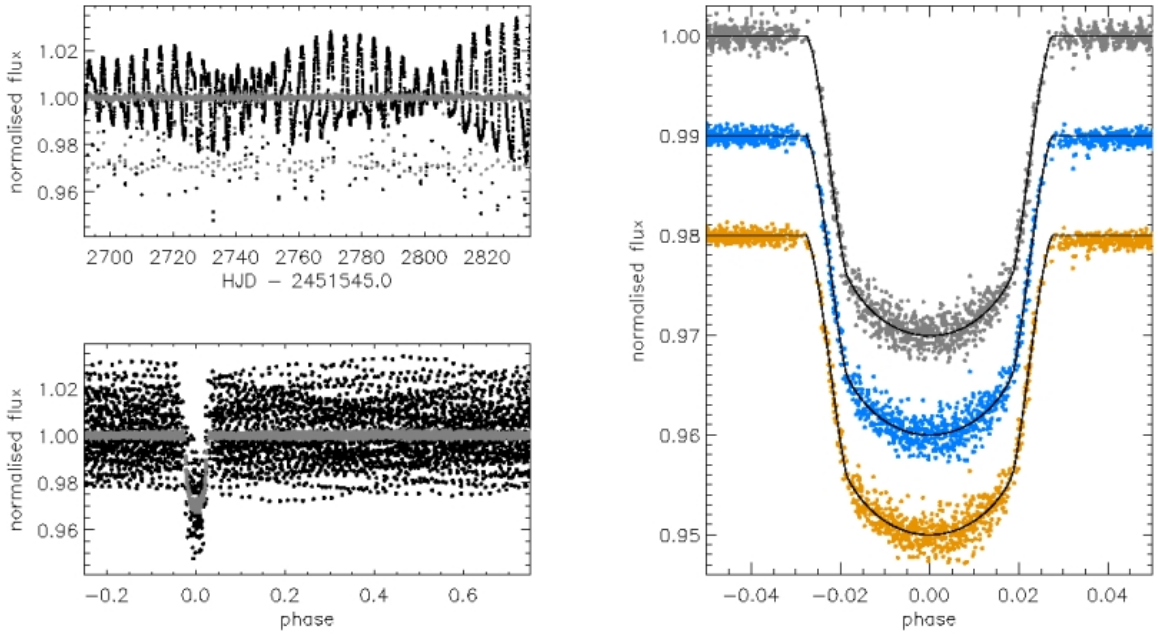


Figure 3.4: The IRF-filtered transit light curve of CoRoT-2b. Same legend as Figure 3.2

Table 3.2: Host star and planet parameters of CoRoT-2b.

| | Alonso et al. (2008) | this study | | |
|---|---|---|---|---|
| **Star** | | IRF 0.5d | IRF 0.25d | IRF 0.1d |
| RA (J2000) | $19^{\rm h}\ 27^{\rm m}\ 06.5^{\rm s}$ | | | |
| Dec (J2000) | $01^\circ\ 23'\ 01.5''$ | | | |
| $V_{\rm mag}$ | 12.57 | | | |
| $T_{\rm eff}$ (K) | $5625 \pm 120$ | | | |
| $M_\star$ ($M_\odot$) | $0.97 \pm 0.06$ | | | |
| $R_\star$ ($R_\odot$) | $0.902 \pm 0.018$ | | | |
| **From light curve** | | | | |
| $P$ (d) | $1.7429964 \pm 0.0000017$ | same (fixed) | same (fixed) | same (fixed) |
| $T_0$-2454237 (d) | $0.53562 \pm 0.00014$ | $0.53535 \pm 0.00003$ | $0.53541 \pm 0.00002$ | $0.53547 \pm 0.00002$ |
| $R_{\rm p}/R_\star$ | $0.1667 \pm 0.0006$ | $0.1663 \pm 0.0008$ | $0.1663 \pm 0.0007$ | $0.1662 \pm 0.0007$ |
| $a/R_\star$ | $6.70 \pm 0.03$ | $6.42 \pm 0.04$ | $6.38 \pm 0.03$ | $6.37 \pm 0.03$ |
| $i$ (°) | $87.8 \pm 0.1$ | $86.8 \pm 0.2$ | $86.6 \pm 0.2$ | $86.6 \pm 0.1$ |
| $u_a$ | $0.41 \pm 0.03$ | $0.47 \pm 0.03$ | $0.45 \pm 0.02$ | $0.43 \pm 0.02$ |
| $u_b$ | $0.06 \pm 0.03$ | $0.03 \pm 0.08$ | $0.07 \pm 0.06$ | $0.11 \pm 0.06$ |
| $e$ | 0 (fixed) | same (fixed) | same (fixed) | same (fixed) |
| $\frac{M_\star^{1/3}}{R_\star}$ ($M_\odot$,$R_\odot$) | $1.099 \pm 0.005$ | | | |
| $b$ | $0.26 \pm 0.01$ | $0.36 \pm 0.02$ | $0.37 \pm 0.04$ | $0.38 \pm 0.02$ |
| **Planet** | | | | |
| $M_{\rm p}$ ($M_{\rm Jup}$) | $3.31 \pm 0.16$ | | | |
| $R_{\rm p}$ ($R_{\rm Jup}$) | $1.465 \pm 0.029$ | | | |

### 3.2.4 CoRoT-3b

CoRoT-3b is a low mass brown dwarf (BD) with a Jupiter radius and 21 Jupiter masses, orbiting its host star in 4.2 days. This planet was observed with CoRoT nearly continuously for 112 days from May 26th 2007. The discovery of this planet was published in Deleuil et al. (2008). Radial velocity measurements of the star were performed with SOPHIE, TLS[9], CORALIE, HARPS, and SANDIFORD[10] to confirm the nature of the transiting companion and derive its mass. The parameters of CoRoT-3b are refined in (Triaud et al., 2009). Table 3.3 lists the parameters derived for CoRoT-3b and its host star.

Before running the IRF, the points affected by sudden jumps in flux before 2698 days, from 2737 to 2741 days and from 2745 to 2748 days (in HJD-2451545), were cut out. The IRF was run with the default values as described in Section 3.2.1. Before fitting the transit, for each of the IRF-filtered versions of CoRoT-3's light curve, a correction from the local slope about the phase-folded transit needed to be applied. A $2^{nd}$ order polynomial function was fitted about the phase-folded IRF-filtered light curve and divided into the phase-folded transit. The IRF-filtered transit signals, with their local polynomial fit removed, were then fitted as described in Section 3.2.1. The resulting IRF-filtered light curves along with their transit fit are shown in Fig. 3.6, and the best fit planet parameters in Table 3.3.

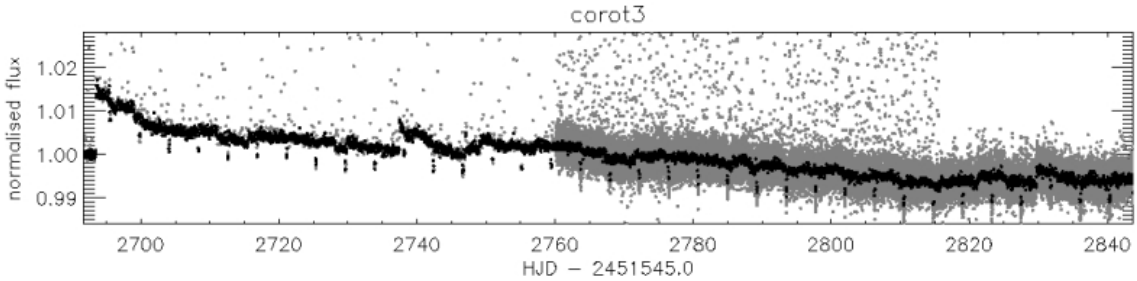


Figure 3.5: CoRoT-3's light curve. Same legend as Figure 3.1.

[9] 30000-resolution echelle spectrograph on the 2-m Alfred Jensch telescope in Tautenburg, Germany

[10] 60000-resolution echelle spectrograph on the 2.1m Otto Struve telescope at the McDonald Observatory, Texas, USA

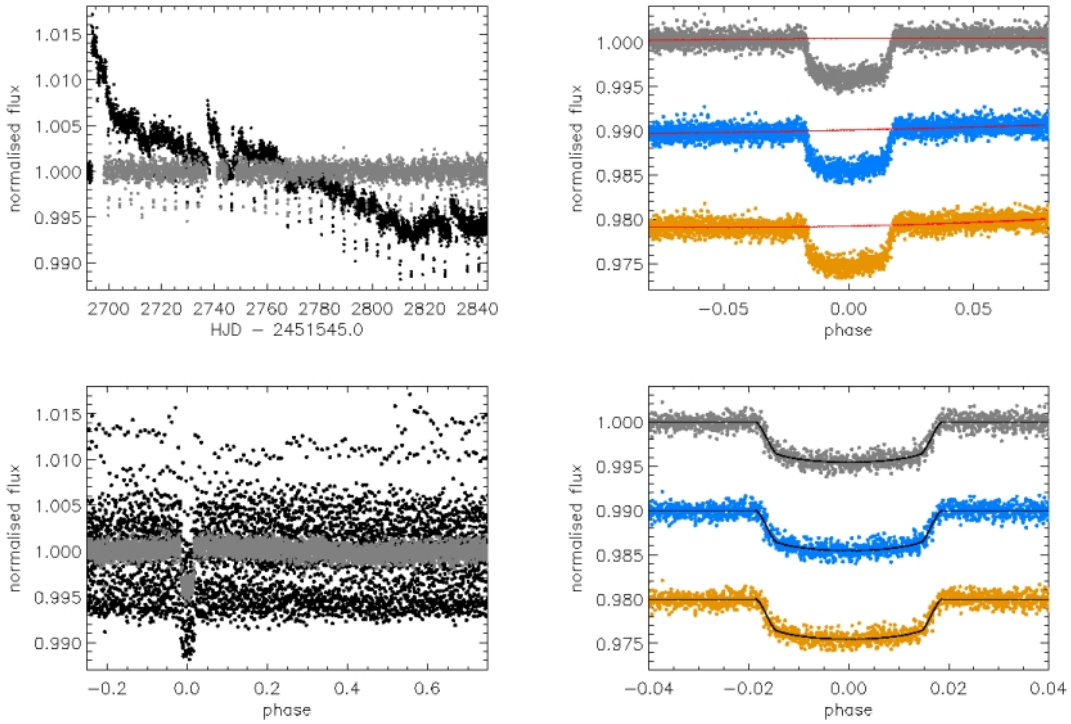


Figure 3.6: The IRF-filtered transit light curve of CoRoT-3b. Same legend as Figure 3.2. The red lines (top right panel) are the $2^{nd}$ order polynomial fits about the phase-folded IRF-filtered transits that were used to produce the corrected phase-folded transits (bottom right panel) which were then fitted to derive the planet parameters.

Table 3.3: Host star and planet parameters of CoRoT-3b.

| | Triaud et al. (2009) & Deleuil et al. (2008) | this study IRF 0.5d | this study IRF 0.25d | this study IRF 0.1d |
|---|---|---|---|---|
| **Star** | | | | |
| RA (J2000) | $19^{\rm h}\ 28^{\rm m}\ 13.26^{\rm s}$ | | | |
| Dec (J2000) | 00° 07' 18.7" | | | |
| $M_\star$ ($M_\odot$) | $1.37\ ^{+0.059}_{-0.043}$ | | | |
| $R_\star$ ($R_\odot$) | $1.540\ ^{+0.083}_{-0.078}$ | | | |
| $T_{\rm eff}$ (K) | $6740 \pm 140$ | | | |
| $\log g$ | $4.22 \pm 0.07$ | | | |
| [Fe/H] | $-0.02 \pm 0.06$ | | | |
| **From light curve** | | | | |
| $P$ (d) | $4.2567994\ ^{+0.0000039}_{-0.0000031}$ | same (fixed) | same (fixed) | same (fixed) |
| $T_0$-2454283 (d) | $0.13388\ ^{+0.00026}_{-0.00022}$ | $0.13945 \pm 0.00022$ | $0.13947 \pm 0.00022$ | $0.13937 \pm 0.00022$ |
| $R_{\rm p}/R_\star$ | $0.06632\ ^{+0.00063}_{-0.00069}$ | $0.0680 \pm 0.0014$ | $0.0676 \pm 0.0014$ | $0.0678 \pm 0.0015$ |
| $a/R_\star$ | $7.96\ ^{+0.43}_{-0.35}$ | $7.36 \pm 0.41$ | $7.39 \pm 0.47$ | $7.38 \pm 0.52$ |
| $i$ (°) | $86.1\ ^{+0.7}_{-0.5}$ | $85.1 \pm 0.8$ | $85.1 \pm 1.0$ | $85.1 \pm 1.2$ |
| $u_a$ | $0.23 \pm 0.09$ | $0.20 \pm 0.27$ | $0.23 \pm 0.25$ | $0.25 \pm 0.24$ |
| $u_b$ | $0.33 \pm 0.09$ | $0.38 \pm 0.39$ | $0.34 \pm 0.39$ | $0.31 \pm 0.38$ |
| $\frac{M_\star^{1/3}}{R_\star}$ ($M_\odot$,$R_\odot$) | $0.71 \pm 0.04$ | | | |
| $b$ | $0.54\ ^{+0.13}_{-0.09}$ | $0.63 \pm 0.15$ | $0.63 \pm 0.17$ | $0.63 \pm 0.20$ |
| **From radial velocities** | | | | |
| $e$ | $0.008\ ^{+0.005}_{-0.015}$ | 0 (fixed) | 0 (fixed) | 0 (fixed) |
| $\omega$ (°) | $179 \pm 170$ | 0 (fixed) | 0 (fixed) | 0 (fixed) |
| **Planet** | | | | |
| $M_{\rm p}$ ($M_{\rm Jup}$) | $21.23\ ^{+0.82}_{-0.59}$ | | | |
| $R_{\rm p}$ ($R_{\rm Jup}$) | $0.9934\ ^{+0.058}_{-0.058}$ | | | |

### 3.2.5 CoRoT-4b

CoRoT-4b is a gas-giant planet orbiting its host star in 9.2 days. This planet was observed with CoRoT nearly continuously for 58 days from February 6th 2007. The discovery of this planet was published in Aigrain et al. (2008). Radial velocity measurements of the star was performed with SOPHIE and HARPS to confirm the planetary nature of the transiting companion and derive the mass of the planet. Table 3.4 lists the parameters derived for CoRoT-4b and its host star.

Before running the IRF, the points affected by sudden jumps in flux before 2595 days (in HJD-2451545) were cut out. The IRF was run with the default values as described in Section 3.2.1. Before fitting the transit, for each of the IRF-filtered versions of CoRoT-3's light curve, a correction from the local slope about the phase-folded transit needed to be applied. A $2^{nd}$ order polynomial function was fitted about ((-0.008,0.008) phase range) the phase-folded IRF-filtered light curve and divided from the phase-folded transit. The IRF-filtered transit signals, with their local polynomial fit removed, were then fitted as described in Section 3.2.1. The resulting IRF-filtered light curves along with their transit fit are shown in Fig. 3.8, and the best fit planet parameters in Table 3.4.

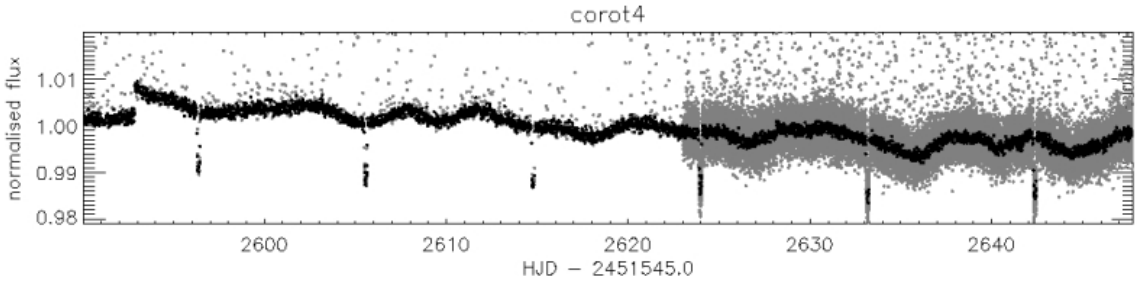


Figure 3.7: CoRoT-4's light curve. Same legend as Figure 3.1.

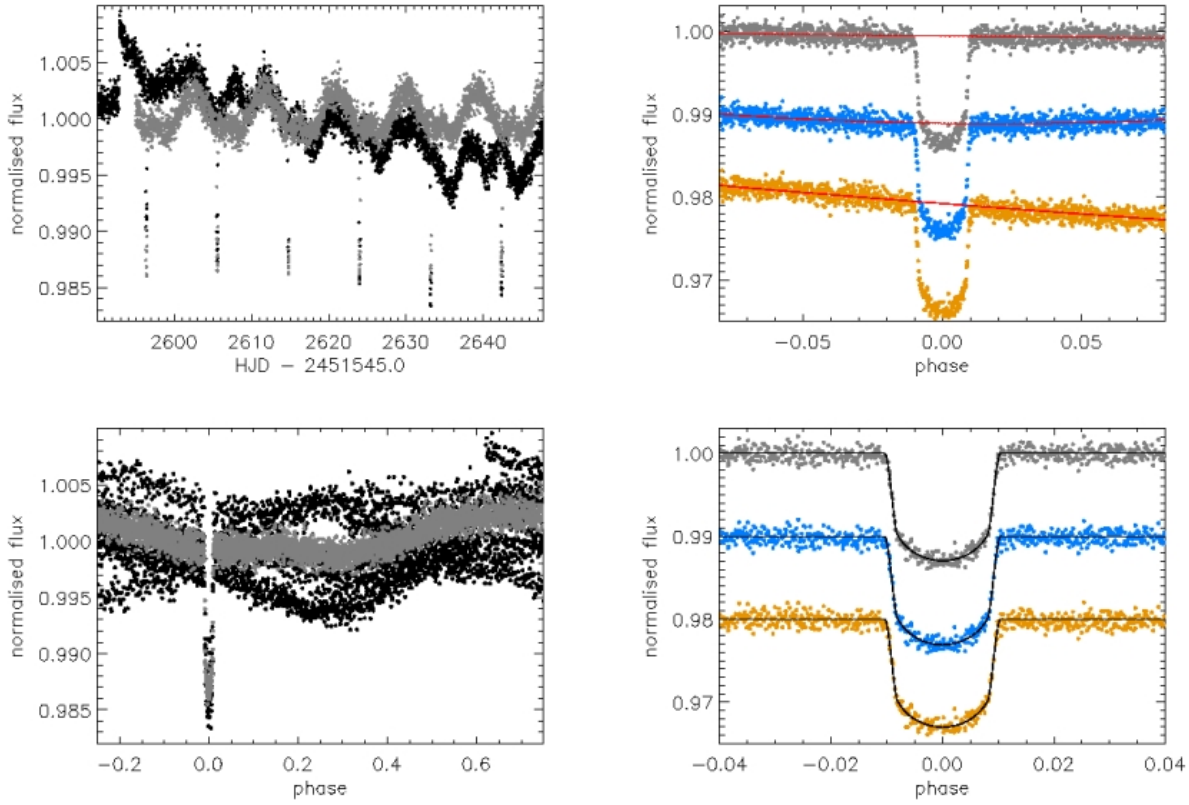


Figure 3.8: The IRF-filtered transit light curve of CoRoT-4b. Same legend as Figure 3.6

Table 3.4: Host star and planet parameters of CoRoT-4b.

| | Aigrain et al. (2008) & Moutou et al. (2008) | | this study IRF 0.5d | this study IRF 0.25d | this study IRF 0.1d |
|---|---|---|---|---|---|
| **Star** | | | | | |
| RA (J2000) | $06^{\rm h}\ 48^{\rm m}\ 46.70^{\rm s}$ | | | | |
| Dec (J2000) | -00° 40′ 21.97″ | | | | |
| $R_{\rm mag}$ | 13.45 | | | | |
| $P_{\rm rot}$ (d) | 8.87 ± 1.12 | | | | |
| $M_\star$ ($M_\odot$) | $1.16\ ^{+0.03}_{-0.02}$ | | | | |
| $R_\star$ ($R_\odot$) | $1.17\ ^{+0.01}_{-0.03}$ | | | | |
| $v \sin i$ (km s$^{-1}$) | 6.4 ± 1.0 | | | | |
| $T_{\rm eff}$ (K) | 6190 ± 60 | | | | |
| $\log g$ | 4.41 ± 0.05 | | | | |
| **From light curve** | | Bayesian range | | | |
| $P$ (d) | 9.20205 ± 0.00037 | | same (fixed) | same (fixed) | same (fixed) |
| $T_0$-2454141 (d) | 0.36416 ± 0.00089 | | 0.36434 ± 0.00022 | 0.36440 ± 0.00021 | 0.36439 ± 0.00020 |
| $R_{\rm p}/R_\star$ | $0.1047\ ^{+0.0041}_{-0.0022}$ | 0.1000 – 0.1125 | 0.1056 ± 0.0011 | 0.1064 ± 0.0012 | 0.1054 ± 0.0011 |
| $a/R_\star$ | $17.36\ ^{+0.05}_{-0.25}$ | 14.30 – 17.80 | 16.84 ± 0.35 | 16.66 ± 0.39 | 16.82 ± 0.34 |
| $i$ (°) | $90.000\ ^{+0.000}_{-0.085}$ | 87.708 – 90.000 | 89.2 ± 0.4 | 89.1 ± 0.4 | 89.3 ± 0.4 |
| $u_a$ | $0.44\ ^{+0.16}_{-0.15}$ | 0.00 – 1.00 | 0.48 ± 0.08 | 0.50 ± 0.09 | 0.45 ± 0.08 |
| $u_b$ | – | | -0.04 ± 0.17 | -0.06 ± 0.18 | 0.05 ± 0.18 |
| $\frac{M_\star^{1/3}}{R_\star}$ ($M_\odot$,$R_\odot$) | $0.899\ ^{+0.003}_{-0.013}$ | 0.741 – 0.922 | | | |
| $e$ | 0.0 ± 0.1 | | 0 (fixed) | 0 (fixed) | 0 (fixed) |
| $b$ | $0.0\ ^{+0.03}_{-0.0}$ | 0 – 0.57 | 0.22 ± 0.14 | 0.26 ± 0.14 | 0.20 ± 0.13 |
| **Planet** | | | | | |
| $M_{\rm p}$ ($M_{\rm Jup}$) | 0.72 ± 0.08 | | | | |
| $R_{\rm p}$ ($R_{\rm Jup}$) | $1.19\ ^{+0.06}_{-0.05}$ | | | | |

### 3.2.6 CoRoT-5b

CoRoT-5b is a Jupiter-size planet orbiting its host star in 4 days. This planet was observed with CoRoT nearly continuously for 112 days from October 24th 2007. The discovery of this planet was published in Rauer et al. (2009). Radial velocity measurements of the host star were performed with SOPHIE and HARPS to confirm the planetary nature of the transiting companion and derive the mass of the planet. Table 3.5 lists the parameters derived for CoRoT-5b and its host star.

Before running the IRF, the points affected by sudden jumps in flux before 2858 days, (time as displayed in Fig 3.9), were cut out. The IRF was run with the default values as described in Section 3.2.1. Before fitting the transit, for each of the IRF-filtered versions of CoRoT-3's light curve, a correction from the local slope about the phase-folded transit needed to be applied. A $2^{nd}$ order polynomial function was fitted about ((-0.008,0.008) phase range) the phase-folded IRF-filtered light curve and divided from the phase-folded transit. The IRF-filtered transit signals, with their local polynomial fit removed, were then fitted as described in Section 3.2.1. The resulting IRF-filtered light curves along with their transit fit are shown in Fig. 3.10, and the best fit planet parameters in Table 3.5.

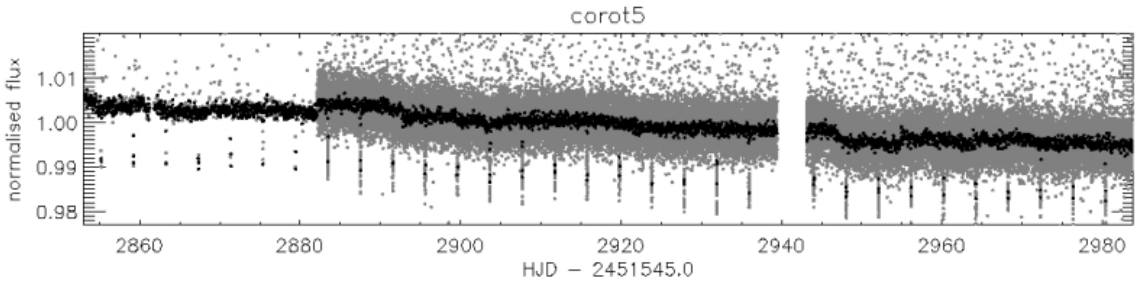


Figure 3.9: CoRoT-5's light curve. Same legend as Figure 3.1.

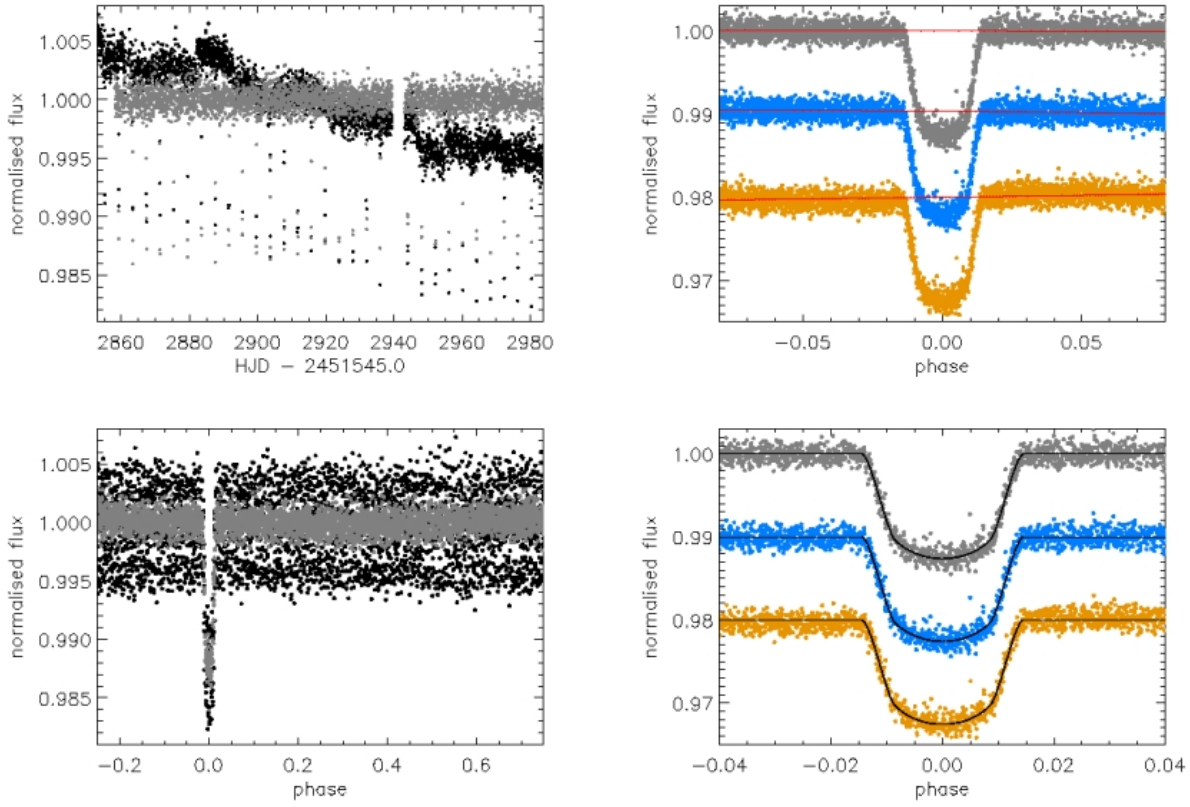


Figure 3.10: The IRF-filtered transit light curve of CoRoT-5b. Same legend as Figure 3.6

Table 3.5: Host star and planet parameters of CoRoT-5b.

| | Rauer et al. (2009) | this study | | |
|---|---|---|---|---|
| | | IRF 0.5d | IRF 0.25d | IRF 0.1d |
| **Star** | | | | |
| RA (J2000) | $06^{\rm h}\ 45^{\rm m}\ 07^{\rm s}$ | | | |
| Dec (J2000) | $00^\circ\ 48'\ 55''$ | | | |
| $V_{\rm mag}$ | 14.0 | | | |
| $M_\star$ ($M_\odot$) | $1.00 \pm 0.02$ | | | |
| $R_\star$ ($R_\odot$) | $1.186 \pm 0.04$ | | | |
| $T_{\rm eff}$ (K) | $6100 \pm 65$ | | | |
| $\log g$ | $4.189 \pm 0.03$ | | | |
| [Fe/H] | $-0.25 \pm 0.06$ | | | |
| **From light curve** | | | | |
| $P$ (d) | $4.0378962 \pm 0.0000019$ | same (fixed) | same (fixed) | same (fixed) |
| $T_0$-2454400 (d) | $0.19885 \pm 0.0002$ | $0.19843 \pm 0.00015$ | $0.19846 \pm 0.00015$ | $0.19799 \pm 0.00018$ |
| $R_{\rm p}/R_\star$ | $0.12087\ ^{+0.00021}_{-0.00023}$ | $0.1135 \pm 0.0021$ | $0.1139 \pm 0.0024$ | $0.1135 \pm 0.0022$ |
| $a/R_\star$ | $8.97 \pm 0.31$ | $9.39 \pm 0.20$ | $9.40 \pm 0.20$ | $9.39 \pm 0.24$ |
| $i$ (°) | $85.83\ ^{+0.99}_{-1.38}$ | $85.7 \pm 0.2$ | $85.7 \pm 0.2$ | $85.7 \pm 0.2$ |
| $u_a$ | 0.308 fixed | $0.13 \pm 0.33$ | $0.24 \pm 0.36$ | $0.19 \pm 0.34$ |
| $u_b$ | 0.308 fixed | $0.69 \pm 0.45$ | $0.54 \pm 0.50$ | $0.62 \pm 0.48$ |
| $\frac{M_\star^{1/3}}{R_\star}$ ($M_\odot$,$R_\odot$) | $0.843 \pm 0.024$ | | | |
| $b$ | $0.90\ ^{+0.25}_{-0.17}$ | $0.71 \pm 0.05$ | $0.71 \pm 0.05$ | $0.71 \pm 0.06$ |
| **From radial velocities** | | | | |
| $e$ | $0.09\ ^{+0.09}_{-0.04}$ | 0 (fixed) | 0 (fixed) | 0 (fixed) |
| $\omega$ (°) | $-128\ ^{+289}_{-48}$ | 0 (fixed) | 0 (fixed) | 0 (fixed) |
| **Planet** | | | | |
| $M_{\rm p}$ ($M_{\rm Jup}$) | $0.467\ ^{+0.047}_{-0.024}$ | | | |
| $R_{\rm p}$ ($R_{\rm Jup}$) | $1.388\ ^{+0.046}_{-0.047}$ | | | |

### 3.2.7 CoRoT-6b

CoRoT-6b is a Jupiter-size planet orbiting its host star in 8.9 days. This planet was observed with CoRoT nearly continuously for 144 days from April 15th 2008. The discovery of this planet was published in Fridlund et al. (2010). Radial velocity measurements of the host star were performed with SOPHIE to confirm the planetary nature of the transiting companion and derive the mass of the planet. Table 3.6 lists the parameters derived for CoRoT-6b and its host star.

Before running the IRF, the points affected by sudden jumps in flux before 3031 days, and from 3152 to 3153.54 days (time as displayed in Fig 3.9), were cut out. The IRF was run with the default values as described in Section 3.2.1. Before fitting the transit, for each of the IRF-filtered versions of CoRoT-6's light curve, a correction from the local slope about the phase-folded transit needed to be applied. A $2^{nd}$ order polynomial function was fitted about the phase-folded IRF-filtered light curve and divided into the phase-folded transit. The IRF-filtered transit signals, with their local polynomial fit removed, were then fitted as described in Section 3.2.1. The resulting IRF-filtered light curves along with their transit fit are shown in Fig. 3.12, and the best fit planet parameters in Table 3.6.

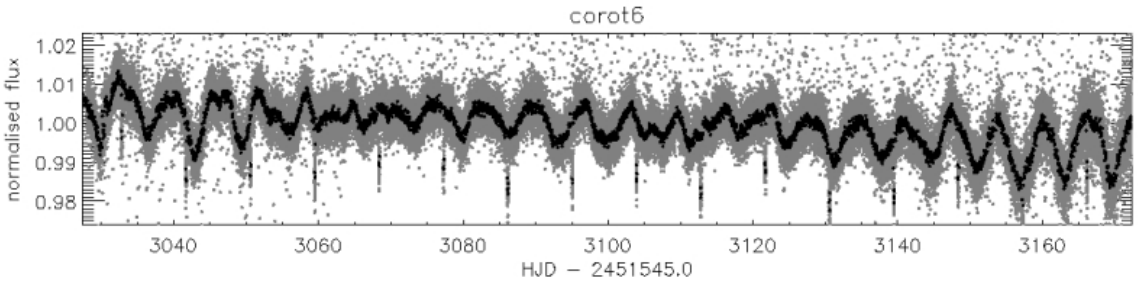


Figure 3.11: CoRoT-6's light curve. Same legend as Figure 3.1.

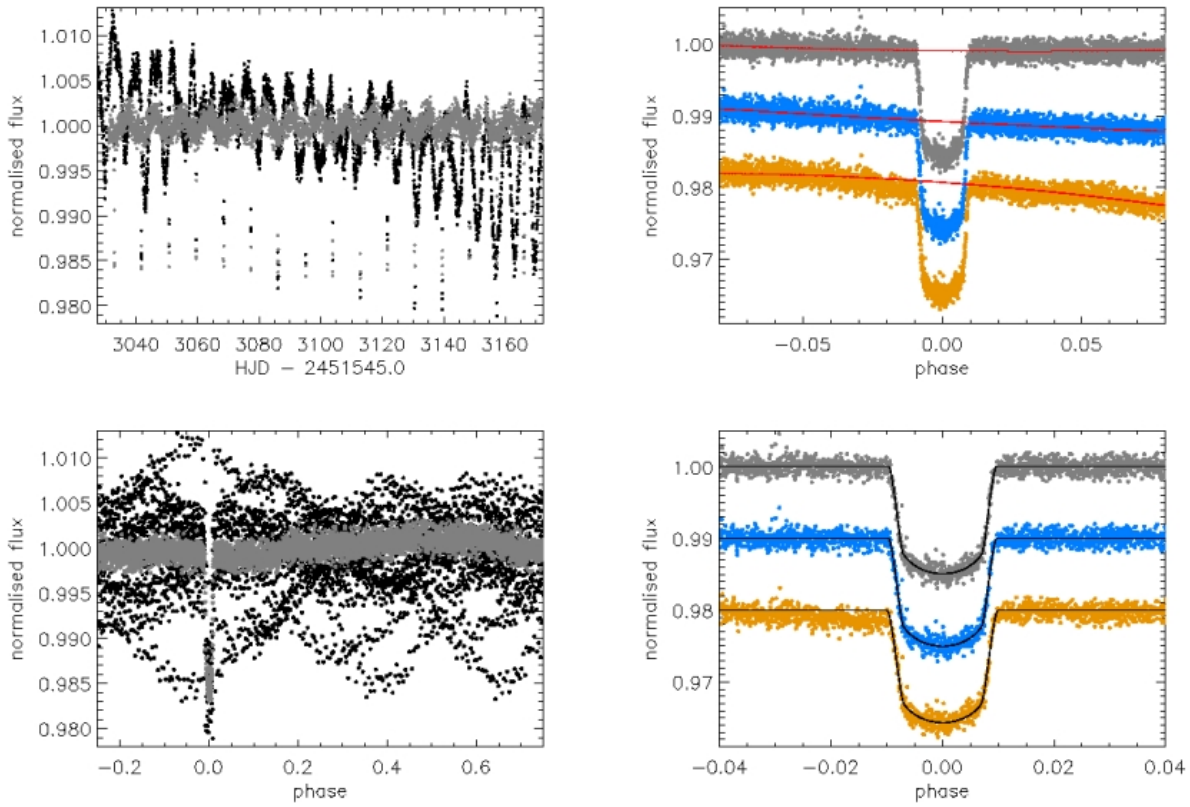


Figure 3.12: The IRF-filtered transit light curve of CoRoT-6b. Same legend as Figure 3.6

Table 3.6: Host star and planet parameters of CoRoT-6b.

| | Fridlund et al. (2010) | this study IRF 0.5d | this study IRF 0.25d | this study IRF 0.1d |
|---|---|---|---|---|
| **Star** | | | | |
| RA (J2000) | $18^{\rm h}\ 44^{\rm m}\ 17.42^{\rm s}$ | | | |
| Dec (J2000) | $06^{\circ}\ 39'\ 47.95''$ | | | |
| $V_{\rm mag}$ | 13.9 | | | |
| $M_\star$ ($M_\odot$) | $1.055 \pm 0.055$ | | | |
| $R_\star$ ($R_\odot$) | $1.025 \pm 0.026$ | | | |
| $T_{\rm eff}$ (K) | $6090 \pm 70$ | | | |
| $\log g$ | $4.3 \pm 0.1$ | | | |
| [Fe/H] | $-0.2 \pm 0.1$ | | | |
| **From light curve** | | | | |
| $P$ (d) | $8.886593 \pm 0.000004$ | same (fixed) | same (fixed) | same (fixed) |
| $T_0$-2454595 (d) | $0.6144 \pm 0.0002$ | $0.61434 \pm 0.00013$ | $0.61424 \pm 0.00013$ | $0.61323 \pm 0.00040$ |
| $R_{\rm p}/R_\star$ | $0.11687 \pm 0.00092$ | $0.1147 \pm 0.0015$ | $0.1150 \pm 0.0014$ | $0.1185 \pm 0.0050$ |
| $a/R_\star$ | $17.9 \pm 0.3$ | $17.62 \pm 0.42$ | $17.51 \pm 0.42$ | $16.39 \pm 1.16$ |
| $i$ (°) | $89.1 \pm 0.3$ | $88.9 \pm 0.3$ | $88.9 \pm 0.3$ | $88.4 \pm 0.5$ |
| $u_a$ | $0.35 \pm 0.14$ | $0.18 \pm 0.10$ | $0.17 \pm 0.10$ | $0.06 \pm 0.16$ |
| $u_b$ | $0.23 \pm 0.14$ | $0.52 \pm 0.21$ | $0.54 \pm 0.21$ | $0.69 \pm 0.35$ |
| $\frac{M_\star^{1/3}}{R_\star}$ ($M_\odot$,$R_\odot$) | $0.993 \pm 0.018$ | | | |
| $b$ | 0.28 (0 – 0.56) | $0.32 \pm 0.10$ | $0.34 \pm 0.10$ | $0.45 \pm 0.20$ |
| **From radial velocities** | | | | |
| $e$ | $< 0.1$ | 0 (fixed) | 0 (fixed) | 0 (fixed) |
| **Planet** | | | | |
| $M_{\rm p}$ ($M_{\rm Jup}$) | $2.96 \pm 0.34$ | | | |
| $R_{\rm p}$ ($R_{\rm Jup}$) | $1.166 \pm 0.035$ | | | |

### 3.2.8 CoRoT-7b

CoRoT-7b is a Super-Earth planet orbiting its host star in 0.85 days. The discovery of this planet was published in Léger et al. (2009). Due to the small size of the planet and the activity level of its host stars, confirming this planet with its mass derived from radial velocity measurement was a very challenging task. The planetary nature of this planet was thus first claimed with an upper limit on its mass $< 21 M_{\oplus}$ (based on radial velocity measurements with SOPHIE) and intensive ground-based follow-up (photometry, imaging, spectroscopy) to exclude probability of the transits been stellar eclipses. Later, HARPS radial velocity follow-up (Queloz et al., 2009) revealed CoRoT-7 as a multiple planetary system. Table 3.7 lists the parameters derived for CoRoT-7b and its host star.

The IRF was run as described in Section 3.2.1 but with a bin size of 0.0024 in phase (IRF $\mathrm{binsize}$ parameter) and a convergence limit of 1. $10^{-8}$ (IRF $\mathrm{cvlim}$ parameter). The three smoothing timescales to estimate the stellar variability were also tested (IRF $\mathrm{timescale}$ parameter): 0.50, 0.25 and 0.10 days. The IRF-filtered transit signals were then fitted as described in Section 3.2.1. For the fits, because of the low signal-to-noise ratio of the transit, the values of the quadratic limb darkening parameters were fixed to the values in CoRoT-7b discovery paper (Léger et al., 2009) – and not adjusted as done for the other planets. The resulting IRF-filtered light curves along with their transit fit are shown in Fig. 3.14, and the best fit planet parameters in Table 3.7.

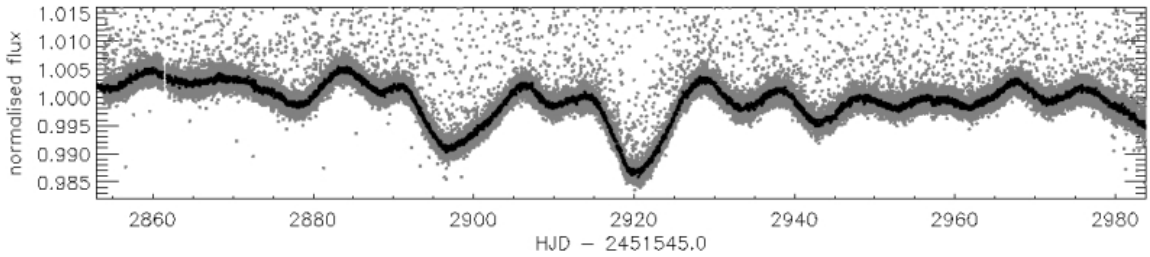


Figure 3.13: CoRoT-7's light curve. Same legend as Figure 3.1.

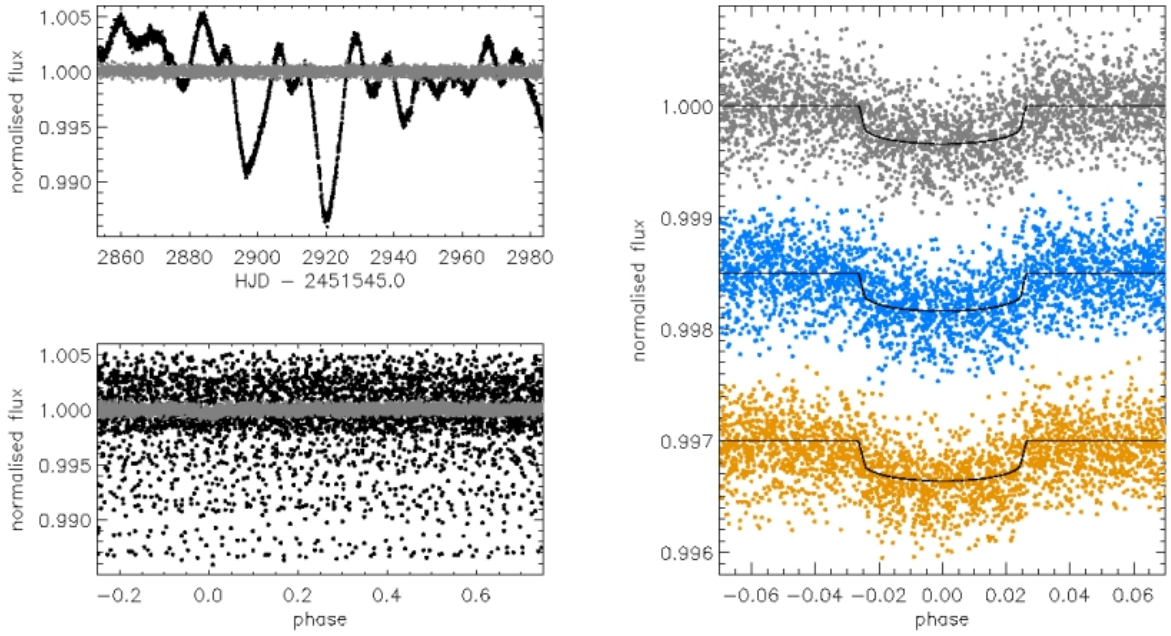


Figure 3.14: The IRF-filtered transit light curve of CoRoT-7b. Same legend as Figure 3.2

Table 3.7: Host star and planet parameters of CoRoT-7b.

| | Léger et al. (2009) & Queloz et al. (2009) | this study IRF 0.5d | this study IRF 0.25d | this study IRF 0.1d |
|---|---|---|---|---|
| **Star** | | | | |
| RA (J2000) | $06^{\rm h}\ 43^{\rm m}\ 49.0^{\rm s}$ | | | |
| Dec (J2000) | -01° 03′ 46.0″ | | | |
| $V_{\rm mag}$ | 11.668 ± 0.008 | | | |
| $T_{\rm eff}$ (K) | 5275 ± 75 | | | |
| $\log g$ | 4.50 ± 0.10 | | | |
| [Fe/H] | +0.03 ± 0.06 | | | |
| Spectral Type | G9 V | | | |
| $M_\star$ ($M_\odot$) | 0.93 ± 0.03 | | | |
| $R_\star$ ($R_\odot$) | 0.87 ± 0.04 | | | |
| **From light curve** | | | | |
| $P$ (d) | 0.853585 ± 0.000024 | same (fixed) | same (fixed) | same (fixed) |
| $T_0$-2454398 (d) | 0.0767 ± 0.0015 | 0.07726 ± 0.00037 | 0.07716 ± 0.00031 | 0.07682 ± 0.00030 |
| $R_{\rm p}/R_\star$ | 0.0187 ± 0.0003 | 0.0184 ± 0.0013 | 0.0182 ± 0.0012 | 0.0186 ± 0.0015 |
| $a/R_\star$ | 4.27 ± 0.20 | 4.13 ± 1.4 | 4.31 ± 1.2 | 4.70 ± 1.3 |
| $i$ (°) | 80.1 ± 0.3 | 79.3 ± 11.1 | 80.1 ± 8.8 | 81.9 ± 12.6 |
| $u_a$ | 0.40 | same (fixed) | same (fixed) | same (fixed) |
| $u_b$ | 0.20 | same (fixed) | same (fixed) | same (fixed) |
| $b$ | 0.73 ± 0.06 | 0.77 (0 – 1) | 0.74 (0 - 1) | 0.66 (0 - 1) |
| **From radial velocities** | | | | |
| $e$ | 0 | 0 (fixed) | 0 (fixed) | 0 (fixed) |
| **Planet** | | | | |
| $M_{\rm p}$ ($M_\oplus$) | 4.8 ± 0.8 | | | |
| $R_{\rm p}$ ($R_\oplus$) | 1.68 ± 0.09 | | | |

### 3.2.9 Discussion

For all the objects studied in this chapter, except CoRoT-6b, the parameters derived from the IRF-filtered light curves with different $\mathrm{timescale}$ are consistent with each other within $1\sigma$ ($\sigma$ being the uncertainty on the parameter). This shows that IRF-filtering down to $\mathrm{timescale}$=0.25 days still preserves the transit shape within the noise limit, but smaller $\mathrm{timescale}$ values affect the transit shape in some cases.

Compare to the planet/brown dwarf parameters published in the discovery of the first seven CoRoT planets/brown dwarfs, the adjusted planet parameters and quadratic limb darkening coefficients, derived from the fitting of the IRF-filtered transit light curve using a Levenberg-Marquardt algorithm, are consistent within $1\sigma$ for CoRoT-2b, CoRoT-4b, CoRoT-6b and CoRoT-7b, consistent within $2\sigma$ for CoRoT-3b, and different (outside the $2\sigma$ range) for CoRoT-1b and CoRoT-5b.

The difference in the limb darkening coefficients is expected to contribute to the difference in the planet parameters, in particular for $R_{\mathrm{p}}/R_{\star}$. This can explain the cases where the parameters derived in this chapter are different by more than $2\sigma$ from the parameters published in the discovery paper of the respective planets.

The errors bars derived in the chapter are smaller for CoRoT-1b and CoRoT-4b, larger for CoRoT-7b, and similar for the other planets and the brown dwarf. Fitting the limb darkening on a light curve with not enough photometric precision increases the error bars on all the other parameters. The alternative approach is to fix the limb darkening coefficients to the value derived from stellar atmosphere models for the stellar atmospheric parameters of the host star ($T_{\mathrm{eff}}$, $\log g$, (M/H)), in the observed filter (here, the CoRoT bandpass), and a chosen limb darkening law. Claret (2000) and Claret (2004) give tables of limb darkening coefficients for different standard filters and Sing (2010) for CoRoT and Kepler bandpasses. The larger uncertainties found for the planet parameters of CoRoT-7b are more representative of the noise level in the light curve than the values publishes in the planet discovery paper. For CoRoT-1b and CoRoT-2b, the smaller uncertainties derived for the planet parameters can come from a reduction in the noise of the filtered transit light curve achieved with the IRF.

In CoRoT-2's light curve, IRF-filtered with $\mathrm{timescale}$ = 0.5 days, some high frequency variations can be seen. What causes these features is not well understood. They often appear when binning the phase folded light curve with a section of the light curve shifted (not in phase) from another one, for instance due to an inaccurate transit period or wrong time stamps.

In CoRoT-3,4,5 's light curves, residual stellar variability at the planet orbital period can be seen even after IRF-filtering down to $\mathrm{timescale}$ = 0.10 days. Thus, the rotation period of these stars must be close to a multiple of the orbital period of their transiting planet, making the residual stellar variability difficult to separate from the transit signal. The additional variability at the orbital period of the planet could be caused by a planet-star interaction.

In CoRoT-6's light curve, IRF-filtered with $\mathrm{timescale}$ = 0.10 days, there is a drop in flux ($\sim$5% of the transit depth lasting for $\sim$0.015 phase units) just before the transit. This feature affects the evaluation of the transit shape and thus the derived planet parameters, which can be seen in the larger difference in the planet parameters derived. This feature is likely to have been created by the IRF (see explanations in Chapter 4, Section 4.2.4).

## 3.3 IRF performance on CoRoT space data

For all the planets, the IRF allows filtering of stellar variability to lower time scales (down to 6 h) without affecting the shape of the phase folded transit. This is a significant improvement from standard filters that would have affected the transit signal with this level of filtering.

For all the planets, the difference between the planet parameter values in the literature and those derived with the IRF-filtered light curves ($\mathrm{timescale}$ 0.50 and 0.25 days) is within the error bar associated to each parameter. This shows, on one hand, that the IRF is performing well as it is not affecting the transit shape, and on the other hand, that the traditional variability filtering method, such as those used in the discovery papers, are appropriate for the levels of stellar variability in those light curves. The improvement in the planet parameters after IRF-filtering was more obvious in the CoRoT BT2 simulated data used in Chapter 2. This reflects the lower level of stellar activity (lower amplitude, longer timescales) of stars with planets discovered by CoRoT, compared to the activity level modelled in the simulated data. The apparent lower activity level of stars with planet could also be a detection bias, as planets around active stars are more difficult to detect.

### 3.3.1 Limitations

The IRF is a post-detection method, it requires a prior knowledge of the period of the signal to be reconstructed, it cannot be used without a good estimate of this period.

The IRF reconstructs the signal in its phase folded shape, and therefore its direct product is an average over all the individual transits and has lost the information on transit shape variation with time due to perturbation by another planet for instance. Another approach would need to be taken to study such time-variations.

### 3.3.2 Future work

Adjusting the limb darkening coefficients simultaneously has an influence on the value of $R_{\mathrm{p}}/R_{\star}$ derived from the transit. It will be interesting to see how the parameters compare with the values in the planet discovery papers, for the same model of the limb

darkening. This will allow to check the difference in transit depth free from the limb darkening-transit depth degeneracy.

It will be interesting to look for time-variations of the transit shape in the residuals of the light curve with the transit fit to the phase-folded IRF-filtered light curve removed. Time-variations in the transit shape can be due for instance to features on the stellar surface or to another planet perturbing the orbit of the transiting planet.

As the IRF reconstructs all signal at the orbital period of the planet, one can attempt a search for other planet orbital feature in the IRF-filtered light curve, such as the planet secondary eclipse and the planet orbital phase variations. This aspect is studied in Chapter 4.

# Chapter 4

# Detecting photons from the CoRoT planets

This chapter focuses on the study of planet's secondary eclipses and the orbital phase variations. The amplitude of the secondary eclipse of a planet gives a measurement of the integrated flux of the planet's day-side hemisphere, relative to the integrated flux from the visible side of the stellar disk. The phase of the secondary eclipse gives a measurement of the eccentricity of the planet's orbit. The amplitude of the planet's orbital phase variation gives a measurement of the flux from the night-side hemisphere of the planet (minimum) relative to the planet's day-side (maximum). The shape of the phase variation gives an insight on the planet atmospheric circulation, if the dominant component of the planet flux is its thermal emission, or an insight on the microscopic properties on the reflective material at the surface of the planet, if the dominant flux is the reflected starlight.

The first detections of the secondary eclipses of an exoplanet were made by Charbonneau et al. (2005) and Deming et al. (2005), followed by the detections of planet's orbital phase variations published in Harrington et al. (2006) and Knutson et al. (2007a). These detections were made from space to increase the photometric precision, and in the infrared where the planet's flux is stronger. The first ground based detections of the thermal emission of an exoplanet was recently made by de Mooij & Snellen (2009) and Sing & López-Morales 2009, and since the secondary eclipse of several other exoplanets were observed (e.g. CoRoT-1b in Gillon et al. 2009, CoRoT-2b in Alonso et al. 2010). The first secondary eclipses in the visible from space were recently detected with CoRoT and Kepler for CoRoT-1b and 2b (Alonso et al. 2009b,a; this work) and HAT-P-7 (Borucki et al., 2009). The observation of secondary eclipses in multiple bandpass give information on the planet's atmospheric properties (e.g. planet temperature, nature of reflective particles).

For planets around active stars, the stellar variability hinders the detection of secondary eclipses and orbital phase variations. As mentioned in Chapter 2, the IRF recon-

structs all signals at the orbital period of the planet, and presented itself as a suitable tool to filter the CoRoT light curves and search for the planet photometric signature.

The theory behind the secondary eclipse of planets and their orbital phase variations is presented in Section 4.1. After describing in Section 4.2 the method followed to search and measure secondary eclipses, the technique is applied to CoRoT-1b and CoRoT-2b in Section 4.3. The achievements of this chapter are then discussed in Section 4.4 and conclusions are drawn in Section 4.5.

Some of the work presented in this chapter was carried out as part of the CoRoT collaboration and published in Alonso et al. (2009a,b). Specifically, the method described in this chapter was one of several methods used to detect the secondary eclipses of CoRoT-1b and 2b. The method was optimised further since this publication, leading to an improvement in the significance of the detections.

## 4.1 Theory of the secondary eclipse and orbital phase variations

This section summarises the equations and concepts on secondary eclipses used in the chapter. It explores the dependence of the secondary depth with $R_{\rm p}/R_\star$, $a/R_\star$, the Bond albedo $A_B$, and the re-distribution parameter $f$. It derives expected depths for the secondary eclipse of the CoRoT planets published to date (or close to publication).

### 4.1.1 Planet's emission

The flux emitted by the planet is:

$$F_{\rm p} = F_{\star,\ \text{reflected by planet}} + F_{\rm p,\ thermal\ emission} + F_{\rm p,\ internal} \tag{4.1}$$

where $F_{\rm p,\ thermal\ emission}$ is the flux from the star absorbed and re-emitted by the planet, and $F_{\rm p,\ internal}$ the planet internal heat (e.g. due to contraction heating or tidal heating).

The Bond Albedo $A_B$ of a planet is defined as the fraction of incident power that is reflected back by the planet, averaged over all the wavelengths and phase angles[1], therefore:

$$F_{\star,\ \text{reflected by planet}} = A_B\ F_{\star,\ \text{received by planet}} \tag{4.2}$$

$$F_{\star,\ \text{absorbed by planet}} = (1 - A_B)\ F_{\star,\ \text{received by planet}} \tag{4.3}$$

The star can be approximated as a black body, thus $F_\star = 4\pi R_\star^2 \sigma_{\rm SB} T_\star^4$ ($\sigma_{\rm SB}$ is the Stefan-Boltzmann constant) and the stellar flux received by the planet can be expressed as:

$$F_{\star,\ \text{received by planet}} = \pi R_{\rm p}^2\ \frac{F_\star}{4\pi a^2} = \frac{1}{4}\left(\frac{R_{\rm p}}{a}\right)^2 F_\star \tag{4.4}$$

[1]The phase angle is the angle between the incident flux and the line of sight

### 4.1.2 Secondary eclipse

#### Depth

The depth of the secondary eclipse is $\frac{\Delta F}{F} = \frac{F_{\rm p}}{F_\star + F_{\rm p}}$. As $F_{\rm p} << F_\star$ (4 or more orders of magnitude smaller), the depth of the secondary eclipse can be approximated by:

$$\frac{\Delta F}{F} = \frac{F_{\rm p}}{F_\star} \tag{4.5}$$

In the case where the planet emission only comes from the stellar flux reflected by the planet ($F_{\rm p} = F_{\star,\text{ reflected by planet}}$) – e.g. for a planet with no thermal emission and internal heat – from equations 4.4 and 4.2 the depth of the secondary eclipse can be expressed as:

$$\frac{F_{\rm p}}{F_\star} = \frac{A_B}{4}\left(\frac{R_{\rm p}}{a}\right)^2 = \frac{A_B}{4}\left(\frac{R_{\rm p}}{R_\star}\right)^2\left(\frac{R_\star}{a}\right)^2 \tag{4.6}$$

In practice, the albedo measured from the depth of the planet's occultation is the geometric albedo $A_g$, which is the fraction of incident light reflected back at zero phase angle (i.e. the configuration at occultation). $A_g = \frac{2}{3}A_B$ for Lambertian isotropic reflectance (i.e. constant for all angles of incidence) (Rowe et al., 2006). The calculations in this chapter are made under the assumption that $A_B = A_g$. The analysis will be repeated in the near future for $A_g = \frac{2}{3}A_B$.

#### Phase

The phase of a planet secondary eclipse $\phi_{sec}$ with regards to the phase of the transit (set to 0) can be computed by solving Kepler's equation numerically, for the range of possible $e$ and $w$ determined by radial velocity measurements. To the first order in $e$ (for $e \leq 0.2$), Winn (2010) give an analytic formula to derive the phase of the secondary eclipse (the transit is at phase 0):

$$\phi_{sec} \approx \frac{P}{2}\left[1 + \frac{2e\cos\omega}{\pi}\right] \tag{4.7}$$

where, $P$ is the planet orbital period, $e$ is the eccentricity and $\omega$ the angle to the periastron. The phase of the secondary eclipse provides a measurement of $e\cos\omega$, and the radial velocity curve a measurement of $e\sin\omega$ (Winn, 2010). When the information derived from both is combined together, $e$ and $\omega$ can be derived individually.

### 4.1.3 Planet's equilibrium temperature

If we approximate the planet as a black body, the thermal emission of the planet is $F_{\text{p, thermal emission}} = F_{\text{p, black body}} = 4\pi R_{\rm p}^2 \sigma_{\rm SB} T_{\rm p}^4$.

To account for the efficiency of the energy transport from the planet surface receiving the stellar flux to the planet surface re-emitting this flux, a redistribution factor $f$ is introduced such that:

$$F_{\mathrm{p,\ thermal\ emission}} = \frac{1}{4f}\ F_{\mathrm{p,\ black\ body}} \tag{4.8}$$

where $\frac{1}{4f}$ represents the fraction of the total planet surface ($4\pi R_{\mathrm{p}}^2$) that is reemitting the absorbed stellar flux. If the energy transport from the day to the night side of the planet is efficient, then the whole planet is reemitting (isothermal reemission over the whole sphere) and $\frac{1}{4f} = 1$, i.e. $f = 1/4$. If the energy transport is inefficient and only the day-side of the planet (half sphere) is reemitting, then $\frac{1}{4f} = 0.5$ and $f = 1/2$. If the energy transport is even less efficient and only a portion on the day-side is reemitting, then $\frac{1}{4f} < 0.5$ and $f > 1/2$.

If the planet is in thermal equilibrium,

$$F_{\mathrm{p,\ thermal\ emission}} = F_{\star,\ \mathrm{absorbed\ by\ planet}} \tag{4.9}$$

From the planet black body approximation and equations 4.8, 4.9, 4.3 and 4.4, the planet equilibrium temperature can be derived as:

$$T_{p,\ eq} = [f\ (1 - A_B)]^{1/4}\ \sqrt{\frac{R_\star}{a}}\ T_\star \tag{4.10}$$

From the black body emissions of the planet and the star, using equations 4.5 and 4.10, and assuming that the planet is in thermal equilibrium and that the planet thermal emission dominates over the other components of the planet flux, the expected depth of the planet secondary eclipse can be expressed as:

$$\frac{\Delta F}{F} = f\ (1 - A_B)\ \left(\frac{R_\star}{a}\right)^2\ \left(\frac{R_{\mathrm{p}}}{R_\star}\right)^2 \tag{4.11}$$

Several effects can take the planet out of thermal equilibrium, in which case equation 4.11 will not reflect the true depth of the secondary eclipse. The secondary eclipse can appear deeper than calculated with equation 4.11, if the planet radiates more than the energy than it receives from its star – for instance if the planet has an internal heat due to the contraction of the planet if the planet is young, or to tidal heating. The secondary eclipse can also appear shallower than calculated with equation 4.11, if the planet does not re-emit all the energy it absorbs from its star. Absorption and emission from the planet's atmosphere will also effect the depth of the secondary eclipse at the corresponding wavelength.

The planet brightness temperature is derived as the temperature of a black body

with a total flux equivalent to the planet flux $F_{\rm p}$, as follow:

$$T_{\rm B} = \left( \frac{F_{\rm p}}{4\pi\sigma_{\rm SB} R_{\rm p}^2} \right)^{1/4} \tag{4.12}$$

$T_{\rm B}$ is the true observable temperature from the eclipse depth calculated independently of any knowledge of the planet's thermal flux and the stellar reflected light components.

### 4.1.4 Variations of secondary eclipse's depth with $R_{\rm p}/R_\star$, $a/R_\star$, $A_B$ and $f$

The CoRoT bandpass is in the optical range, where both thermal emission and reflected light are expected to be significant contributions to the planet's flux. As these two components of the planet flux can not be disentangled with optical detection alone, the relation between the depth of the secondary and other parameters is investigated and the fraction of each component in each case extracted.

#### Method

The star is treated as a black body, and the stellar flux is calculated using Planck's law (equation 4.13) for a given stellar temperature (5800 K in the section). The stellar light reflected by the planet is calculated from the stellar black body using Equations 4.2 and 4.4. The planet is assumed to radiate like a black body and the planet thermal emission is calculated using Planck's law (equation 4.13) with a planet temperature calculated using Equation 4.10. The total flux of the planet is calculated as the sum of the stellar light reflected by the planet and the planet thermal emission.

The black body radiation follows the Planck's law:

$$F(\lambda) = \frac{2hc^2}{\lambda^5} \frac{1}{e^{\frac{hc}{\lambda k T}} - 1} \tag{4.13}$$

where $F(\lambda)$ is the flux intensity of the black body as a function of wavelength $\lambda$, $h$ is the Planck constant, $c$ is the speed of light, $k$ is the Boltzmann constant, and $T$ is the temperature of the black body.

All the fluxes are multiplied by the CoRoT response spectrum (Auvergne et al. 2009, wavelength range: (370,1000) nm), and the integral of each flux is calculated to give the total flux received within the CoRoT bandpass ($F_\star$ for the star, $F_{\rm p}$ for the planet). Figure 4.1 shows two examples ($A_B = 0.9$ and $A_B = 0.1$) of an implementation of stellar black body, stellar light reflected by the planet and planet black body view through the CoRoT bandpass. The depth of the secondary eclipse is calculated as $\frac{F_{\rm p}}{F_\star}$.

The lowest wavelength of the CoRoT red channel is calculated as the wavelength marking 60% of the total flux from the largest wavelength in the CoRoT bandpass, and the largest wavelength in the CoRoT blue channel as the wavelength marking 20% of

the total flux from the lowest wavelength in the CoRoT bandpass. These limits depend on the stellar temperature chosen; with the 5800 K chosen here the red channel is at (585,1000) nm, the green channel at (507,585) nm, and the blue channel at (370,507) nm). The planet and stellar fluxes in each of the CoRoT colour channels are calculated as the sum of the fluxes within the wavelength range associated to each channel.

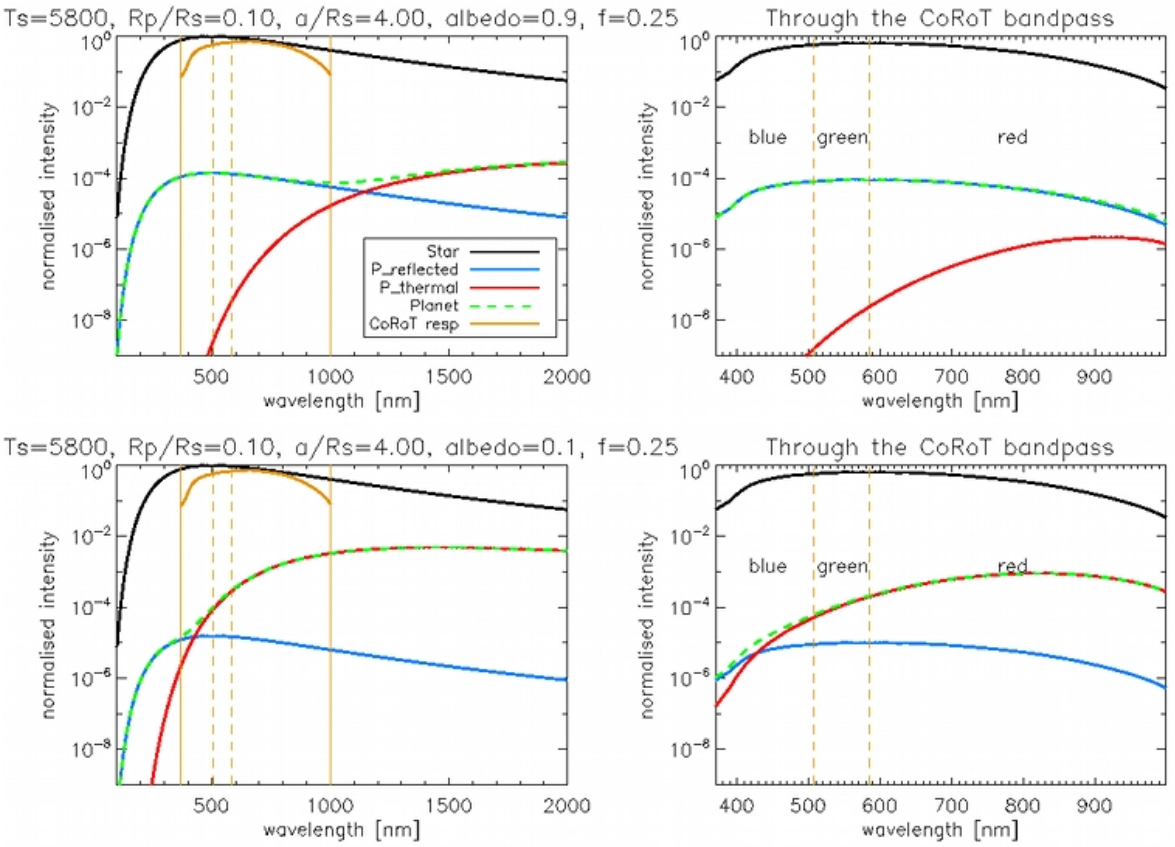


Figure 4.1: This figure shows the star emission (black) as a black body at 5800 K, and the planet emission (green dashed) composed of the stellar light reflected by the planet (blue) calculated as a fraction of the star emission (equations 4.2 and 4.4) and the planet thermal emission (red) derived as a black body at a temperature calculated with equation 4.10. The planet is set with $R_{\rm p}/R_\star$=0.1 and $a/R_\star$=4, with an albedo $A_B = 0.9$ (top panels) or $A_B = 0.1$ (bottom panels), and a redistribution factor $f = 0.25$. The different emissions are multiplied by the CoRoT response spectrum (orange) and plotted in the right panels. The CoRoT bandpass is divided into red, green and blue channels defined as respectively containing 60%, 20% and 20% of the stellar flux within the CoRoT bandpass.

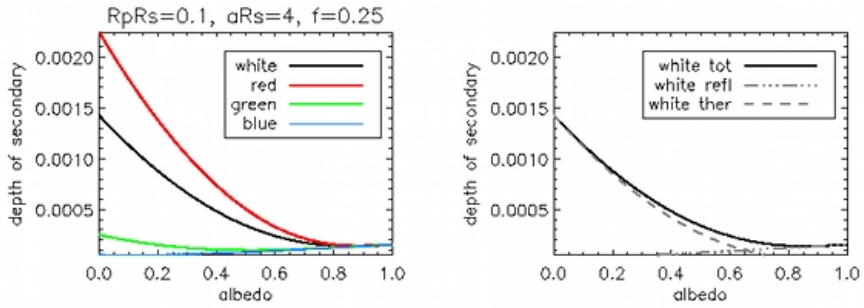


Figure 4.2: This figure shows the depth of the secondary eclipse $\frac{F_{\rm p}}{F_\star}$ in the CoRoT bandpass (black), red channel (red), green channel (green) and blue channel (blue) for a 5800 K star and a planet with radius $R_{\rm p}/R_\star$=0.1, orbital distance $a/R_\star$=4, redistribution factor $f$=0.25, and an albedo varied from $10^{-8}$ to 1. The depth of the eclipse taking into account only the reflected light (dash-dots grey) or only the thermal emission (dash grey) falling within the CoRoT bandpass is plotted in the right panel.

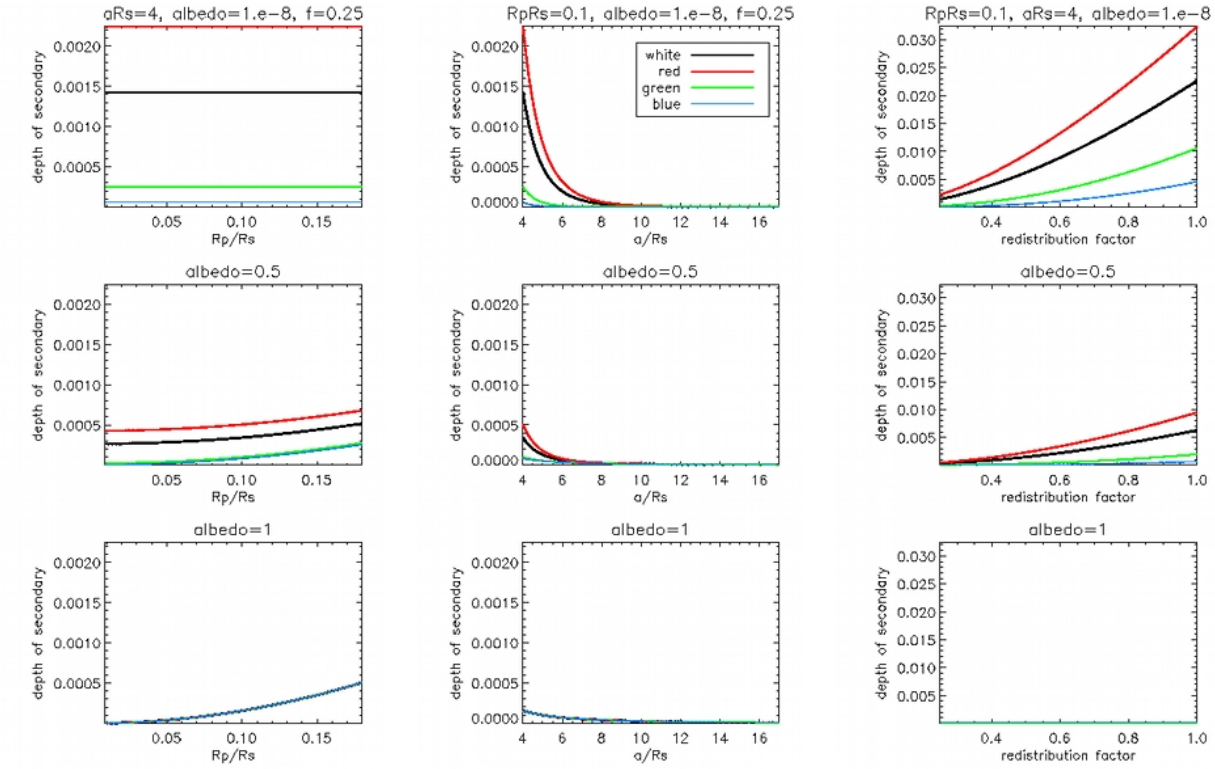


Figure 4.3: The depth of the secondary eclipse $\frac{F_{\rm p}}{F_\star}$ of a planet around a 5800 K star is plotted for a range of planet radii $R_{\rm p}/R_\star$ (left column), a range of planet orbital distances $a/R_\star$ (middle column), and a range of energy redistribution factor $f$ (right column), and albedos of $10^{-8}$ ($\sim$ 0), 0.5 and 1 (from top to bottom). The depth is calculated for the stellar and planet fluxes falling within the CoRoT bandpass (black), the CoRoT red channel (red), green channel (green), and blue channel (blue).

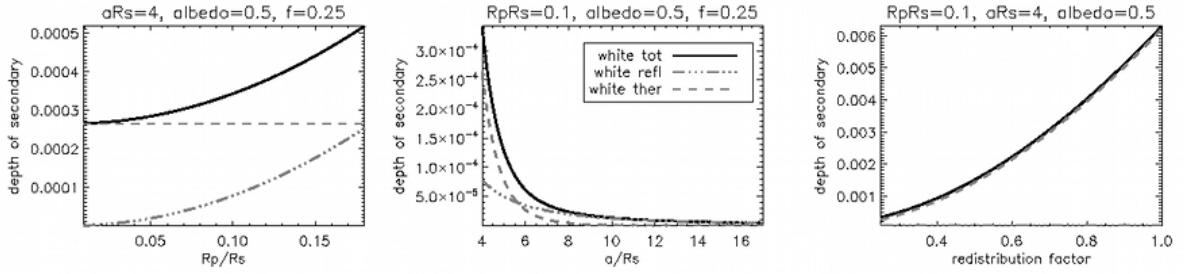


Figure 4.4: The black curves are the same as Figure 4.3 for albedo=0.5. The depth of the secondary over the CoRoT bandpass in stellar reflected light only (dash-dot) and in planet thermal emission only (dash) are plotted in grey.

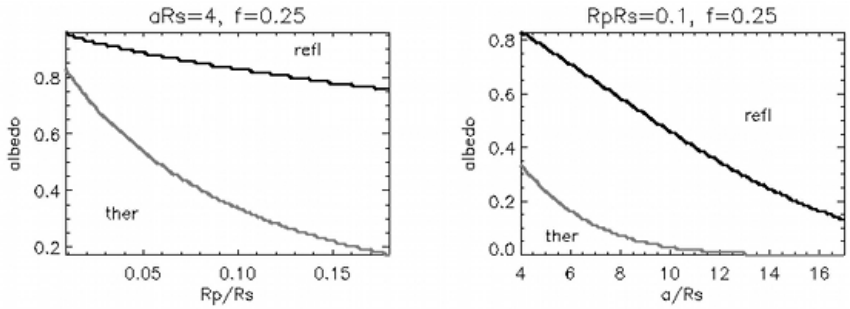


Figure 4.5: This figure shows which component of the planet emission dominates in the CoRoT bandpass depending on the albedo, the planet radius $R_{\rm p}/R_\star$ and the planet orbital distance $a/R_\star$, for a stellar $T_{\rm eff}$ fixed at 5800 K, and a planet redistribution factor fixed at 0.25. For this star-planet system, for (albedo,$R_{\rm p}/R_\star$) and (albedo,$a/R_\star$) combinations below the grey line, the thermal emission is 10 times larger than the reflected light, and for combinations above the black line, the reflected light is 10 times larger than the thermal emission.

Several observations can be extracted from this analysis:

- At large albedos, the stellar light reflected by the planet dominates over the planet thermal flux and the flux ratio $\frac{F_{\rm p}}{F_\star}$ in the different CoRoT colour channels is the same. At small albedos (bottom panels), the planet thermal flux dominates over the reflected light and the flux ratio $\frac{F_{\rm p}}{F_\star}$ is larger in the red channel than in the blue channel (Figure 4.1 top panels; Figure 4.2 right panel; Figure 4.5). This can be used on secondary eclipses in the CoRoT light curves to test which type of emission dominates in the planet radiation.

- The planet to star flux ratio is a) larger in the red CoRoT channel than in the integrated CoRoT bandpass, b) similar in amplitude in the green and in the blue CoRoT channels but smaller than over the integrated CoRoT bandpass, c) mainly influenced, in the green and blue CoRoT channels, by the amount of stellar light reflected by the planet, and d) mainly influenced, in the red CoRoT channel, by the amount of thermal emission by the planet (Figure 4.2 left panel; Figure 4.3 top

6 panels).

- The maximum planet to star flux ratio is the highest when $A_B = 0$, has lower values at intermediate albedos between 0 and 1, and has another smaller local maximum at $A_B = 1$ (Figure 4.2; Figure 4.3).
- The planetary thermal emission (dominant component when $A_B \sim 0$) is independent of the radius of the planet $R_{\rm p}/R_\star$, decreases with the orbital distance $a/R_\star$, and increases with the redistribution factor $f$(Figure 4.3; Figure 4.4 left panel)). This is as expected from Equation 4.10.
- The stellar light reflected by the planet (dominant component at $A_B \sim 0$) increases with the radius of the planet $R_{\rm p}/R_\star$, decreases with the orbital distance $a/R_\star$, and is independent of the redistribution factor $f$ (Figure 4.3; Figure 4.4). This is as expected from Equation 4.6.
- The planetary thermal emission and the stellar reflected light both drop with increasing orbital distance $a/R_\star$, and the reflected light drops down to 0 at shorter orbital distance faster than the thermal emission (Figure 4.4 middle panel).
- The depth of the secondary eclipse increases with $f$ (Figure 4.4 right panel), as the amount of observable thermal emission increases with $f$.
- The value of the albedo at which the stellar reflected light dominates ($10\times$ larger) over the planet thermal emission (like in Figure 4.2 right panel) decreases with $R_{\rm p}/R_\star$ and $a/R_\star$ (Figure 4.5).

This study assumes that the planet is in thermal equilibrium, although in general some planets can be out of equilibrium, for instance due to chemical processes. Additionally, even if the planet is in global equilibrium, the depth of the secondary eclipse in a given band can differ strongly from the black body prediction because of the presence of strong absorbers in the atmosphere of the planet (e.g. hazes, molecules).

The absence of detection of optical secondary eclipses before those of CoRoT-1b and 2b (e.g. upper limits on HD209458b by MOST, Rowe et al. 2008) suggests that many Hot Jupiters typically have very low albedos ($\leq$ 0.1).

### 4.1.5 Expected depth and phase for the secondary eclipse of CoRoT planets

From the equation 4.6 and 4.11, one can derive expected depths for the planet secondary eclipses if the planet flux is dominated by reflected flux or thermal emission respectively. These values are presented in Table 4.1. The values of the secondary depth are only upper limits if the planet flux is purely one type or the other. In the CoRoT optical bandpass we expect both contributions to be significant, so the values presented in Table 4.1 are not upper limits in the CoRoT band pass and should only be

used to give an order of magnitude of the secondary eclipse depth.

Table 4.1: Secondary eclipse depth $\Delta F/F$ and phase range $\phi_{sec}$ for the eight first CoRoT planets and CoRoT-3b, based on equations 4.6, 4.11 and 4.7. $N_{tr}$ is the number of transits, i.e. the number of planet orbital period observed. $\sigma_{2h}$ is the total noise over 2h in the CoRoT light curve before the stellar variability is filtered out, $N_{2h}$ is the number of points in the light curve over 2h (13 points at 516s sampling).

| | $R_{\rm p}/R_\star$ | $a/R_\star$ | $e$ | R [1] | $N_{tr}$ | $\frac{\sigma_{2h}}{N_{2h}}$ [2] | $\Delta F/F$ [3] $A_B = 1$ | $\Delta F/F$ [4] $A_B = 0, f = 1$ | $\phi_{sec}/P$ [5] |
|---|---|---|---|---|---|---|---|---|---|
| CoRoT-1b | 0.1433 | 4.92 | 0(fixed) | 13.4 | 38 | $2.0\ 10^{-3}$ | $2.1\ 10^{-4}$ | $8.4\ 10^{-4}$ | 0.5(fixed) |
| CoRoT-2b | 0.1622 | 6.34 | 0.03±0.03 | 12.0 | 87 | $1.4\ 10^{-3}$ | $1.6\ 10^{-4}$ | $6.4\ 10^{-4}$ | (0.481,0.519) |
| CoRoT-3b | 0.0665 | 7.03 | $0.008^{+0.015}_{-0.005}$ | 13.1 | 34 | $1.9\ 10^{-3}$ | $0.2\ 10^{-4}$ | $0.8\ 10^{-4}$ | (0.493,0.507) |
| CoRoT-4b | 0.1053 | 16.8 | 0.0±0.1 | 13.4 | 6 | $2.0\ 10^{-3}$ | $0.1\ 10^{-4}$ | $0.4\ 10^{-4}$ | (0.468,0.532) |
| CoRoT-5b | 0.1120 | 8.97 | $0.09^{+0.09}_{-0.04}$ | 13.8 | 27 | $2.3\ 10^{-3}$ | $0.4\ 10^{-4}$ | $1.6\ 10^{-4}$ | (0.471,0.529) |
| CoRoT-6b | 0.1162 | 16.8 | <0.1 | 14.2 | 16 | $2.5\ 10^{-3}$ | $0.1\ 10^{-4}$ | $0.4\ 10^{-4}$ | (0.468,0.532) |
| CoRoT-7b | 0.0184 | 4.13 | 0.07±0.07 | 11.4 | 153 | $1.2\ 10^{-3}$ | $0.05\ 10^{-4}$ | $0.2\ 10^{-4}$ | (0.478,0.522) |
| CoRoT-8b | 0.075 | 17.6 | 0(fixed) | 14.3 | 22 | $2.5\ 10^{-3}$ | $0.1\ 10^{-4}$ | $0.4\ 10^{-4}$ | 0.5(fixed) |
| CoRoT-9b | 0.115 | 93 | 0.11 | 13.8 | 1 | $2.2\ 10^{-3}$ | $0.05\ 10^{-4}$ | $0.2\ 10^{-4}$ | (0.465,0.535) |

The values of $R_{\rm p}/R_\star$, $a/R_\star$ and $e$ for CoRoT-1b to 7b are taken planet parameter tables in Chapter 3 Section 3.2. The values for CoRoT-8b and 9b and taken from the planet discovery papers (Bordé et al. 2010, and Deeg et al. 2010 respectively).
[1] R is the magnitude of the planet's host star in the R filter. [2] $\sigma_{2h}$ is calculated using equation 4.14. [3] Assuming the planet flux only comes from the stellar reflected light, using equation 4.6 and $A_B = 1$, this is an upper limit when the planet flux is dominated by the stellar reflected light. [4] Assuming the planet flux only comes from the planet thermal emission, using equation 4.11, $A_B = 0$ and $f = 1$. [5] $\phi_{sec}$ is derived using equation 4.7 for $\cos\omega$= 0 to 1.

Aigrain et al. (2009) derive the following empirical relations between the total noise over 2h (timescale comparable to the duration of a secondary eclipses) and the R-magnitude for dwarf stars:

$$\log \sigma_{2h} = 0.25\ R\ +\ z \tag{4.14}$$

where $z$ ($\sim$-7 for the three first CoRoT fields) indicates the gradual degradation of CoRoT photometric performance over time – which can be associated with the increase in incidence of hot pixel events.

The value of $\frac{\sigma_{2h}}{N_{tr}}$ for each of the nine first CoRoT planets is reported in Table 4.1. The noise level in the unfiltered CoRoT light curve compared to the amplitude of the signal searched for in this chapter, illustrates the complexity of the task.

So far the smallest transit signal detected in the CoRoT light curves is the transit of CoRoT-7b with a depth of 3 $10^{-4}$. Thus, if we have enough orbits (large S/N), we can expect to detect in the phase-folded light curve the secondary eclipses of CoRoT-1b and 2b. The secondary eclipses of CoRoT-3b to 9b are expected to be too shallow to be detected in the CoRoT light curves. For these planets, a larger-diameter space telescope and more orbit coverage will increase the S/N of the secondary eclipse which might then become detectable depending on the level of systematics.

The expected range for the secondary eclipse of all the planets in Table 4.1 are between 0.45 and 0.56. The search for secondary eclipses is therefore run over the phase range (0.4,0.6).

#### Remarks

Some remarks can been made at this point:

- CoRoT broadband filter does not cover the whole wavelength range of the emission of the planet and the star (assumed in Table 4.1). To calculate the real expected depth of the secondary eclipses in the CoRoT optical band pass, one should thus convolute the Plank black body functions of the star ($4\pi R_\star^2 \sigma_{\rm SB} T_\star^4$) and the planet ($4\pi R_p^2 \sigma_{\rm SB} T_p^4$) with the CoRoT spectral reponse function given in Auvergne et al. (2009).
- $F_{\rm p}$ is a combination of $F_{\star,\ \text{reflected by planet}}$, $F_{\rm p,\ thermal\ emission}$ and $F_{\rm p,\ internal}$. At shorter wavelength, $F_{\star,\ \text{reflected by planet}}$ dominates and at longer wavelength $F_{\rm p,\ thermal\ emission}$ dominates. In the CoRoT optical bandpass both contributions are significant. Therefore, for secondary eclipse detections in the CoRoT light curves, one can only give an upper limit on $T_{p,\ eq}$ as equal to the planet brightness temperature based on the assumptions of a a total absorption of the stellar incident flux and a thermal equilibrium.
- Treating the planet thermal flux as a black body is an approximation as a planet spectrum has many and wide absorption features which results in the planet thermal flux being overestimated if approximated to a black body.

## 4.2 Method

In this section, I describe the methods used to process the CoRoT light curve and search for planet secondary eclipses and orbital phase variations in the white and colour channels.

### 4.2.1 The IRF as a reconstruction tool

As shown in Table 4.1, the noise level (mainly stellar variability) in the original CoRoT light curve of CoRoT-1b and CoRoT-2b is too high to allow the direct detection of a secondary eclipse. The light curves thus need to be filtered before searching for secondary eclipses. The IRF reconstructs all signals at the orbital period of the planet and is therefore an interesting tool to carefully filter the stellar variability from the original light curve. The IRF is described in Chapter 1 and applied in Chapter 2 to the CoRoT light curve of the first seven planets discovered by CoRoT. The IRF uses the knowledge

of the period of the transits to simultaneously estimate the transit signal and the stellar variability signal.

### 4.2.2 Light curve processing

The light curves are processed using the IRF as described in Chapter 3 Section 3.1.3. The amplitude of the signal searched for in this chapter is at least two order of magnitude smaller than the amplitude of the primary transit. The search for this signal is thus more sensitive to light curve discontinuities such as the sharp jumps in flux pointed out in Chapter 3. Several approaches can be taken to remove these flux discontinuities:

1. identify sections of the light curve around observed "jump" in flux, and work on the light curve excluding these sections. This approach is limited when using the IRF to filter large amplitude stellar variability (e.g. CoRoT-2). The IRF treats the whole light curve as a succession of points ignoring gaps in time. Thus if the flux level at the end of a chunk of the light curve is very different from the flux level at the start of the following chunk, the IRF will still see a sharp jump in flux at the transition between the two sections.

2. remove these jumps in flux directly with the IRF using larger $\mathrm{timescale}$ and $\mathrm{binsize}$ to smoothen out sharp jumps in flux in the unfolded light curve and phase-folded one respectively. This is a trade off as using a large $\mathrm{timescale}$ and $\mathrm{binsize}$ will be less efficient in estimating the stellar variability and the planet signal. Nevertheless, residuals of the jumps are still present at the $10^{-4}$ level.

3. therefore, the adopted approach is to filter the whole light curve with the IRF and post-filtering to cut out the planetary orbits which have a large jump in flux in the original light curve (typically 2 to 3 orbits over the whole light curve). This method works even for large amplitudes in stellar variability. If large jumps in flux are identified at the beginning and at the end of the light curve, the sections of light curve kept can start after the first jump and end before the second one (e.g. blue light curve of CoRoT-1), though caution should be used as keeping the maximum number of planet orbits increases the S/N of the planet secondary eclipse and the orbital phase variation.

The IRF-filtering is performed with $\mathrm{timescale}$ of 0.5 days or 0.25 days depending on the level of stellar activity. Choosing the correct $\mathrm{timescale}$ is important. If some stellar variability is kept and binned up in the transit signal, the residuals of this variability will then be present at all the planet orbits, "polluting" the orbits where the stellar signal was originally well estimated. This residual stellar variability is then more difficult to filter out as it is now at the planet orbital period, and the IRF will attempt to reconstruct it with the planet signal.

The values chosen for the IRF $\mathrm{binsize}$ parameter – used to estimate the transit-signal – are 0.01 or 0.005 phase units depending on how they model the transit – instead of 0.0006 phase units as used in Chapter 3. For small values of the IRF $\mathrm{timescale}$ parameter ($< 0.25$ day), the IRF starts decomposing the noise in the light curve into a component at the reconstructed period and a component filtered out (see Section 4.2.4 of this chapter for more explanation). To counter this effect, one needs to use a larger IRF $\mathrm{binsize}$ parameter so that the component of the noise kept at the reconstructed period is smoothened out in the transit signal estimate.

To avoid the issue of non-uniform weighting associated with non-uniform coverage of the phase-folded planetary orbit, which can bias the search for a secondary eclipse, only full planetary orbits are kept. The light curves searched for secondary eclipses are selected to start at first minimum and end at last minimum of IRF-filtered light curve (which correspond with good approximation to the centre of the first and the last transits in the light curve).

The resulting light curve is phase-folded at the orbital period of the satellite. If there is an apparent variation at this period (Figure 4.6), this signal is boxcar-smoothened and divided into the IRF-filtered light curve. The flux variations at the satellite orbital phase are due to the satellite entering and exiting the Earth's shadow. The thermal shock at the exit of the Earth's shadow and the change to battery power at the entry to the Earth's shadow, cause pointing changes in the telescope. These variation have a $10^{-3}$ amplitude level which hinders the detection of secondary eclipses expected at a $10^{-4}$ level.

CoRoT has three colour channels which are added up together to create the white light curve (see Chapter 3 Section 3.1.2). The three colour channels, although with less photons an thus more photon noise than the white light curve, can be studied individually. This gives some colour information on the planet photometric signal. The individual colour light curves are processed in the same way as the white lights.

Over the light curves studied in this chapter, only the colour light curves (CoRoT red, blue and green channels) needed a correction at the satellite's orbital period around the Earth. The white light curve was either corrected in the light curve production pipeline, or the effects average out when combining the three colours.

### 4.2.3 Search for secondary eclipses and orbital phase variations

#### Secondary eclipse

We searched the phase-folded IRF-filtered white light curves for secondary eclipses using a 2-parameter sliding box varying the phase and the total duration of the secondary eclipse. The duration is varied as an additional test of the reliability of the detection. The detection significance of each putative secondary eclipses is evaluated

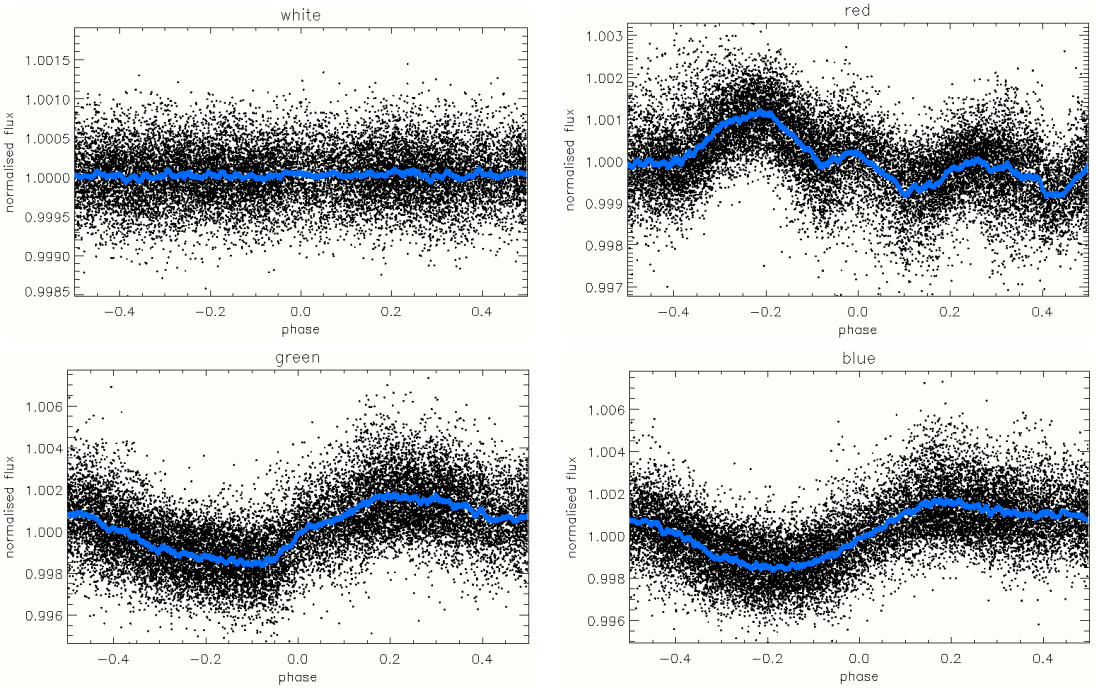


Figure 4.6: The white and colour light curves of CoRoT-2, IRF-filtered ($\mathrm{timescale}$=0.25, $\mathrm{timescale}$=0.005), and phase-folded at the orbital period of the CoRoT satellite around the Earth (P$\sim$103 min). The blue curve is the smoothed version (bins of 100 points). The figure shows the variations at the period of the satellite.

as:

$$S = \frac{\delta}{\sigma_N} \tag{4.15}$$

where $\delta$ is the depth of the putative secondary eclipse and $\sigma_N$ is the noise level for this putative secondary eclipse. $\delta = f_{\mathrm{out}} - f_{\mathrm{in}}$ where $f_{\mathrm{in}}$ and $f_{\mathrm{out}}$ are the median level in and out of transit respectively. $f_{\mathrm{out}}$ is calculated over the points between one and one-half the trial total-eclipse-duration from the trial phase. The duration-in-full-eclipse is derived for each trial eclipse-total-duration so that the ratio between the two is the same as that of the primary transit. $f_{\mathrm{in}}$ is calculated over the points within one-half the duration-in-full-eclipse from the trial phase, the number of points in this interval is called $N$. $\sigma_N = \sigma/N$ where $\sigma$ is the $1.48 * \mathrm{MAD}$ ($\mathrm{MAD}$=median absolute deviation) of all the points one transit-total-duration away from the centre of the primary transit).

The phase of the secondary eclipse is varied from 0.4 to 0.6 phase units, for a primary transit centred at phase 0. The phase range is taken to cover the range of eccentricity determined with radial velocity measurements. The secondary eclipse total duration is varied from a quarter to twice the total duration of the primary transit. We perform the search for a secondary eclipse over a 100 to 200 $\times$ 100 to 200 grid in order to reach a sampling of the phase and the duration of 0.001 phase units.

The values of $S$ at each trial phase and duration are combined into a 2-D significance map with in grey scale the value of the significance (white and black for high

and low values of $S$ respectively). This map allows to visually evaluate the shape of the (phase,duration) parameter space with regards to the significance of the putative secondary eclipses. If the planetary orbit is circular, the secondary eclipse is expected at phase 0.5 with the same total duration as that of the primary transit.

If the phase-folded light curve is not flat around the putative secondary eclipse, a $1^{st}$ or $2^{nd}$ order polynomial fit is performed about each putative secondary eclipse before $f_{\rm out}$ and $f_{\rm in}$ are calculated.

The "best" secondary eclipse is the one with the highest significance $S$, and has an associated "best" phase and "best" duration.

For the same phase and duration as the secondary eclipse with the highest significance in the white light curve, the depth of the secondary eclipse in the different colour channels is estimated. The values are compared to the depth in the white light curve.

#### Trapeze model of the secondary eclipse with the highest significance

For the "best" secondary eclipse, a simple trapeze model is produced at the "best" phase with a total duration equal to the "best" duration, and an internal duration (planet fully eclipsed) with the same total to internal duration ratio as the transit. The in-full-eclipse level is calculated as the median of the points within the internal duration of the eclipse. The out-of-eclipse level is calculated as the median of the points in the range of $1\times$ to $1.5\times$ the "best" duration each side of the centre of the eclipse. This range was chosen as a compromise between being close enough to the eclipse to evaluate the local out-of-eclipse level, and far enough from the edge of the eclipse to avoid been biased by the eclipse.

#### Uncertainty on the depth of the secondary eclipse

The uncertainty on the depth can be calculated in the following ways:

1. as the $1\sigma$ dispersion ($1.48 * \mathrm{MAD}$) of the points one transit-total-duration or more away from the centre of the primary transit, dividing this value by the square root of the number of points in-full-eclipse. This is how $\sigma$ is calculated in the expression of the significance of the detection (equation 4.15). However, this method under estimates the uncertainty as it does not take into account the correlated noise in the phase-folded light curve.

2. residuals shuffled: as the $1\sigma$ dispersion ($1.48*\mathrm{MAD}$) of the depths of the secondary eclipse measured with different residual shuffling from the model of the "best" secondary eclipse $S_{best}$. This calculation is performed by subtracting $S_{best}$ from the light curve, shuffling the residuals randomly, adding back $S_{best}$, and re-evaluating the depth of the secondary eclipse at the same phase and duration as $S_{best}$.

The above is done 100 times and the uncertainty on the depth are taken as the standard deviation of all the measured depths. However this method also underestimates the uncertainties as it treats the residuals as white noise and does not take into account any correlated noise present in the phase-folded IRF-filtered light curve.

3. residuals shifted: to take into account both the white and the correlated noise, the uncertainty on the depth can be estimated as in option (2) but with the residuals shifted circularly. Residual circular shuffling conserves the correlation between successive points, while residual random shuffling destroys it. This approach is the most conservative, i.e. should return the largest error bars. It is the one used in this chapter to evaluate the uncertainty on the depth of the secondary eclipse depth.

4. residuals permuted: the uncertainty on the depth can be estimated as in option (2) but with the residuals divided into bins of $\sim$1h and shuffled randomly. As each bin is shuffled as a whole, the detailed time sampling of individual bins is preserved. This method takes into account correlated noise on hour timescales.

#### Uncertainty on the phase and duration of the secondary eclipse

In the case of non-correlated noise, the 1 and 2 $\sigma$ confidence level are respectively at $\Delta\chi^2 = 1$ and 2 from the minimum $\chi^2$. Here we also have correlated noise, so the above relation is not directly applicable.

For $\sigma$ the uncertainty on the depth, the $1\sigma$ confidence level in the secondary eclipse phase is defined as the range in orbital phase where the depth is larger than the depth with the highest significance minus $1\sigma$. The $2\sigma$ confidence level is defined where the depth is larger than the depth with the highest significance minus $2\sigma$.

The $1\sigma$ and $2\sigma$ confidence levels in the secondary eclipse total-duration can be evaluated in the same way, i.e. by taking the range in eclipse total-duration where the depth is larger than the depth with the highest significance minus $1\sigma$ or $2\sigma$ respectively.

These $1\sigma$ and $2\sigma$ confidence level contours are plotted over the 2D-significance map of the search for a secondary eclipse in the phase-folded IRF-filtered light curve.

The $1\sigma$ uncertainty on the phase of the secondary eclipse is taken as the phase range of the $1\sigma$ confidence level, at the eclipse total-duration of the secondary eclipse with the highest significance. The $1\sigma$ uncertainty on the duration of the secondary eclipse is taken as the duration range corresponding to range within the $1\sigma$ confidence level and within the $1\sigma$ uncertainty phase range.

To consider a detection real, the depth of the secondary eclipse needs to be at least $2\sigma$ above the uncertainty associated with this depth. If the $1\sigma$ level in phase

includes phase 0.5 and the $1\sigma$ level in duration includes the duration of the primary transit, then the planet orbit is circular at a $1\sigma$ level.

### Orbital phase variations

The amplitude of the orbital phase variation signal is of the same order of magnitude as that of the secondary eclipse. In theory, if a secondary eclipse is detected, an orbital phase variation can also be detected. In practice, systematics in the phase-folded light curve can easily reduce the significance of the detection of an orbital phase variation. Also, if the stellar variability has a residual component at the orbital period of the planet, it is difficult to separate this stellar signal from the planet orbital phase variation. Nevertheless, when a secondary eclipse is detected with at least a $2\sigma$ confidence level, we look in the phase-folded IRF-filtered light curves for sinusoidal flux variations at the planet orbital period that could be of planetary origin.

The filtered light curve is divided by the transit model and the secondary eclipse model. A $3\sigma$ clipping is performed on the resulting light curve to remove any large residuals from the models, with $\sigma = 1.48 * \mathrm{MAD}$ of the transit-free and eclipse-free light curve. The resulting light curve is phase-folded at the orbital period of the planet and fitted by a sinusoid. The sinusoid fit is performed varying the half amplitude of the sinusoid (typically with 100 steps between 0.5 and 5. $10^{-4}$) and keeping the period fixed at the planet orbital period and the phase of the maximum fixed at the phase of the secondary eclipse. The best fit is identified as the one with the minimum $\chi^2$ to the data. The current implementation of the planet orbital phase modelling makes two assumptions: 1) the phase variation is sinusoidal and 2) the hottest point on the planet is the point directly facing the star. In actual fact, this is not always true. The phase variation due to the planet thermal emission is sinusoidal, but the phase variation due to the stellar reflected light can deviate from the sinusoidal shape depending on the phase function of the reflective material at the surface of the planet. The maximum amplitude on the phase variation can deviate from the time of the secondary eclipse (i.e. the hottest point on the planet can deviate from the point directly facing the star) if there is a strong atmospheric circulation when observing the planet's thermal emission (e.g. HD189733b, Knutson et al. 2007a), or depending on the phase function of the reflective material at the surface of the planet when observing the planet in reflected light. The simplicity of the current implementation of the phase curve modelling is justified by the level of white noise and residual stellar variability observed in the filtered light curves studied in this chapter. In the near future, for planet phase curves not affected by stellar variability, the orbital phase modelling can be modified to allow the above parameters to vary.

The amplitude of the "best" sinusoid is compared to the amplitude of the planet flux which should be similar to the depth of the secondary eclipse estimated in Table 4.1. If the values are compatible within the error bar, the sinusoidal flux variation seen at the

orbital period of the planet is due to the planet orbital phases, and the amplitude of the sinusoid is a measure of the ratio of the night-side to the day-side of the planet.

The current model of the planet's orbital phase is not yet evaluated in a robust way. i.e. with appropriate confidence limits. The following approach to derive the uncertainty on this model will be implemented in the near future: 1) remove the best model of the planet photometric signature (transit + secondary eclipse + orbital phase variations) from the original unfiltered light curve, 2) shift the unfolded time array, 3) re-insert the best model of the planet photometric signature into the original unfiltered light curve, 4) re-filter the light curve with the IRF and re-evaluate the model of the orbital phase variation, 5) repeat many times (e.g. 100) and evaluate the uncertainty on the parameters of the planet's orbital phase model from the scatter in their value.

A model of the planet photometric orbit is obtained by multiplying together the transit model (Chapter 3, Section 3.2), the secondary eclipse model (Section 4.2.3) and the orbital phase model (this section).

This bootstrap method will evaluate the uncertainties of the orbital phase model take into account both the noise created by residual stellar activity and the noise created by the IRF. The noise created by the IRF is explained in Section 4.2.4.

### 4.2.4 Optimising the parameters of the IRF

The level of stellar variability hinders the detection of the secondary eclipse and orbital phase variations. The stellar signal is filtered out using the IRF. As the signal of interest is small in amplitude ($\sim$0.01mmag), the filtering parameters of the IRF ($\mathrm{timescale}$, $\mathrm{binsize}$) need to be optimised to best filter each light curve. The analysis performed below presents a method to identify the best IRF filtering parameters for each light curve.

#### Method

The IRF is tested over $\mathrm{timescale}$=(0.02, 0.05, 0.1, 0.2, 0.25, 0.5, 0.75, 1) days and $\mathrm{binsize}$=(0.0005, 0.001, 0.005, 0.01) phase units, with a transit period chosen at 1.7423 days. The transits and eclipses are cut from the filtered light curve. The resulting dispersion of the points (1.48*$\mathrm{MAD}$), and the amplitude of the variations in the binned phase-folded and corrected light curve are measured and compared to the values of the light curve pre-filtering.

A synthetic light curve is computed with a mean value of 1, a time coverage of 80 transit orbits, a time sampling of 512s, and white noise. The white noise is created from random selections from a Gaussian distribution with mean of 0 and standard deviation of $10^{-4}$. The resulting simulated light curve with white noise only has a time coverage of 80 transit orbits (i.e. $\sim$140 days, similar to CoRoT long runs). A truncated light curve with white noise only and a time coverage of 30 transit orbits (i.e. $\sim$50 days, similar to CoRoT short runs) is created by taking the first 30 orbits of the previous synthetic light curve.

The IRF with different $\mathrm{timescale}$ and $\mathrm{binsize}$ is tested on these two white-noise-only light curves (Figure 4.7, top and bottom panels). Transits and secondary eclipses are then inserted at the transit period into the 30-orbits white-noise-only light curve, with transit and eclipse duration of 0.15 phase units, a transit depth of $10^{-3}$ and a secondary eclipse depth of $10^{-4}$. The IRF is tested on this light curve (Figure 4.7, middle panels), and on the light curve of CoRoT-1 (Figure 4.8) and CoRoT-2 (Figure 4.9). On top of the white noise, the transits and the secondary eclipses, the light curve of CoRoT-1 has instrumental and environmental systematics and a low level of stellar variability, and the light curve of CoRoT-2 has a higher level of stellar variability.

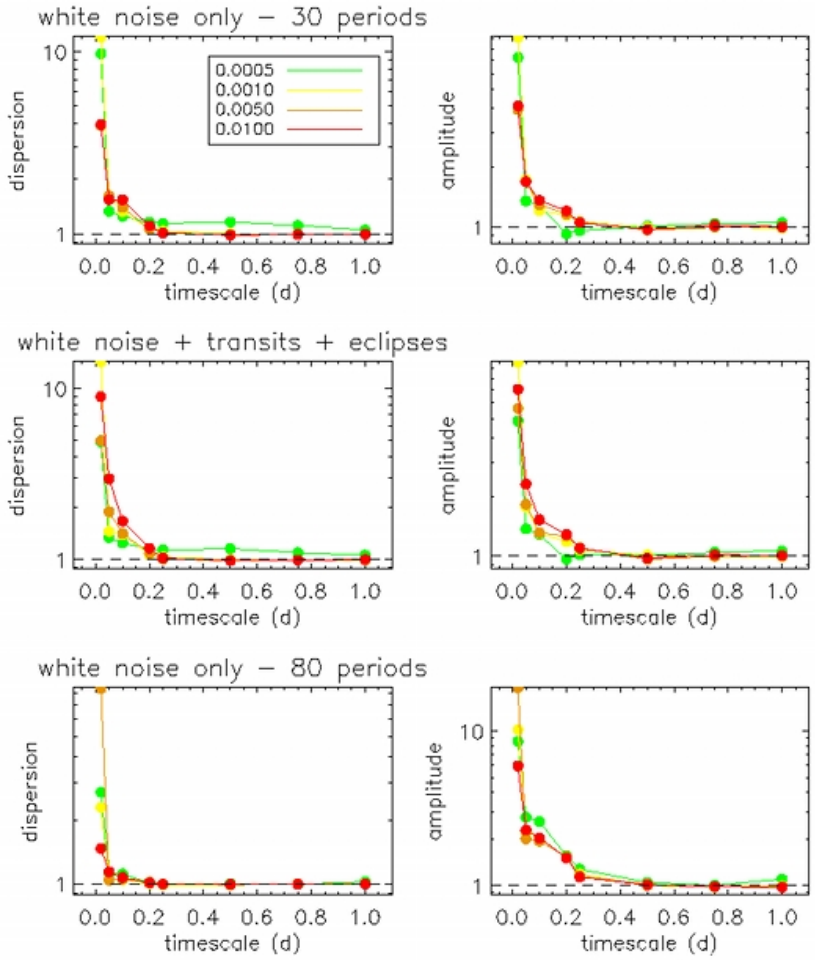


Figure 4.7: The IRF is tested with a range of $\mathrm{timescale}$ (x-axis) and $\mathrm{binsize}$ (green to red) on a simulated light curve over 30 planet orbits with white noise only (top panels) and with inserted transits and secondary eclipses (middle panel), and over 80 planet orbits with the same white noise component (bottom panels). The dispersion is calculated as the 1.48*$\mathrm{MAD}$ of the points in the filtered light curve compared to the original light curve (black dash line), and the amplitude is calculated as the minimum to maximum level of the phase-folded filtered light curve binned at 0.001 phase units with transit and eclipse cut out, compared to the same measurement in the original light curve.

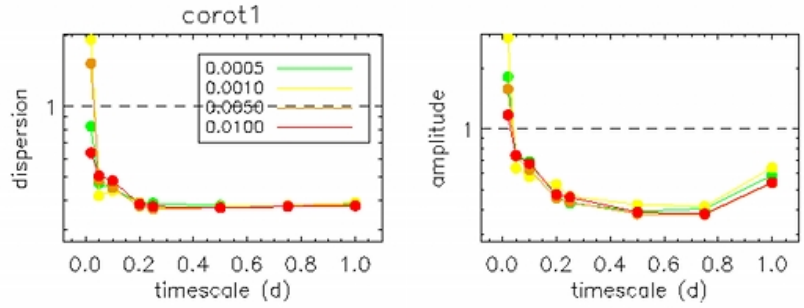


Figure 4.8: Same legend as Figure 4.7 but for the light curve of CoRoT-1.

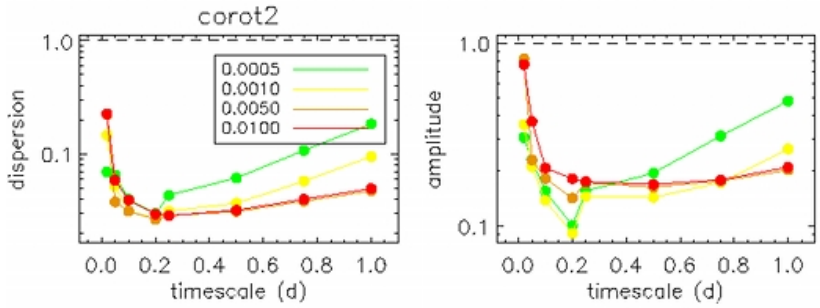


Figure 4.9: Same legend as Figure 4.7 but for the light curve of CoRoT-2.

**Observations:**

Based on the above analysis of figures 4.7, 4.8 and 4.9:

- In the case of the white noise only, the dispersion and the amplitude of the points in the filtered light curve increase suddenly for $\mathrm{timescale}$ lower than 0.2. In general, a large $\mathrm{binsize}$ (0.01) provides a lower increase in dispersion and amplitude as it smoothens out features in the phase-folded light curve during the filtering.
  The increase in dispersion and amplitude at small $\mathrm{timescale}$ is due to the fact that for these $\mathrm{timescale}$ the IRF has very few points per smoothing length, and through iterative smoothing and binning, it creates and emphases features picked up from the binned white noise.

- Adding transits and eclipses does not change the behaviour above $\mathrm{timescale} = 0.2$, but for $\mathrm{timescale}$ smaller than 0.2 the dispersion and amplitude are larger at large $\mathrm{binsize}$.
  The additional increase in the dispersion and amplitude at small $\mathrm{timescale}$ and large $\mathrm{binsize}$ is due to the edges of the phase-folded transit and eclipse affecting the value of the surrounding bins.

- Having a time coverage of 80 orbits – instead of 30 – gives similar results for the amplitude (sudden increase for $\mathrm{timescale}$ smaller than 0.25) but allows for smaller

$\mathrm{timescale}$ (0.05) with a small dispersion. This is because with more orbits, the noise averages out better in the phase-folded light curve and less features are picked up from the binned noise.

- In the case of CoRoT-1, down to $\mathrm{timescale} = 0.1$, the dispersion and the amplitude are smaller in the filtered light curve than in the original light curve; this is because most of the stellar variability has been filtered out. The amplitude is the lowest at $\mathrm{timescale} \sim 0.5$ then increases, the dispersion is constant until $\mathrm{timescale} \sim 0.2$ then increases, and down to $\mathrm{timescale} = 0.2$ a large $\mathrm{binsize}$ (0.01) gives a lower dispersion and amplitude; these are for the same reason as the first and second points.
  A low dispersion means a low level of residual noise and a low amplitude means small correlated residuals. The optimal set of IRF parameters occurs when both the dispersion and the amplitude are at their minimum. In the case of the transit light curve of CoRoT-1b, this is found at $\mathrm{timescale} = 0.5$ and $\mathrm{binsize} = 0.01$.

- CoRoT-2: With the same logic as the previous point, the optimal set of IRF parameters in the case of transit light curve of CoRoT-2b is for $\mathrm{timescale} = 0.2$ and $\mathrm{binsize} = 0.001$.
  However, in practice for this planet (section 4.3.2) $\mathrm{timescale}$ of 0.25 and 0.5 and $\mathrm{binsize}$ of 0.005 and 0.01 are used as they give a flux modulation at the planet orbital period more consistent in shape with the flux variation due to the planet orbital phases.

## 4.3 Application to CoRoT planets

In this section, the IRF is used to filter the white and colour light curves of CoRoT-1 and CoRoT-2. The search for secondary eclipses and orbital phase variations are then performed on the phase-folded light curves. The results are compared with the discovery papers of the secondary eclipses of these planets.

### 4.3.1 CoRoT-1b

The detection of the secondary eclipse and the orbital phase variation of CoRoT-1b in the red channel of CoRoT was published in Snellen et al. (2009a). An independent measurement of the secondary eclipse of CoRoT-1b in the CoRoT white light curve was also published in Alonso et al. (2009a).
The white and colour light curves are processed as described in section 4.2.2. The search for a secondary eclipse and an orbital phase variation in the white and colour light curves is performed as described in sections 4.2.3 and 4.2.3.

#### Secondary eclipse and orbital phase variation in the white light curve

The IRF-filtering is performed with $\mathrm{timescale}$ of 0.5 and $\mathrm{binsize}$ of 0.01. After filtering, two orbits affected by sudden jumps are cut from the analysis (Figure 4.10).

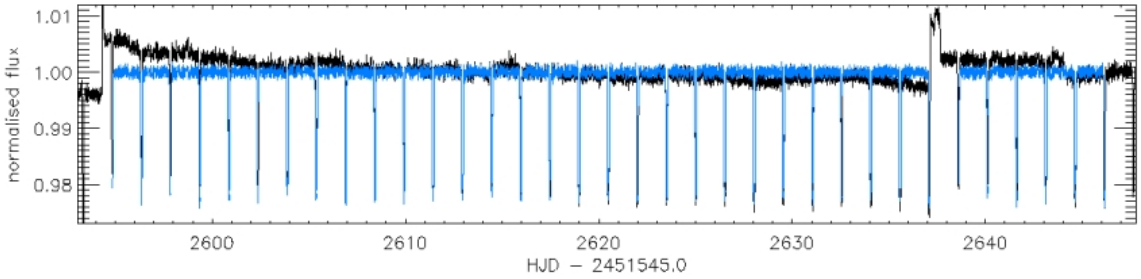


Figure 4.10: CoRoT-1 original white light curve with outliers removed (black) and its IRF-filtered version (blue) on which the secondary eclipse search is performed.

The search for a secondary eclipse is performed on the phase-folded white transit light curve of CoRoT-1b (blue, Figure 4.10) in a grid of $200 \times 100$ over the phase range (0.4,0.6) and the duration range (0.018,0.145) phase units.

Figure 4.11 shows the map of the significance of detection at each trial phase and duration. The secondary eclipse with the highest significance is at phase 0.500 and duration 0.066, and has a depth of 2.9 $10^{-4}$. Figure 4.12 shows the binned phase-folded transit light curve with the secondary eclipse model with the highest significance. The uncertainty on the depth is 0.8 $10^{-4}$, calculated as described in section 4.2.3; this corresponds to a detection of the secondary eclipse of CoRoT-1b at $3.6\sigma$.

The $1\sigma$ and $2\sigma$ levels are plotted in Figures 4.11 as the level where the depths of the putative secondary eclipses are $1\sigma$ and $2\sigma$ respectively smaller than that of the secondary with the highest significance. The phase range associated to the $1\sigma$ confidence levels is measured in Figure 4.11 (bottom), and corresponds to (0.481,0.505). The duration range associated to the $1\sigma$ phase range is measured in Figure 4.11 (top), and corresponds to (0.042,0.091) in phase units. The total duration of the primary transit is 0.072 in phase units, therefore the duration of the secondary eclipse is compatible with that of the primary transit at a $1\sigma$ level.

In Figure 4.11 (top), the features at the 1 and 2 $\sigma$ levels at duration shorter than 0.04 phase units are due to correlated noise. For duration at time scales close to that of the correlated noise, the search algorithm detects features of significant amplitude, though at longer duration the amplitude of these features average out. These correlated noise features are disregarded when evaluating the $1\sigma$ ranges in phase and duration.

The fit to the orbital phase variation is performed as in section 4.2.3. 74 outliers (out of 7026 data points) are clipped out by a $3\sigma$ clipping (where $\sigma$ is the dispersion of the points out of transits). The amplitude found for the orbital phase variation is 2.1 $10^{-4}$ (as shown in Figure 4.12) which is compatible with the planet to star flux ratio estimated in Table 4.1 and with the depth of the secondary eclipse measured in this section.

### Analysis of the colour channels

The red light curve of CoRoT-1 is filtered with the IRF using $\mathrm{timescale} = 0.25$ and $\mathrm{binsize} = 0.01$, the green light curve with $\mathrm{timescale} = 0.5$ and $\mathrm{binsize} = 0.005$, and the blue light curve with $\mathrm{timescale} = 0.5$ and $\mathrm{binsize} = 0.01$. In the case of the blue channel, the filtering is done only over the middle section of the light curve (2595 to 2637 days in CoRoT's date) as the start and the end of the blue light curve are affected by sudden jumps in flux. Three orbits are affected by a sudden discontinuity in flux are are cut out in the green channel after filtering. The three IRF-filtered colour light curves are then corrected from the flux variations at the satellite's orbital period (due to the crossing of the Earth's shadow).

The depth of the secondary eclipse in each colour is measured at the same phase and duration as the secondary eclipse with the largest significance in the white light curve. The uncertainty on the depth in each colour channel is derived as the standard deviation of the depth measured with the residuals shuffled circularly. The measured depths are (2.0$\pm$1.0) $10^{-4}$ in red, (3.1$\pm$1.9) $10^{-4}$ in green, and (2.7$\pm$2.4) $10^{-4}$ in blue.

The orbital phase modulation is measured as 3.0 $10^{-4}$ in the red light curve, larger but compatible with the depth of the secondary eclipse in red. In the blue and green light curves, the noise level – mainly due to the photon noise as these channels receive 3 times less flux than the red channel – is too large to measure a significant orbital phase modulation.

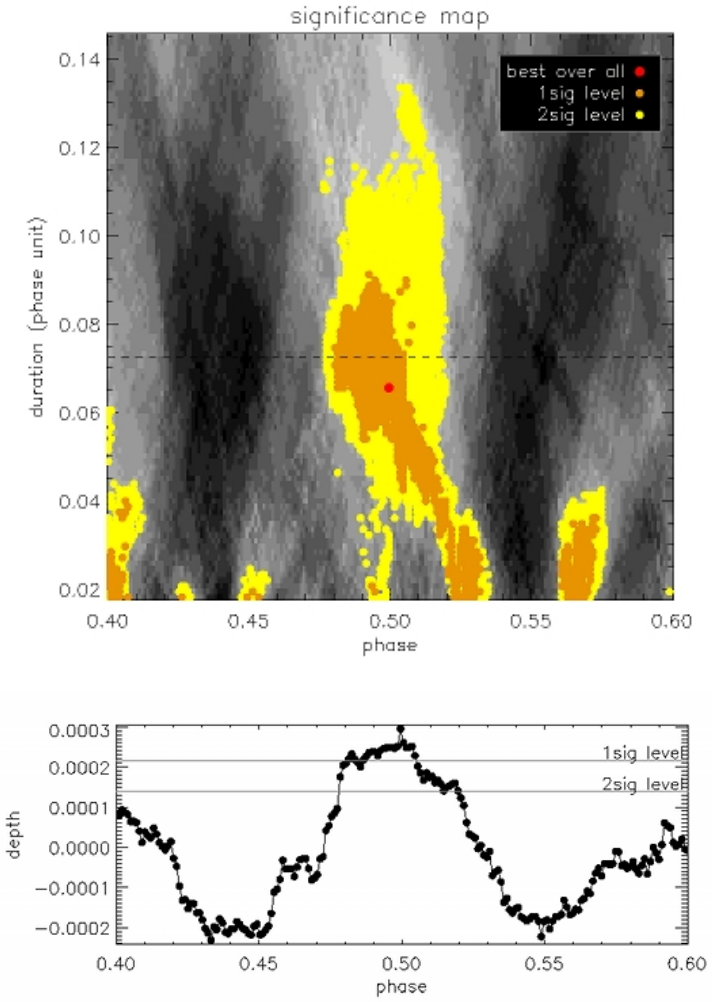


Figure 4.11: Top panel: Detection significance map displaying the significance of putative secondary eclipse of CoRoT-1b at different phases and duration calculated with equation 4.15 (darker grey indicating lower significance) in the IRF-filtered white light curve. The red dot is the best secondary, i.e. with the highest significance. The orange and yellow regions are the putative secondaries with depth within 1 and $2\sigma$ respectively of the depth of the best secondary ($\sigma$ being the uncertainty on the depth of the best secondary). The black dashed line marks the duration of the primary transit. The significance goes down either side of the maximum as the out-of-eclipse window used to evaluate the out-of-eclipse level falls in the actual eclipse, thus returning a shallower depth of putative eclipse. Bottom panel: Depth of the putative secondary eclipses of CoRoT-1b (white light curve) as a function of phase and for a total duration fixed at that of the secondary with the highest significance. The highest peak shows the depth and phase of the best secondary eclipse. The grey lines show the 1 and $2\sigma$ confidence levels defined as in the top figure.

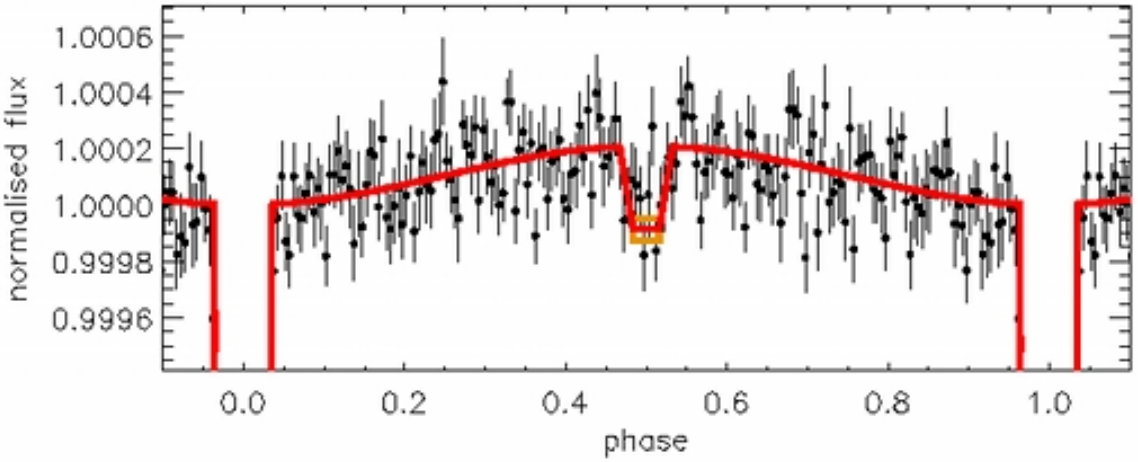


Figure 4.12: The phase-folded white transit light curve of CoRoT-1b binned with a bin size of 0.005 phase units (black), with the planet photometric orbit in red. The photometric orbit contains a models of the primary transit, a model of the secondary eclipse (the uncertainty on the secondary eclipse depth is marked with orange lines) and a model of the orbital phase variations. The model of the secondary eclipse is a trapeze at phase 0.5 with a total duration of 0.066 phase units, an internal duration (planet fully eclipsed) with the same duration ratio as the transit, and a depth of (2.9$\pm$0.8) $10^{-4}$. The model of the orbital phase variation is a sinusoid with an amplitude of 2.1 $10^{-4}$, a period fixed to the planet orbital period and a phase at maximum amplitude fixed to the phase of the secondary eclipse.

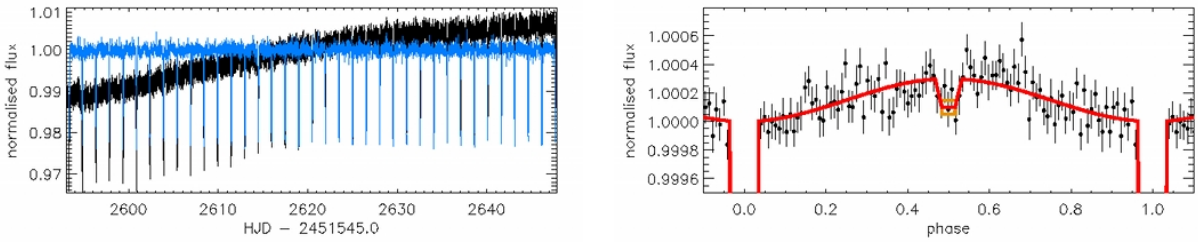


Figure 4.13: Red channel of CoRoT-1. The legend is the same as Figure 4.10 (left panel) and 4.12 (right panel). The phase-folded light curve is binned (bins of 0.009 phase units) for clarity of display. The phase and duration of the secondary eclipse is fixed to the detection with the highest significance in the white light curve. In the red channel, the depth of the secondary eclipse is (2.0±1.0) $10^{-4}$ and the amplitude of the best fit sinusoid to the orbital modulation is 3.0 $10^{-4}$.

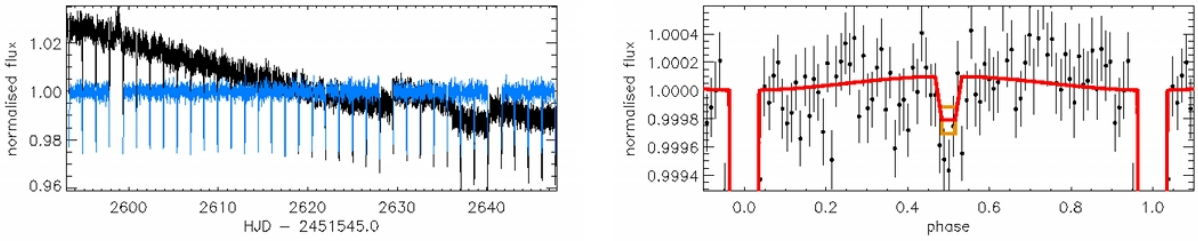


Figure 4.14: Green channel of CoRoT-1. The legend is the same as Figure 4.13. The phase-folded light curve is binned (bins of 0.011 phase units) for clarity of display. In the green channel, the depth of the secondary eclipse ((3.1±1.9) $10^{-4}$) is largely affected by the noise level and the amplitude of the best fit sinusoid to the orbital modulation (1.0 $10^{-4}$) is negligible within the noise.

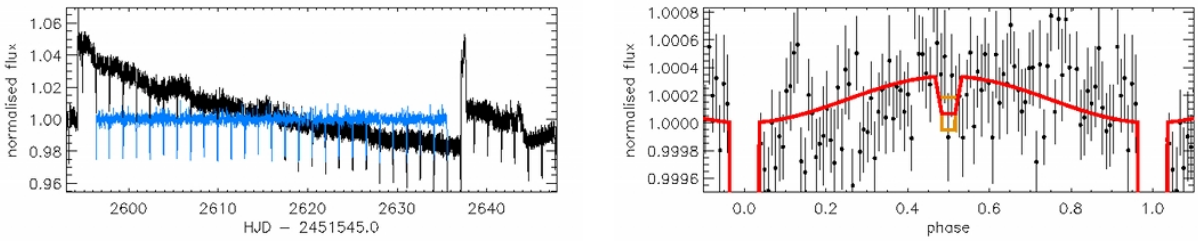


Figure 4.15: Blue channel of CoRoT-1. The legend is the same as Figure 4.13. In the blue channel, the depth of the secondary eclipse ((2.7±2.4) $10^{-4}$) and the amplitude of the best fit sinusoid to the orbital modulation (3.4 $10^{-4}$) are negligible within the noise.

### Results

A convincing detection of the secondary eclipse of CoRoT-1b, and to some extent of its orbital variation, were achieved in the IRF-filtered CoRoT white light curve. The measurements are summarised in Table 4.2. The phase and duration are compatible with a planet circular orbit at a $1\sigma$ level. The depth is compatible within $1\sigma$ with the depth for an emission purely in reflected light (Table 4.1), but the depth is larger suggesting that there is a component of planet thermal emission within the planet flux which is in favour of an albedo $A_B < 1$. In the white light curve, a phase modulation is observed. The amplitude of the orbital phase variation in the white channel suggests a bright day side and a dark night side with a small redistribution of the energy between the two (small $f$).

At the same phase and duration as the secondary eclipse in the white light curve, the depth of the secondary eclipse of CoRoT-1b in the red channel is measured at (2.0 $\pm$ 1.0) $10^{-4}$,

The precision at which the depths of the secondary eclipse of CoRoT-1b are measured in the green and blue channels does not allow us to differentiate between a planet emission dominated by the reflected light (in which case we would observe the same secondary eclipse depth in the three colour channels) and a planet emission dominated by thermal radiation (in which case we would have observed a larger depth in the red channel than in the blue and white light curves).

In the case of CoRoT-1b, the detection of its secondary eclipse and orbital phase variation with a large signal to noise ratio, is limited by the photon noise.

Table 4.2: Summary table of the secondary eclipse depths and phase modulation of CoRoT-1b in the different colour channels of CoRoT

| | white | red | green | blue | theoretical$^{(1)}$ | |
|---|---|---|---|---|---|---|
| | | | | | $A_B = 1$ | $A_B = 0$ $f = 1$ |
| Phase | $0.500^{+0.005}_{-0.019}$ | same(fixed) | same(fixed) | same(fixed) | 0.5(fixed) | |
| Duration | $0.066^{+0.023}_{-0.026}$ | same(fixed) | same(fixed) | same(fixed) | | |
| Depth | (2.9 $\pm$ 0.8) $10^{-4}$ | (2.0 $\pm$ 1.0) $10^{-4}$ | (3.1 $\pm$ 1.9) $10^{-4}$ | (2.7 $\pm$ 2.4) $10^{-4}$ | 2.1 $10^{-4}$ | 8.4 $10^{-4}$ |
| Phase variation | 2.1 $10^{-4}$ | 3.0 $10^{-4}$ | - | - | | |

The phase and duration are expressed in phase units.
$^{(1)}$ from Table 4.1

### 4.3.2 CoRoT-2b

The detection of the secondary eclipse of CoRoT-2b in the white CoRoT light curve was first published in Alonso et al. (2009b). An independent measurement of its secondary eclipse in the red CoRoT light curve was published in Snellen et al. (2009b).

#### Search for secondary eclipse and orbital phase variation in the white light curve

To keep a uniform coverage of the planet orbital period and the stellar rotation period, only the first 24 full planet orbits are selected in the white light curve – 24 is a multiple of the planet orbital period and the stellar rotation period (4.5-5 days, Alonso et al. 2008). The IRF is then applied to this section of the CoRoT-2 white light curve, using $\mathrm{timescale} = 0.25$ and $\mathrm{binsize} = 0.005$ (Figure 4.16).

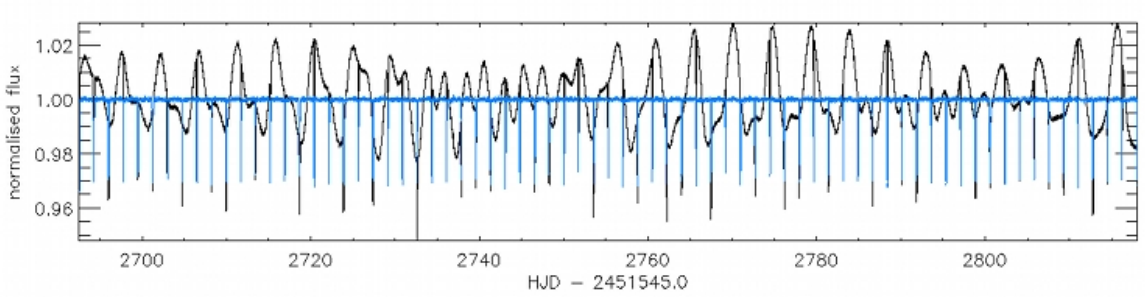


Figure 4.16: The 24 first planet periods of the white light curve of CoRoT-2 (black) and the IRF-filtered version (blue).

The search for a secondary eclipse is performed over a grid of $200 \times 100$ with a phase range of (0.4,0.6) and a duration range of (0.014,0.110) phase units.

The detection significance map is plotted in Figure 4.17. The secondary eclipse with the highest significance is at phase 0.496 and duration 0.071 phase units, and has a depth of 8 $10^{-5}$ (plotted in Figure 4.18). The uncertainty on the depth is 1 $10^{-5}$, calculated as described in the section 4.2.3. This value seems underestimated compared to the visual evaluation of the residuals in the light curve. However, as we know where to expect the secondary eclipse and at which duration, the search window has been reduced and the level of systematics is lower within that window. A robust determination of the residuals would include the systematics outside the searched range in phase, in which case the detection of CoRoT-2b in the current light curve would be unsuccessful.

The phase range associated to the $1\sigma$ confidence levels corresponds to (0.482,0.501) and the associated duration range is (0.041,0.082) phase units.

The sinusoidal fit to the modulation at the planet orbital period is performed as described in Sections 4.2.3 and 4.3.1. The amplitude of the orbital modulation in the IRF-filtered white light curve of CoRoT-2 is measured at 14 $10^{-5}$ (plotted in Figure 4.18).

### Analysis of the colour channels

The red and green light curve of CoRoT-2 are filtered with IRF $\mathrm{timescale} = 0.25$ and $\mathrm{binsize} = 0.01$, and the blue one with $\mathrm{timescale} = 0.5$ and $\mathrm{binsize} = 0.01$. The filtered light curves are corrected from the flux modulation at the period of the satellite. These modulations are seen to evolve over the CoRoT light curve (probably due to residual stellar variability), and are modelled and corrected using individual chunks of two planetary orbital periods – instead of over the whole light curve all at once.

In each processed colour light curve, the depth of the secondary eclipse is measured at the same phase and duration as the secondary eclipse in the white light curve. The secondary eclipse in the different colours are plotted in Figures 4.19, 4.20 and 4.21, and are summarised in Table 4.3.

### Results

At a $1\sigma$ level, the duration of the secondary eclipse is compatible with that of the primary transit (0.055 phase units) and the phase of the secondary eclipse is compatible with phase 0.5. The orbit of CoRoT-2b is thus compatible with a circular orbit.

The depth of the secondary eclipse measured in the white light curve is smaller than the maximum values calculated in Table 4.1, meaning that in the CoRoT bandpass, the planetary flux is composed of both reflected and thermal emission.

The depth of the secondary eclipse in the red channel is compatible with the one found in the white channel.

No secondary eclipses are observed in the green and blue light curves at a level larger than the noise estimated at 3-5 $10^{-5}$. This can be associated to the smaller amount of flux in these two channels compared to the red channel.

The value of the orbital modulation in the IRF-filtered light curves of CoRoT-2 are larger than the associated depths of the secondary eclipses. They are likely due to residual stellar variability at the orbital period of the planet, and not the the planet itself.

Table 4.3: CoRoT-2b secondary eclipse: summary of results

| | white | red | green | blue | theoretical[(1)] | |
|---|---|---|---|---|---|---|
| | | | | | $A_B = 1$ | $A_B = 0$ |
| | | | | | | $f = 1$ |
| phase | 0.496 $^{+0.005}_{-0.014}$ | same(fixed) | same(fixed) | same(fixed) | (0.481,0.519) | |
| duration | 0.071 $^{+0.011}_{-0.030}$ | same(fixed) | same(fixed) | same(fixed) | | |
| depth | (8 $\pm$ 1) $10^{-5}$ | (5 $\pm$ 3) $10^{-5}$ | - | - | 1.6 $10^{-4}$ | 6.4 $10^{-4}$ |

The phase and duration are expressed in phase units.
[(1)] from Table 4.1

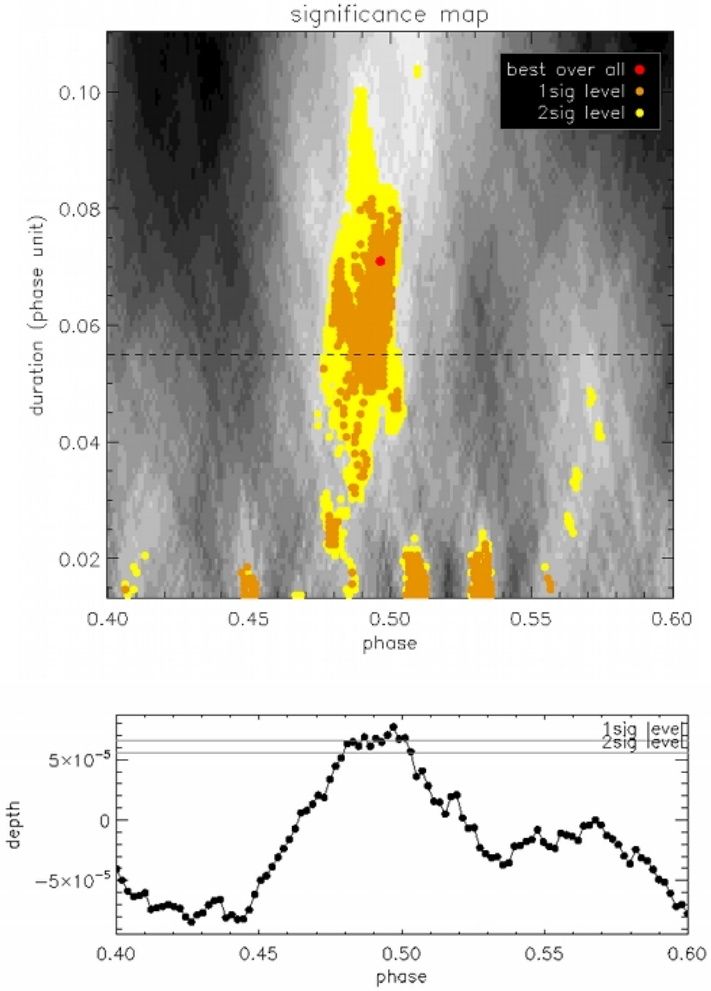


Figure 4.17: Search for a secondary eclipse in the phase folded white light curve of CoRoT-2. Same legend as Figure 4.11.

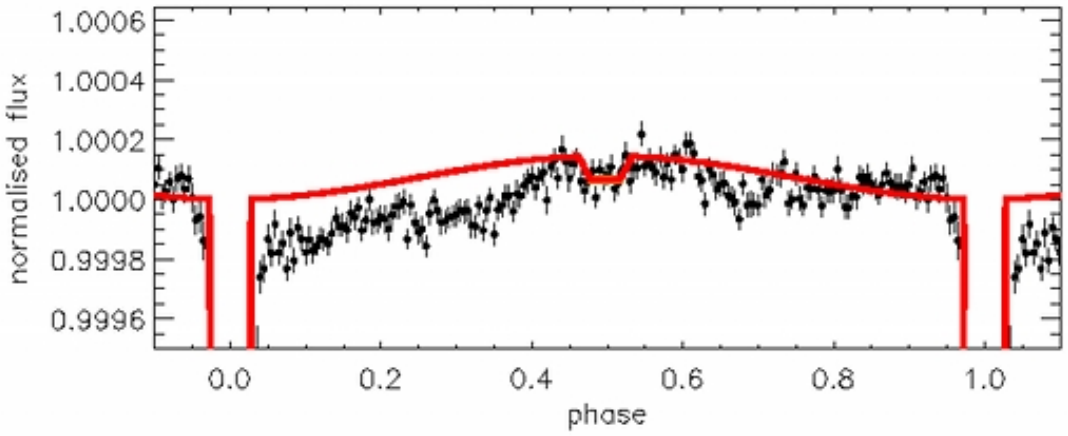


Figure 4.18: Model of the secondary eclipse and the phase modulation of CoRoT-2b (red). Same legend as Figure 4.12.

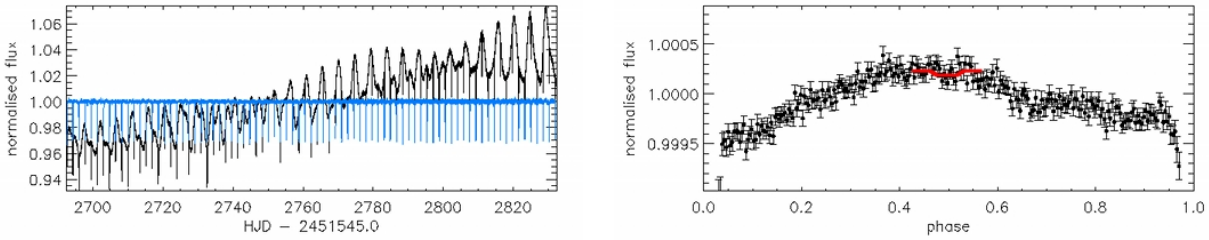


Figure 4.19: Red channel of CoRoT-2 (left, black) and IRF-filtered version (left, blue) phase-folded and binned on the right. The depth of the secondary eclipse in the red light curve, at the same phase and duration as in the white light curve, is (5±3) $10^{-5}$ (model in red). The modulation at the planet orbital period is 10 times larger than the depth of the secondary eclipse due to residual stellar variability at the orbital period of the planet.

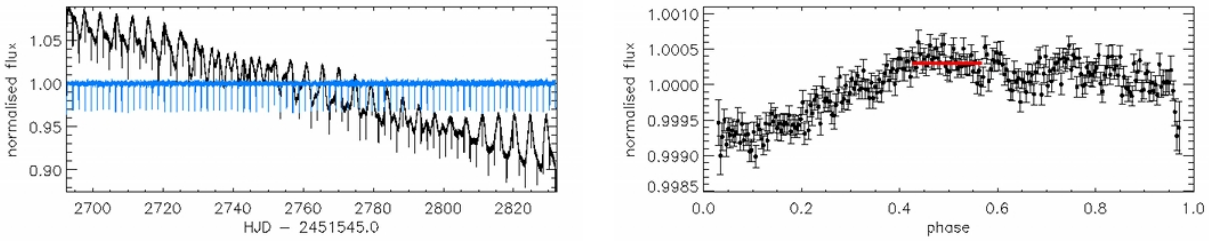


Figure 4.20: Green channel of CoRoT-2. Same legend as Figure 4.19. No secondary eclipse is detected in the green light curve at a level larger than the noise level (3 $10^{-5}$).

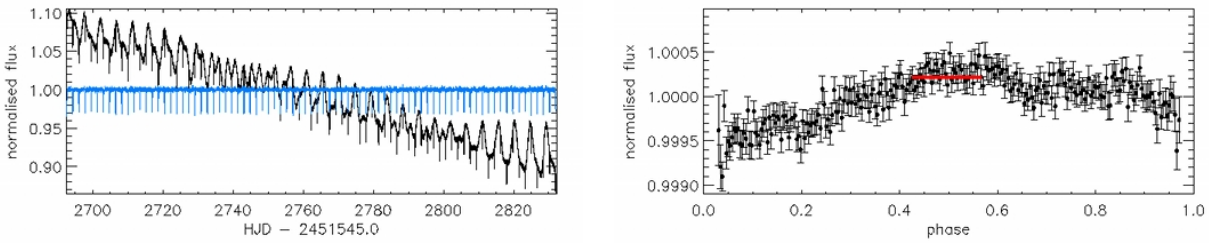


Figure 4.21: Blue channel of CoRoT-2. Same legend as Figure 4.19. No secondary eclipse is detected in the blue light curve at a level larger than the noise level (5 $10^{-5}$).

## 4.4 Discussion

### 4.4.1 Comparison with the literature

The secondary eclipse of CoRoT-1b was detected at $4\sigma$. The value found for the depth in the white light curve is larger but compatible within $2\sigma$ with the $1.6\pm0.6\ 10^{-4}$ measured by Alonso et al. (2009a) in the white light curve. The phase modulation of the planet was observed here in the IRF-filtered white light curve, though this detection was not achieved in Alonso et al. (2009a) due to differences in light curve processing. Observing the planetary phase modulations in the IRF-filtered light curve shows the high quality of the light curve processing. The depth of the secondary eclipse in the CoRoT red channel is compatible within $1\sigma$ with the $1.26\pm0.33\ 10^{-4}$ measured by Snellen et al. (2009a) in the red light curve. A modulation in phase in the red channel is also observed, as in Snellen et al. (2009a). The difference between Snellen's analysis and this one is in the processing of the light curve and the modelling of the signal. Snellen modelled the depth of the secondary eclipse as the difference between the maximum of the phase variations and the night emission (which he modelled as zero), while in this chapter the transit depth was measured without accounting for a zero-level night emission. This means that the method described in this chapter can derive deeper secondary eclipse's depth than Snellen's method, simply from the choice of planet orbital variation modelling (i.e. modelling the planet night side emission simultaneously or not).

The secondary eclipse of CoRoT-1b was also observed in the K-band by (Rogers et al., 2009) and Gillon et al. (2009) (narrower band). Figure 4.22 presents these measurements compared to the ones in the CoRoT bandpass as published in the literature and as derived in this chapter. As expected, the depth of the secondary eclipse in the optical is smaller than in the infrared.

The secondary eclipse of CoRoT-2b was observed with a much lower confidence level than CoRoT-1b due to the level of residual stellar variability at the orbital period of the planet. Nevertheless, this value of secondary eclipse depth is compatible within $1\sigma$ with the measurement by Alonso et al. (2009b). The depth in the red channel is $2\sigma$ smaller than the value published in Snellen et al. (2009b). The difference in the values is expected to come from the difference in light curve processing.

The secondary eclipse of CoRoT-2b was also measured with Spitzer (Gillon et al., 2010), and in H and K bands (Alonso et al., 2010). In Figure 4.23, these values are compared to the secondary eclipse depths in the CoRoT bandpass.

In the near future, it will be interesting to compare these measurements of secondary eclipses for CoRoT-1b and CoRoT-2b with planet atmosphere models (e.g. Barman et al. 2005) and with black bodies, to see how the models compare to the observations.

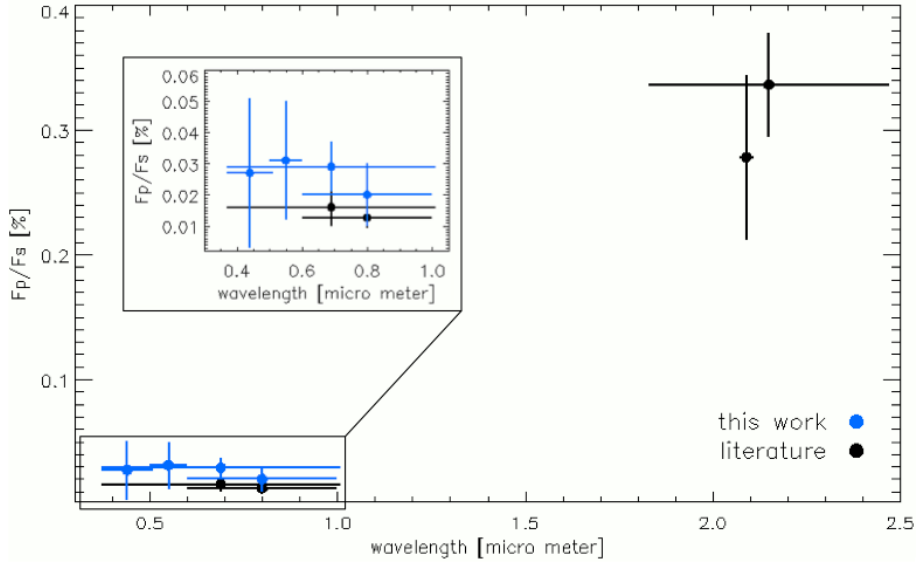


Figure 4.22: The depth of the secondary eclipse of CoRoT-1b is plotted against the wavelength of the observations.

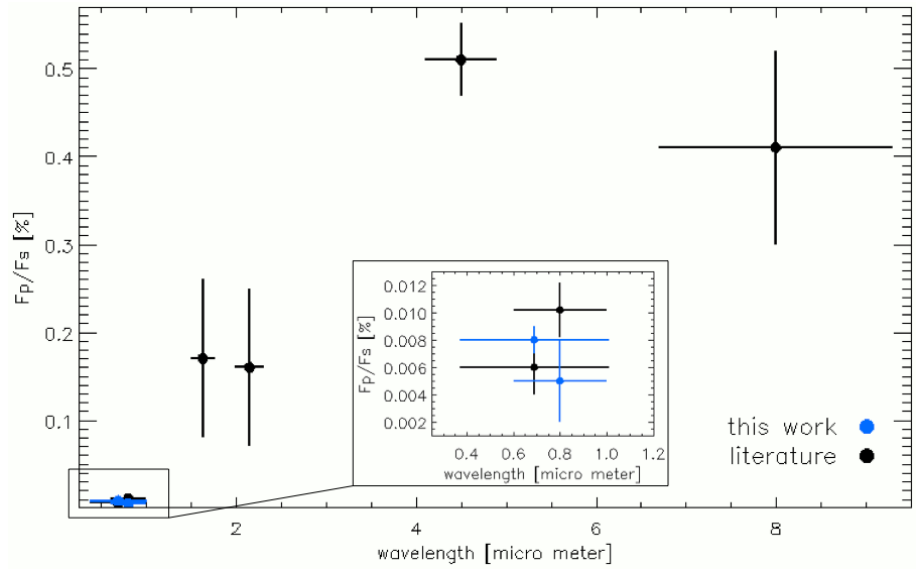


Figure 4.23: The depth of the secondary eclipse of CoRoT-2b is plotted against the wavelength of the observations.

### 4.4.2 Performance of the IRF

The IRF filters the stellar variability down to a level that allows us to detect, in their phase-folded light curve, the secondary eclipse of close-in large planets (e.g. CoRoT-1b and CoRoT-2b) and the planet orbital phase variation in some cases (e.g. CoRoT-1b).

In order to keep the noise level low in the phase-folded light curve, it helps to:

- chose the appropriate IRF-filtering parameters ($\mathrm{timescale}$ and $\mathrm{binsize}$), small enough to filter as much variability as possible but large enough not to change the noise

propriety (Section 4.2.4).

- cut out all the orbits containing a jump in flux, before filtering
- select an integer number of planetary orbits
- select an integer number of the stellar rotation period (in the case of active stars)
- evaluate (over the whole light curve or over re-combined individual chunks) and remove flux modulations at orbital period of the CoRoT satellite, post filtering
- remove planet orbits with residual discontinuities in the filtered light curve, post filtering
- keep as many planetary orbits as possible to increase the signal to noise ratio
- clip $3\sigma$ outliers, post filtering

### 4.4.3 Limitations

In the case of CoRoT-1b, the main limitation is the level of photon noise which can only be improved by observing more planet orbits and/or by using a larger space telescope. In the case of CoRoT-2b, the main limitation is the residual stellar variability at the planetary orbital phase (localise or spread over the phase-folded light curve).

A $2\sigma$ difference between the secondary eclipse depth for CoRoT-1b published in Alonso et al. (2009b) and that found here highlights the fact that secondary eclipse depths derived from optical light curves at the limit of significance are still strongly dependent on the details of the light curve preprocessing.

Even after careful filtering (as described above), some significant correlated noise features can remain in the phase-folded light curve (e.g. CoRoT-2) and can create false detection or reduce the detection significance of a real secondary eclipse. These correlated noise features can come from:

- the original light curve, as a large feature in a single planet orbit can still be apparent in the phase-folded light curve, even after averaging with non affected orbits. One can attempt to remove these correlated features by improving the filtering of the signal outside that of the planetary orbital period (smaller $\mathrm{timescale}$ and $\mathrm{binsize}$), and/or by cutting out before the filtering the planetary orbits where these correlated features occur.
- the filtering process (see Section 4.2.4), in which case re-doing the IRF-filtering with a smaller $\mathrm{timescale}$ and/or a larger $\mathrm{binsize}$ might smooth out these features. Smaller $\mathrm{timescale}$ will identify these features as stellar variability and they will not be passed into the transit signal. If the features are too sharp, smaller $\mathrm{timescale}$ will not be enough, and some residual features will end up in the transit signal.

These features will be binned with the non-affected orbits, and will contaminate them. In this case, a larger $\mathrm{binsize}$ will sum over features with more non-affected points, smoothing out the irregularity. Nevertheless, using a small $\mathrm{timescale}$ and large $\mathrm{binsize}$ is a trade off between filtering out the maximum of stellar variability signal and still preserving the transit signal intact.

Both these options were tried in the case of CoRoT-2b, but still leave stellar variability residuals at the planet orbital period larger than the amplitude of the secondary eclipse.

Once the secondary eclipse of a planet is detected and its depth measured, the next step is to extract the albedo and the equilibrium temperature of the planet from this measurement.

When observing in the infrared, the dominating flux of the planet is its thermal emission. Assuming the planet is in thermal equilibrium, the planet equilibrium temperature can be derived from the planet's brightness temperature. This gives access to a series of combinations of albedo and redistribution factors compatible with the planet.

When observing at shorter wavelengths (blue and shorter), the dominating flux of the planet is reflected light (for large value of the albedo, value depending on the size of the planet and the distance to its star) and the albedo can be measured. The orbital phase variation in thermal emission can give a clue about the redistribution factor. If the redistribution is small, the point of maximum flux in the phase curve will correspond to the phase of the secondary eclipse, and the larger the distribution factor the larger the difference in phase between the maximum in flux of the phase variation and the secondary eclipse. When these three measurements can be obtained, the possible combinations of albedos and redistribution factors compatible with the planet can be narrowed down.

When integrating the planetary flux over the visible, such as in the CoRoT light curve, the thermal emission and the reflected light are both present. With the CoRoT light curve, we have one measurement of the depth of the secondary eclipse and three unknowns: the albedo, the redistribution factor, and the fraction of thermal to reflected emission. If the depth of the secondary eclipse can be significantly measured in the CoRoT colour channel, an approximation of the fraction of thermal to reflected light can be derived. Unfortunately, in practice the flux level in the red and green CoRoT channel are too small, even when combining two colour channels.

### 4.4.4 Future work

Other methods will need to be investigated to remove residual stellar variability at the planet orbital period, without affecting the planet orbital phase signal.

To extract a value for the albedo and the energy redistribution factor of a transiting planet, one would in general need a) a brighter star (low photon noise), b) a bright

planet (close-in and large giving a larger S/N) c) a rather quiet star (low residual stellar variability), d) a stable telescope and CCD camera (low correlated noise), and e) multi-wavelength observations of the secondary eclipse (e.g. ultra-violet, blue, green, red and infra-red, to separate the planet thermal emission from the reflected light).

In the near future, for planetary phase curves not affected by stellar variability, the orbital phase modelling will be modified to allow for non-sinusoidal periodic variations and maximum amplitude of the phase variation shifted from the phase of the secondary eclipse.

In addition, the method suggested in Section 4.2.3, to derive the uncertainty on this model will be implemented.

## 4.5 Conclusions

The performance of the IRF for the detection of planet secondary eclipses and orbital phases, was demonstrated. The parameters of the IRF were optimised for this task. The limits of the performance of the IRF are now better understood.

A convincing detection of the secondary eclipse of CoRoT-1b, and to some extent of its orbital variation, were achieved in the CoRoT white and red bandpasses. A less secure detection of the secondary eclipse of CoRoT-2b was also achieved in the CoRoT white bandpass.

Compared to the depths of the secondary eclipses at longer wavelengths, the depths in the CoRoT bandpass (optical) are smaller. This is expected as at longer wavelengths, planets are more luminous (thermal flux) compared to their star.

# Chapter 5

# Stellar temperatures using equivalent width line-ratios

The photometric transit of a planet across the disk of its parent star allows the measurement of the planet to star radius ratio. The measurement of the radial velocity or astrometry wobbles of a star due to an orbiting planet allows the measurement of the planet to star mass ratio. If the stellar radius and mass are precisely measured, the planet radius and mass can be derived more precisely. For bright stars, precise stellar radii can be measured by interferometry or asteroseismology, but for most of the transiting planets, the host stars are not bright enough and other techniques must be used. The most widely used technique, for stars with transiting planets, is to find the stellar evolutionary track corresponding to the density (e.g. $M_s^{1/3}/R_s$) measured from the planetary transit and the stellar temperature measured from the stellar spectrum. Stellar evolution models (e.g. Baraffe et al. 1998, Siess et al. 2000, Girardi et al. 2002) allow us to derive the stellar radius and mass associated to a given stellar atmosphere obtained from comparing the stellar spectrum with stellar atmosphere models (e.g. the ATLAS models, Kurucz 1993).

Precise stellar effective temperatures ($T_{\rm eff}$) are fundamental to many areas in astrophysics, and in particular, to derive precise stellar radii. The $T_{\rm eff}$ of a star can be derived using photometric methods or spectroscopic methods. An example of photometric methods, for bright stars, includes deriving the stellar bolometric flux recovered from multi-band photometry allows us to derive the stellar temperature knowing the stellar radii (see equation 5.1). For instance, the stellar radii can be measured from stellar evolution tracks, interferometry or asteroseismology. Examples of spectroscopic methods include studying the line profile of the H$\alpha$ line, or comparing observed spectra to synthesised spectra from stellar atmosphere models.

Assuming the star radiates as a black body, the stellar luminosity $L$, radius $R_\star$ and effective temperature $T_{\rm eff}$ are related as followed:

$$L = 4\pi R_\star^2 \sigma_{\rm SB} T_{\rm eff}^4 \tag{5.1}$$

where $\sigma_{\rm SB}$ is the Stefan-Boltzmann constant.

Using equation 5.1, the stellar effective temperatures can be derived photometrical, e.g. using temperature calibrated colour bands (e.g. Nordström et al. 2004), spectroscopically, e.g. using $H_\alpha$ wings (e.g. Fuhrmann 1998) or iron lines (e.g. Santos et al. 2004), or through interferometry using the measured stellar radius to derive the stellar temperature. These methods derive uncertainty on the temperature typical down to 80 or 20 K depending on the method and on the star.

This chapter presents a method based on temperature calibrated equivalent width (EW) ratios which allows us to derive stellar relative temperatures with a precision down to 10 K. The current line-ratio temperature calibrations in the literature are based on line depth ratios (e.g. Gray 1994; Kovtyukh et al. 2003). The temperature calibration of equivalent width ratios presented in this chapter are then used to show that such calibration is possible and works well.

After the calibration presented in the chapter was built and tested, an improved version of this calibration was implemented, based on the knowledge gathered from this first calibration. The new calibration is now published in Sousa et al. (2009).

## 5.1 $T_{\rm eff}$ calibration of equivalent width line-ratios

The equivalent width[1] of a spectral line is a measure of the line strength which is sensitive to the temperature (equation 5.2). The ratio of the equivalent widths of two spectral lines can be used as temperature sensors. Each calibrated equivalent width line-ratio can be used to obtain a measurement of the stellar temperature. The larger the number of ratios used, the larger the number of individual measurements of the temperature, which can then be combined together to statistically improve the precision of the stellar temperature.

In Local Thermal Equilibrium (LTE), the ratio of electrons population of two levels $n$ and $m$, i.e. the ratio of the strength of the two spectral lines corresponding to the energy level $n$ and $m$, is:

$$\frac{N_n}{N_m} = \frac{g_n}{g_m}\, e^{-(\chi_n - \chi_m)/kT} \tag{5.2}$$

where $g_n$ and $g_m$ are the statistical weight of level $n$ and $m$ (number of degenerate states at the given energy), $\chi_n$ and $\chi_m$ are the excitation potential (the energy from the ground level) of level $n$ and $m$, $k$ is the Boltzmann constant and, $T$ is the temperature (Gray, 2005).

[1] The equivalent width of a spectral line is the width of a rectangle of length one and an area equal to the area of the spectral line.

### 5.1.1 Choosing the line ratios

The different spectral lines have a different sensitivity to temperature. In this study, the lines are selected and combined into ratios, in order to optimise the response of the line ratios with temperature.

#### Selecting the spectral lines

A list of 268 lines from different chemical elements was computed from Kovtyukh et al. (2003), Kovtyukh (private communication), Santos et al. (2004), and Gilli et al. (2006). The lines used are all located outside telluric absorption lines, and have wavelengths ranging from 5200 to 6800 Å.

Only weak lines (10 mÅ$<$ EW $<$ 200 mÅ in the solar spectrum) were kept, as they are independent of microturbulence and the ratio of such lines show little or no dependence on metallicity variations (Gray, 1994). The lower limit on EWs was set to 10 mÅ as weaker lines are more sensitive to continuum level estimations, as for some sub-solar metallicity, and might not be detectable.

Finally, among the selected lines, only the lines which appear unblended in a high metallicity low temperature stellar spectrum of our sample (HD59686: (Fe/H)=0.28, T=4871 K, Santos et al. 2005) were kept. The criterion for blends was to visually exclude lines overlapped by another line by more than $\sim 5\%$ of their EW. Identifying blended lines in the spectrum of a cool-metal rich star, provides a worse case scenario for blends within our sample of stellar spectra.

Applying the above criteria resulted in a list of 155 spectral lines from different chemical elements with wavelength ranging from 5490 to 6722 Å, excitation potentials ranging from 0.8 to 5.0 eV.

#### Combining the spectral lines into line ratios

To maximise the dependence of the equivalent width line-ratios on temperature and minimise their dependence on other parameters, the 155 selected spectral lines are combined into line ratios following four criteria:

1. Lines close in wavelength are combined into ratios. The continuum level is the same for these lines and will cancel out in the ratio of the lines, minimising the influence of the uncertainty on the continuum evaluation in the equivalent width line-ratios. Here lines within $70$ Å from each other were combined together (value used in Kovtyukh et al. 2003).

2. Lines with large differences in excitation potential were combined. Lines with high excitation potential will be highly responsive to any temperature variations. Combining them with lines of low excitation potentials (low response to temperature variations) will give ratios to build ratios highly sensitive to temperature variations.

Here, lines with excitation potential difference greater than $3\,eV$ were combined together.

3. Lines from different chemical elements are combined into ratios. The electronic population of the energy levels of a single chemical element can be dependent on other effects than the temperature (e.g. in NLTE[2] where the relative strength of the lines of a chemical element is dependent on the density of the medium), in which case combining lines from the same element will avoid this.

4. Lines from chemical elements with the same or similar behaviour of abundance ratio $[\mathrm{X/Fe}]$ with metallicity $[\mathrm{Fe/H}]$ are combined into ratios, to avoid a dependence of the ratios on metallicity. The calibration stars have different metallicities, and among the sample, the chemical elements – which EW are combined into ratios – should have a similar response of relative abundances with metallicity. The chemical elements are classified into 5 categories, according to the variation of their abundance ratio $[\mathrm{X/Fe}]$ with metallicity (Gilli et al., 2006). FeI, MgI, SiI and TiI are classified as abundance ratio constant with metallicity, VI, AlI, NaI, NiI as abundance ratio weakly increasing with metallicity, CaI as abundance ratio weakly decreasing with metallicity, CoI and MnI have as abundance ratio strongly increasing with metallicity.

Applying these criteria returned 278 line ratios (Table 5.6) built with 116 spectral lines (Table 5.3) from 8 different chemical elements.

### 5.1.2 Calibrating the line ratios with temperature

The selected line ratios need to be temperature calibrated. This is done using a set of calibration stars as described below .

#### The calibration stars

The starting set of stars used to calibrate the equivalent width line-ratios with temperature, is composed of 101 stars with a high resolution and high signal-to-noise ratio (200-400) spectrum. The spectra of 50 of the stars were taken with UVES[3] and the spectra of the 51 other stars with FEROS[4]. Using high resolution spectra allows a more accurate measurement of the equivalent widths. The stars are solar-type (F-K) with temperature ranging from 4500 to 6200 K, metallicity (Fe/H) from $-0.5$ to $0.5$, and $\log g$ from 2.5 to 4.7. Their temperatures are taken from Santos et al. (2004), Santos et al. (2005) and

[2]NLTE = Non Local Thermodynamic Equilibrium, which happens when the density of the medium is low enough that the dominant mode of energy transport becomes radiation and not collisions.

[3]UVES: echelle spectrograph with a maximum resolution of 100000, mounted on the VLT/UT2 8m Kueyen Telescope at ESO Paranal Observatory, Chile.

[4]FEROS: 100000-resolution echelle spectrograph on the 2.2m Telescope in ESO La Silla Observatory, Chile.

Sousa et al. (2006). These authors all used the same technique to derive the stellar parameters and provide a set of calibration temperature homogeneously determined which allows us to minimise the scatter in temperature within each line ratios. The stellar temperature derived in these papers were obtained using the line abundance code $\mathrm{MOOG}$[5]. MOOG uses ATLAS9 (Kurucz, 1993) stellar atmosphere models to create model spectra. These models are compared to the equivalent widths measured on the observed stellar spectrum, and with a condition on the Fe ionisation balance MOOG returns the stellar atmospheric parameters ($T_{\rm eff}$, $\log(g)$, metallicity (Fe/H), and microturbulence) corresponding to the data.

The spectra used in this work are the same as the ones used in Santos et al. (2004), Santos et al. (2005) and Sousa et al. (2006). They were pre-reduced by these authors using UVES and FEROS reduction pipelines.

### Measuring the equivalent widths with $\mathrm{ARES}$

A standard method to measure the equivalent width of a spectral line is to use an interactive routine – such as $\mathrm{IRAF}$ – where the continuum position is fitted by eye for each individual line. In this case, the measurement has an intrinsic human error that is difficult to estimate. Using an automatic process to measure the equivalent width reduces the human error. In this chapter, the equivalent widths are measured using the software $\mathrm{ARES}$[6] (Sousa et al., 2007) which measures the equivalent width of an input list of absorption spectral lines for a given parameter list and a given stellar spectrum. $\mathrm{ARES}$ currently does not return uncertainties on the measured equivalent widths; this suggestion has been sent to the author and should be implemented in a future version of the software. Using a Linux script, this software is run automatically over the 101 stellar spectra of the data set to measure the equivalent width of the 116 selected spectral lines in each spectrum. The 278 equivalent width line-ratios are then computed for each star using an $\mathrm{IDL}$ code.

$\mathrm{ARES}$ has a list of input parameters. The $rejt$ parameter determines the points in the spectrum used to evaluate the local continuum. This parameter needs to be adjusted according to the signal to noise ratio ($S/N$) of each spectrum (see Sousa et al. (2008) for a table of correspondence between the $S/N$ and the optimal $rejt$). To keep the equivalent width measurements as automated as possible, and because in our data set the different spectra obtained from the same spectrograph have a similar S/N, a single value of $rejt$ is adopted for each spectrograph (0.998 for the UVES spectra and 0.990 for the FEROS spectra). Sousa et al. (2009) discusses on the effect of the $rejt$ value on the derived temperature using temperature calibrated equivalent width line-ratios similar to the one presented in this chapter. The $smoothder$ parameter corresponds to the width (in pixels) of the boxcar used to reduce the noise in the spectra and allow

[5]http://verdi.as.utexas.edu/moog.html
[6]http://www.astro.up.pt/ sousasag/ares/

a better fit of the lines. The $space$ parameter sets the wavelength range used on each side of the lines to evaluate the local continuums. The $lineresol$ parameter defines the minimum separation (in Å) between consecutive lines. The $miniline$ parameter sets the lower value of the equivalent width returned by ARES. The default values used here are $smoothder = 4$, $space = 3$, $lineresol = 0.1$, and $miniline = 2$.

The number of stars with successfully measured equivalent width ratios varies for each line ratio, depending on whether ARES successfully measured the equivalent width of the two spectral lines of the ratio. If a star is visually far from the other stars (e.g. more than $4\sigma$) when plotted in an equivalent width ratio – e.g. due to a line miss-measured by ARES or affected by a cosmic ray) – the star is removed from the sample of calibration stars. After this selection, 62 stars are left to calibrate the line ratios (Figure 5.1).

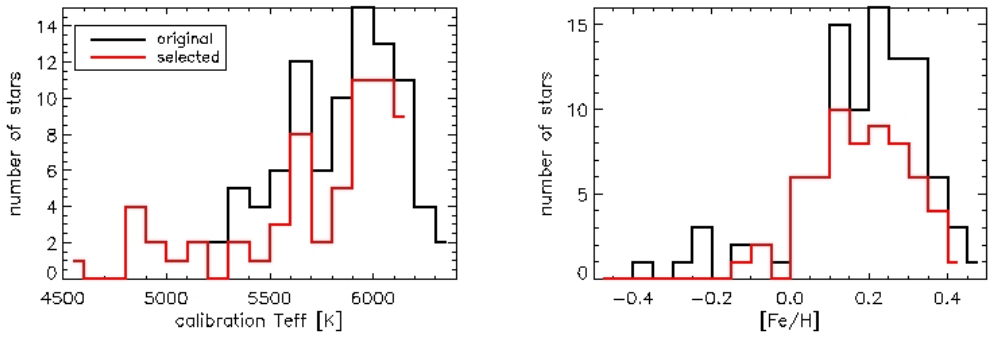


Figure 5.1: Distribution in temperature (left) and metallicity (right) of the 62 calibration stars (red) and the original sample of 101 stars (black).

### Fitting function

For each of the 278 line ratios, the dependence of the equivalent width line-ratios $r^{j}_{\rm EW}$ with the stellar effective temperatures $T^{S,j}_{\rm eff}$ ($j$ for each calibration star, $S$ for calibration temperature taken from Santos et al. (2004), Santos et al. (2005) and Sousa et al. (2006)) was fitted with a $3^{rd}$ order polynomial function. For each line ratio, a best fit is derived with the POLYFIT function of IDL[7], weighing each data points ($r^{j}_{\rm EW}$,$T^{S,j}_{\rm eff}$) with the uncertainty on the $T^{S,j}_{\rm eff}$.

The equivalent width ratios are calibrated against temperature as follows:

$$T^{S,j}_{\rm eff} = c_0 + c_1\, r^{i,j}_{\rm EW} + c_2\, {r^{i,j}_{\rm EW}}^{2} + c_3\, {r^{i,j}_{\rm EW}}^{3} \tag{5.3}$$

where $c_0$, $c_1$, $c_2$ and $c_3$ are respectively the zeroth, first, second and third order of the $3^{rd}$ order polynomial function, and $i$ is the line ratio.

[7]IDL: Interactive Data Language

### Selection of the final calibration set

For each line ratios, the standard deviation of the points around the best fit is calculated and taken as the uncertainty in temperature of the calibration of this ratio. The uncertainties on the individual calibrations ranges from 30 K to 240 K.

To minimise the uncertainties on the final temperature $T_{\rm eff}^{f}$ derived from the calibrated line ratios, the first 68% of the ratios with the lowest standard deviation from the fit are selected, which corresponds to standard deviation less than 100 K. This selection resulted in 190 ratios, composed of 88 spectral lines.

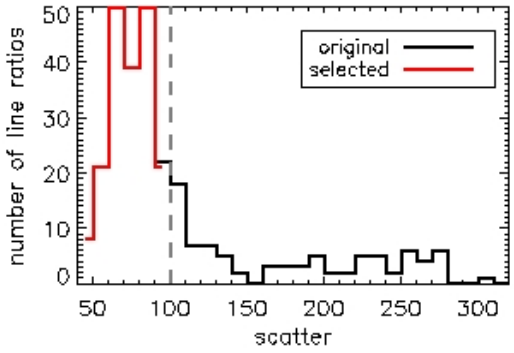


Figure 5.2: Distribution in standard deviation of the equivalent width line-ratios calibrated in temperature. The 278 original line ratios are plotted in black and the 190 selected line ratios in red. The 100 K limit in standard deviation, used for the selection, is marked by the dashed line.

## 5.1.3 Using the calibration to derive stellar temperatures

In a spectrum, the equivalent width of a spectral line can be inaccurately measured (e.g. due to line blends or cosmic rays affecting the determination of the local continuum). This will affect the value derived for the associated line ratio and return a wrong $T_{\rm eff}^{k}$ for this ratio. This temperature is classified as an "outlier" and to avoid taking it into account in the final temperature $T_{\rm eff}^{f}$, a $2\sigma$ clipping from the median of the $T_{\rm eff}^{k}$s (equation 5.8) is applied, where $\sigma$ is the 1.48*MAD[8] of the $T_{\rm eff}^{k}$s (equation 5.9).

There are several ways to combine the remaining individual temperature measurements into a final temperature. The weighted average of the measurements (equation 5.4, and equation 5.5 for the associated uncertainty) can be used when the accuracy of the individual measurements (values and uncertainties) can be trusted. The mean of the measurements (equation 5.6, and equation 5.7 for the associated uncertainty) can be used when the exactitude of the individual measurements can be trusted but not the associated uncertainties. The median of the measurements (equa-

[8]MAD: Median Absolute Deviation

tion 5.8, and equation 5.9 for the associated uncertainties) can be used when the exactitude of the individual measurements (values and uncertainties) cannot be trusted.

As the outlying temperatures have already been removed, the final temperature can be obtained by taking the mean of the remaining individual measurements of the temperature (equation 5.6, and equation 5.7 for the uncertainty). The weighted mean is not used as it is not certain that the uncertainties associated to the individual temperature take into account all the sources of uncertainties.

Weighted average:

$$T_{\rm eff}^{f} = \frac{\sum_k \frac{T_{\rm eff}^{k}}{{\sigma_k}^2}}{\sum_k \frac{1}{{\sigma_k}^2}} \tag{5.4}$$

where $\sigma_k$ is the uncertainty on the individual measurement of temperature ($T_{\rm eff}^{k}$) for the line ratio $k$. The uncertainty associated to the weighted average is

$$\sigma_{T_{\rm eff}^{f}} = \frac{1}{\sum_k \frac{1}{{\sigma_k}^2}} \tag{5.5}$$

Mean:

$$T_{\rm eff}^{f} = \frac{\sum_k T_{\rm eff}^{k}}{N} \tag{5.6}$$

where $N$ is the number of individual measurements of temperature combined together. The uncertainty associated to the mean is

$$\sigma_{T_{\rm eff}^{f}} = \sqrt{\frac{\sum_k (T_{\rm eff}^{k} - T_{\rm eff}^{f})^2}{N}}\ \frac{1}{\sqrt{N_i}} \tag{5.7}$$

where $N_i$ is the number of independent measurements of the temperature. In this work the number of independent measurements is taken as the number of unique combinations of chemical elements into line ratios. It is not taken as the total number of line ratios as several ratios are made of the same combination of elements and are therefore not independent from each other.

Median:

$$T_{\rm eff}^{f} = T_{\rm eff}^{k}|_{k=med} \tag{5.8}$$

When ordering the $T_{\rm eff}^{k}$, $med$ is the index of the $T_{\rm eff}^{k}$ with as many individual temperatures larger than $T_{\rm eff}^{med}$ than smaller. The uncertainty associated to the median is

$$\sigma_{T_{\rm eff}^{f}} = 1.48 * |T_{\rm eff}^{k} - T_{\rm eff}^{f}|_{k=med}\ \frac{1}{\sqrt{N_i}} \tag{5.9}$$

### 5.1.4 Testing the calibration

To evaluate the performance of the equivalent width line-ratio calibration set built in the previous sections, the three following tests were performed:

#### The inverse test

The first test is an inverse experiment where the 62 stars used to build the calibration are run back into the calibration and the resulting temperatures are compared to the values used to build the calibration. If the calibration is working well, both sets of temperature should be consistent within the error bars.

The resulting temperatures are plotted versus the original ones in Figure 5.3. For the stars with calibration temperature between 5000 and 6100 K, there is a good agreement between the calibration $T_{\rm eff}$ and the equivalent width $T_{\rm eff}$. But for the stars with calibration temperature lower than 5000 K, the current calibration overestimates the $T_{\rm eff}$ by up to 200 K, and for the stars with calibration temperature larger than 6100 K, the current calibration underestimates the $T_{\rm eff}$ by up to 100 K.

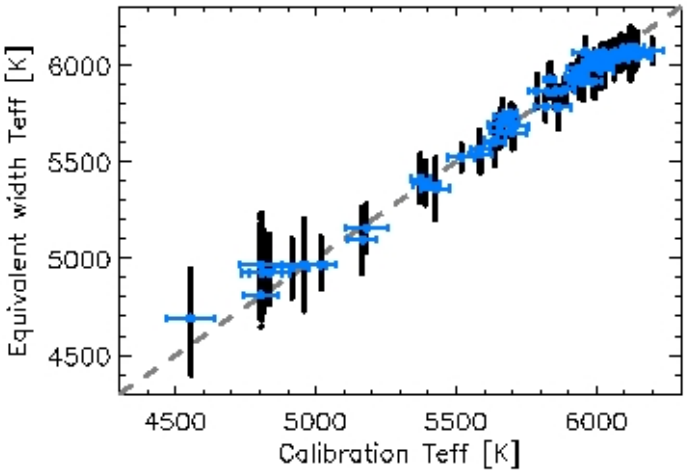


Figure 5.3: In blue, the $T_{\rm eff}$ of the 62 calibration stars derived using the equivalent width line-ratio calibration (y-axis), compared to the value of their $T_{\rm eff}$ with error bars used to build the calibration (x-axis). For each star (x-axis), the black dots along the y-axis are the $T_{\rm eff}$ measured from the individual line-ratios. The equivalent width $T_{\rm eff}$ and the associated error bars (along the y-axis, in blue) are derived as described in section 5.1.3. The grey dashed line is the identity line between the calibration $T_{\rm eff}$ and the equivalent width $T_{\rm eff}$.

#### Test on lower resolution spectra

The second test evaluates the performance of the calibration when using a spectrum with a resolution smaller than that of the spectra used to build the calibration.

The equivalent width line-ratio calibration is run on four stars with 50000-resolution spectra taken with CORALIE [9]. These spectra were reduced in Santos et al. (2004) using the standard tasks in the IRAF echelle package. The spectra have an $S/N$ of about 190 so the equivalent width are measured with ARES using $rejt = 0.992$. The individual $T_{\rm eff}$ derived from each calibrated equivalent width line-ratios are presented in Figure 5.4. The final $T_{\rm eff}$, derived as described in section 5.1.3, are compared in Table 5.1 to the value in Santos et al. (2004).

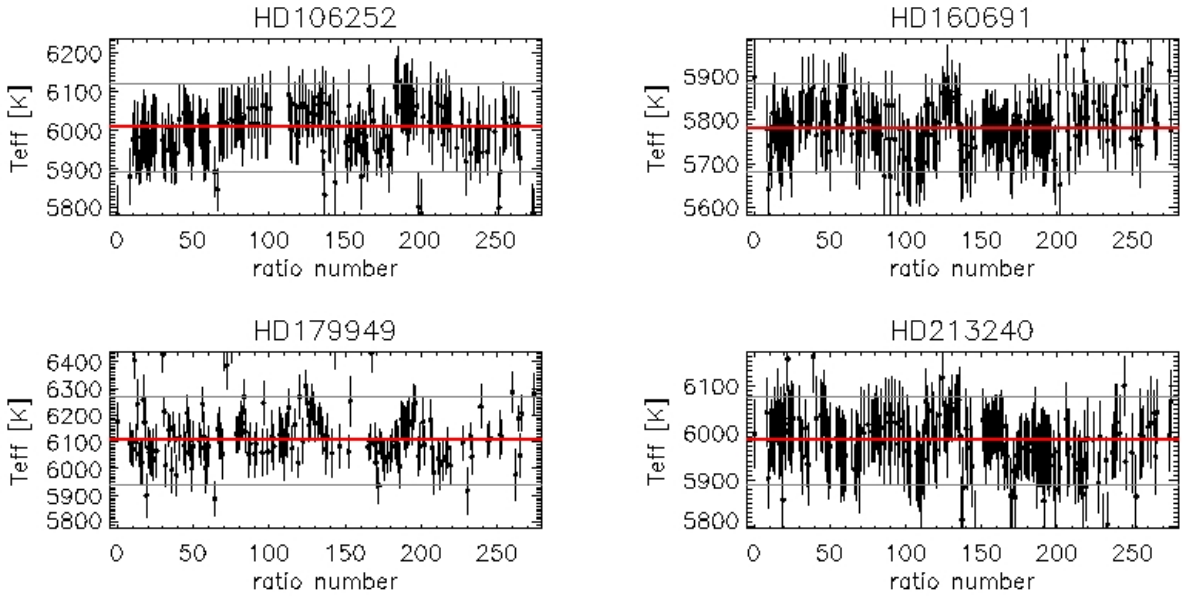


Figure 5.4: Test of the equivalent width line-ratio calibration on four stars with CORALIE spectra. Each point marks the $T_{\rm eff}$ and its uncertainty derived with the corresponding equivalent width line-ratio (numbered on the x-axis). The grey lines marks the levels at plus and minus twice the scatter from the median of the individual $T_{\rm eff}$, outside which the individual $T_{\rm eff}$ are considered as outliers. The red line marks the final $T_{\rm eff}$ derived as the mean of the $T_{\rm eff}$ within the grey lines.

Table 5.1: $T_{\rm eff}$ derived using the equivalent width calibration on the CORALIE spectra, compared to the values obtained by Santos et al. (2004) on the same spectra. $N_r$ is the number of ratios used to compute the final $T_{\rm eff}$, $N_i$ is the number of independent ratio, used to derive the uncertainty on the $T_{\rm eff}$, taken as the number of unique combinations of chemical elements in the line ratios.

| | This Chapter | | | Santos et al. (2004) |
|---|---|---|---|---|
| | $T_{\rm eff}$ | $N_r$ | $N_i$ | $T_{\rm eff}$ |
| HD106252 | 6009±14 | 159 | 11 | 5899±35 |
| HD160691 | 5782±13 | 177 | 12 | 5798±33 |
| HD179949 | 6111±20 | 139 | 12 | 6260±43 |
| HD213240 | 5986±11 | 168 | 12 | 5984±33 |

[9] CORALIE: 50000-resolution spectrograph on the 1.2m Euler Swiss Telescope at the ESO La Silla Observatory, Chile

For the two cooler stars, the final $T_{\rm eff}$ derived is consistent within the error bars with Santos et al. (2004), while the uncertainties derived with the equivalent width line-ratio calibration are smaller (half) than those from Santos et al. (2004). The two hotter stars have derived $T_{\rm eff}$ 110 and 150 K different from the value cited in Santos et al. (2004). For the star with $T_{\rm eff}$>6100 K, the underestimation of the temperature by the equivalent width line-ratio calibration was also identified in the previous test. The mis-match in temperature for the other star is not understood.

This test shows that the equivalent width measurements with $\rm ARES$ and the method used to combine the individual $T_{\rm eff}$ return consistent temperatures even for lower resolution spectra, as long as the temperature is within the temperature range where the calibration performs well ((5000,6100) K as defined in the previous test).

#### Test stars at various $rejt$

The $rejt$ parameter is used in $\rm ARES$ to select which points of the spectrum are used to evaluate the local continuum. This parameter is dependent on the signal to noise ratio of the spectrum. To keep the procedure automated, and as all the spectra used to calibrate the equivalent width line-ratios have similar $S/N$ (200-400), a unique $rejt$ is used for all the UVES spectra (0.998) and for all the FEROS spectra (0.990). For S/N varying from 200 to 400, the $rejt$ value should vary from 0.993 to 0.996. To evaluate the effect on the temperature derived from the equivalent width line-ratio calibration, of a $rejt$ value not optimised to the $S/N$ of the spectrum, the following test is performed. Three stars ($T_{\rm eff}$=4810, 5699, 6143 K), with similar (Fe/H) and spectra taken with the same spectrograph (UVES), the equivalent widths are measured for $rejt$ ranging from 0.990 to 0.999. The $T_{\rm eff}$ is derived for each of the $rejt$ value using the equivalent width line-ratio calibration. An additional star ($T_{\rm eff}$=5696 K) with a similar metallicity which has a spectrum taken with FEROS is studied in the same way. Figure 5.5 plots the resulting $T_{\rm eff}$ versus the value of $rejt$.

Figure 5.5 shows that the stellar $T_{\rm eff}$ can vary by 12 to 25 K depending on the $rejt$ value used to measure the equivalent widths. Within the explored range of $rejt$, the $T_{\rm eff}$ of the three UVES stars remain different to the value in Santos et al. (2004) by 30 to 100 K. The $T_{\rm eff}$ for the FEROS star is consistent with Santos et al. (2004).

This test indicates that choosing a $rejt$ value not optimised to the spectrum, introduces an additional uncertainty in the final $T_{\rm eff}$. To take this into account, an uncertainty of $\sim$25 K – coming from the uncertainty of the equivalent width measurements – should be added in quadrature. To reduce this additional source of uncertainty, the $rejt$ parameter should be adjusted for each spectrum. This is not aways straight forward as even a small difference (e.g. 0.001) in $rejt$ results in a difference of 5 to 10 K in the final $T_{\rm eff}$.

The unique values of $rejt$ used for the UVES and the FEROS calibration spectra can explain the large number of calibration stars (21 UVES, 18 FEROS) that were dropped

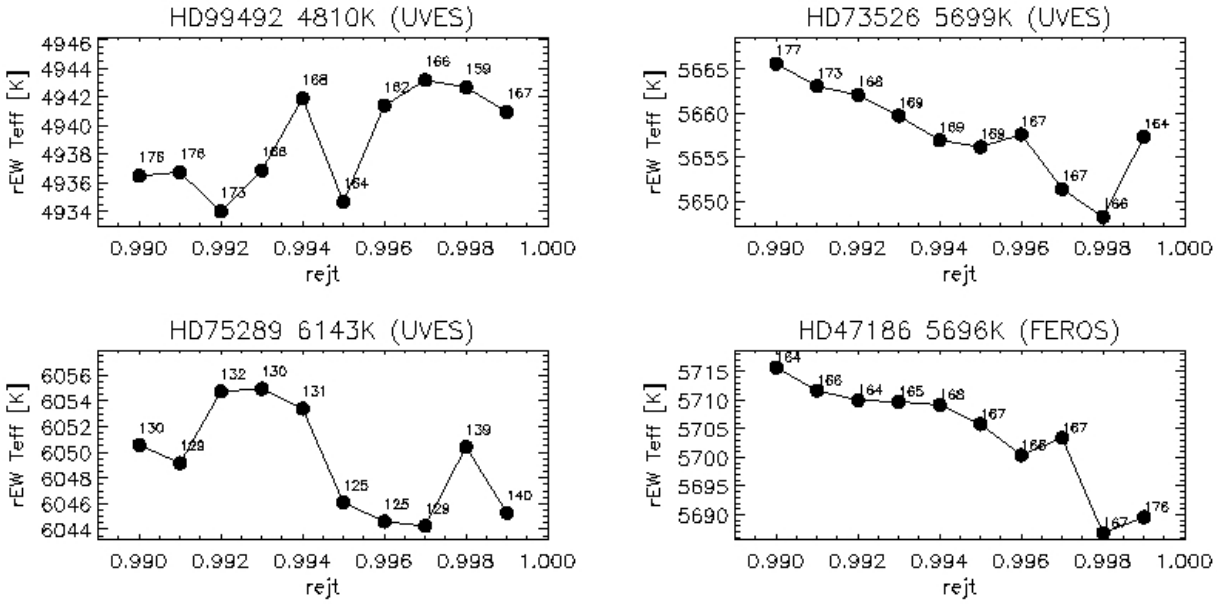


Figure 5.5: $T_{\rm eff}$ derived from the equivalent width line-ratio calibration, versus the $rejt$ value used to measure the EWs. The $T_{\rm eff}$ as derived by Santos et al. (2004) is indicated above each plot. The number of equivalent width line-ratios used to derive the $T_{\rm eff}$ in each $rejt$ trial is indicated in small prints by the side of each point.

out of the calibration sample as their equivalent width line-ratio $T_{\rm eff}$ were outliers.

This test shows on how the choice of $rejt$ value when measuring the EWs with $\rm ARES$ impacts the $T_{\rm eff}$ derived with the equivalent width line-ratio calibration.

### 5.1.5 Discussion

This section summarises the strengths and limitations of the equivalent width line-ratio calibration. It then lists some suggestions to improve this calibration.

#### Strengths

The calibration presented in this chapter is composed of 190 equivalent width line ratios calibrated for temperatures ranging from $4500\,K$ to $6200\,K$., with equivalent width measured uniformly using $\rm ARES$ and calibration temperature derived uniformly by previous authors.

This calibration is the first to present such a large number of calibrated equivalent width ratios. It was developed further and published in Sousa et al. (2009). Previous works on this subject calibrated line-depth ratios, not equivalent width ratios, and published less ratios (e.g. Kovtyukh et al. (2003) published 105 calibrations of line-depth ratios). This calibration demonstrates that equivalent width ratios are as good as line-depth ratios to measure stellar temperatures, contrarily to previous believes that they would not be precise enough as they are more sensitive to blends.

With its large number of calibrated line ratios, this calibration allows temperatures to be to derived with smaller relative uncertainties. The calibration was tested on 4 stars and, within the error bars, the temperatures are consistent with Santos et al. (2004), while our relative temperature error bars are at least a factor of two smaller.

The calibration can be applied to the monitoring of stellar variation in temperature, e.g. due to spots. From an exoplanet point of view, this could be used to tell apart spots mimicking planetary transits from real planetary transits (e.g. Biazzo et al. 2006).

### Limitations

The calibration is valid only over the calibrated temperature range (4500 to 6200 K), and loses precision below 5000 K and above 6100 K.

Only a temperature relative to another measurement, with the same calibration, can be determined with a better precision. The absolute temperature suffers from the same systematic offsets in temperature as the sample of calibration stars (e.g. $\sim$10 K compared to Ramírez & Meléndez 2004 as derived in Santos et al. 2005). In the case of exoplanets, to derive an accurate and precise stellar radius, one needs an accurate and precise stellar temperatures. The calibration of equivalent width line ratios is thus limited when it comes to deriving absolute temperature.

The accuracy on the $T_{\rm eff}$ is also dependent on that of the equivalent width measurements. For instance, the equivalent widths measured with $\rm ARES$ have an uncertainty due to the continuum determination controlled by the $rejt$, which is difficult to optimise for each spectrum. This uncertainty translates into $\sim$25 K in temperature, and needs to be added in quadrature to the uncertainty from the calibration itself – derived as the scatter in the individual $T_{\rm eff}$ measured). When using another tool to measure the equivalent widths, the user should evaluate and propagate the uncertainty on their equivalent width measurements to the final $T_{\rm eff}$.

### Improvements

The calibration can be improved by having more calibration stars. The 59 stars removed from the calibration sample can be revisited with adjusted $rejt$ to derive better equivalent widths and thus better values of the equivalent width line-ratios for these stars. Also, for a given star, if only some of the equivalent width line-ratio measurements are outliers, the star can be selectively removed from the affected ratios instead of systematically from the whole calibration.

The sample of stars can also be extended to lower $T_{\rm eff}$ to improve the quality of the calibration in that temperature range. The sample can also be extended outside the current calibration range in order to extend the temperature range over which the calibration can be applied.

The quality of the calibration can be in general improved with more precise measurements of equivalent widths, e.g. by using a $rejt$ value adapted to each spectrum.

The choice in fitting function used to model the dependence of the equivalent width with temperature can be diversified, e.g. by adding the functions $\frac{1}{x}$ and $\log x$ to the $3^{rd}$ order polynomial functions, and by selecting the function modelling each ratio with the smallest residuals.

The number of spectral lines can be increased, by widening the wavelength range or by changing the criteria of selection of good line ratios (e.g. loosening the 100 K limit in standard deviation). This will increase the number of line ratios, and thus theoretically improve the precision on the derived $T_{\rm eff}$. Adding spectral lines at shorter wavelength will improve the determination of the $T_{\rm eff}$ of hotter stars which have less lines at longer wavelengths.

In practice they are sources of uncertainty on the derived $T_{\rm eff}$ (e.g. from the $\rm ARES$ parameter $rejt$, or from the calibration temperatures) that should be taken into account when associating an uncertainty to an absolute temperature. These other sources of uncertainties are larger than the precision achieved by the current calibration. Thus, developing a more precise calibration (large number of ratios, fitting function, accuracy of the EWs measurements) will not make a major difference on the uncertainties associated with the absolute temperature.

## 5.2 Comparison to the calibration of Sousa et al. (2009)

An improved version of the calibration described in the previous sections, taking into account most of the points mentioned in Section 5.1.5, was published in Sousa et al. (2009).

In this new calibration, a larger number of calibration stars (451) are used, all with high resolution HARPS spectra (R$\sim$110000), with 90% of the spectra with a $S/N > 200$, and with calibration temperatures homogeneously derived in Sousa et al. (2008). The sample of calibration stars covers more uniformly the (4500,6500) K range.

This calibration is composed of a larger number of equivalent width line ratios. The initial line list was extended to 498 spectral lines. The spectra lines were combined into ratios only on the basis of their proximity in wavelength ($<$ 70 Å) and their difference in excitation potential $>$ 3 eV). The equivalent width measurements were obtained with $\rm ARES$ adjusting the $rejt$ parameter for each spectra. Ratios with a very weak and/or a very strong spectral line were removed as the equivalent width measured for these lines can be affected by the continuum estimate (for the weak lines) or by the gaussian fit to the line (for the strong lines).

In Sousa et al. (2009), the best fit to each equivalent width line-ratio $r$, calibrated in temperature ($T_{\rm eff}$), is selected among 6 models: a linear fit and a 3$^r d$ order polynomial fit to the relations ($T_{\rm eff}$ vs. $r$), ($T_{\rm eff}$ vs. $1/r$) and ($T_{\rm eff}$ vs. $\log r$). Finally, only the equivalent

width line-ratios measured in more than 300 stars and with a standard deviation to the best temperature calibration fit smaller than 120 K, were kept. Based on these criteria, the calibration published in Sousa et al. (2009) is composed of 433 line ratios built with 171 spectral lines.

In Sousa et al. (2009), the final temperature is derived as the weighted average of the temperatures from the individual equivalent with ratios, after having removed those temperatures outside the (4200,6800) K range and the ones outside a $2\sigma$ range from the average temperature. The uncertainty associated to this final temperature is derived as the standard deviation of the individual temperatures used to derived the final temperature, divided by the square root of the number of independent line ratios (i.e. the number of line ratios with unique combination of chemical elements). Sousa et al. (2009) published a correction function to the final temperature, to be applied if the temperature derived is greater than 6000 K.

The calibration derived in Sousa et al. (2009) is applied to the 62 calibration stars used to build the calibration presented in this chapter. The $T_{\rm eff}$ are plotted in Figure 5.6 and compared to the value derived with the calibration presented in this chapter.

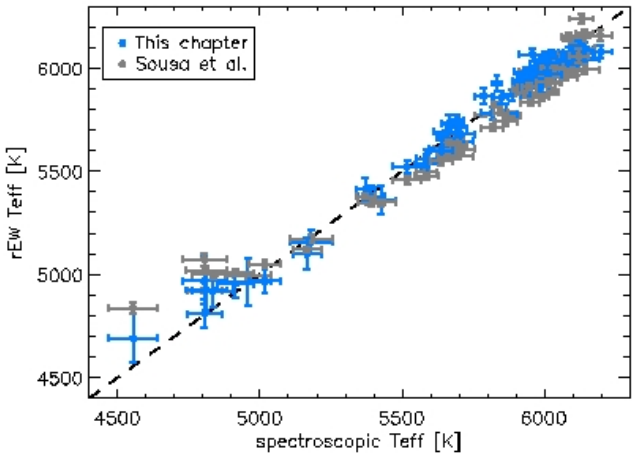


Figure 5.6: The $T_{\rm eff}$ derived with the calibration presented in this chapter (blue) versus the $T_{\rm eff}$ derived with the calibration presented in Sousa et al. (2009) (grey), for the 62 calibration stars used to build the calibration presented in this chapter. The dashed line is the identity line between the spectroscopic $T_{\rm eff}$ and the equivalent width ratio $T_{\rm eff}$.

The $T_{\rm eff}$ derived by the two calibrations are consistent within the errors bars. In general, the $T_{\rm eff}$ from Sousa et al. (2009) calibration have smaller error bars than the $T_{\rm eff}$ from the calibration described in this chapter. For the high $T_{\rm eff}$ stars, the calibration of Sousa et al. (2009) derives a $T_{\rm eff}$ closer to the identity line than this chapter's calibration, due to the systematic temperature correction applied to the high $T_{\rm eff}$ stars in the calibration of Sousa et al. (2009). For the low $T_{\rm eff}$ stars, this chapter's calibration derives $T_{\rm eff}$ slightly closer to the identity line than the calibration of Sousa et al. (2009). The difference observed between the two calibrations, is likely due to the approach

used when combining the individual $T_{\rm eff}$, as Sousa et al. (2009) derive the final $T_{\rm eff}$ as the weighted average which is more sensitive to wrong measurements of equivalent width line-ratio associated to line-ratios with small internal errors.

## 5.3 Applying the calibration to the host stars of CoRoT planets

In this section, the effective temperature $T_{\rm eff}$ of the host stars of the planets CoRoT-1b to 9b, are derived using the temperature calibrated equivalent width line-ratio technique. Two calibration sets and methods to combine the individual $T_{\rm eff}$ are used: the calibration set described in this chapter and the calibration set derived in Sousa et al. (2009), and re-described in section 5.2.

### 5.3.1 Spectra and equivalent width measurements

The spectra used in this section are UVES spectra for CoRoT-1,2,3,6,8,9 and HARPS spectra for CoRoT-4,5,7. The spectra are the same as the ones used for the determination of the stellar parameters in the discovery papers of the associated orbital companion. The UVES and HARPS spectra were reduced prior to this work with the standard instrument pipelines. Additionally, as the HARPS spectra were originally taken to measure the variations in radial velocity due to the orbital companion; after correcting each order of the spectra from its blaze function, the spectra were weight averaged order per order according to their $S/N$, to increase the $S/N$ of the spectrum used to derive the stellar atmosphere parameters.

In this work, the following additional reduction steps were performed on the spectra using the IRAF software: 1) the spectra were normalised order per order using the CONTINUUM task and the spline function of order 3 to 5, 2) the orders were merged using the SCOMBINE task, and 3) the stellar radial velocity was corrected, when needed, using the DOPCOR task.

The list of spectral lines used in the calibration presented in this chapter and in the calibration by Sousa et al. (2009) are combined into a single line list which is inputed into ARES to uniformly measure the equivalent width of all the spectral lines and avoid biases in equivalent width measurements between the two calibrations. The default ARES parameters used are $smoothder = 4$, $space = 3$, $lineresol = 0.15$ and $miniline = 2$. The values of $space$ and $lineresol$ have been slightly increased to account for the slighly noisier spectra compared to the spectra used to built the calibration presented in this chapter.

The $S/N$ of the different spectra vary from 40 to 240 so the $rejt$ parameter is adjusted for each spectrum. For the UVES spectra (CoRoT-1,2,6,8), the $S/N$ can vary from 70 to 180 across a single spectrum due to the level of fringing in the redder part of the spectrum which increases the noise in this range. For these spectra a single $rejt$ value

(0.990) is used to compromise between the different values of the $S/N$. The spectrum of CoRoT-4,5,9 have smaller $S/N$ (70, 50 and 90 respectively) so smaller values of $rejt$ are used (0.989, 0.985 and 0.989 respectively). The spectrum of CoRoT-7 has a larger $S/N$ (150-240) so a larger $rejt$ is used (0.993). For CoRoT-3, the spectral lines are broad, so the values used for $lineresol$ and $space = 8$ are increased to 0.4 and 8 respectively. These parameters set the minimum resolution between consecutive spectral lines and the wavelength range around the spectral lines used to evaluate the continuum. The value of both needs to be larger for broader lines.

### 5.3.2 Deriving the effective temperatures

The measured equivalent widths of each star are run through the calibrated equivalent width line-ratios described in this chapter. Figure 5.7 shows the individual $T_{\rm eff}$ derived from each ratio and the value of the combined $T_{\rm eff}$ (red line).

The measured equivalent widths are then run through the calibration of Sousa et al. (2009), also described in section 5.2, and the corresponding $T_{\rm eff}$ are extracted. If the derived $T_{\rm eff}$ is larger than 6000 K, a temperature correction is applied as described in Sousa et al. (2009). For CoRoT-6, the $T_{\rm eff}$ was corrected by -10 K.

The $T_{\rm eff}$ of the host stars of CoRoT-1b to 9b, derived from the two calibration sets, are presented in Table 5.2, along with the number of ratios used in each case and the value of the $T_{\rm eff}$ taken from the discovery paper.

Table 5.2: $T_{\rm eff}$ of CoRoT 1b to 9b derived using the two sets of equivalent width ratio calibrations, compared to the value in the literature. $N_r$ is the number of ratios used to compute the $T_{\rm eff}$, $N_i$ the number of independent ratios used to derive the uncertainty.

| | This chapter | | | Sousa et al. (2009) | | | Literature | |
|---|---|---|---|---|---|---|---|---|
| | $T_{\rm eff}$ | $N_r$ | $N_i$ | $T_{\rm eff}$ | $N_r$ | $N_i$ | $T_{\rm eff}$ | Ref. |
| CoRoT-1 | 6015±35 | 131 | 11 | 5919±77 | 264 | 19 | 5950±150 | Barge et al. (2008) |
| CoRoT-2 | 5663±50 | 163 | 12 | 5516±33 | 325 | 20 | 5625±120 | Alonso et al. (2008) |
| CoRoT-3 | 5974±84 | 66 | 11 | 5856±100 | 111 | 14 | 6740±140 | Triaud et al. (2009) |
| CoRoT-4 | 5971±46 | 158 | 12 | 5927±60 | 324 | 23 | 6190±60 | Aigrain et al. (2008) |
| CoRoT-5 | 5832±56 | 161 | 12 | 5736±66 | 333 | 22 | 6100±65 | Rauer et al. (2009) |
| CoRoT-6 | 6069±44 | 113 | 11 | 6014±73 | 184 | 16 | 6090±70 | Fridlund et al. (2010) |
| CoRoT-7 | 5333±34 | 181 | 12 | 5291±9 | 383 | 29 | 5275±75 | Léger et al. (2009) |
| CoRoT-8 | 5122±46 | 163 | 12 | 5134±40 | 354 | 20 | 5150±75 | Bordé et al. (2010) |
| CoRoT-9 | 5741±44 | 161 | 12 | 5563±35 | 331 | 18 | 5625±80 | Deeg et al. (2010) |

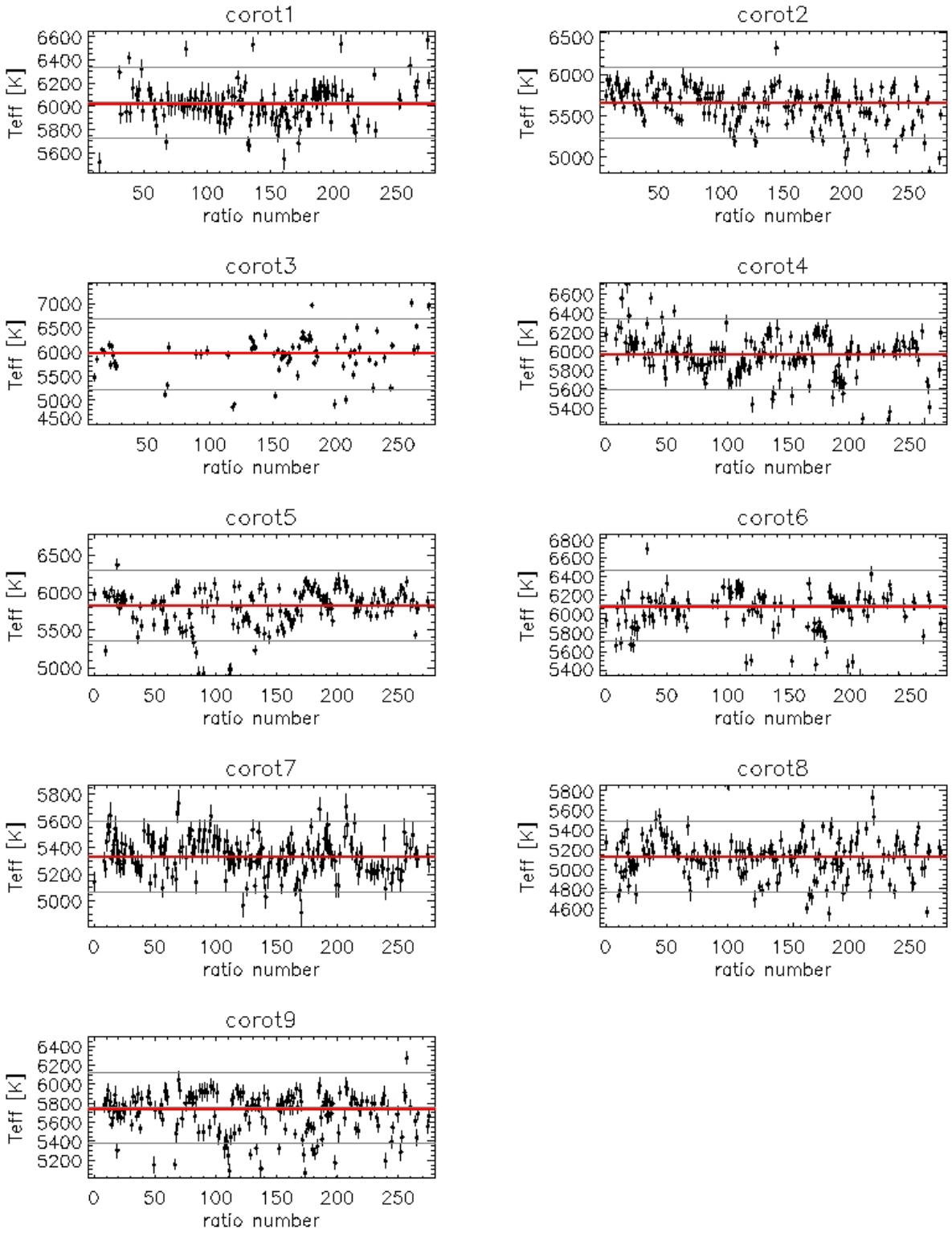


Figure 5.7: The $T_{\rm eff}$ of the CoRoT planet host stars derived from the equivalent width line-ratio calibration described in this chapter, based on UVES spectra for CoRoT-1,2,3,6,8,9 and HAPRS spectra for CoRoT-4,5,7. Same legend as Figure 5.4.

### 5.3.3 Discussion

The $T_{\rm eff}$ of the CoRoT planet host stars derived with the equivalent width line-ratios technique (both calibration set) are consistent within the error bars with the stellar $T_{\rm eff}$ published in the discovery papers, except for CoRoT-3,4,5. The uncertainties derived using the equivalent with ratios technique are in general smaller than those from the discovery papers (expect for CoRoT-4,5,6) when using the calibration set of Sousa et al. (2009).

The values of the $T_{\rm eff}$ derived from the calibration of this chapter are consistent within the error bars with those derived from the calibration of Sousa et al. (2009), except for CoRoT-2 and 9. The uncertainties derived with the calibration described in this chapter are smaller than those derived with the calibration of Sousa et al. (2009), except for CoRoT-2,7,8,9.

For CoRoT-2 and 9, the values of $T_{\rm eff}$ derived with the calibration set described in this chapter are 70 and 100 K higher than the values of $T_{\rm eff}$ derived with the calibration of Sousa et al. (2009). The reason for this difference is unclear as the $T_{\rm eff}$ are well within the calibrated temperature range of the two calibration sets, and as the equivalent widths of all the spectral lines were measured uniformly and should return uniform line ratios and thus uniform $T_{\rm eff}$. A possible difference could be in the approach used to combine the individual $T_{\rm eff}$. The weighted average used by Sousa et al. (2009) is more sensitive to outlier equivalent width measurements associated to well calibrated line ratios. This could explain the $T_{\rm eff}$ derived with the calibration of Sousa et al. (2009) but not the $T_{\rm eff}$ derived with the calibration of this chapter as the latter uses normal averaging of the individual $T_{\rm eff}$.

CoRoT-3 is a hot and fast rotating star, therefore its spectrum has less lines in the visible, and the spectral lines are broad so more likely to be blended. This results in fewer line ratios well measured by $\rm ARES$, which in turn limits the accuracy of the $T_{\rm eff}$ derived from the temperature calibrated equivalent width line-ratios. For this star, the $T_{\rm eff}$ of the two calibration sets are consistent with each other, which is as expected given the equivalent widths of the two sets were measured at the same time. But these $T_{\rm eff}$ are not consistent with the value in the discovery paper because the temperature of the star is outside the temperature range calibrated.

The $T_{\rm eff}$ of CoRoT-3,4,5, derived from equivalent width ratios, are underestimated. Their $T_{\rm eff}$ are larger than 6100 K, temperatures above which the calibration derived in this chapter are known to underestimate the $T_{\rm eff}$, as seen in section 5.1.4. The calibration of Sousa et al. (2009) has a correction function at $T_{\rm eff}>$6000 K, integrated into the derivation of the final $T_{\rm eff}$, but for these CoRoT host stars, the $T_{\rm eff}$ derived by the calibration is smaller than 6000 K, so the correction is not applied.

## 5.4 Conclusion

The equivalent width line ratios calibrated against temperature, is a successful method to derive stellar effective temperature, within the temperature calibrated range, and using medium to high resolution (R>50000) and signal-to-noise ($S/N$ >40) spectra.

The limitation to the precision of the $T_{\rm eff}$ derived with this method is not in the number of line ratios used but in the precision of the equivalent width measurements and local continuum. Using softwares (such as $\rm ARES$) to automatically measure the equivalent width of a large number of spectral lines makes the derivation of the $T_{\rm eff}$ faster and removes biases due to human "eye-ball" intervention in line fitting (such as with $\rm IRAF$), but the derived equivalent width measurements largely depend on the input parameters (such as $rejt$ in $\rm ARES$) which introduces an additional source of uncertainties in the derived $T_{\rm eff}$.

The equivalent width line ratio technique was applied to the host stars of CoRoT-1b to 9b and the derived $T_{\rm eff}$ are consistent with the discovery papers, except for the stars hotter than 6100 K. The associated uncertainties derived purely from the combination of the individual temperatures are smaller than the uncertainties published in the discovery papers, but are highly sensitive to the $\rm ARES$ $rejt$ value chosen.

The two sets of equivalent width line ratios presented in this chapter combine the individual $T_{\rm eff}$ differently. A larger and more uniform calibration set than the one presented in this chapter was developed in Sousa et al. (2009). Although the $T_{\rm eff}$ derived with the two calibrations are consistent, the calibration of Sousa et al. (2009) is an improvement to the calibration presented in this chapter. Thus, the $T_{\rm eff}$ and uncertainties kept for CoRoT-1b to 9b are those derived from the calibration of Sousa et al. (2009).

This chapter has presented an alternative method to measure the stellar temperature from the stellar spectrum. The $T_{\rm eff}$ derived with this method provides an additional measurement to compare with the values from the other methods, and increase or reduce the confidence on the value of the stellar temperature. The method presented here also has the advantages of been fast, automated and homogeneous, even if, like for the other methods, the temperature scale is not absolute.

## 5.5 Appendix

### 5.5.1 Line list

Table 5.3: List of the 116 spectral lines in the 278 lines ratios identified in section 5.1.2, with $\lambda$ the wavelength, $EP$ (Excitation Potential) the energy of the level above the ground state, $\log gf$ the weighted oscillator strength (product of the oscillator strength $f$ of the atomic transition and the statistical weight $g$ of the lower level), and $A$ the atomic number of the chemical element. The values of $EP$ and and $\log gf$ are taken from the VALD atomic database (Piskunov et al., 1995).

| $\lambda$ | $EP$ | $\log gf$ | $\lambda$ | $EP$ | $\log gf$ | $\lambda$ | $EP$ | $\log gf$ |
|---|---|---|---|---|---|---|---|---|
| **NaI (A = 11)** | | | 6090.21 | 1.081 | -0.150 | 6200.32 | 2.608 | -2.437 |
| 5688.22 | 2.104 | -0.625 | 6111.65 | 1.043 | -0.715 | 6213.43 | 2.223 | -2.482 |
| 6154.23 | 2.102 | -1.607 | 6135.36 | 1.051 | -0.746 | 6215.15 | 4.186 | -1.320 |
| 6160.75 | 2.104 | -1.316 | 6216.35 | 0.280 | -0.900 | 6226.73 | 3.880 | -2.066 |
| **MgI (A = 12)** | | | 6251.82 | 0.287 | -1.340 | 6232.65 | 3.654 | -1.223 |
| 5711.09 | 4.346 | -1.706 | **CrI (A = 24)** | | | 6240.66 | 2.223 | -3.233 |
| 6318.72 | 5.108 | -1.996 | 6330.13 | 0.941 | -2.920 | 6246.32 | 3.602 | -0.733 |
| **SiI (A = 14)** | | | **FeI (A = 26)** | | | 6252.55 | 2.404 | -1.687 |
| 5517.53 | 5.082 | -2.384 | 5619.60 | 4.386 | -1.700 | 6254.26 | 2.279 | -2.443 |
| 5621.60 | 5.082 | -2.500 | 5633.97 | 4.991 | -0.270 | 6265.13 | 2.176 | -2.550 |
| 5690.43 | 4.930 | -1.790 | 5650.71 | 5.085 | -0.960 | 6271.29 | 3.332 | -2.703 |
| 5701.11 | 4.930 | -2.020 | 5651.47 | 4.473 | -2.000 | 6330.86 | 4.733 | -1.740 |
| 5753.65 | 5.616 | -0.830 | 5662.52 | 4.178 | -0.573 | 6380.75 | 4.190 | -1.321 |
| 5772.15 | 5.082 | -1.620 | 5680.26 | 4.186 | -2.580 | 6392.55 | 2.280 | -3.932 |
| 5948.55 | 5.080 | -1.110 | 5701.54 | 2.559 | -2.216 | 6592.91 | 2.727 | -1.473 |
| 6125.03 | 5.610 | -1.520 | 5705.99 | 4.607 | -0.530 | 6608.03 | 2.279 | -4.030 |
| 6142.49 | 5.619 | -1.480 | 5717.85 | 4.284 | -1.130 | 6609.12 | 2.559 | -2.692 |
| 6145.02 | 5.616 | -1.480 | 5731.77 | 4.256 | -1.300 | 6627.56 | 4.548 | -1.680 |
| 6155.14 | 5.619 | -0.750 | 5753.12 | 4.260 | -0.688 | 6677.99 | 2.692 | -1.418 |
| 6237.33 | 5.614 | -0.530 | 5852.23 | 4.550 | -1.187 | 6703.58 | 2.758 | -3.160 |
| 6244.48 | 5.616 | -0.690 | 5855.08 | 4.610 | -1.529 | 6710.33 | 1.485 | -4.880 |
| 6414.99 | 5.871 | -1.100 | 5856.09 | 4.290 | -1.564 | 6750.15 | 2.424 | -2.621 |
| 6583.71 | 5.954 | -1.640 | 5862.36 | 4.549 | -0.058 | **NiI (A = 28)** | | |
| 6721.85 | 5.863 | -1.090 | 5956.70 | 0.859 | -4.605 | 5578.72 | 1.676 | -2.650 |
| **ScII (A = 21)** | | | 5983.69 | 4.549 | -1.878 | 5587.86 | 1.930 | -2.380 |
| 5526.82 | 1.770 | 0.150 | 5987.05 | 4.795 | -0.556 | 5682.20 | 4.100 | -0.390 |
| 6245.62 | 1.510 | -1.040 | 6007.96 | 4.652 | -0.966 | 5754.68 | 1.935 | -2.330 |
| 6604.60 | 1.360 | -1.160 | 6027.06 | 4.080 | -1.180 | 6007.31 | 1.676 | -3.330 |
| **TiI (A = 22)** | | | 6055.99 | 4.733 | -0.460 | 6086.29 | 4.266 | -0.440 |
| 5490.15 | 1.460 | -0.980 | 6056.01 | 4.730 | -0.498 | 6108.12 | 1.676 | -2.450 |
| 5866.45 | 1.070 | -0.840 | 6065.48 | 2.608 | -1.530 | 6111.07 | 4.090 | -0.800 |
| 6091.18 | 2.267 | -0.460 | 6078.50 | 4.795 | -0.424 | 6128.99 | 1.680 | -3.370 |
| 6126.22 | 1.067 | -1.410 | 6089.57 | 4.580 | -3.112 | 6130.14 | 4.260 | -0.950 |
| 6258.11 | 1.440 | -0.440 | 6098.28 | 4.558 | -1.880 | 6175.42 | 4.089 | -0.559 |
| 6261.11 | 1.430 | -0.490 | 6102.18 | 4.835 | -0.627 | 6176.81 | 4.088 | -0.260 |
| **VI (A = 23)** | | | 6105.15 | 4.548 | -2.050 | 6186.74 | 4.105 | -0.960 |
| 5670.85 | 1.081 | -0.460 | 6127.91 | 4.143 | -1.399 | 6204.64 | 4.088 | -1.100 |
| 5703.59 | 1.051 | -0.211 | 6151.62 | 2.176 | -3.299 | 6223.99 | 4.105 | -0.910 |
| 5727.05 | 1.080 | -0.000 | 6157.73 | 4.070 | -1.240 | 6327.60 | 1.676 | -3.150 |
| 5737.07 | 1.060 | -0.770 | 6159.38 | 4.610 | -1.860 | 6586.33 | 1.951 | -2.810 |
| 6039.73 | 1.064 | -0.650 | 6165.37 | 4.140 | -1.503 | 6767.77 | 1.826 | -2.170 |
| 6081.44 | 1.051 | -0.579 | 6188.00 | 3.940 | -1.631 | | | |

### 5.5.2 List of the calibration stars

Table 5.4: List of the final 62 calibration stars used to calibrate the line ratios, as described in section 5.1.2. The stellar parameters were taken from Santos et al. (2004), Santos et al. (2005) and Sousa et al. (2006).

| star | $T_{\rm eff}$ $(K)$ | (Fe/H) | $\log g$ $(cms^{-2})$ | | star | $T_{\rm eff}$ $(K)$ | (Fe/H) | $\log g$ $(cms^{-2})$ | |
|---|---|---|---|---|---|---|---|---|---|
| HD4203 | 5636±40 | 0.40±0.05 | 4.23±0.14 | (1) | HD73256 | 5518±49 | 0.26±0.06 | 4.42±0.12 | (1) |
| HD7199 | 5426±52 | 0.39±0.06 | 4.41±0.07 | (2) | HD73524 | 6012±50 | 0.23±0.06 | 4.40±0.03 | (2) |
| HD7570 | 6198±39 | 0.24±0.05 | 4.44±0.09 | (1) | HD73526 | 5699±49 | 0.27±0.06 | 4.27±0.12 | (1) |
| HD7727 | 6131±41 | 0.16±0.05 | 4.34±0.02 | (2) | HD74156 | 6112±39 | 0.16±0.05 | 4.34±0.10 | (1) |
| HD8326 | 4914±63 | 0.10±0.07 | 4.30±0.11 | (2) | HD75289 | 6143±53 | 0.28±0.07 | 4.42±0.13 | (1) |
| HD9562 | 5937±36 | 0.26±0.05 | 4.13±0.02 | (2) | HD78429 | 5786±31 | 0.11±0.05 | 4.34±0.02 | (2) |
| HD9782 | 6023±36 | 0.15±0.05 | 4.40±0.02 | (2) | HD82943 | 6028±19 | 0.29±0.02 | 4.45±0.07 | (1) |
| HD81110A | 5818±38 | 0.31±0.05 | 4.50±0.03 | (2) | HD99492 | 4810±72 | 0.26±0.07 | 4.21±0.21 | (1) |
| HD10180 | 5912±24 | 0.13±0.04 | 4.33±0.01 | (2) | HD102117 | 5708±46 | 0.33±0.06 | 4.31±0.09 | (2) |
| HD11226 | 6099±32 | 0.09±0.04 | 4.31±0.01 | (2) | HD114386 | 4834±77 | -0.06±0.06 | 4.33±0.29 | (1) |
| HD11964A | 5372±35 | 0.14±0.05 | 3.99±0.04 | (2) | HD117618 | 6013±41 | 0.06±0.06 | 4.39±0.07 | (1) |
| HD13043A | 5934±21 | 0.14±0.03 | 4.33±0.01 | (2) | HD121504 | 6075±40 | 0.16±0.05 | 4.64±0.12 | (1) |
| HD19994 | 6121±33 | 0.19±0.05 | 4.19±0.12 | (1) | HD128311 | 4835±72 | 0.03±0.07 | 4.44±0.21 | (1) |
| HD20201 | 6064±34 | 0.19±0.05 | 4.43±0.02 | (2) | HD177565 | 5664±28 | 0.14±0.04 | 4.43±0.09 | (2) |
| HD23079 | 5959±46 | -0.11±0.06 | 4.35±0.12 | (1) | HD177830 | 4804±77 | 0.33±0.09 | 3.57±0.17 | (1) |
| HD28185 | 5656±44 | 0.22±0.05 | 4.44±0.05 | (1) | HD183263 | 5991±28 | 0.34±0.04 | 4.38±0.17 | (2) |
| HD33214 | 5180±74 | 0.17±0.08 | 4.40±0.11 | (2) | HD183658 | 5833±19 | 0.08±0.03 | 4.42±0.01 | (2) |
| HD33636B | 6046±49 | -0.08±0.06 | 4.71±0.09 | (1) | HD190248 | 5638±40 | 0.39±0.05 | 4.33±0.04 | (2) |
| HD37605 | 5391±49 | 0.31±0.06 | 4.37±0.18 | (2) | HD190360A | 5584±36 | 0.24±0.05 | 4.37±0.06 | (1) |
| HD37986 | 5586±42 | 0.35±0.05 | 4.38±0.05 | (2) | HD192310 | 5166±52 | 0.04±0.06 | 4.39±0.08 | (2) |
| HD39091 | 5991±27 | 0.10±0.04 | 4.43±0.07 | (1) | HD199190 | 5946±25 | 0.20±0.04 | 4.25±0.01 | (2) |
| HD43745 | 6086±28 | 0.14±0.04 | 3.98±0.01 | (2) | HD204385 | 6022±24 | 0.09±0.04 | 4.31±0.01 | (2) |
| HD47186 | 5696±29 | 0.27±0.04 | 4.39±0.03 | (2) | HD208487 | 6141±29 | 0.06±0.04 | 4.52±0.15 | (2) |
| HD47536 | 4554±85 | -0.54±0.12 | 2.48±0.23 | (1) | HD209458 | 6117±26 | 0.02±0.03 | 4.48±0.08 | (1) |
| HD50554 | 6026±30 | 0.01±0.04 | 4.41±0.13 | (1) | HD213240 | 5984±33 | 0.17±0.05 | 4.25±0.10 | (1) |
| HD52265 | 6103±52 | 0.20±0.07 | 4.27±0.15 | (1) | HD216435 | 5938±42 | 0.24±0.05 | 4.12±0.05 | (1) |
| HD55693 | 5951±34 | 0.32±0.04 | 4.41±0.02 | (2) | HD216437 | 5887±32 | 0.25±0.04 | 4.30±0.07 | (1) |
| HD61606 | 4958±80 | 0.01±0.08 | 4.45±0.19 | (2) | HD221420 | 5864±43 | 0.37±0.06 | 4.06±0.03 | (2) |
| HD66221 | 5655±33 | 0.21±0.05 | 4.39±0.03 | (2) | HD222480 | 5848±24 | 0.21±0.04 | 4.20±0.01 | (2) |
| HD70642 | 5693±26 | 0.18±0.04 | 4.40±0.15 | (1) | HD224022 | 6134±46 | 0.15±0.06 | 4.30±0.02 | (2) |
| HD72659 | 5995±45 | 0.03±0.06 | 4.30±0.07 | (1) | HD330075 | 5017±53 | 0.08±0.06 | 4.22±0.11 | (1) |

(1) = UVES spectrum
(2) = FEROS spectrum

### 5.5.3 Plot of the line ratio and their calibration

Table 5.5: Plot of the 190 equivalent width line-ratios calibrated against temperature, with the $3^{rd}$ order polynomial function (coefficients in Table 5.6) modelling the dependency of the ratios with temperature (red line). Each dot is a calibration star with its $T_{\rm eff}$ taken from Santos et al. (2004), Santos et al. (2005) or Sousa et al. (2006), and its equivalent width is measured with ARES. "sdev" is the scatter of the points.

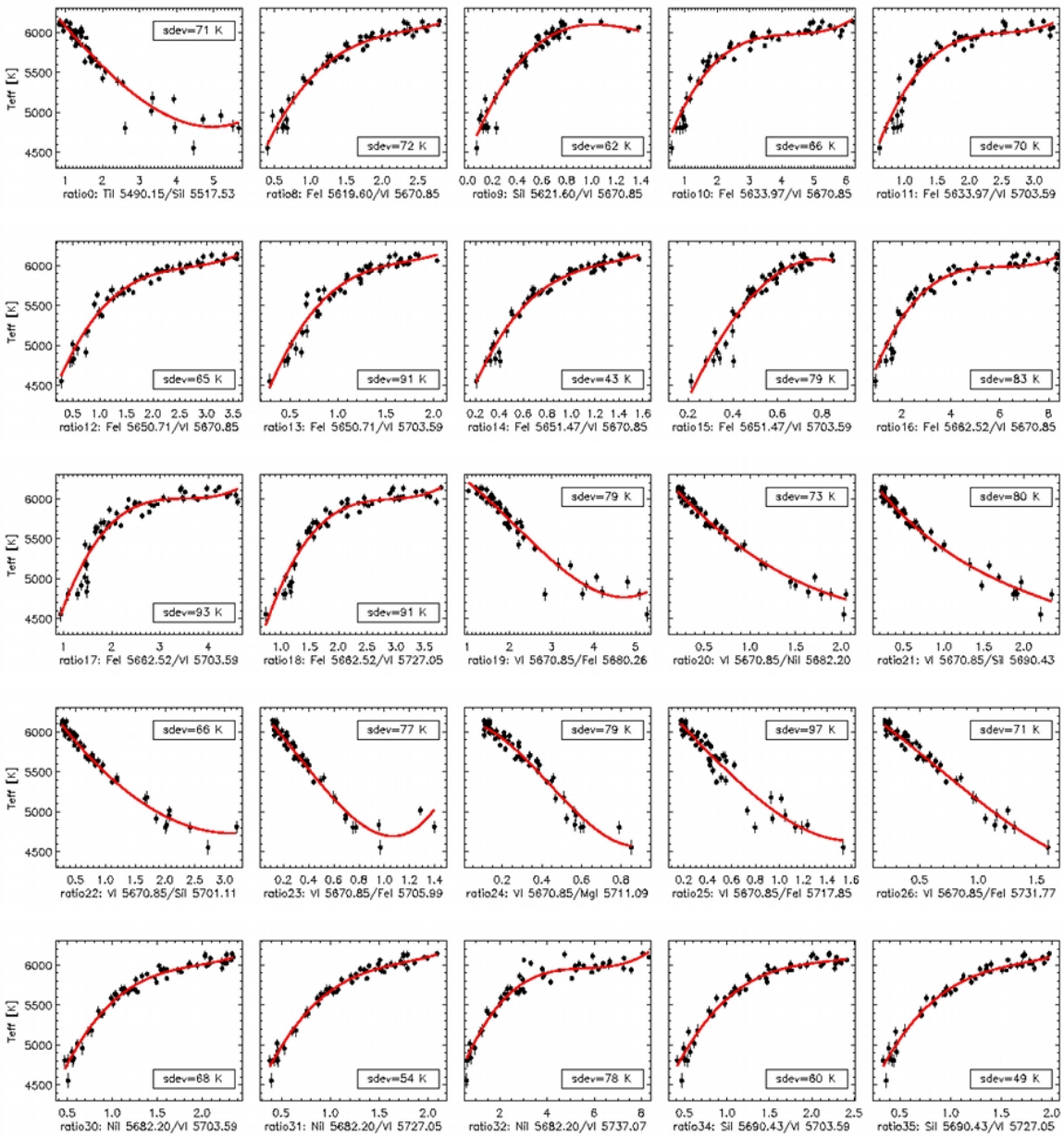

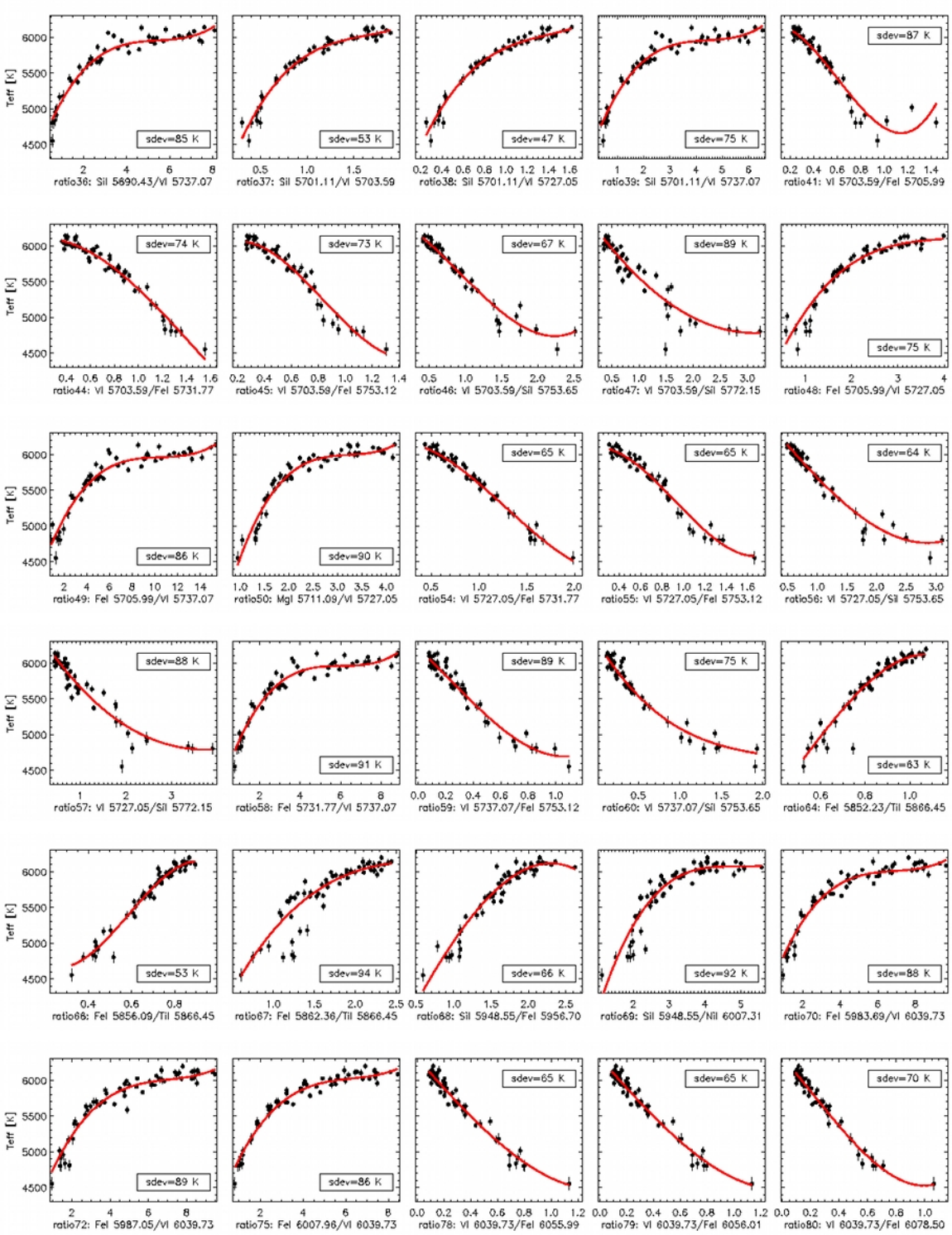
Teff [K]
sdev=85 K
ratio36: SiI 5890.43/VI 5737.07
sdev=53 K
ratio37: SiI 5701.11/VI 5703.59
sdev=47 K
ratio38: SiI 5701.11/VI 5727.05
sdev=75 K
ratio39: SiI 5701.11/VI 5737.07
sdev=87 K
ratio41: VI 5703.59/FeI 5705.99
sdev=74 K
ratio44: VI 5703.59/FeI 5731.77
sdev=73 K
ratio45: VI 5703.59/FeI 5753.12
sdev=67 K
ratio46: VI 5703.59/SiI 5753.65
sdev=89 K
ratio47: VI 5703.59/SiI 5772.15
sdev=75 K
ratio48: FeI 5705.99/VI 5727.05
sdev=86 K
ratio49: FeI 5705.99/VI 5737.07
sdev=90 K
ratio50: MgI 5711.09/VI 5727.05
sdev=65 K
ratio54: VI 5727.05/FeI 5731.77
sdev=65 K
ratio55: VI 5727.05/FeI 5753.12
sdev=64 K
ratio56: VI 5727.05/SiI 5753.65
sdev=88 K
ratio57: VI 5727.05/SiI 5772.15
sdev=91 K
ratio58: FeI 5731.77/VI 5737.07
sdev=89 K
ratio59: VI 5737.07/FeI 5753.12
sdev=75 K
ratio60: VI 5737.07/SiI 5753.65
sdev=83 K
ratio64: FeI 5852.23/TiI 5866.45
sdev=53 K
ratio66: FeI 5856.09/TiI 5866.45
sdev=94 K
ratio67: FeI 5862.36/TiI 5866.45
sdev=66 K
ratio68: SiI 5948.55/FeI 5956.70
sdev=92 K
ratio69: SiI 5948.55/NiI 6007.31
sdev=88 K
ratio70: FeI 5983.69/VI 6039.73
sdev=89 K
ratio72: FeI 5987.05/VI 6039.73
sdev=86 K
ratio75: FeI 6007.96/VI 6039.73
sdev=65 K
ratio78: VI 6039.73/FeI 6055.99
sdev=65 K
ratio79: VI 6039.73/FeI 6056.01
sdev=70 K
ratio80: VI 6039.73/FeI 6078.50

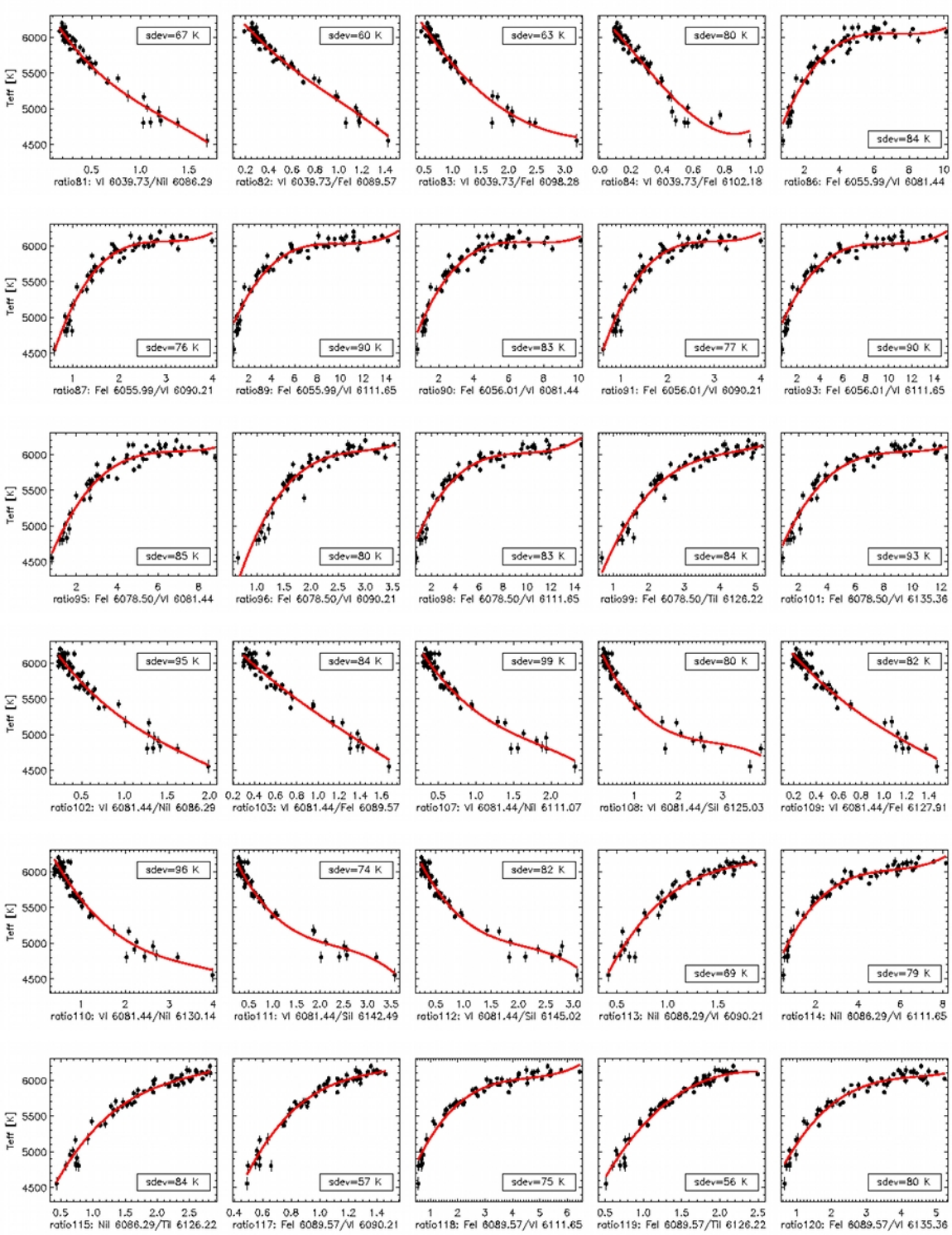
Teff [K]
sdev=67 K
ratio81: VI 6039.73/NiI 6086.29
sdev=60 K
ratio82: VI 6039.73/FeI 6089.57
sdev=63 K
ratio83: VI 6039.73/FeI 6098.28
sdev=80 K
ratio84: VI 6039.73/FeI 6102.18
sdev=84 K
ratio86: FeI 6055.99/VI 6081.44
sdev=76 K
ratio87: FeI 6055.99/VI 6090.21
sdev=90 K
ratio89: FeI 6055.99/VI 6111.65
sdev=83 K
ratio90: FeI 6056.01/VI 6081.44
sdev=77 K
ratio91: FeI 6056.01/VI 6090.21
sdev=90 K
ratio93: FeI 6056.01/VI 6111.65
sdev=85 K
ratio95: FeI 6078.50/VI 6081.44
sdev=80 K
ratio96: FeI 6078.50/VI 6090.21
sdev=83 K
ratio98: FeI 6078.50/VI 6111.65
sdev=84 K
ratio99: FeI 6078.50/TiI 6126.22
sdev=93 K
ratio101: FeI 6078.50/VI 6135.36
sdev=95 K
ratio102: VI 6081.44/NiI 6086.29
sdev=84 K
ratio103: VI 6081.44/FeI 6089.57
sdev=99 K
ratio107: VI 6081.44/NiI 6111.07
sdev=80 K
ratio108: VI 6081.44/SiI 6125.03
sdev=82 K
ratio109: VI 6081.44/FeI 6127.91
sdev=96 K
ratio110: VI 6081.44/NiI 6130.14
sdev=74 K
ratio111: VI 6081.44/SiI 6142.49
sdev=82 K
ratio112: VI 6081.44/SiI 6145.02
sdev=69 K
ratio113: NiI 6086.29/VI 6090.21
sdev=79 K
ratio114: NiI 6086.29/VI 6111.65
sdev=84 K
ratio115: NiI 6086.29/TiI 6126.22
sdev=57 K
ratio117: FeI 6089.57/VI 6090.21
sdev=75 K
ratio118: FeI 6089.57/VI 6111.65
sdev=56 K
ratio119: FeI 6089.57/TiI 6126.22
sdev=80 K
ratio120: FeI 6089.57/VI 6135.36

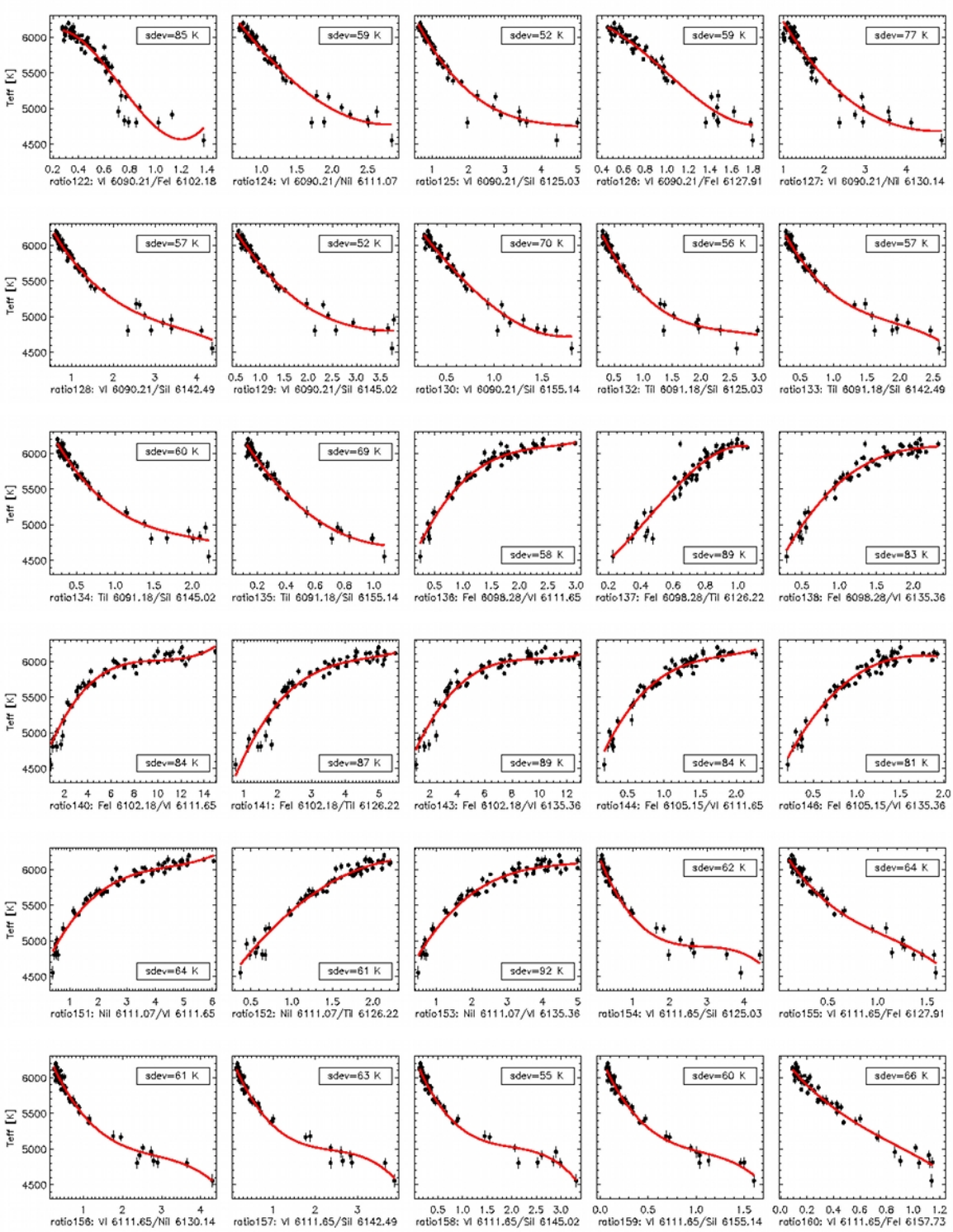
Teff [K]
sdev=85 K
ratio122: VI 6090.21/FeI 6102.18
sdev=59 K
ratio124: VI 6090.21/NiI 6111.07
sdev=52 K
ratio125: VI 6090.21/SiI 6125.03
sdev=59 K
ratio126: VI 6090.21/FeI 6127.91
sdev=77 K
ratio127: VI 6090.21/NiI 6130.14
sdev=57 K
ratio128: VI 6090.21/SiI 6142.49
sdev=52 K
ratio129: VI 6090.21/SiI 6145.02
sdev=70 K
ratio130: VI 6090.21/SiI 6155.14
sdev=56 K
ratio132: TiI 6091.18/SiI 6125.03
sdev=57 K
ratio133: TiI 6091.18/SiI 6142.49
sdev=60 K
ratio134: TiI 6091.18/SiI 6145.02
sdev=69 K
ratio135: TiI 6091.18/SiI 6155.14
sdev=58 K
ratio136: FeI 6098.28/VI 6111.65
sdev=89 K
ratio137: FeI 6098.28/TiI 6126.22
sdev=83 K
ratio138: FeI 6098.28/VI 6135.36
sdev=84 K
ratio140: FeI 6102.18/VI 6111.65
sdev=87 K
ratio141: FeI 6102.18/TiI 6126.22
sdev=89 K
ratio143: FeI 6102.18/VI 6135.36
sdev=84 K
ratio144: FeI 6105.15/VI 6111.65
sdev=81 K
ratio146: FeI 6105.15/VI 6135.36
sdev=64 K
ratio151: NiI 6111.07/VI 6111.65
sdev=61 K
ratio152: NiI 6111.07/TiI 6126.22
sdev=92 K
ratio153: NiI 6111.07/VI 6135.36
sdev=62 K
ratio154: VI 6111.65/SiI 6125.03
sdev=64 K
ratio155: VI 6111.65/FeI 6127.91
sdev=61 K
ratio156: VI 6111.65/NiI 6130.14
sdev=63 K
ratio157: VI 6111.65/SiI 6142.49
sdev=55 K
ratio158: VI 6111.65/SiI 6145.02
sdev=60 K
ratio159: VI 6111.65/SiI 6155.14
sdev=66 K
ratio160: VI 6111.65/FeI 6157.73

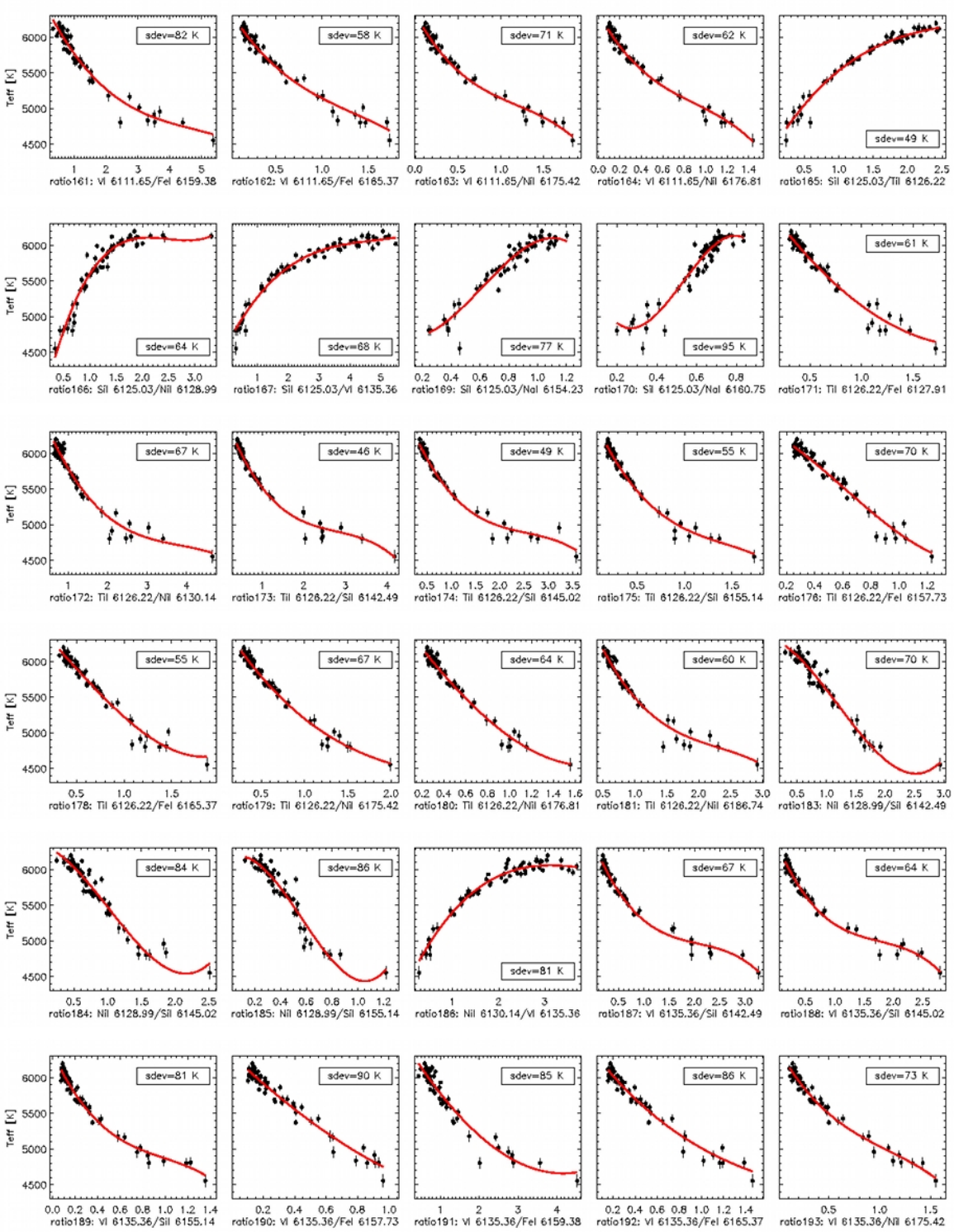
Teff [K]
sdev=82 K
ratio161: VI 6111.65/FeI 6159.38
sdev=58 K
ratio162: VI 6111.65/FeI 6165.37
sdev=71 K
ratio163: VI 6111.65/NiI 6175.42
sdev=62 K
ratio164: VI 6111.65/NiI 6176.81
sdev=49 K
ratio165: SiI 6125.03/TiI 6126.22
sdev=64 K
ratio166: SiI 6125.03/NiI 6128.99
sdev=68 K
ratio167: SiI 6125.03/VI 6135.36
sdev=77 K
ratio169: SiI 6125.03/NaI 6154.23
sdev=95 K
ratio170: SiI 6125.03/NaI 6160.75
sdev=61 K
ratio171: TiI 6126.22/FeI 6127.91
sdev=67 K
ratio172: TiI 6126.22/NiI 6130.14
sdev=46 K
ratio173: TiI 6126.22/SiI 6142.49
sdev=49 K
ratio174: TiI 6126.22/SiI 6145.02
sdev=55 K
ratio175: TiI 6126.22/SiI 6155.14
sdev=70 K
ratio176: TiI 6126.22/FeI 6157.73
sdev=55 K
ratio178: TiI 6126.22/FeI 6165.37
sdev=67 K
ratio179: TiI 6126.22/NiI 6175.42
sdev=64 K
ratio180: TiI 6126.22/NiI 6176.81
sdev=60 K
ratio181: TiI 6126.22/NiI 6186.74
sdev=70 K
ratio183: NiI 6128.99/SiI 6142.49
sdev=84 K
ratio184: NiI 6128.99/SiI 6145.02
sdev=86 K
ratio185: NiI 6128.99/SiI 6155.14
sdev=81 K
ratio186: NiI 6130.14/VI 6135.36
sdev=67 K
ratio187: VI 6135.36/SiI 6142.49
sdev=64 K
ratio188: VI 6135.36/SiI 6145.02
sdev=81 K
ratio189: VI 6135.36/SiI 6155.14
sdev=90 K
ratio190: VI 6135.36/FeI 6157.73
sdev=85 K
ratio191: VI 6135.36/FeI 6159.38
sdev=86 K
ratio192: VI 6135.36/FeI 6165.37
sdev=73 K
ratio193: VI 6135.36/NiI 6175.42

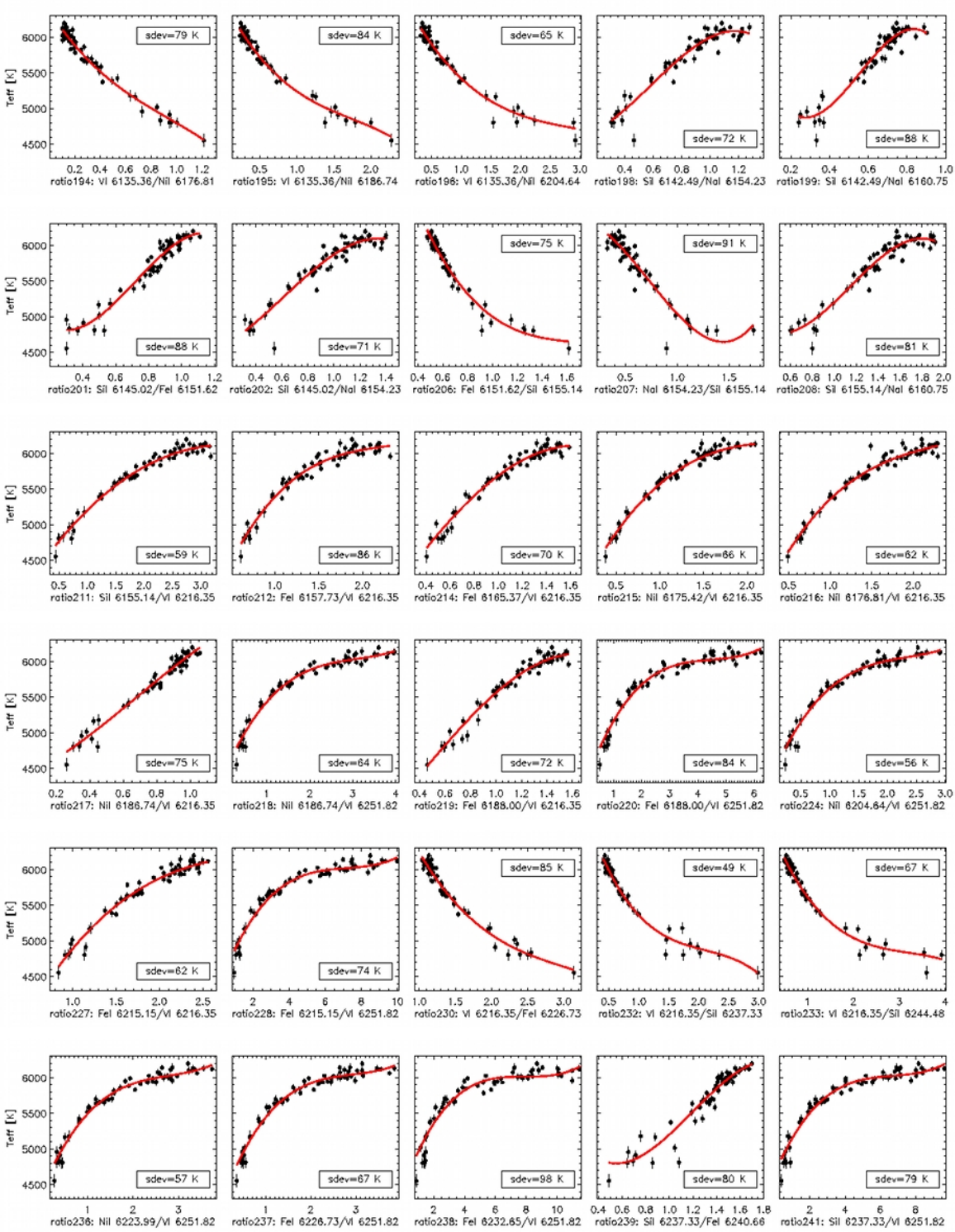
Teff [K]
sdev=79 K
ratio194: VI 6135.36/NII 6176.81
sdev=84 K
ratio195: VI 6135.36/NII 6186.74
sdev=65 K
ratio196: VI 6135.36/NII 6204.64
sdev=72 K
ratio198: SII 6142.49/NaI 6154.23
sdev=88 K
ratio199: SII 6142.49/NaI 6160.75
sdev=88 K
ratio201: SII 6145.02/FeI 6151.62
sdev=71 K
ratio202: SII 6145.02/NaI 6154.23
sdev=75 K
ratio206: FeI 6151.62/SII 6155.14
sdev=91 K
ratio207: NaI 6154.23/SII 6155.14
sdev=81 K
ratio208: SII 6155.14/NaI 6160.75
sdev=59 K
ratio211: SII 6155.14/VI 6216.35
sdev=86 K
ratio212: FeI 6157.73/VI 6216.35
sdev=70 K
ratio214: FeI 6165.37/VI 6216.35
sdev=66 K
ratio215: NII 6175.42/VI 6216.35
sdev=62 K
ratio216: NII 6176.81/VI 6216.35
sdev=75 K
ratio217: NII 6186.74/VI 6216.35
sdev=64 K
ratio218: NII 6186.74/VI 6251.82
sdev=72 K
ratio219: FeI 6188.00/VI 6216.35
sdev=84 K
ratio220: FeI 6188.00/VI 6251.82
sdev=56 K
ratio224: NII 6204.64/VI 6251.82
sdev=62 K
ratio227: FeI 6215.15/VI 6216.35
sdev=74 K
ratio228: FeI 6215.15/VI 6251.82
sdev=85 K
ratio230: VI 6216.35/FeI 6226.73
sdev=49 K
ratio232: VI 6216.35/SII 6237.33
sdev=67 K
ratio233: VI 6216.35/SII 6244.48
sdev=57 K
ratio236: NII 6223.99/VI 6251.82
sdev=67 K
ratio237: FeI 6226.73/VI 6251.82
sdev=98 K
ratio238: FeI 6232.65/VI 6251.82
sdev=80 K
ratio239: SII 6237.33/FeI 6240.66
sdev=79 K
ratio241: SII 6237.33/VI 6251.82

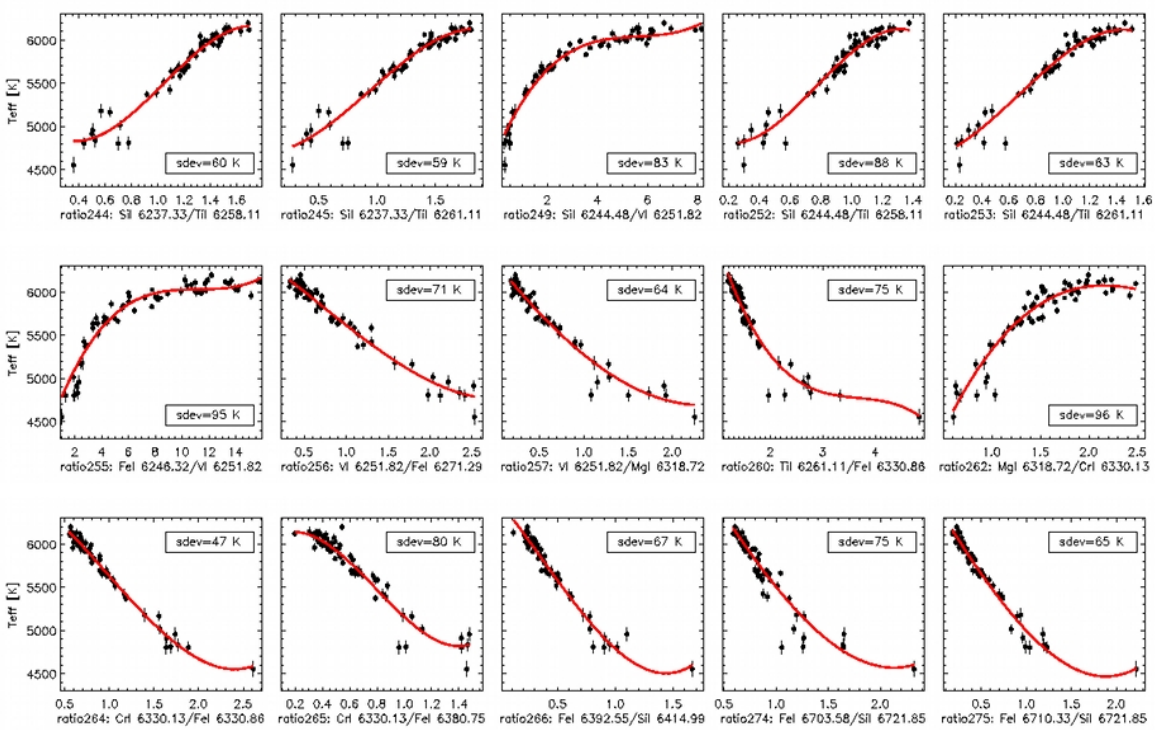
Teff [K]
sdev=60 K
ratio244: SiI 6237.33/TiI 6258.11
sdev=59 K
ratio245: SiI 6237.33/TiI 6261.11
sdev=83 K
ratio249: SiI 6244.48/VI 6251.82
sdev=88 K
ratio252: SiI 6244.48/TiI 6258.11
sdev=83 K
ratio253: SiI 6244.48/TiI 6261.11
sdev=95 K
ratio255: FeI 6246.32/VI 6251.82
sdev=71 K
ratio256: VI 6251.82/FeI 6271.29
sdev=64 K
ratio257: VI 6251.82/MgI 6318.72
sdev=75 K
ratio260: TiI 6261.11/FeI 6330.86
sdev=96 K
ratio262: MgI 6318.72/CrI 6330.13
sdev=47 K
ratio264: CrI 6330.13/FeI 6330.86
sdev=80 K
ratio265: CrI 6330.13/FeI 6380.75
sdev=67 K
ratio266: FeI 6392.55/SiI 6414.98
sdev=75 K
ratio274: FeI 6703.58/SiI 6721.85
sdev=65 K
ratio275: FeI 6710.33/SiI 6721.85

### 5.5.4 List of the line ratios and their calibration coefficients

Table 5.6: List of the 190 equivalent width ratios ($rEW_k$) calibrated against temperature ($T_{\rm eff}$) as $3^{rd}$ order polynomial functions. The polynomial function is $T^k_{eff} = c_0 + c_1 * rEW_k + c_2 * rEW_k^2 + c_3 * rEW_k^3$ with $c_0$, $c_1$, $c_2$ and $c_3$ the coefficients of the $2^{nd}$ order polynomial function. "ratio" is the ratio identification number given in this study. "std" is the standard deviation (1.48*MAD) of the points around the polynomial fit (printed as "sdev" in Figure 5.5).

| ratio | std | line 1 | line 2 | $c_0$ | $c_1$ | $c_2$ | $c_3$ |
|---|---|---|---|---|---|---|---|
| 0 | 71 | TiI 5490.15 | SiI 5517.53 | 6651.07 | -586.95 | 13.40 | 6.15 |
| 8 | 72 | FeI 5619.60 | VI 5670.85 | 3719.77 | 2565.28 | -1008.76 | 142.20 |
| 9 | 62 | SiI 5621.60 | VI 5670.85 | 4437.02 | 3985.89 | -3032.56 | 708.43 |
| 10 | 66 | FeI 5633.97 | VI 5670.85 | 4090.92 | 1262.39 | -286.55 | 22.09 |
| 11 | 70 | FeI 5633.97 | VI 5703.59 | 2957.03 | 3479.63 | -1349.64 | 177.58 |
| 12 | 65 | FeI 5650.71 | VI 5670.85 | 4151.17 | 1848.12 | -653.23 | 81.52 |
| 13 | 91 | FeI 5650.71 | VI 5703.59 | 3495.73 | 3983.64 | -2170.97 | 418.24 |
| 14 | 43 | FeI 5651.47 | VI 5670.85 | 3743.38 | 4476.96 | -3096.91 | 774.50 |
| 15 | 79 | FeI 5651.47 | VI 5703.59 | 2964.10 | 7837.76 | -4851.15 | -94.44 |
| 16 | 83 | FeI 5662.52 | VI 5670.85 | 3902.30 | 1017.41 | -166.92 | 9.20 |
| 17 | 93 | FeI 5662.52 | VI 5703.59 | 2337.74 | 3095.76 | -875.30 | 82.88 |
| 18 | 91 | FeI 5662.52 | VI 5727.05 | 2313.54 | 3701.09 | -1256.53 | 144.21 |
| 19 | 79 | VI 5670.85 | FeI 5680.26 | 6509.60 | -154.64 | -169.33 | 26.25 |
| 20 | 73 | VI 5670.85 | NiI 5682.20 | 6367.58 | -1351.32 | 318.97 | -22.80 |
| 21 | 80 | VI 5670.85 | SiI 5690.43 | 6359.31 | -1327.39 | 386.69 | -50.97 |
| 22 | 66 | VI 5670.85 | SiI 5701.11 | 6356.71 | -1029.41 | 160.05 | 0.90 |
| 23 | 77 | VI 5670.85 | FeI 5705.99 | 6282.13 | -1580.51 | -1211.63 | 1217.36 |
| 24 | 79 | VI 5670.85 | MgI 5711.09 | 6123.64 | 10.83 | -6115.10 | 4657.15 |
| 25 | 97 | VI 5670.85 | FeI 5717.85 | 6368.22 | -1524.61 | -140.82 | 261.48 |
| 26 | 71 | VI 5670.85 | FeI 5731.77 | 6293.14 | -1006.38 | -296.36 | 153.82 |
| 30 | 68 | NiI 5682.20 | VI 5703.59 | 3327.65 | 3672.50 | -1763.17 | 298.53 |
| 31 | 54 | NiI 5682.20 | VI 5727.05 | 3611.60 | 3580.20 | -1871.07 | 351.96 |
| 32 | 78 | NiI 5682.20 | VI 5737.07 | 4390.77 | 811.85 | -142.30 | 8.46 |
| 34 | 60 | SiI 5690.43 | VI 5703.59 | 3722.71 | 2957.22 | -1304.30 | 200.26 |
| 35 | 49 | SiI 5690.43 | VI 5727.05 | 3793.06 | 3373.91 | -1804.31 | 347.64 |
| 36 | 85 | SiI 5690.43 | VI 5737.07 | 4461.86 | 787.29 | -140.96 | 8.60 |
| 37 | 53 | SiI 5701.11 | VI 5703.59 | 3566.43 | 4023.01 | -2314.45 | 473.85 |
| 38 | 47 | SiI 5701.11 | VI 5727.05 | 3733.14 | 4225.35 | -2760.41 | 656.32 |
| 39 | 75 | SiI 5701.11 | VI 5737.07 | 4424.06 | 995.87 | -219.87 | 16.55 |
| 41 | 87 | VI 5703.59 | FeI 5705.99 | 6152.58 | 549.08 | -4380.79 | 2413.51 |
| 44 | 74 | VI 5703.59 | FeI 5731.77 | 6035.30 | 663.39 | -1671.33 | 367.88 |
| 45 | 73 | VI 5703.59 | FeI 5753.12 | 5884.85 | 1692.04 | -4416.16 | 1764.89 |
| 46 | 67 | VI 5703.59 | SiI 5753.65 | 6409.02 | -522.77 | -537.28 | 195.41 |
| 47 | 89 | VI 5703.59 | SiI 5772.15 | 6460.62 | -1085.55 | 179.41 | -1.22 |
| 48 | 75 | FeI 5705.99 | VI 5727.05 | 3822.58 | 1629.31 | -400.31 | 33.82 |
| 49 | 86 | FeI 5705.99 | VI 5737.07 | 4390.87 | 440.72 | -41.68 | 1.33 |
| 50 | 90 | MgI 5711.09 | VI 5727.05 | 1750.73 | 3865.29 | -1184.85 | 122.32 |
| 54 | 65 | VI 5727.05 | FeI 5731.77 | 6151.00 | 336.93 | -1207.43 | 313.34 |
| 55 | 65 | VI 5727.05 | FeI 5753.12 | 6021.76 | 898.15 | -2639.55 | 949.23 |
| 56 | 64 | VI 5727.05 | SiI 5753.65 | 6619.42 | -993.22 | 11.97 | 37.94 |
| 57 | 88 | VI 5727.05 | SiI 5772.15 | 6493.94 | -1000.77 | 171.07 | -6.78 |
| 58 | 91 | FeI 5731.77 | VI 5737.07 | 4187.47 | 874.82 | -144.46 | 7.99 |
| 59 | 89 | VI 5737.07 | FeI 5753.12 | 6205.50 | -1809.29 | -621.43 | 929.32 |
| 60 | 75 | VI 5737.07 | SiI 5753.65 | 6302.65 | -1900.57 | 813.35 | -129.06 |

| ratio | std | line 1 | line 2 | $c_0$ | $c_1$ | $c_2$ | $c_3$ |
|---|---|---|---|---|---|---|---|
| 64 | 63 | FeI 5852.23 | TiI 5866.45 | 2862.44 | 1680.16 | 5380.29 | -3835.08 |
| 66 | 53 | FeI 5856.09 | TiI 5866.45 | 5667.04 | -8307.49 | 20059.59 | -11372.40 |
| 67 | 94 | FeI 5862.36 | TiI 5866.45 | 3128.31 | 2843.11 | -883.86 | 90.41 |
| 68 | 66 | SiI 5948.55 | FeI 5956.70 | 3158.16 | 2110.05 | -153.28 | -88.88 |
| 69 | 92 | SiI 5948.55 | NiI 6007.31 | 2017.67 | 2509.53 | -517.22 | 35.51 |
| 70 | 88 | FeI 5983.69 | VI 6039.73 | 4171.05 | 764.58 | -108.24 | 5.23 |
| 72 | 89 | FeI 5987.05 | VI 6039.73 | 4093.37 | 753.59 | -102.35 | 4.83 |
| 75 | 86 | FeI 6007.96 | VI 6039.73 | 4213.30 | 801.07 | -122.41 | 6.50 |
| 78 | 65 | VI 6039.73 | FeI 6055.99 | 6312.44 | -2149.28 | 145.51 | 323.98 |
| 79 | 65 | VI 6039.73 | FeI 6056.01 | 6311.11 | -2133.79 | 99.70 | 353.27 |
| 80 | 70 | VI 6039.73 | FeI 6078.50 | 6328.51 | -2287.81 | -864.99 | 1350.92 |
| 81 | 67 | VI 6039.73 | NiI 6086.29 | 6485.36 | -2301.72 | 1193.10 | -304.55 |
| 82 | 60 | VI 6039.73 | FeI 6089.57 | 6561.61 | -2185.47 | 1107.17 | -372.24 |
| 83 | 63 | VI 6039.73 | FeI 6098.28 | 6789.35 | -1429.67 | 287.16 | -16.71 |
| 84 | 80 | VI 6039.73 | FeI 6102.18 | 6320.05 | -2217.56 | -1597.46 | 2228.72 |
| 86 | 84 | FeI 6055.99 | VI 6081.44 | 4293.63 | 735.90 | -101.59 | 4.63 |
| 87 | 76 | FeI 6055.99 | VI 6090.21 | 3074.97 | 2943.33 | -971.68 | 107.61 |
| 89 | 90 | FeI 6055.99 | VI 6111.65 | 4657.40 | 410.46 | -40.89 | 1.36 |
| 90 | 83 | FeI 6056.01 | VI 6081.44 | 4291.53 | 737.11 | -101.80 | 4.64 |
| 91 | 77 | FeI 6056.01 | VI 6090.21 | 3066.86 | 2953.01 | -975.36 | 108.06 |
| 93 | 90 | FeI 6056.01 | VI 6111.65 | 4656.65 | 410.77 | -40.93 | 1.36 |
| 95 | 85 | FeI 6078.50 | VI 6081.44 | 4010.17 | 849.49 | -119.80 | 5.71 |
| 96 | 80 | FeI 6078.50 | VI 6090.21 | 2328.04 | 3628.28 | -1207.11 | 137.32 |
| 98 | 83 | FeI 6078.50 | VI 6111.65 | 4518.26 | 442.06 | -44.25 | 1.51 |
| 99 | 84 | FeI 6078.50 | TiI 6126.22 | 3389.50 | 1618.83 | -346.54 | 26.25 |
| 101 | 93 | FeI 6078.50 | VI 6135.36 | 4306.61 | 527.26 | -54.36 | 1.90 |
| 102 | 95 | VI 6081.44 | NiI 6086.29 | 6503.44 | -1860.41 | 693.46 | -124.54 |
| 103 | 84 | VI 6081.44 | FeI 6089.57 | 6537.99 | -1567.43 | 399.57 | -82.37 |
| 107 | 99 | VI 6081.44 | NiI 6111.07 | 6667.95 | -2049.50 | 861.20 | -153.21 |
| 108 | 80 | VI 6081.44 | SiI 6125.03 | 6504.55 | -1549.44 | 520.84 | -62.19 |
| 109 | 82 | VI 6081.44 | FeI 6127.91 | 6497.62 | -2072.23 | 844.96 | -193.58 |
| 110 | 96 | VI 6081.44 | NiI 6130.14 | 6641.71 | -1322.00 | 320.60 | -29.08 |
| 111 | 74 | VI 6081.44 | SiI 6142.49 | 6482.59 | -1590.74 | 599.55 | -84.96 |
| 112 | 82 | VI 6081.44 | SiI 6145.02 | 6490.29 | -1805.29 | 768.02 | -122.15 |
| 113 | 69 | NiI 6086.29 | VI 6090.21 | 3181.81 | 4216.20 | -2122.91 | 380.77 |
| 114 | 79 | NiI 6086.29 | VI 6111.65 | 4555.56 | 717.86 | -121.52 | 7.18 |
| 115 | 84 | NiI 6086.29 | TiI 6126.22 | 3767.75 | 2165.20 | -732.89 | 92.56 |
| 117 | 57 | FeI 6089.57 | VI 6090.21 | 1796.06 | 8272.26 | -5482.17 | 1266.13 |
| 118 | 75 | FeI 6089.57 | VI 6111.65 | 4412.66 | 973.78 | -203.52 | 14.87 |
| 119 | 56 | FeI 6089.57 | TiI 6126.22 | 3546.35 | 2566.59 | -816.51 | 80.89 |
| 120 | 80 | FeI 6089.57 | VI 6135.36 | 4160.82 | 1181.74 | -254.48 | 18.97 |
| 122 | 85 | VI 6090.21 | FeI 6102.18 | 5782.13 | 2907.25 | -7343.66 | 3398.69 |
| 124 | 59 | VI 6090.21 | NiI 6111.07 | 7194.51 | -1580.02 | 198.05 | 20.70 |
| 125 | 52 | VI 6090.21 | SiI 6125.03 | 6850.89 | -1231.87 | 248.36 | -17.19 |
| 126 | 59 | VI 6090.21 | FeI 6127.91 | 6207.53 | 594.07 | -1952.97 | 655.31 |
| 127 | 77 | VI 6090.21 | NiI 6130.14 | 7337.94 | -1310.85 | 198.56 | -8.45 |
| 128 | 57 | VI 6090.21 | SiI 6142.49 | 6828.16 | -1301.18 | 313.41 | -29.40 |
| 129 | 52 | VI 6090.21 | SiI 6145.02 | 6768.10 | -1295.37 | 273.41 | -18.09 |
| 130 | 70 | VI 6090.21 | SiI 6155.14 | 6588.87 | -1754.46 | 157.93 | 134.53 |
| 132 | 56 | TiI 6091.18 | SiI 6125.03 | 6690.51 | -2039.99 | 760.01 | -98.89 |
| 133 | 57 | TiI 6091.18 | SiI 6142.49 | 6680.19 | -2184.20 | 986.58 | -171.45 |
| 134 | 60 | TiI 6091.18 | SiI 6145.02 | 6647.95 | -2278.64 | 1012.81 | -164.87 |
| 135 | 69 | TiI 6091.18 | SiI 6155.14 | 6536.00 | -3535.05 | 2050.48 | -317.21 |
| 136 | 58 | FeI 6098.28 | VI 6111.65 | 4305.49 | 1929.15 | -722.75 | 95.13 |
| 137 | 89 | FeI 6098.28 | TiI 6126.22 | 4165.96 | 1105.33 | 3324.08 | -2493.09 |
| 138 | 83 | FeI 6098.28 | VI 6135.36 | 4047.30 | 2284.61 | -848.08 | 105.20 |
| 140 | 84 | FeI 6102.18 | VI 6111.65 | 4510.74 | 432.30 | -42.08 | 1.39 |

| ratio | std | line 1 | line 2 | $c_0$ | $c_1$ | $c_2$ | $c_3$ |
|---|---|---|---|---|---|---|---|
| 141 | 87 | FeI 6102.18 | TiI 6126.22 | 3401.96 | 1537.51 | -310.82 | 22.06 |
| 143 | 89 | FeI 6102.18 | VI 6135.36 | 4318.85 | 502.50 | -49.56 | 1.65 |
| 144 | 84 | FeI 6105.15 | VI 6111.65 | 4344.02 | 2480.20 | -1246.48 | 223.82 |
| 146 | 81 | FeI 6105.15 | VI 6135.36 | 4142.15 | 2703.59 | -1190.02 | 159.38 |
| 151 | 64 | NiI 6111.07 | VI 6111.65 | 4532.10 | 872.62 | -179.73 | 13.41 |
| 152 | 61 | NiI 6111.07 | TiI 6126.22 | 4097.05 | 1678.04 | -358.40 | 6.53 |
| 153 | 92 | NiI 6111.07 | VI 6135.36 | 4370.54 | 982.79 | -195.78 | 13.58 |
| 154 | 62 | VI 6111.65 | SiI 6125.03 | 6311.94 | -1391.68 | 471.78 | -54.33 |
| 155 | 64 | VI 6111.65 | FeI 6127.91 | 6371.37 | -2358.61 | 1592.89 | -487.47 |
| 156 | 61 | VI 6111.65 | NiI 6130.14 | 6444.33 | -1347.38 | 424.69 | -49.66 |
| 157 | 63 | VI 6111.65 | SiI 6142.49 | 6309.60 | -1480.01 | 580.14 | -80.78 |
| 158 | 55 | VI 6111.65 | SiI 6145.02 | 6320.53 | -1718.80 | 806.34 | -135.22 |
| 159 | 60 | VI 6111.65 | SiI 6155.14 | 6295.15 | -3084.65 | 2571.62 | -807.15 |
| 160 | 66 | VI 6111.65 | FeI 6157.73 | 6316.00 | -2377.82 | 1579.68 | -592.26 |
| 161 | 82 | VI 6111.65 | FeI 6159.38 | 6531.14 | -923.32 | 170.58 | -11.98 |
| 162 | 58 | VI 6111.65 | FeI 6165.37 | 6367.28 | -2041.60 | 1088.46 | -270.55 |
| 163 | 71 | VI 6111.65 | NiI 6175.42 | 6334.45 | -2229.90 | 1446.35 | -405.24 |
| 164 | 62 | VI 6111.65 | NiI 6176.81 | 6337.87 | -2741.73 | 2217.93 | -821.53 |
| 165 | 49 | SiI 6125.03 | TiI 6126.22 | 4366.21 | 1611.03 | -502.22 | 56.72 |
| 166 | 64 | SiI 6125.03 | NiI 6128.99 | 3452.30 | 3338.67 | -1374.99 | 184.53 |
| 167 | 68 | SiI 6125.03 | VI 6135.36 | 4597.15 | 832.19 | -165.35 | 11.65 |
| 169 | 77 | SiI 6125.03 | NaI 6154.23 | 4789.24 | -1204.61 | 5412.64 | -2938.84 |
| 170 | 95 | SiI 6125.03 | NaI 6160.75 | 6213.43 | -11523.86 | 28659.88 | -17971.25 |
| 171 | 61 | TiI 6126.22 | FeI 6127.91 | 6716.18 | -2062.53 | 501.65 | -1.37 |
| 172 | 67 | TiI 6126.22 | NiI 6130.14 | 7058.67 | -1625.93 | 396.46 | -34.47 |
| 173 | 46 | TiI 6126.22 | SiI 6142.49 | 6690.16 | -1652.12 | 544.13 | -65.01 |
| 174 | 49 | TiI 6126.22 | SiI 6145.02 | 6683.80 | -1822.27 | 656.93 | -85.87 |
| 175 | 55 | TiI 6126.22 | SiI 6155.14 | 6605.17 | -3093.99 | 1869.77 | -436.02 |
| 176 | 70 | TiI 6126.22 | FeI 6157.73 | 6398.68 | -905.13 | -1348.64 | 732.82 |
| 178 | 55 | TiI 6126.22 | FeI 6165.37 | 6630.51 | -1405.85 | -219.90 | 219.33 |
| 179 | 67 | TiI 6126.22 | NiI 6175.42 | 6634.37 | -1967.49 | 594.97 | -63.72 |
| 180 | 64 | TiI 6126.22 | NiI 6176.81 | 6585.46 | -2080.90 | 337.35 | 105.37 |
| 181 | 60 | TiI 6126.22 | NiI 6186.74 | 7263.94 | -2645.08 | 1021.40 | -147.03 |
| 183 | 70 | NiI 6128.99 | SiI 6142.49 | 6338.91 | -198.62 | -744.87 | 207.42 |
| 184 | 84 | NiI 6128.99 | SiI 6145.02 | 6354.53 | -253.29 | -933.85 | 306.67 |
| 185 | 86 | NiI 6128.99 | SiI 6155.14 | 6155.73 | 912.59 | -6390.65 | 3771.88 |
| 186 | 81 | NiI 6130.14 | VI 6135.36 | 4379.06 | 1337.90 | -339.65 | 26.76 |
| 187 | 67 | VI 6135.36 | SiI 6142.49 | 6383.84 | -1731.06 | 755.16 | -121.13 |
| 188 | 64 | VI 6135.36 | SiI 6145.02 | 6389.86 | -1974.28 | 1008.34 | -191.61 |
| 189 | 81 | VI 6135.36 | SiI 6155.14 | 6348.89 | -3419.76 | 2923.22 | -985.49 |
| 190 | 90 | VI 6135.36 | FeI 6157.73 | 6314.54 | -2063.00 | 391.82 | 65.27 |
| 191 | 85 | VI 6135.36 | FeI 6159.38 | 6570.02 | -887.59 | 95.11 | 1.87 |
| 192 | 86 | VI 6135.36 | FeI 6165.37 | 6402.93 | -2028.32 | 751.95 | -115.22 |
| 193 | 73 | VI 6135.36 | NiI 6175.42 | 6404.91 | -2528.13 | 1675.67 | -515.87 |
| 194 | 79 | VI 6135.36 | NiI 6176.81 | 6371.88 | -2771.62 | 1857.47 | -660.58 |
| 195 | 84 | VI 6135.36 | NiI 6186.74 | 6547.48 | -2077.52 | 951.92 | -182.12 |
| 196 | 65 | VI 6135.36 | NiI 6204.64 | 6592.69 | -1607.78 | 494.39 | -55.91 |
| 198 | 72 | SiI 6142.49 | NaI 6154.23 | 4592.53 | -44.37 | 3339.47 | -1887.20 |
| 199 | 88 | SiI 6142.49 | NaI 6160.75 | 6074.37 | -9786.17 | 23624.87 | -14186.05 |
| 201 | 88 | SiI 6145.02 | FeI 6151.62 | 5481.57 | -4850.00 | 10136.05 | -4691.07 |
| 202 | 71 | SiI 6145.02 | NaI 6154.23 | 4480.67 | 505.59 | 1954.58 | -1068.74 |
| 206 | 75 | FeI 6151.62 | SiI 6155.14 | 8627.01 | -6789.43 | 3944.25 | -783.23 |
| 207 | 91 | NaI 6154.23 | SiI 6155.14 | 6379.82 | 23.60 | -2530.62 | 1165.35 |
| 208 | 81 | SiI 6155.14 | NaI 6160.75 | 5505.77 | -3285.43 | 4201.39 | -1218.84 |
| 211 | 59 | SiI 6155.14 | VI 6216.35 | 4240.13 | 1152.70 | -192.73 | 4.73 |
| 212 | 86 | FeI 6157.73 | VI 6216.35 | 2929.13 | 3820.32 | -1589.74 | 230.07 |
| 214 | 70 | FeI 6165.37 | VI 6216.35 | 3741.62 | 2492.09 | -397.55 | -147.42 |

| ratio | std | line 1 | line 2 | $c_0$ | $c_1$ | $c_2$ | $c_3$ |
|---|---|---|---|---|---|---|---|
| 215 | 66 | NiI 6175.42 | VI 6216.35 | 3825.95 | 2560.29 | -920.34 | 107.02 |
| 216 | 62 | NiI 6176.81 | VI 6216.35 | 3500.33 | 2739.20 | -1020.57 | 140.44 |
| 217 | 75 | NiI 6186.74 | VI 6216.35 | 4386.23 | 1024.44 | 1356.25 | -668.51 |
| 218 | 64 | NiI 6186.74 | VI 6251.82 | 4416.97 | 1396.75 | -423.30 | 45.65 |
| 219 | 72 | FeI 6188.00 | VI 6216.35 | 3553.23 | 2066.35 | 339.51 | -396.36 |
| 220 | 84 | FeI 6188.00 | VI 6251.82 | 4280.94 | 1108.25 | -241.19 | 18.03 |
| 224 | 56 | NiI 6204.64 | VI 6251.82 | 4391.23 | 1869.13 | -739.26 | 105.03 |
| 227 | 62 | FeI 6215.15 | VI 6216.35 | 2826.97 | 2738.04 | -740.68 | 67.25 |
| 228 | 74 | FeI 6215.15 | VI 6251.82 | 4285.67 | 690.31 | -93.85 | 4.37 |
| 230 | 85 | VI 6216.35 | FeI 6226.73 | 8805.03 | -3491.99 | 1046.24 | -115.13 |
| 232 | 49 | VI 6216.35 | SiI 6237.33 | 7067.14 | -2706.02 | 1185.79 | -188.29 |
| 233 | 67 | VI 6216.35 | SiI 6244.48 | 6910.79 | -1760.62 | 522.44 | -54.71 |
| 236 | 57 | NiI 6223.99 | VI 6251.82 | 4427.37 | 1512.21 | -504.36 | 60.25 |
| 237 | 67 | FeI 6226.73 | VI 6251.82 | 4224.50 | 1716.74 | -561.76 | 64.16 |
| 238 | 98 | FeI 6232.65 | VI 6251.82 | 4444.99 | 594.25 | -75.02 | 3.16 |
| 239 | 80 | SiI 6237.33 | FeI 6240.66 | 5784.57 | -4004.60 | 4746.01 | -1323.72 |
| 241 | 79 | SiI 6237.33 | VI 6251.82 | 4652.83 | 577.31 | -83.43 | 4.16 |
| 244 | 60 | SiI 6237.33 | TiI 6258.11 | 5234.95 | -2260.85 | 3605.92 | -1150.10 |
| 245 | 59 | SiI 6237.33 | TiI 6261.11 | 4703.68 | -100.87 | 1375.47 | -488.66 |
| 249 | 83 | SiI 6244.48 | VI 6251.82 | 4716.94 | 676.72 | -117.71 | 6.99 |
| 252 | 88 | SiI 6244.48 | TiI 6258.11 | 5003.67 | -1820.76 | 4698.58 | -2025.39 |
| 253 | 63 | SiI 6244.48 | TiI 6261.11 | 4633.20 | 356.28 | 1646.00 | -816.49 |
| 255 | 95 | FeI 6246.32 | VI 6251.82 | 4378.48 | 440.32 | -39.23 | 1.17 |
| 256 | 71 | VI 6251.82 | FeI 6271.29 | 6383.44 | -715.40 | -106.41 | 55.41 |
| 257 | 64 | VI 6251.82 | MgI 6318.72 | 6352.97 | -1291.30 | 191.10 | 24.57 |
| 260 | 75 | TiI 6261.11 | FeI 6330.86 | 9186.18 | -3487.31 | 933.99 | -84.83 |
| 262 | 96 | MgI 6318.72 | CrI 6330.13 | 2964.81 | 3400.01 | -1143.57 | 109.63 |
| 264 | 47 | CrI 6330.13 | FeI 6330.86 | 6633.91 | -656.44 | -534.35 | 185.91 |
| 265 | 80 | CrI 6330.13 | FeI 6380.75 | 6037.16 | 1172.08 | -3537.36 | 1484.66 |
| 266 | 67 | FeI 6392.55 | SiI 6414.99 | 6480.93 | -1660.87 | -556.96 | 525.34 |
| 274 | 75 | FeI 6703.58 | SiI 6721.85 | 7317.80 | -2006.40 | 66.05 | 126.73 |
| 275 | 65 | FeI 6710.33 | SiI 6721.85 | 6467.06 | -1713.33 | 129.43 | 114.98 |

# Chapter 6

# Joint modelling of transit and stellar temperature using a Markov Chain Monte Carlo approach

When searching for small differences between the transit parameters of different light-curve de-trending approaches, we noted the presence of strong correlations between parameters. These were to some extent accounted for by using a residual permutation algorithm to estimate the uncertainties in the transit parameters. However, a more robust method to explore these correlations was desirable.

Additionally, as pointed out by many authors (e.g Seager & Mallén-Ornelas 2003), the detailed shape of the observed transit depends on the stellar density as well as the planet's parameters. This means that if we have any external (or prior) constraints on the stellar density, we should incorporate them in the transit fitting process, in a Bayesian manner. The spectroscopic measurement of the stellar temperature, discussed in Chapter 5, constitutes such a prior constraint. The stellar temperature is directly, although not uniquely, linked to the stellar density as stellar evolution models predict a particular temperature and density for stars of a given mass, age and composition.

The Markov Chain Monte Carlo (MCMC) technique uses a random walk approach to explore a parameter space of arbitrary dimensionality. The MCMC is well suited to the problem of modelling planetary transits, because a) it avoids getting trapped in local minima in the figure of merit space; b) it enables prior information to be incorporated in the figure of merit seamlessly and c) in the process of exploring the parameter space to find the best fit, it also samples the posterior distribution for each parameter, and thus yields robust uncertainty estimates.

In this chapter, I implement a Metropolis-Hastings MCMC algorithm for transit fitting, with specific Bayesian priors on stellar properties. The transits are modelled using the formalism of Mandel & Agol (2002), but care was taken to re-formulate the MCMC

such that the jump parameters (the parameters over which the MCMC random walk occurs) are parameters for which it is reasonable to assume a flat prior distribution. Our formalism, which is derived from that briefly described in Pont et al. (2009), can also optionally incorporate an external constraint on a particular stellar parameter, in the present case the effective stellar temperature, which is implemented as an additional term in the MCMC merit function. The conversion between stellar temperature and density is done using the theoretical stellar evolution models of Girardi et al. (2002).

The MCMC formalism is described in Section 6.1 and applied to the case of CoRoT-2b in Section 6.2. The results are discussed, along with possibilities for future work in this direction, in Section 6.2.3.

## 6.1 Markov Chain Monte Carlo

A Markov chain is a succession of states where the next state depends only on the current state. The term "Monte Carlo" means that the transition between states is randomly determined based on a probabilistic distribution. The strength of the Markov Chain Monte Carlo method (MCMC) is in the way it samples the grid of parameters, and in the fact that it can identify the global best fit model in the parameters space, rather than a locally best fit model. In the chain, when the current model is worse that the precedent one, instead of systematically disregarding it, the MCMC uses a probabilistic approach to invalidate or validate this step, with lower probability for poorer models. This property gives the MCMC the capability of exploring areas of the parameter space that would not have been explored otherwise. For instance, in a standard $\chi^2$ minimisation technique, only the parameters improving the fit are considered, which means that the convergence algorithm can get stuck in a local minimum and never explore the rest of the parameter space to find the global minimum, especially if only one set of initial conditions are used. Another key advantage of the MCMC is that it enables the posterior probability distributions of the parameters to be estimated.

### 6.1.1 MCMC implementation

There are different types of Markov Chain Monte Carlo methods, which differ in their random walk nature. The one used in this chapter is a Metropolis-Hastings algorithm which generates a random walk from a proposal distribution of the next step (here, flat or Gaussian probability distributions are used as explained in Section 6.1.3) and proscribes a method to reject the proposed move if the new model is worse than the previous one (here, a function of how much worse the new model is compared to the previous one, is used).

The input to the MCMC are a) the data to be modelled (here, the IRF-filtered planet transit light curve), b) the model to be compared to the data (here, the transit formula-

tion of Mandel & Agol 2002), c) the initial values (which model the data sufficiently well to start the chain), d) the scale sizes (the typical step size in each parameter), and e) the constraints on the model (here, a Gaussian prior distribution on the stellar temperature). The output of the MCMC are the posterior probability distribution of the values of each adjusted parameter. These distributions are used to derive the $1\sigma$ uncertainty ranges on the parameters, as explained in Section 6.1.7.

The steps of the MCMC used in this chapter are as follow. The flow chart of this MCMC is presented in Figure 6.1.

1. Compute the model for the initial values set.
2. Calculate the merit function of this model. The merit function used here is the likelihood $L = e^{-\frac{\chi^2}{2}}$ where $\chi^2 = \frac{\sum(\mathrm{data}-\mathrm{model})^2}{\mathrm{DOF}}$ with the number of degree of freedom ($\mathrm{DOF}$ ) being the difference between the number of data points and the number of adjusted parameters.
3. Select a new set of parameters by making a random step in each parameter. The size of the step in each parameter is drawn from a Gaussian distribution cantered at 0 with standard deviation equal to scale size inputed for this parameter (see section 6.1.4). The scale sizes of the steps need to be large enough to allow a wide exploration of the parameter space, and small enough to keep a reasonable number of accepted steps, steps which are used to build a statistically robust posterior distribution.
4. Compute the model associated to this new set of parameters and calculate its figure of merit (likelihood as explained in step 2).
5. Compute the ratio of the figure of merit of the new set of parameters and the current ones.
   (a) If the ratio is greater than 1, the likelihood of the model has improved and the step is validated by storing the new values of the parameters and the likelihood.
   (b) If the ratio is smaller than 1, the likelihood of the model has worsened and a random number is drawn from a uniform distribution between 0 and 1.
      i. If the value of the ratio is greater than the randomly pulled value, the step is validated by storing the new values of the parameters and the likelihood. The closer to 1 the value of the ratio is, the higher the probability of the new step to be kept, as there are more values between 0 and 1 smaller than the value of the ratio.
      ii. If the value of the ratio is smaller than this number, the new step and likelihood are disregarded and the current parameters are re-stored.

6. Go back to step 3, and iterate N times. The number of iterations used in this chapter is 500000.

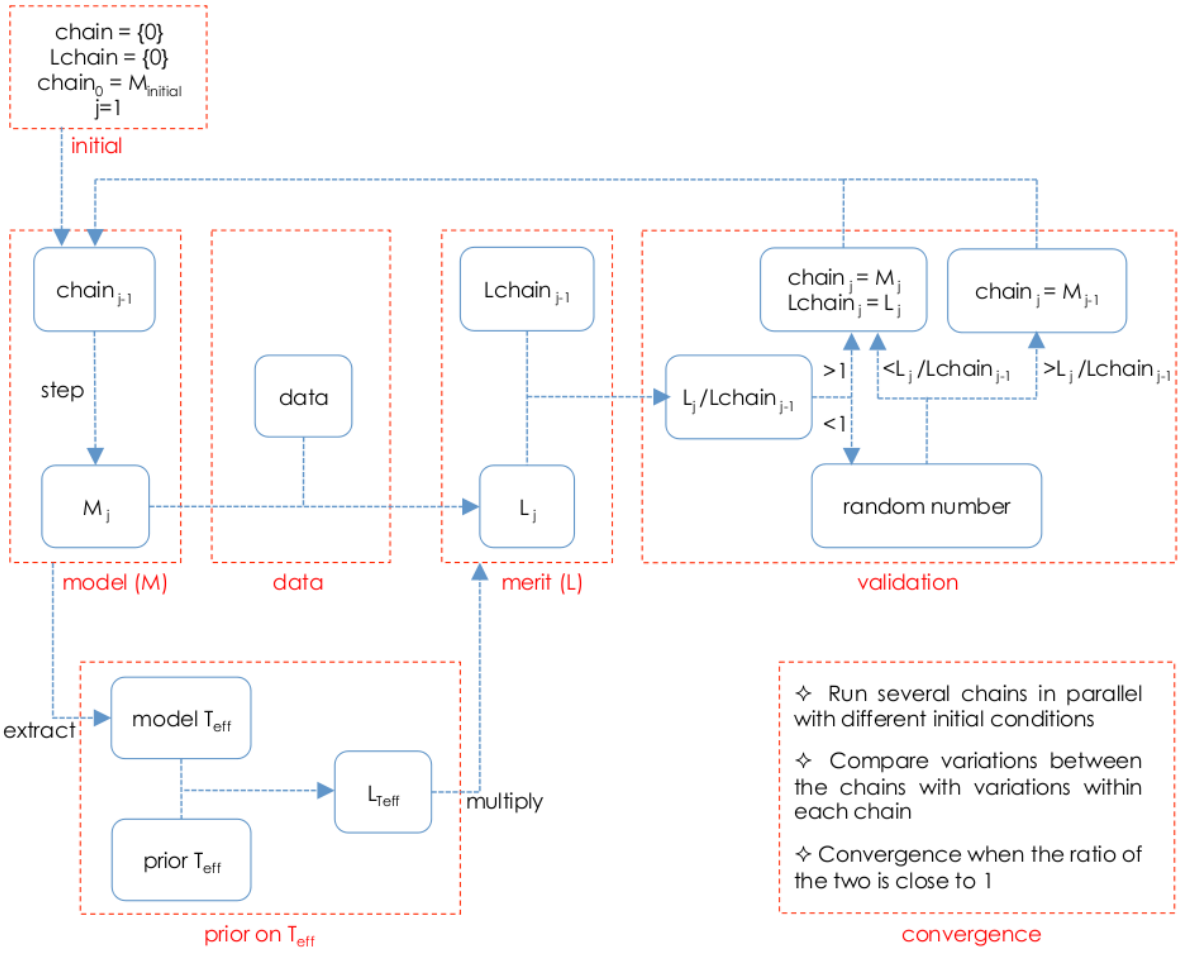


Figure 6.1: MCMC flow chart

### 6.1.2 Jump parameters

When using the MCMC chain to construct posterior probability distributions for the parameters of the model, a flat prior for the jump parameters are implicitly assumed. Another prior can be applied by multiplying the distributions with the relevant prior distribution, but it is easier and more robust to formulate the model in terms of parameters for which a flat prior is a reasonable assumption.

The input parameters of the Mandel & Agol (2002) formalism is the projected separation between the stellar and planetary disk centres $z$, in units of stellar radii, the planet-to-star radius ratio $R_{\rm p}/R_\star$, and the linear and quadratic limb-darkening coefficients $u_a$ and $u_b$. Kepler's laws of planetary motion yield $z$ as a function of time for a given period $P$, orbital inclination $i$ relative to the plane of the sky, system scale $a/R_\star$, eccentricity $e$, longitude of periastron $w$, and time of passage at periastron $T_0$.

Random inclinations in three dimensions give rise to a flat distribution in $\cos i$ rather than in $i$. We therefore use the impact parameter $b \equiv \frac{a}{R_\star} \cos i$ as one of the jump parameters. At each step of the MCMC, $b$ is converted to an inclination using:

$$i = \arccos\left( b \left[\frac{a}{R_\star}\right]^{-1} \right) \tag{6.1}$$

Whilst the radial velocity signal of a planet is exclusively sensitive to $e \sin w$, the light curve can (if a secondary eclipse occurs) constrain $e \cos w$. The jump parameters adopted in the most general implementation of the MCMC formalism used here are $e \cos w$ and $e \sin w$, rather than $e$ and $w$, though in any case, we do not deal with radial velocity data or with eccentric orbits in the present thesis.

As the stellar density is directly constrained by the transit, it is a natural choice of jump parameters (instead of the system scale). However, in a random population of stars in the Galactic disk, there is no reason to expect a uniform density distribution (most stars would be found on the low-mass end of the main sequence). To take this into account, we use a grid of stellar evolutionary models (Girardi et al., 2002) interpolated by Aparicio & Gallart (2004) and resampled by Pont & Eyer (2004), with the density of models proportional to the number of stars expected at a given mass and evolutionary stage, assuming the initial mass function (IMF) derived for the Galaxy, and a uniform age distribution.

This resampled grid, kindly supplied by F. Pont (private communication) was sorted in density, and sorted in a file which we refer to as Padova2002 in the rest of this chapter. We use $k$, the index in the grid of models contained in the file Padova2002, as one of the jump parameters of the MCMC. To each $k$ corresponds a particular star mass, luminosity and temperature. We use the luminosity and temperature to calculate a stellar radius, and obtain a system scale as follows:

$$\frac{a}{R_\star} = \left[\frac{P^2 G}{4\pi^2}\right]^{1/3} \frac{M_\star^{1/3}}{R_\star} \tag{6.2}$$

The stellar temperature in Padova2002 span from 2300 to 26800 K, the stellar masses span from 0.668 to 10.716 $M_\odot$, and the stellar radii from 0.628 to 455.361 $R_\odot$.

### 6.1.3 Incorporating external constraints

A gaussian prior is associated to the effective temperature of the star $T_{\rm eff}$which can be derived from the spectroscopic analysis of its atmosphere. The transit model gives an estimate of the density of the star, from which using stellar evolution tracks, an associated stellar temperature can be derived. These two temperatures can be compared in the MCMC with a likelihood function which favours transit models with an associated temperature close to the effective temperature. This prior on the stellar temperature is included in the MCMC evaluation of best transit model by calculating the likelihood

$L = e^{-\frac{\chi^2}{2}}$ of the stellar temperature associated to each transit model compared to the spectroscopic temperature – where $\chi^2$ measures the difference between the two temperatures –, and by multiplying the likelihood in step 2 of the MCMC by the likelihood on the temperature.

### 6.1.4 Step size

The size of the step in each parameter needs to be chosen so that in each parameter chain it takes the MCMC several steps to reach the extremes of the explored values. This gives confidence in the accuracy and coverage of the MCMC exploration, as small steps mean good sampling. However, if the steps are too small, it will take the MCMC a larger number of iterations to explore the same region of the parameter space. The method used to find the optimal scale size for each parameter is as follows:

1. Run a short chain (e.g. 1000 iterations) with initial step sizes equal to the uncertainty on the initial parameters
2. Calculate the standard deviation of the chain for each parameter and the number of accepted steps
3. Adjust the step size of each parameter so that it is smaller or of the same order as the standard deviation of the short chain for this parameter, and so that the number of accepted steps is close to 50%.

### 6.1.5 Chain length

The number of steps in the MCMC chain needs to be several times the correlation length of each parameter chain. There are two methods to test if the chain is long enough: 1) calculate the correlation length as explained below and compare to the length of the chain, or 2) calculate the Gelman & Rubin statistic of convergence as explained in Section 6.1.6.

A chain length several times the parameter correlation length means that the chain has explored the structure of the parameter space several times. There is thus less chance for the convergence to get stuck in a local minimum and the best model solution is thus more robust. The method used to check if the number of MCMC iterations used allows to derive statistically robust parameters is as follows:

1. Calculate the autocorrelation of the chain: $A_j(\theta) = \sum_i \theta_i \times \theta_{i+j}$ for each parameter $\theta$. The autocorrelation length is given by the number of iterations needed to bring the autocorrelation from maximum to zero
2. The length of the chain should be several times (e.g. $>$10) the value of the autocorrelation length. The longer the chain the more robust the solution found for the best model.

When the MCMC has done a sufficient number of iterations, it will have sampled the posterior distributions of each parameter evenly, so that the distributions of the values of each parameter along the chain should be relatively smooth, and representative of the true underlying distributions. But running more iterations requires more computing time. For instance, running 100000 MCMC steps with four free parameters, on a 150-day-long and 516s-sampling light curve (CoRoT long run) takes close to 48h on an intel MAC pro (pre 2008 model) with 32Gb of RAM and 4 processor cores of 2.66GHz each. Here are two approaches used in this work to reduce the computing time:

1. The MCMC can be sped up by reducing the number of data points: 1) by binning the light curve, and 2) by using only the light curve around the transits. In the case of the transit light curve of CoRoT-2b studied here, the number of points was reduced from $\sim$19000 to $\sim$1200, by binning each 8 points in the phase folded light curve and by keeping only the points within 0.2 phase units of the transits. This speeds up the MCMC by a factor 10.

2. To increase the number of iterations with limited computing time, several independent chains can be run simultaneously. Each chain has a different starting point, and needs to be longer than the burn-in phase. The burn-in phase of a chain is the number of steps the chain takes before converging on the area of the true parameter and starts exploring the uncertainty area of this parameter. In this chapter, after visual check of the chains, the burn-in phase is taken as 7000 steps. A longer burn-in phase made little difference in the posterior distributions while shortening the valid length of the chain. The chains can then be combined together to obtain distributions with a larger number of iterations, i.e more statistically robust distributions with shapes that will not evolve with more iterations.

### 6.1.6 Gelman & Rubin diagnostic for convergence

To get a long chain, another option is to combine independent chains which have different starting points but same statistics, i.e. which have converge to their common distribution.

The Gelman & Rubin statistic test of convergence (Gelman & Rubin, 1992; Brooks & Gelman, 1997) checks if independent chains of the same length have converged to the same probability distribution, i.e. have similar statistics. It does so by comparing the variance between several chains $B$ (Equation 6.5) with separate starting points and the variance within each chain $W$ (Equation 6.6). If all the chains are sampling the same distribution and doing it in a complete way, these variances should be the same, i.e $S$=1 for $S$ defined in Equation 6.3.

When the chains have converged, the statistic $S$ (equation 6.3) is equal to 1, as the variations between the chains ($V$, equation 6.4) should be of the same order as the variations within the chains ($W$, equation 6.6). The independent chains can then

be combined together to form a longer chain with a more statistically robust posterior distribution. In this chapter, all chains are started within one scale size of the initial value.

For each parameter, the statistic $S$ comparing several chains (m chains or n iterations each after cutting away the burn-in phase) can be calculated with:

$$S = \sqrt{\frac{V}{W}} \tag{6.3}$$

where $V$ is calculated as:

$$V = \left(1 - \frac{1}{n}\right) W + \frac{1}{n} B \tag{6.4}$$

with $B$, the variance between the chains, calculates as:

$$B = \frac{n}{m-1} \sum_{j=1}^{m} (\bar{C}_j - \bar{C})^2 \tag{6.5}$$

where $\bar{C}_j$ is the mean of the $j^{th}$ chain, and $\bar{C}$ is the mean of all the chains.
$W$, the sum of the variance of each chain, is calculated as:

$$W = \frac{1}{m(1-n)} \sum_{j=1}^{m} \sum_{l=1}^{n} (C_{j,l} - \bar{C}_j)^2 \tag{6.6}$$

where $C_{j,l}$ is the parameter value of the $l^{th}$ step of the $j^{th}$ chain.

The MCMC runs are presented by a group of three chains, to evaluate the convergence of the individual chains, before combining them into a longer one. Usually, groups of five chains are run and compared to each other to check their convergence. Here, three chains were used to start with. Future work will include running the MCMC on more individual chains.

### 6.1.7 Posterior distributions

Once the chain has converged, the shape of the posterior distribution is statistically robust and will not change significantly with more iterations. This distribution is a good representation of the true posterior distributions of the parameter. The best model parameters and associated uncertainties can be derived from it as follows. The best model is taken as the one with the largest likelihood, i.e. the minimum $\chi^2$ to the data. The uncertainty on the best model value is defined by the $1\sigma$ spread of the posterior distribution, which is calculated as the range in value enclosing the 68% of the chain around the median, i.e. 34% each side of the median value of the chain.

The set of parameters with the largest occurrence in the posterior distributions can be slightly different from the parameter set with the largest likelihood, but should be

consistent within the $1\sigma$ spread of the distribution. If this is not the case, it is an indication that the length of the chain is not long enough.

The choice of the "best" value depends on what the value is going to be used for. The "best-fit" set of parameters maximises the figure of merit. It is an appropriate choice for the "best" value when creating a transit model to compare to data of the same nature, or when comparing between different data analysis techniques such as in Table 6.3. The most probable value of the chain maximises the posterior probability distribution. This value is a better estimate of the true physical value of that parameter, which is true despite the fact that the model generated from the median or most probable values of each parameter may not have a high merit function. The median or most probable values should be used, for example, when making comparisons with theory. Usually, the median is used rather than the most probable value because the median is a better single-number representation of a distribution (e.g. the case of a distribution with two peaks).

### 6.1.8 Limitations

The main limitation of the MCMC method is that it requires a lot of computing time to derive chains which have convergence, especially if the number of data point is large. However, it is still faster than a systematic exploration of the same parameter space at similar resolution using a regular grid.

The computing time of the MCMC can be reduced by decreasing the number of data points. One way of reducing the number of data points in a light curve is by binning the points. However, too much binning reduces the resolution of the light curve in the ingress and egress of the transit, which translates into a lower precision on the derived planet parameters.

In this chapter, the chain is left to start not far from the parameter values in the discovery paper. The advantage of this choice is that the burn-in phase of the chain is shorter (fewer iterations) and the valid part of the chain longer. The drawback is that if the region around the initial value is a local minimum and if the MCMC steps are too small, the MCMC will spend a lot of time in this area before exploring other regions of the parameter space. If the step size is too large, more iterations will be rejected on the basis of being worse than the previous steps, and the chain will need to be longer to count sufficient accepted steps and build statistically robust posterior distributions.

An MCMC is also only as good as the priors assumed in it. It is a caveat that should be kept in mind when comparing the method to other fitting techniques.

Another limit to the current MCMC is the sampling of the stellar evolution model that it uses. The accuracy and precision of the derived parameters can only be as good as the finest mesh of the grid of models.

## 6.2 Application to CoRoT-2b

### 6.2.1 Method

The IRF-filtered light curve of CoRoT-2 is corrected for the 5.6% contaminant flux due to a star falling into the CoRoT mask of CoRoT-2. This is done by subtracting 0.056 to the normalised IRF-filtered light curve and re-normalising the resulting light curve.

The MCMC is applied to fit the transit of CoRoT-2b in the IRF-filtered CoRoT light curve of CoRoT-2. The IRF-filtered light curve used is filtered with a time scale for stellar variability of 0.25 days, as this version has less residual stellar variability than the 0.5 day version while the transit shape is still well recovered (Chapter 3 Section 3.2.3). To speed up the MCMC and allow us to run a larger number of iterations, the number of data points are reduced by binning the phase folded filtered light curve with bin size of 0.0006 phase units (0.06% of the planet's orbit), and keeping only the section within $\pm$0.2 phase units of the transit centre. The uncertainty associated to each bin is taken as the standard deviation of the points binned together in this bin. In the MCMC, the uncertainty associated to the data set is taken as the maximum of these uncertainties. The data points were re-normalised by fitting a $2^{nd}$ order polynomial function about the transit and the data points were divided by this fit.

The MCMC is run varying the time of transit $T_0$, the impact parameter $b$, the planet-to-star radius ratio $R_{\rm p}/R_\star$, and $k$ the line index of stellar density in Padova2002. $P$, $e$ and $w$ are fixed to the value in Alonso et al. (2008). The limb darkening coefficients are fixed to the quadratic limb darkening coefficients corresponding to the CoRoT bandpass, derived from Sing (2010). The adjusted parameters are then translated into $T_0$ ($T_{0p}+cst$) the epoch of the transit centre, $a/R_\star$ and $i$.

When the MCMC is run with the prior on the $T_{\rm eff}$ the stellar atmosphere parameters of CoRoT-2 are $T_{\rm eff}$=5516$\pm$33 K, $\log g$=4.3$\pm$0.2, (M/H)=0.0$\pm$0.1. The value of $T_{\rm eff}$, used here, is the one derived using the equivalent width ratios, the other parameters have not been re-calculated and are kept the same as in the discovery paper. The associated quadratic limb darkening coefficients in the CoRoT bandpass are $u_a$=0.478$\pm$0.010 and $u_b$= 0.205$\pm$0.007. These are the coefficient used in all the fitting procedures below , including the LMA, to allow a direct comparison of the derived parameters.

First, no prior on the stellar temperature is applied, then a gaussian prior on the $T_{\rm eff}$ is added later. The stellar temperature used as prior is the temperature derived for CoRoT-2 in Chapter 5 using the temperature calibrated equivalent width line ratios: $T_{\rm eff}$=5516$\pm$33 K.

The scale stepe sizes chosen when no prior on the $T_{\rm eff}$ was applied, is $2\ 10^{-5}$ for $T_0$, $4\ 10^{-3}$ for $b$, $2\ 10^{-4}$ for $R_{\rm p}/R_\star$, and 1000 for $k$. The scales were obtained by trial and errors starting from scale sizes equal to the uncertainty on the initial values and reducing the scale size until the number of accepted steps was close to 50% when no prior on the $T_{\rm eff}$ was used, and close to 30% when a prior on the $T_{\rm eff}$ was applied. When the prior

on the $T_{\rm eff}$ is used, the number of accepted steps decreases due to the additional constraint on the $T_{\rm eff}$. If less steps are accepted, a longer chain is needed to keep the statistic of the posterior distributions robust. To avoid having to run longer chains, two adjustments are made to increase the number of accepted steps when a prior on the $T_{\rm eff}$ is applied. First, prior to running the chain, the stellar evolution model file was re-arranged to keep only the models with a $T_{\rm eff}$ at the prior temperature plus or minus 4$\times$ the uncertainty on this prior, so that when stepping in $k$ the $T_{\rm eff}$ of more models will be compatible with the prior on the $T_{\rm eff}$. Secondly, the scale size in $k$ was reduced to 100.

The planetary parameters ($T_0$, $R_{\rm p}/R_\star$, $b$) from Alonso et al. (2008) were first used as initial values to run the MCMC. The MCMC translates $k$ into $a/R_\star$ using stellar evolution models, and $b$ and $a/R_\star$ into $i$. As the sampling of the grid in the stellar evolution models is finite, the derived $a/R_\star$ and $i$ do not correspond exactly to the values in the discovery paper, and the transit model derived from these value is too different from the data (large $\chi^2$) to allow the MCMC to start. The initial parameters used are $T_0$ from the discovery paper, $b$=0.05, $R_{\rm p}/R_\star$=0.16, and $k$=509965 (no prior on $T_{\rm eff}$) or $k$=81492 (prior on $T_{\rm eff}$). $k$=509965 correspond to $T_{\rm eff}$=5521 K, $M_\star$=0.888 $M_\odot$, $R_\star$=0.881 $R_\odot$ in the full stellar evolution model file used. $k$ = 81492 corresponds to the same model in the file re-arranged to increase the number of accepted steps when using a prior on the $T_{\rm eff}$. $T_{\rm eff}$=5521 K is the closest to $T_{\rm eff}$=5516$\pm$33 K in our list of stellar evolution models. $M_\star$=0.888 $M_\odot$ and $R_\star$=0.881 $R_\odot$ are the closest to $R_\star$=(0.88$\pm$0.03)$R_\odot$ and $M_\star$=(0.89$\pm$0.09)$M_\odot$ corresponding to $T_{\rm eff}$=5516$\pm$33 K. The corresponding $R_\star$ is calculated using $L_\star = 4\pi\sigma R_\star^2 T_{\rm eff}^4$. $L_\star$ calculated using the values in Alonso et al. (2008): $R_\star$=(0.90$\pm$0.02)$R_\odot$ and $T_{\rm eff}$=5625$\pm$120 K . The corresponding $M_\star$ is derived from the range of models in Padova2002 corresponding to the range in $T_{\rm eff}$ and $R_\star$.

Three chains of 500000 iterations each are run simultaneously with different starting points, all starting points being within a scale size from the initial value. The first 7000 steps of each chain are cut away, as considered part of the burn-in phase. A visual check of the chains, showed that it takes that many steps for a chain to fall within the 1$\sigma$ range of the total chain. These chains are then compared to each other using Gelman and Rubin's statistic (described in section 6.1.6) to check their convergence. If the convergence criteria is reached, the three chains are combined together (put one after the other) to form a longer chain, statistically more robust. The distribution of the values stored in the MCMC chain for each parameter is plotted, and used to derive the 1$\sigma$ uncertainty range of each parameter as described in Section 6.1.7.

### 6.2.2 Results

#### Without a prior on the stellar temperature

Three 500000-step MCMC chains are run on the binned and truncated IRF-filtered transit light curve of CoRoT-2b. The resulting chains (Figure 6.3) have 56 to 57% of the steps accepted which shows that the scale sizes allowed the MCMC to explore the surrounding parameter space while keeping a large number of steps around the best model. The transition between value extrema in each parameter chain is checked to be done in several steps, which confirms that the scale size in each parameter is not too large.

The 7000 steps of the burn-in phase are cut away in each chain. The resulting three chains have similar position of maximum and $1\sigma$ range in their posterior distributions, and the best fit model of each chain are consistent with each other within the uncertainty range of their posterior distributions. The correlation length of each parameter chain is several times smaller than the length of the chain, i.e. the correlated features of the parameter space were explored several times. The Gelman & Rubin's convergence statistic run on the three 500000-step chains returns $S_{T_0}$ = 1.02, $S_{R_p/R_\star}$ = 1.40, $S_k$ = 1.47, and $S_b$ = 1.87. These numbers show that the 500000-step chain has not fully converged in $R_{\rm p}/R_\star$, $k$ and $b$, although the correlation length of the chain was several times smaller than the total length of the chain. Gelman & Rubin's convergence statistic is a more robust test for chain convergence than the correlation length of a chain. In future work, longer chains will be run to ensure that the individual chains have fully converged in all the parameters. An alternative to lengthening the chains will be to increase the scale sizes. This allows the chain to explore more of the parameter space, but at the detriment of the number of accepted steps. Chains with slightly larger scale sizes than the ones giving the optimal number of accepted steps, have shown to have $S$ values closer to 1, i.e. to converge faster.

The three chains are combined together to increase the statistical robustness and the precision of the posterior distributions. The posterior distributions of the combined chain are plotted in Figure 6.2. The planetary parameters derived from the model with the highest likelihood, and the associated $1\sigma$ range derived from the posterior distributions are shown in Table 6.1.

Using equation 6.2 and the posterior distribution of $k$ translated into $M_\star$ and $R_\star$ the posterior distribution of $a/R_\star$ can also be derived. In addition, using equation 6.1, the posterior distribution of $b$ and the posterior distribution of $a/R_\star$, the posterior distribution of $i$ can also be derived. The posterior distribution of $a/R_\star$ and $i$ are shown in Figure 6.4, along with the posterior distribution in $T_{\rm eff}$, $M_\star$ and $R_\star$ derived from $k$. The best model value and the $1\sigma$ uncertainty range are shown in Table 6.1.

$k$, $b$ and $R_{\rm p}/R_\star$ show a strong correlation with each other, which is expected as they are all dependent on the stellar radius $R_\star$.

Table 6.1: Table of parameters for CoRoT-2b derived from the posterior distribution of the MCMC with no prior on the stellar temperature. The table presents the model with the highest likelihood (best-fit), and the median value (median) and $1\sigma$ uncertainty range ($1\sigma$ range) of each distribution of parameters.

| | Best-fit | Median | $1\sigma$ range |
|---|---|---|---|
| $P$ (d) | <—— 1.7429964 $\pm$ 0.0000017 (fix) ——> | | |
| $T_0$-2454237 (d) | 0.53518 | 0.53518 | (0.53511 - 0.53524) |
| $R_{\rm p}/R_\star$ | 0.1618 | 0.1615 | (0.1608 - 0.1623) |
| $b$ | 0.25 | 0.22 | (0.18 - 0.29) |
| $a/R_\star$ | 6.56 | 6.60 | (6.48 - 6.72) |
| $i$ (°) | 87.9 | 88.1 | (87.5 - 89.0) |
| $u_a$ | <———— 0.478 $\pm$ 0.010 (fix) ————> | | |
| $u_b$ | <———— 0.205 $\pm$ 0.007 (fix) ————> | | |
| $e$ | <———————— 0 (fix) ————————> | | |

### With a prior on the stellar temperature

Three chains of 500000 steps each are run, with the prior on the temperature equal to 5516$\pm$33 K, and a smaller scale size in $k$ as mentioned previously. The chains are presented in Figure 6.5. The number of accepted steps was between 29 and 31%. This is smaller than in the case with no prior on $T_{\rm eff}$ despite the reduced scale sizes. With the new constraint on the temperature, the MCMC disregards the models which have a $T_{\rm eff}$ incompatible with the prior on the $T_{\rm eff}$, while these models were kept in the chains without a prior on the $T_{\rm eff}$.

The first 7000 steps of each chains are part of the burn-in phase and cut away. The Gelman & Rubin's convergence statistic is applied and returned $S_{T0}$ = 1.02, $S_b$ = 1.87, $S_{R_p/R_\star}$ = 1.40, and $S_k$ = 1.47. These numbers show that the 500000-step chains have not fully converged in $b$, $R_{\rm p}/R_\star$, and $k$, and that longer chains still need to be run to ensure the statistical robustness of the posterior distributions.

The three chains are combined together. The planet parameters are derived from the model with the highest likelihood and the $1\sigma$ uncertainty range from the posterior distributions (Figure 6.6); the values are shown in Table 6.2. The model with the highest likelihood is for a $k$ corresponding to $T_{\rm eff}$=5521 K, $M_\star$=0.947 $M_\odot$, $R_\star$=0.912 $R_\odot$. The median of the $k$ corresponds to $T_{\rm eff}$=5495 K, $M_\star$=0.952 $M_\odot$, $R_\star$=0.910 $R_\odot$.

The posterior distributions of $T_{\rm eff}$, $M_\star$, $R_\star$, $a/R_\star$ and $i$ are shown in Figure 6.7. The distribution in $a/R_\star$ is calculated from $M_\star$ and $R_\star$ extracted from the distribution in $k$. The posterior distribution of the inclination is derived from the posterior distributions of $b$ and $a/R_\star$; the values are shown in Table 6.2.

The MCMC coverage in the 2-D parameter spaces is plotted in Figure 6.6. The correlation between $k$, $b$ and $R_{\rm p}/R_\star$ is present and a range in $R_\star$ values is covered under the uncertainty range of the prior on $T_{\rm eff}$. The posterior distribution of $T_{\rm eff}$ reproduces the prior distribution of $T_{\rm eff}$. This is as expected given that the prior distribution on the $T_{\rm eff}$ is applied as a constraint to select the models with compatible $T_{\rm eff}$. The current distribution in $k$ has two peaks (at 75000 and 85000), corresponding $T_{\rm eff}$ of 5407 and 5470 K, $R_\star$

of 0.897 and 0.884 $R_\odot$, and $M_\star$ of 0.895 and 0.922 $M_\odot$respectively. The stellar density associated to these two peaks is different ($M_\star/R_\star^3 \sim$ 1.240 and 1.336 $M_\odot/R_\odot^3$), which translated into a double peak distribution in $a/R_\star$ peaking at $\sim$ 6.55 and 6.75. The first peak ($a/R_\star$=6.55) is the same as the peak of the probability distribution of $a/R_\star$ in the MCMC run with no prior on the $T_{\rm eff}$ (Figure 6.4). The second peak is therefore added by the prior in $T_{\rm eff}$. This indicates that the current prior on $T_{\rm eff}$ is different from the $T_{\rm eff}$ that would naturally be derived from models of the transit with no prior constraint on the stellar temperature.

A longer chain should be run to check the statistical robustness of this double peak probability distribution in $k$, or if one of the peaks will dominate the distribution. Additionally, another chain should be run with a different prior on the $T_{\rm eff}$ to investigate the relative position of the peaks with different priors on the stellar temperature.

Table 6.2: Table of parameters for CoRoT-2b derived from the posterior distribution of the MCMC with a prior on $T_{\rm eff}$ of 5516$\pm$33 K. The table presents the model with the highest likelihood (best-fit), the median value and the 1$\sigma$ uncertainty range of each distribution of parameters.).

| | Best-fit | Median | 1$\sigma$ range |
|---|---|---|---|
| $P$ (d) | <—— 1.7429964 $\pm$ 0.0000017 (fix) ——> | | |
| $T_0$-2454237 (d) | 0.53518 | 0.53518 | (0.53511 - 0.53524) |
| $R_{\rm p}/R_\star$ | 0.1618 | 0.1616 | (0.1607 - 0.1624) |
| $b$ | 0.24 | 0.23 | (0.10 - 0.29) |
| $a/R_\star$ | 6.57 | 6.59 | (6.48 - 6.74) |
| $i$ (°) | 87.9 | 88.0 | (87.4 - 89.1) |
| $u_a$ | <———— 0.478 $\pm$ 0.010 (fix) ————> | | |
| $u_b$ | <———— 0.205 $\pm$ 0.007 (fix) ————> | | |
| $e$ | <———————— 0 (fix) ————————> | | |

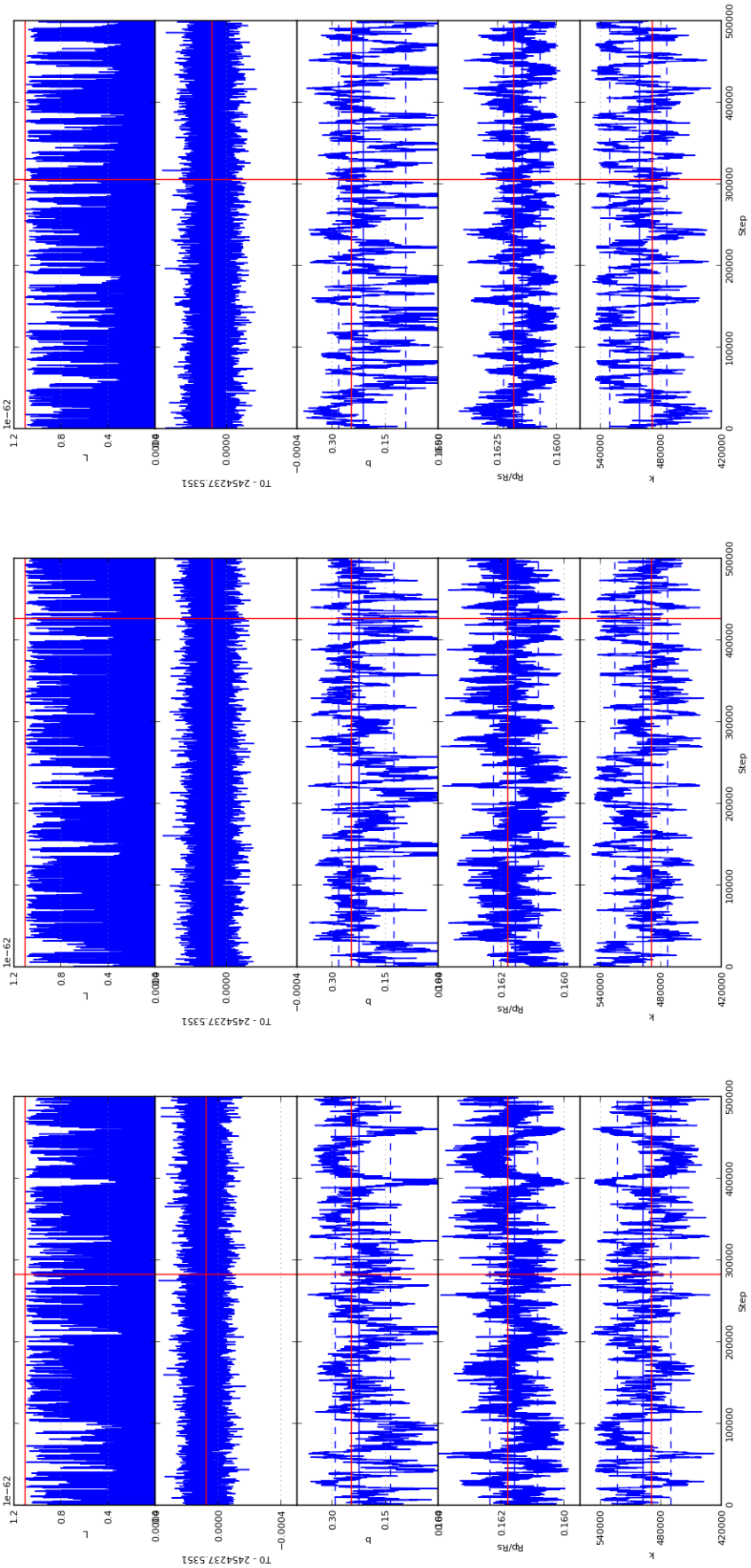


Figure 6.2: The three independent 500000-step MCMC runs on the transit of CoRoT-2b, without a prior on the $T_{\rm eff}$. The adjusted parameters are the transit epoch $T_0$, the impact parameter $b$, the planet to star radius ratio $R_{\rm p}/R_{\star}$, and $k$ the stellar density line index in the re-arranged Padova2002 stellar evolution models. The likelihood $L$ of the model stored at each step is plotted in the top panel. The model with the highest likelihood is marked by the red lines. The $1\sigma$ uncertainty range on this model is marked by the blue dashed lines. The median value of each distribution is marked by a vertical blue line. These three MCMC runs are combined together in Figure 6.3.

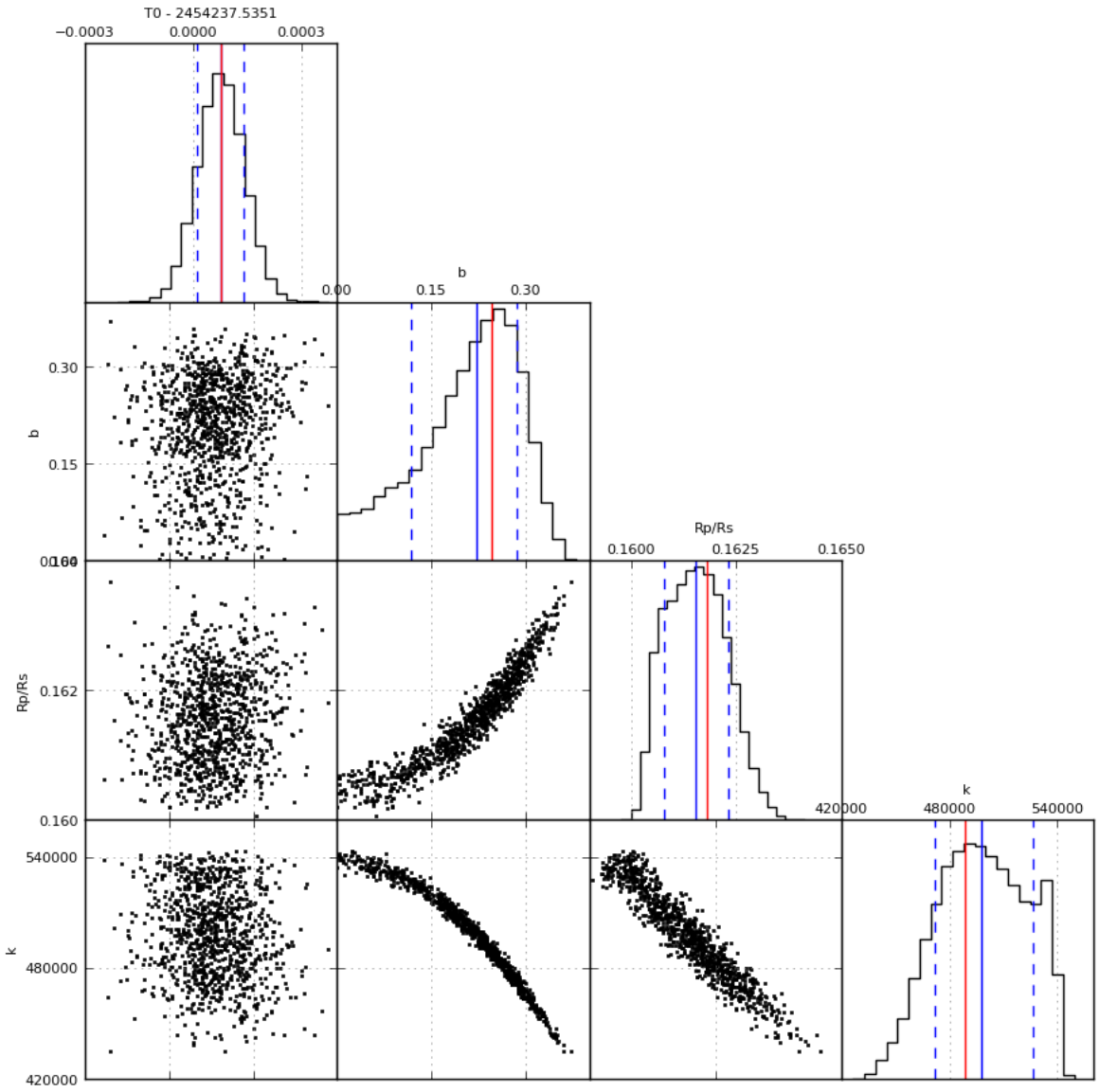


Figure 6.3: The 2D MCMC chains with no prior on the $T_{\rm eff}$, and their posterior distributions. The chains are 1479000 steps long. Same colour line legend as Figure 6.2.

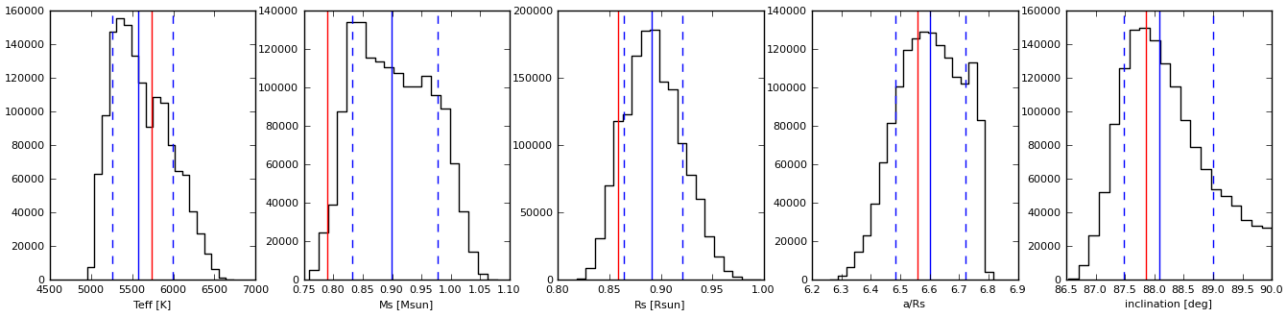


Figure 6.4: The posterior distributions of $a/R_\star$ and $i$ derived from the posterior distributions of $k$ and $b$. The posterior distributions of $T_{\rm eff}$, $M_\star$ and $R_\star$ derived from $k$, are shown for comparison with Figure 6.7. Same colour line legend as Figure 6.2.

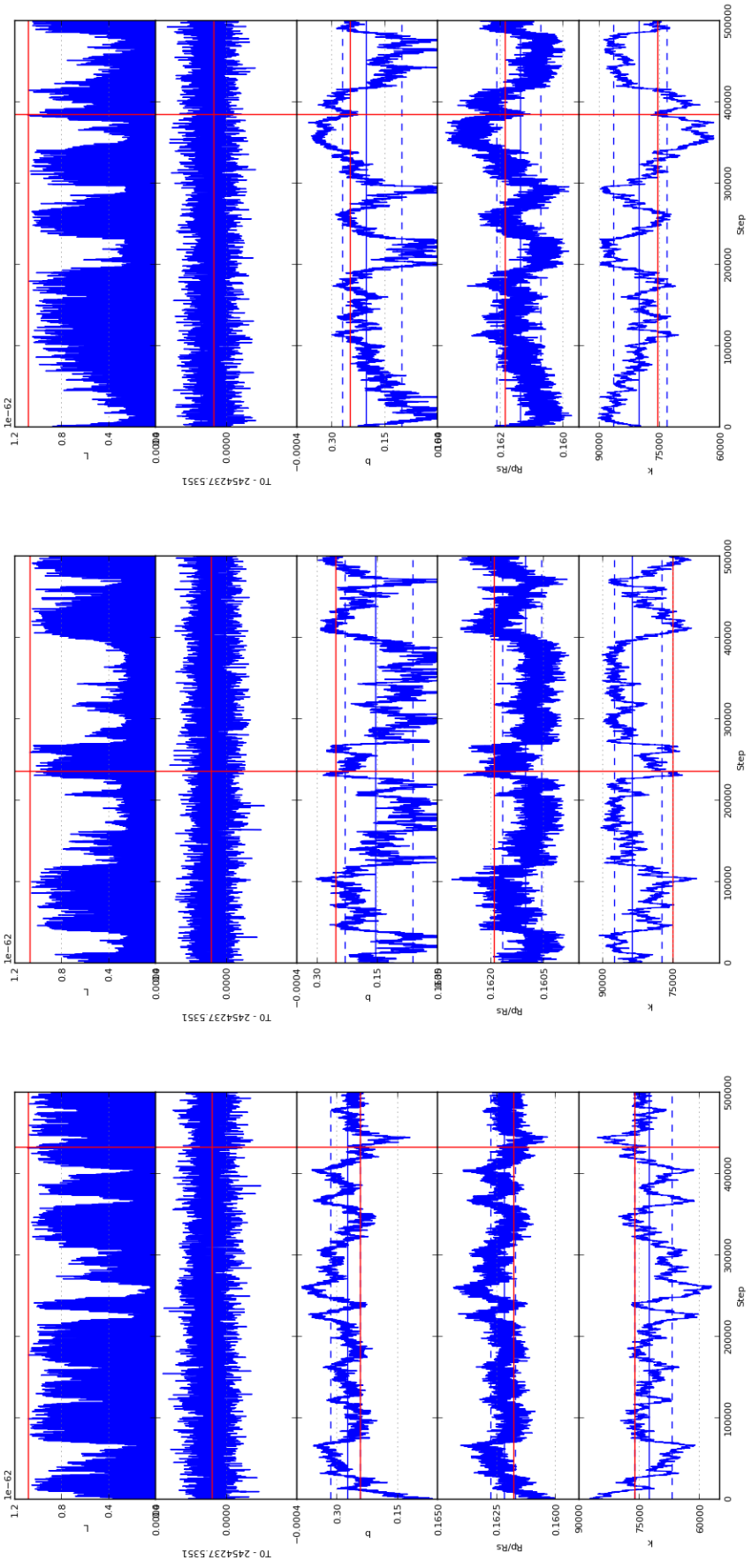


Figure 6.5: Same legend as Figure 6.2, but for the MCMC run with a prior on the $T_{\rm eff}$ equal to 5516±33 K, temperature found for CoRoT-2 in the previous chapter using the equivalent width line ratios. These three MCMC runs are combined together in Figure 6.6.

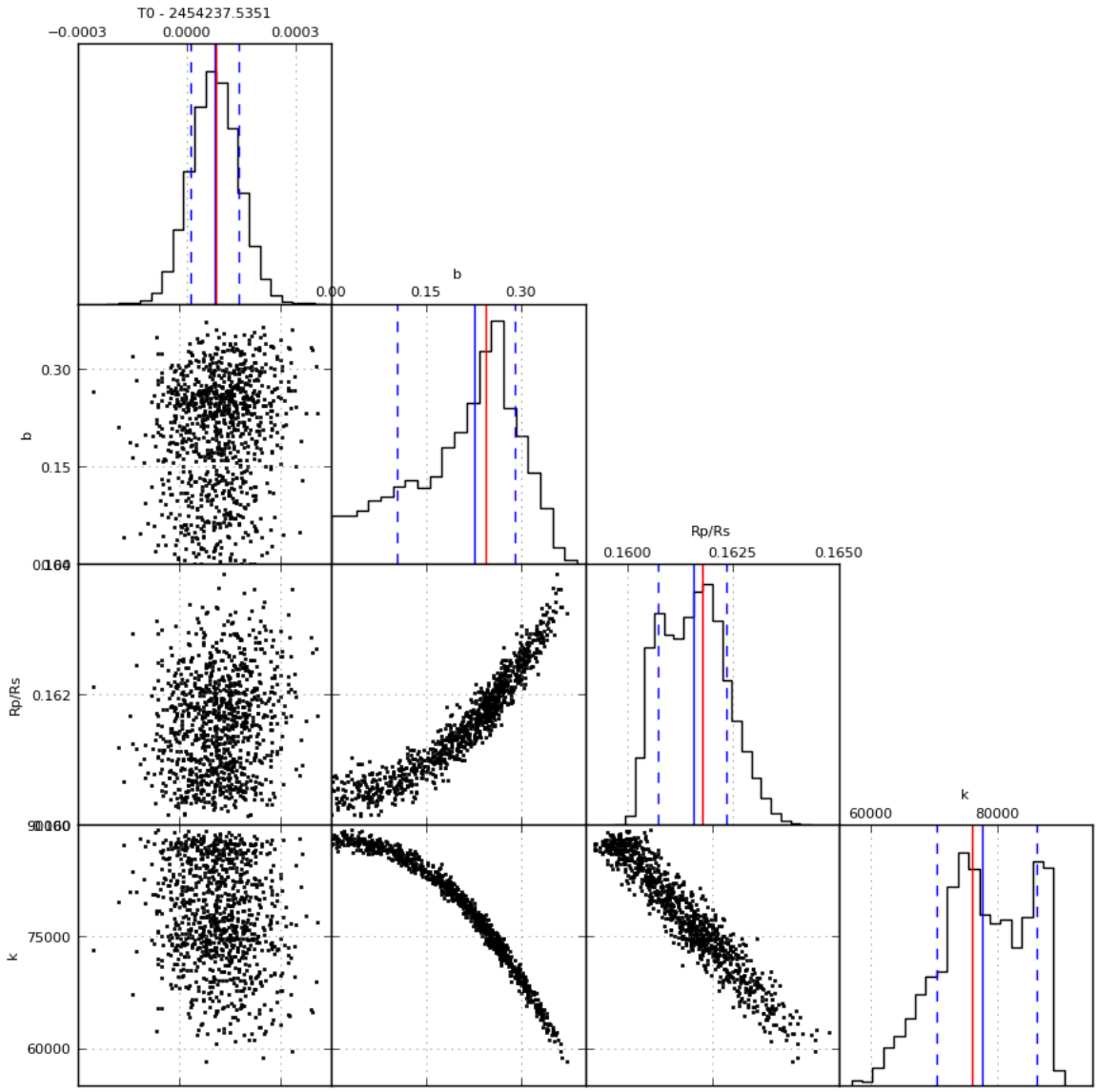


Figure 6.6: 2D MCMC chains, run with a prior of $T_{\rm eff}$=5516±33 K, and their posterior distributions. Same legend as Figure 6.3.

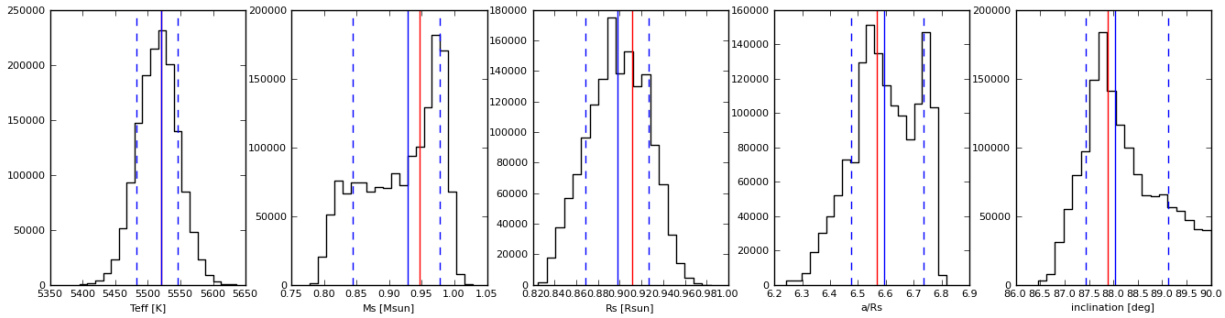


Figure 6.7: The posterior distributions of $T_{\rm eff}$, $a/R_\star$ and $i$ derived from the posterior distributions of $k$ and $b$ of Figure 6.6. The posterior distribution of $M_\star$ and $R_\star$, derived from $k$, are also shown as used to derive $a/R_\star$. Same legend as Figure 6.4.

### 6.2.3 Discussion

The MCMC best-fit models of CoRoT-2b's IRF-filtered transit light curve are presented in Figure 6.8, and the parameters are summarised in Table 6.3. These models and values are compared to the parameters from Alonso et al. (2008) and the parameters derived with the Levenberg-Marquardt algorithm (fitting method used in Chapter 3).

Table 6.3: Comparison table of the parameters of CoRoT-2b presented in the discovery paper, derived using the Levenberg-Marquardt algorithm (LMA), and derived using the Markov Chain Monte Carlo (MCMC) without and with a prior on the $T_{\rm eff}$.

| | Alonso et al. (2008) | LMA | MCMC | |
|---|---|---|---|---|
| | | | no $T_{\rm eff}$ | $T_{\rm eff}$=5516±33K |
| $P$ (d) | <——— | 1.7429964 ± 0.0000017 | ——— | ———> |
| $T_0$-2454237 (d) | 0.53562 ± 0.00014 | 0.53534 ± 0.00002 | $0.53518^{+0.00006}_{-0.00006}$ | $0.53518^{+0.00006}_{-0.00007}$ |
| $R_{\rm p}/R_\star$ | 0.1667 ± 0.0006 | 0.1621 ± 0.0003 | $0.1618^{+0.0005}_{-0.0010}$ | $0.1618^{+0.0006}_{-0.0011}$ |
| $b$ | 0.26 ± 0.01 | 0.25 ± 0.02 | $0.25^{+0.04}_{-0.13}$ | $0.24^{+0.05}_{-0.14}$ |
| $a/R_\star$ | 6.70 ± 0.03 | 6.56 ± 0.04 | $6.56^{+0.16}_{-0.08}$ | $6.57^{+0.17}_{-0.09}$ |
| $i$ (°) | 87.8 ± 0.1 | 87.8 ± 0.2 | $87.9^{+1.1}_{-0.4}$ | $87.9^{+1.2}_{-0.4}$ |
| $u_a$ | 0.41 ± 0.03 | <——— | 0.478 ± 0.010 (fix) | ———> |
| $u_b$ | 0.06 ± 0.03 | <——— | 0.205 ± 0.007 (fix) | ———> |
| $e$ | <——— | 0 (fix) | ——— | ———> |

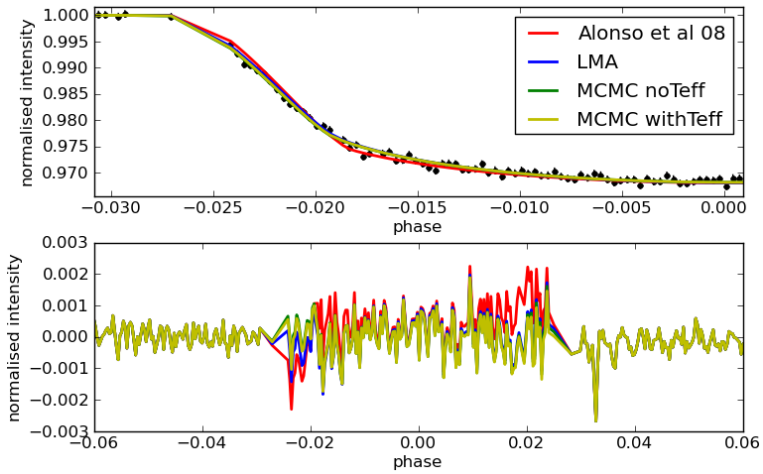


Figure 6.8: Top panel: the binned phase-folded transit of CoRoT-2b, zoomed over the first half of the IRF-filtered transit. Over-plotted are the best transit models derived with the LMA and with the different MCMC runs. Bottom panel: the residual to the data of the LMA and MCMC transit models.

Table 6.3 and Figure 6.8 show that both the LMA and the MCMC derive consistent planet parameters and transit model to the data. However, the uncertainties on the parameters derived from the MCMC are more conservative and better representative of the shape of the parameter space around the best model. The comparison show that the LMA has also found the global best minimum for this light curve. It also shows that adding a constraint on the $T_{\rm eff}$ does not change the planet parameters derived

from this light curve. However, it has changed the shape of the posterior distribution in $k$, adding a second peak to the distribution. This also creates a second peak in the distribution of $a/R_\star$ at $\sim$6.75. A longer chain needs to be run to check the robustness of the shape of this distribution and see if the peak due to the prior on the $T_{\rm eff}$ shifts the value of $a/R_\star$.

The prescribed MCMC walk in stellar density allows us to derive a posterior distribution for $T_{\rm eff}$. This provides an additional method to derive the stellar temperature from the photometric transit of an orbiting planet, and to map the likelihood space in $T_{\rm eff}$ around the best value. In the case of CoRoT-2, the temperature derived from the posterior probability distribution of a chain stepping in stellar densities, is 5741 K for the best-fit value, 5571 K for the median value and $\sim$5400 K for the most probable value (Figure 6.4). These values are smaller, but consistent within the $1\sigma$ uncertainty range of the distribution in $T_{\rm eff}$ (5260 - 5998), with the stellar temperature derived from the equivalent width ratios in Chapter 5 (5516$\pm$33 K), and with the stellar temperature published in Alonso et al. (2008) (5625$\pm$120 K).

The larger residuals to the model from Alonso et al. (2008) in Figure 6.8 show that the phase-folded IRF-filtered transit light curve is slightly shifted in $T_0$ compared to the processing done by Alonso et al. (2008). Additionally, the stellar limb darkening coefficients of Alonso et al. (2008) do not reproduce the shape of the IRF-filtered transit as well as the ones of Sing (2010) used in this chapter.

The uncertainty on $R_{\rm p}/R_\star$ derived from the phase-folded IRF-filtered transit light curve of CoRoT-2b is smaller than the value published in Alonso et al. (2008), although derived more robustly. This shows an improvement in the light curve processing when using the IRF.

The planetary parameters derived from the LMA and the MCMC applied to the IRF-filtered transit light curve of CoRoT-2b makes the planet appear smaller and closer to its star than published in Alonso et al. (2008). CoRoT-2b is classified as an inflated planet, i.e. its radius is larger than what can be explained with the current planet composition and evolution models as discussed in Alonso et al. (2008). This new set of parameters makes CoRoT-2b appear less inflated and thus less challenging for the models.

One difference between the two analyses is the choice of different limb darkening coefficients. Using different limb darkening coefficients changes the shape of the transit model forcing the other parameters to adjust to reproduce the data points. In the discovery paper of CoRoT-2b, the limb darkening coefficients were fitted at the same time as the planet parameters, thus the degeneracy of their values with the value of $R_{\rm p}/R_\star$ depend strongly on the broadness and the finesse of the exploration of the parameter space performed by the authors, as well as on the light curve processing. In this thesis, the limb darkening coefficients were kept fixed to aid the comparison of the derived planet parameters obtained with the different methods used.

Stellar isochrones can be plotted in stellar luminosity versus temperature diagrams.

The constraint in stellar density, from the transit shape, allows us to derive probability distributions for the stellar ages, along with the other stellar parameters, using the resampled Padova stellar evolution models. In the MCMC, each $k$ is related to a combination of stellar density, temperature and age. The MCMC posterior distribution in $k$ is dependent on the constraints from the stellar density, from the transit shape, and from the stellar effective temperature from the equivalent width ratios. The distribution in stellar age can be directly produced from the distribution in $k$, as each $k$ is related to a stellar age in the resampled Padova stellar evolution models. However, one should keep in mind that the validity of the derived age distribution will be both stellar-evolution-model and contaminant-flux-free-light-curve dependent. When a prior on the temperature is applied, the derived age distribution will also be stellar-temperature dependent.
Quantifying the improvement in the determination of the stellar age from the probabilistic distribution of the stellar density, and the new stellar temperature, will be an interesting study to perform as future work. It will be interesting to see if the new age estimate makes the host star of CoRoT-2b younger than currently thought. A younger star would also infer that the planet is younger, which better explains the inflated aspect of CoRoT-2b. Younger planets are intrinsically hotter and larger, as a planet cools and contracts after formation.

## 6.3 Conclusion and future work

The work presented in this chapter is in progress. Improvements on the code and the science included in the MCMC are ongoing.

### 6.3.1 Conclusions

The greatest strength of the MCMC is its capability to map the parameter space around the best model, showing structures in the likelihood of the surrounding models and correlations between parameters. If the MCMC is run for long enough, it derives a robust uncertainty range on the value of the parameter and a finesse of exploration sufficient to derive accurate values of the best model.

The other major advantage of the MCMC is that it allows the inclusion of a-priori knowledge to the search for best model. This makes the solution a better representation of the true reality. However, the probability distributions it returns are only as good as the priors assumed.

The greatest drawback of the MCMC approach is that it takes time to run. A lot of iterations are needed to derive statistically robust probability distributions. The Levenberg-Marquardt algorithm is much faster but more sensitive to the initial conditions, as it converges towards the first minimum in $\chi^2$ it finds in the parameter space

which might not be the global minimum.

The set-up stage of an MCMC can also be lengthy, as opposed to the setting up of a grid search for instance. Factors to take into account in the setting-up stage on a MCMC include: a) the format of the data (number of points) as it can lengthen the calculation time, b) the choice of priors and their distributions, c) the initial values, d) the typical step sizes, e) the length of the chain to ensure convergence. However, once the MCMC is set-up, for the same resolution and statistical robustness of the solution, running an MCMC can be faster than a grid search.

The transit modelling using the MCMC approach described in this chapter makes use of a new photometric method to derive the stellar temperature. This method uses stellar evolution models to translate the stellar densities (adjusted in the MCMC) into stellar temperature. The precision of the derived $T_{\rm eff}$ will depend on the finesse and intrinsic accuracy of the grid of stellar evolution models.

Applied to the phase-folded IRF-filtered transit light curve of CoRoT-2b, the MCMC approach derived is a more robust method to determine error bars on the planet parameters. It also provides an independent measurement of the stellar temperature from the transit shape. The addition of a prior in the stellar temperature was not found to change the final values of the planet parameters, but did change the shape of the distribution in stellar density.

### 6.3.2 Future work

Longer chains still need to be run to ensure the convergence for each parameter. This will secure a robust solution for the parameters, for the given data and priors.

The uncertainties on the contaminant flux needs to be taken into account in the uncertainties derived for the parameters. The suggested approach is to add to the transit model, at each MCMC iteration, a constant flux drawn from a Gaussian distribution (with a zero mean and a standard deviation equal to the uncertainty on the contaminant flux), then re-normalise the model and use it in the calculation of the likelihood. The posterior distribution of the parameter will thus include the uncertainty of the contaminant flux.

The red noise in the light curve needs to be taken into account as a good merit function needs to use a true estimate of the noise. The red noise can be taken into account by replacing the $\sigma_{white}$ in the merit function by $\sigma_{pink} = \sigma_{white} + N * \sigma_{red}$ (Pont et al., 2006). $\sigma_{red}$ can be evaluated by binning the unfolded light curves with different bin sizes and evaluating each time the standard deviation of the resulting signal. The $\sigma_{white}$ will go as $\sigma_{no\ bin}/N$, $N$ being the number of points binned together, while $\sigma_{red}$ should be constant, so the difference between the $\sigma_{bin}$ and $\sigma_{no\ bin}/N$, e.g. for bin size of 1 or 2h, is $\sigma_{red}$.

The IRF filtered light curve was binned in order to reduce the number of data points to speed up the MCMC. It will be interesting to see how this binning affects the ac-

curacy and precision of the planet parameters and their $1\sigma$ uncertainty range. The binning of the light curve by half, for instance.

It will be also be interesting to see how the posterior probability distributions vary with different values of the prior in $T_{\rm eff}$, especially for the distribution in $k$ and thus $a/R_\star$. The MCMC can be run with the prior on the $T_{\rm eff}$ set to the value published in Alonso et al. (2008) (5625$\pm$120 K).

The grid of stellar evolution models used in the MCMC can also be refined to include a finer sampling in the stellar parameters. This should improve the accuracy of the posterior distribution in $k$, and thus in $a/R_\star$ and $i$.

The MCMC performs steps in $k$, and at each $k$ is associated a $T_{\rm eff}$. The limb darkening of a star depends on the stellar temperature (as well as on the stellar surface gravity and metallicity, and on the observational bandpass). Currently the limb darkening coefficients are not adjusted when the MCMC steps into another value of $T_{\rm eff}$. To be more consistent, the MCMC should be adjusted to allow the limb darkening coefficients to vary according to the $T_{\rm eff}$ associated to the $k$ of each step. For a chosen limb darkening law and filter, the limb darkening coefficients can be calculated given the stellar atmosphere parameters ($T_{\rm eff}$, $\log g$, (M/H)). Claret (2000) and Claret (2004) give tables of limb darkening coefficients for different standard filters and Sing (2010) for CoRoT and Kepler bandpasses.

Finally, it will be interesting to homogeneously derive the planet parameters ($1\sigma$ uncertainty range and best model) of the other CoRoT planets using the MCMC approach presented in this chapter, on the IRF-filtered transit light curve of the planet, including the prior knowledge on the stellar temperature. The value of the prior in $T_{\rm eff}$ can be set to the value from the discovery paper, or to the values derived from the equivalent width ratios. The derived planetary parameters can then be compared to each other, e.g. in a mass-radius diagram. This approach will reduce current biases on the type of light curve processing and fitting used to analyses the individual planets. It also provides the advantage of systematically taking into account more information on the planets and their host star.

# Chapter 7

# Conclusions and prospects

The knowledge of both the radius and the mass of an exoplanet, obtained with combined observations of the planet's transit and the star's radial velocity variations, allows the determination of the planet's density. The observed planet densities provide important constraints on planet structure and evolution models.

The uncertainties on the planet parameters need to be small in order to test the physics used in the planet evolution models, and to discriminate between different structures and compositions.

The motivation of this thesis was to derive more accurate and precise planet in a two-fold approach. The first aim was to improve the precision and accuracy of the planet parameters in the presence of stellar activity, by meticulously processing and fitting the planet's transit signal. The second aim was to improve the precision on stellar temperatures which are fundamental to derive precise stellar radii and masses. The fist aim was tackled in Chapters 2, 3 and 6, and the second in Chapter 5.

The new light curve filtering method presented in Chapter 2 also conserves all signals at the orbital period of the planet. In Chapter 4, this property was exploited by searching re-processed light curves for lower amplitude planet signals such as the planet's secondary eclipse and orbital phase variations.

## 7.1 Summary of achievements

### 7.1.1 A post-detection stellar variability filter

Stellar photometric variability on timescales of hours to days hinders the characterisation of the planet's transit signal. The frequency content of the transit signal and the stellar variability signal overlap in the timescale range of hours. Current stellar variability filters, which are used to filter the stellar variability prior to the transit detection, do not differentiate between the transit component and the stellar variability component on these overlapping timescales. This results in either filtering out some of the transit signal

or not filtering out enough stellar variability. Either affects the accuracy and precision of the derived planet parameters.

In Chapter 2, we used a pre-detection filter, the non-linear iterative filter (NIF) of Aigrain & Irwin (2004), to show that such filters induce a deformation in the transit shape which can induce errors (up to 50%) in the star-planet radius ratio. A new post-detection stellar variability filter, the Iterative Reconstruction Filter (IRF), was thus developed and tested. This filter simultaneously evaluates the stellar photometric signal and the planet photometric signal. It uses the prior knowledge of the planet orbital period to estimate the transit signal, and a median filter to estimate the stellar variability.

Tests on 20 simulated CoRoT light curves showed that the IRF especially improves the shape of the transit for light curves with strong stellar variability (large amplitude and high frequency variations). Nonetheless, residual noise in the filtered transit light curve allows for transit models (with different combinations of system scale and impact parameters) to fit the data equally well. This effect limits the direct comparison of the planet parameters derived from different filtering methods.

The IRF is limited to stellar variability filtering of light curves with a precise knowledge of the planet orbital period. It evaluates the phase-folded signal of the transit and is therefore limited to the determination of mean parameters, i.e. it is not sensitive to the transit shape or timing variations due to additional planets or moons in the system.

### 7.1.2 Application to the transit of CoRoT planets

CoRoT's light curves have a photometric precision of the order of 0.2 mmag. At this level of precision most stars show intrinsic stellar variability. The first seven CoRoT space light curves with confirmed planetary transits were run through the IRF in Chapter 3. The planet parameters were derived from the IRF-filtered light curves using the analytical transit formulation of Mandel & Agol (2002) and a Levenberg-Marquardt convergence algorithm.

Compared to the values in the planet discovery papers, the planet parameters derived from the IRF-filtered light curve were consistent at the $1\,\sigma$ level. The level of stellar activity in the real CoRoT light curves is observed to be smaller than that in the simulated light curves used prior to launch. The effect of stellar variability on the planet's transit is thus limited, and the treatment by the IRF did not provide a major improvement. However, a few advantages in using the IRF were highlighted through this work. The IRF allows stellar variability to be filtered out down to timescales of 6h without affecting the transit shape, which is not the case for the NIF. Despite the more robust error analysis used, the error bars associated to the parameters from the IRF-filtered light curves were comparable to (or smaller than) those in the literature, except for CoRoT-7b, where we would argue the error bars are underestimated in the discovery paper.

This study also confirmed that the planet transit modelling is highly sensitive to the

modelling of the stellar limb darkening. The evaluation of the true impact of the IRF on the planet parameters was limited by this effect.

### 7.1.3 Photons from the CoRoT planets

The IRF preserves any signal at the period of the transit. This property was investigated in Chapter 4 to search for secondary eclipses and orbital phase variations in the phase-folded IRF-filtered light curves of CoRoT-1 and CoRoT-2. These planets were chosen due to their expected strong secondary eclipse signals.

The search for a secondary eclipse was performed in the phase-folded IRF-filtered light curve, sliding a box of varying duration over the phase range 0.4–0.6 (range adapted to the low eccentricity of the planets). The search for orbital phase variations was also performed by a visual check of the phase-folded IRF-filtered light curve.

A clear detection of the secondary eclipse of CoRoT-1b was achieved in its IRF-filtered white CoRoT light curve. In addition, a low amplitude phase modulation was also observed. The detailed characterisation of the eclipse and phase variations were limited by the level of white noise in the filtered light curve. A noisier detection of CoRoT-1b's secondary eclipse in CoRoT red and green channels was made.

The detection of the secondary eclipse of CoRoT-2b in its IRF-filtered white CoRoT light curve was also made, but with a lower signal to noise ratio. The secondary eclipse of CoRoT-2b was expected to be more challenging to detect as the planet is further away from its host star and its star is more active than CoRoT-1b. The characterisation of this eclipse was limited by the level of residual systematics in the filtered light curve.

In order to improve the filtering by the IRF of the transit light curve of CoRoT-2b, the behaviour of the IRF with different minimum timescales of stellar variability was studied. This work revealed that the IRF improves the filtering of the stellar variability down to timescales of 0.25 days, below which it unintentionally reconstructs noise features along with the transit signal. The optimal stellar variability filtering timescales was found to be between 12 and 6 hours.

### 7.1.4 Precise relative stellar temperature measurement

The transit and radial velocity methods, respectively, derive the planet's radius and mass relative to the radius and mass of the host star. The precision on the parameters of large exoplanets are limited by uncertainties on the stellar parameters. The derivation of the latter, starts with estimating the stellar temperature, so a more precise temperature will help reduce the uncertainties on the stellar parameters.

This issue was tackled in Chapter 5, where a new temperature calibration was derived based on equivalent width ratios. This calibration derives relative stellar temperatures with precision down to 10 K, for $T_{\rm eff}$ within the calibrated temperature range, i.e.

between 5000 and 6100 K. This method was improved on, and published in Sousa et al. (2009).

The method was used to successfully derive an independent measurement of the temperatures of the CoRoT planet host stars with $T_{\rm eff}$<6100 K. The temperatures derived with this method are sensitive to the accuracy of the equivalent width measurements, so special care should be taken, at this step, to ensure the method derives an accurate stellar temperatures. This method is also limited by the absolute precision of the temperatures used to calibrate it, which are model-dependent. Therefore, like all other available temperature determination methods for single stars, it may suffer from systematic shifts in the absolute scale.

### 7.1.5 Joint modelling of transits and stellar temperatures

The planet's orbital inclination $i$ and system scale $a/R_\star$ are correlated in transit models, which limit the precision on the derived planet parameters. Additionally, the detailed shape of a transit depends on the stellar density, which is linked to the stellar temperature. The stellar temperature can be determined spectroscopically (e.g. as described in Chapter 5). All the above information can be taken into account when fitting the best model to the transit using a Markov Chain Monte Carlo (MCMC).

In Chapter 6, an MCMC is used to jointly model the transit shape and the stellar temperature. Transit models of Mandel & Agol (2002) with different planet parameters and stellar densities are compared to the IRF-filtered transit of CoRoT-2b, to derive the best transit model and the planet parameters most consistent with the available information on the planet and its host star.

The planet parameters derived from the MCMC (with a prior on the stellar temperature) are consistent with those derived from using the same method without this prior. These parameters are also consistent, as expected, with the transit fit derived using the Levenberg-Marquardt algorithm. All the planet parameters derived from the IRF-filtered light curve are marginally compatible ($2\sigma$ and above) with the parameters in the discovery paper (Alonso et al., 2008). The differences come from the difference in light curve processing and modelling, and from the modelling of the stellar limb darkening.

## 7.2 Conclusions

The aims of this thesis, in terms of developing new techniques to better characterise transiting exoplanets in the presence of stellar activity, were achieved. However, the absolute improvement on the planet parameters of real planets were smaller than expected, due to the smaller level of stellar activity of the first seven CoRoT planets, than previously simulated.

The techniques developed were applied to study aspects of the planets that were not originally planned, such as the the planet's emission in the visible. In general, the work undertaken in this thesis has highlighted the complexity inherent to detailed characterisation of transit light curves. The detailed analysis of planetary transits, secondary eclipses and orbital phase variations are sensitive to the light curve processing and transit fitting strategies. When characterising a planet from its transit light curve, important aspects to keep in mind are a) the correction from all contaminant fluxes in the light curve, b) the residual stellar variability and systematics on the transit light curve, c) the modelling of the stellar limb darkening, d) the chosen methods used to find the best transit model and estimate uncertainties, and e) the incorporation of all prior knowledge on the planet and its host star in the transit fit.

## 7.3 Future improvements and prospects

Some of the work presented in the thesis is still in progress and can be improved in a number of ways.

The IRF can be further tested to understand, and suppress if possible, its behaviour when filtering the stellar variability with a timescale smaller than 6h. It would also be interesting to test it further on very active stars with planetary transits, to probe the limits of its performance in reconstructing the transit signal. It may be possible to use the IRF at the detection stage to improve the detectability of borderline transits which would otherwise be masked by stellar variability. This would be computationally challenging, however, as the IRF would need to be run at each trial period. There is also a danger that it may lead to an increased rate of false alarms if the IRF parameters are not carefully chosen.

It may be possible to fine-tune the filtering of the light curve of CoRoT-2 further and to reduce the residual stellar variability at the transit period in order to improve on the detection of CoRoT-2b's secondary eclipse. The tentative detection of CoRoT-1b's orbital phase variations in the visible also deserves further attention. Generally, however, the scientific usefulness of CoRoT secondary eclipses is limited by the degeneracy, in the CoRoT bandpass, between the planet's thermal emission and stellar reflected light. This degeneracy may be lifted by combining the CoRoT measurements with other bandpasses and/or by detecting the signal in individual CoRoT channels. There is also scope for applying the IRF to other, good candidates from CoRoT and other similar surveys searching for similar signals.

The sensitivity of the $\mathrm{ARES}$ equivalent width measurements to the $\mathrm{rejt}$ parameter to evaluate the continuum needs to be better understood, as it currently limits the reliability of the stellar temperatures derived using equivalent width ratios. It would also be desirable to extend $\mathrm{ARES}$ to produce error bars on its equivalent width measurements, or to explore alternative automated methods to measure precise equivalent

widths. The equivalent width temperature calibration may be extended by including cooler and hotter stars outside the current calibrated range in the calibration set.

Additional prior knowledge could be incorporated in the MCMC transit fits, starting with the stellar limb darkening coefficients: these can be linked to the stellar temperature using theoretical models in the same way as the stellar density. Ultimately, a homogenous detailed analysis of all the CoRoT planets using the tools presented in this thesis – the IRF, the $T_{\rm eff}$ calibration, and joint modelling of the transit light curves and the stellar temperature – would enable a more direct comparison of the planets' radii, free from the side-effects of different light curve processing and fitting methods.

As seen throughout this thesis, stellar variability is an important limitation to the precision and accuracy of planet parameters, and to the detection of the planet's secondary eclipse and orbital phase variations. It is likely to be even more important in future missions such as PLATO and TESS, and many more planets around active stars will certainly be discovered. The IRF should therefore prove increasingly useful in the future, and may be indispensable to characterise small planets around active stars.

# Appendix A

# Constants and acronyms

## A.1 Table of constants

Table A.1: Table of constants

| Symbol | Value | Units | Description |
|---|---|---|---|
| $h$ | 6.626068 $10^{-34}$ | J.s | Planck constant |
| $k$ | 1.3806504 $10^{-23}$ | J.K$^{-1}$ | Boltzmann constant |
| $\sigma_{\rm SB}$ | 5.6704 $10^{-8}$ | J.s$^{-1}$.m$^{-2}$.K$^{-4}$ | Stefan-Boltzmann constant |
| $G$ | 6.673 $10^{-11}$ | m$^3$.kg$^{-1}$.s$^{-2}$ | Gravitational constante |
| $c$ | 2.99792458 $10^{8}$ | m.s$^{-1}$ | Speed of light in vaccum |
| $AU$ | 1.496 $10^{11}$ | m | Astronomical Units – distance of the Earth to the Sun |
| $pc$ | 3.08568025 $10^{16}$ | m | Parsec – distance of ... |
| $ly$ | 0.306601 | pc | Light year – distance covered by the light in one year |
| $M_\odot$ | 1.989 $10^{30}$ | kg | Mass of the Sun |
| $R_\odot$ | 6.955 $10^{8}$ | m | Radius of the Sun |
| $M_{\rm Jup}$ | 1.89 $10^{27}$ | kg | Mass of Jupiter |
| $R_{\rm Jup}$ | 6.9911 $10^{7}$ | m | Radius of Jupiter |
| $M_\oplus$ | 5.97 $10^{24}$ | kg | Mass of the Earth |
| $R_\oplus$ | 6.3728 $10^{6}$ | m | Radius of the Earth |

## A.2 Some acronyms

BT2 = $2^{nd}$ CoRoT blind test exercise
CCD = Charged Coupled Device
EW = equivalent width
IRF = Iterative Reconstruction Filter (Alapini & Aigrain, 2009)
LC = light curve
NIF = Non-linear Iterative Filter (Aigrain & Irwin, 2004)
PSF = Point Spread function
$T_{\rm eff}$ = stellar effective temperature
RV = radial velocity

# Bibliography


Aigrain, S., Collier Cameron, A., Ollivier, M., et al. 2008, A&A, 488, L43

Aigrain, S., Favata, F., & Gilmore, G. 2004, A&A, 414, 1139

Aigrain, S. & Irwin, M. 2004, MNRAS, 350, 331

Aigrain, S., Pont, F., Fressin, F., et al. 2009, A&A, 506, 425

Alapini, A. & Aigrain, S. 2009, MNRAS, 397, 1591

Alonso, R., Alapini, A., Aigrain, S., et al. 2009a, A&A, 506, 353

Alonso, R., Auvergne, M., Baglin, A., et al. 2008, A&A, 482, L21

Alonso, R., Deeg, H. J., Kabath, P., & Rabus, M. 2010, AJ, 139, 1481

Alonso, R., Guillot, T., Mazeh, T., et al. 2009b, A&A, 501, L23

Aparicio, A. & Gallart, C. 2004, AJ, 128, 1465

Auvergne, M., Bodin, P., Boisnard, L., et al. 2009, A&A, 506, 411

Auvergne, M., Boisnard, L., Buey, J.-T. M., et al. 2003, in Proc. SPIE, Vol. 4854, Future EUV/UV and Visible Space Astrophysics Missions and Instrumentation, ed. J. C. Blades & O. H. W. Siegmund, 170–180

Baglin, A., Auvergne, M., Barge, P., et al. 2006, in ESA Special Publication, Vol. 1306, ESA Special Publication, ed. M. Fridlund, A. Baglin, J. Lochard, & L. Conroy, 33–+

Bakos, G. Á., Noyes, R. W., Kovács, G., et al. 2007, ApJ, 656, 552

Baraffe, I., Chabrier, G., Allard, F., & Hauschildt, P. H. 1998, A&A, 337, 403

Baraffe, I., Chabrier, G., & Barman, T. 2008, A&A, 482, 315

Baraffe, I., Chabrier, G., & Barman, T. 2010, Reports on Progress in Physics, 73, 016901

Barge, P., Baglin, A., Auvergne, M., et al. 2008, A&A, 482, L17

Barman, T. S., Hauschildt, P. H., & Allard, F. 2005, ApJ, 632, 1132

Baudin, F., Baglin, A., Orcesi, J.-L., et al. 2006, in ESA Special Publication, Vol. 1306, ESA Special Publication, ed. M. Fridlund, A. Baglin, J. Lochard, & L. Conroy, 145–+

Bennett, D. P. 2009, ArXiv e-prints arXiv:astro-ph/0902.1761

Biazzo, K., Frasca, A., Catalano, S., & Marilli, E. 2006, A&A, 446, 1129

Boisnard, L. & Auvergne, M. 2006, in ESA Special Publication, Vol. 1306, ESA Special Publication, ed. M. Fridlund, A. Baglin, J. Lochard, & L. Conroy, 19–+

Boisse, I., Moutou, C., Vidal-Madjar, A., et al. 2009, A&A, 495, 959

Bonomo, A. S. & Lanza, A. F. 2008, A&A, 482, 341

Bordé, P., Bouchy, F., Deleuil, M., et al. 2010, in prep.

Borucki, W. J., Koch, D., Jenkins, J., et al. 2009, Science, 325, 709

Brooks, S. P. & Gelman, A. 1997, Journal of Computational and Graphical Statistics, 7, 434

Brown, T. M., Charbonneau, D., Gilliland, R. L., Noyes, R. W., & Burrows, A. 2001, ApJ, 552, 699

Charbonneau, D., Allen, L. E., Megeath, S. T., et al. 2005, ApJ, 626, 523

Charbonneau, D., Brown, T. M., Latham, D. W., & Mayor, M. 2000, ApJL, 529, L45

Charbonneau, D., Winn, J. N., Everett, M. E., et al. 2007, ApJ, 658, 1322

Claret, A. 2000, A&A, 363, 1081

Claret, A. 2004, A&A, 428, 1001

Collier Cameron, A., Wilson, D. M., West, R. G., et al. 2007, MNRAS, 380, 1230

de Mooij, E. J. W. & Snellen, I. A. G. 2009, A&A, 493, L35

Deeg, H. 2009, in IAU Symposium, Vol. 253, IAU Symposium, 388–391

Deeg, H., Moutou, C., Eriksson, A., et al. 2010, Nature, 464, 384

Deleuil, M., Deeg, H. J., Alonso, R., et al. 2008, A&A, 491, 889

Deming, D., Seager, S., Richardson, L. J., & Harrington, J. 2005, Nature, 434, 740

Drummond, R., Lapeyrere, V., Auvergne, M., et al. 2008, A&A, 487, 1209

Favata, F. & Micela, G. 2003, Space Science Reviews, 108, 577

Fridlund, M., Hebrard, G., Alonso, R., et al. 2010, ArXiv e-prints arXiv:astro-ph/1001.1426

Fuhrmann, K. 1998, A&A, 338, 161

Gaudi, B. S. 2010, ArXiv e-prints arXiv:astro-ph/1002.0332

Gaudi, B. S. & Winn, J. N. 2007, ApJ, 655, 550

Gelman, A. & Rubin, D. B. 1992, Statistical Science, 7, 457

Gilli, G., Israelian, G., Ecuvillon, A., Santos, N. C., & Mayor, M. 2006, A&A, 449, 723

Gillon, M., Demory, B., Triaud, A. H. M. J., et al. 2009, A&A, 506, 359

Gillon, M., Lanotte, A. A., Barman, T., et al. 2010, A&A, 511, A3+

Giménez, A. 2006, A&A, 450, 1231

Girardi, L., Bertelli, G., Bressan, A., et al. 2002, A&A, 391, 195

Gray, D. F. 1994, PASP, 106, 1248

Gray, D. F. 2005, The Observation and Analysis of Stellar Photospheres, third edition edn. (Cambridge University Press)

Guillot, T. 2005, Annual Review of Earth and Planetary Sciences, 33, 493

Harrington, J., Hansen, B. M., Luszcz, S. H., et al. 2006, Science, 314, 623

Hebb, L., Collier-Cameron, A., Loeillet, B., et al. 2009, ApJ, 693, 1920

Jenkins, J. M. 2002, ApJ, 575, 493

Jenkins, J. M., Caldwell, D. A., Chandrasekaran, H., et al. 2010, ArXiv e-prints arXiv:astro-ph/1001.0256

Kjeldsen, H., Bedding, T. R., & Christensen-Dalsgaard, J. 2009, in IAU Symposium, Vol. 253, IAU Symposium, 309–317

Knutson, H. A., Charbonneau, D., Allen, L. E., et al. 2007a, Nature, 447, 183

Knutson, H. A., Charbonneau, D., Noyes, R. W., Brown, T. M., & Gilliland, R. L. 2007b, ApJ, 655, 564

Kovács, G., Bakos, G., & Noyes, R. W. 2005, MNRAS, 356, 557

Kovtyukh, V. V., Soubiran, C., Belik, S. I., & Gorlova, N. I. 2003, A&A, 411, 559

Kurucz, R. L. 1993, VizieR Online Data Catalog, 6039, 0

Lanza, A. F., Rodonò, M., & Pagano, I. 2004, A&A, 425, 707

Léger, A., Rouan, D., Schneider, J., et al. 2009, A&A, 506, 287

Lin, D. N. C., Bodenheimer, P., & Richardson, D. C. 1996, Nature, 380, 606

Lunine, J. I., Fischer, D., Hammel, H., et al. 2008, ArXiv e-prints arXiv:astro-ph/0808.2754

Mandel, K. & Agol, E. 2002, ApJL, 580, L171

Mandushev, G., O'Donovan, F. T., Charbonneau, D., et al. 2007, ApJL, 667, L195

Markwardt, C. B. 2009, in Astronomical Society of the Pacific Conference Series, Vol. 411, Astronomical Society of the Pacific Conference Series, ed. D. A. Bohlender, D. Durand, & P. Dowler, 251–+

Marois, C., Macintosh, B., Barman, T., et al. 2008, Science, 322, 1348

Mayor, M. & Queloz, D. 1995, Nature, 378, 355

Mazeh, T., Guterman, P., Aigrain, S., Zucker, S., & Grinberg, N. 2009, A&A, 506, 431

Mazeh, T., Naef, D., Torres, G., et al. 2000, ApJL, 532, L55

Moutou, C., Aigrain, S., Almenara, J., et al. 2007, in Astronomical Society of the Pacific Conference Series, Vol. 366, Transiting Extrasolar Planets Workshop, ed. C. Afonso, D. Weldrake, & T. Henning, 127–+

Moutou, C., Bruntt, C., Guillot, T., et al. 2008, A&A, 488

Moutou, C., Pont, F., Barge, P., et al. 2005, A&A, 437, 355

Nordström, B., Mayor, M., Andersen, J., et al. 2004, A&A, 418, 989

Perryman, M. A. C. 2000, Reports of Progress in Physics, 63, 1209

Phillips, J. A. & Thorsett, S. E. 1994, Ap&SS, 212, 91

Piskunov, N. E., Kupka, F., Ryabchikova, T. A., Weiss, W. W., & Jeffery, C. S. 1995, A&AS, 112, 525

Pollack, J. B., Hubickyj, O., Bodenheimer, P., et al. 1996, Icarus, 124, 62

Pont, F. & Eyer, L. 2004, MNRAS, 351, 487

Pont, F., Hébrard, G., Irwin, J. M., et al. 2009, A&A, 502, 695

Pont, F., Melo, C. H. F., Bouchy, F., et al. 2005, A&A, 433, L21

Pont, F., Zucker, S., & Queloz, D. 2006, MNRAS, 373, 231

Queloz, D., Bouchy, F., Moutou, C., et al. 2009, A&A, 506, 303

Ramírez, I. & Meléndez, J. 2004, ApJ, 609, 417

Rauer, H., Queloz, D., Csizmadia, S., et al. 2009, A&A, 506, 281

Rogers, J. C., Apai, D., López-Morales, M., Sing, D. K., & Burrows, A. 2009, ApJ, 707, 1707

Rosenblatt, F. 1971, Icarus, 14, 71

Rowe, J. F., Matthews, J. M., Seager, S., et al. 2006, ApJ, 646, 1241

Rowe, J. F., Matthews, J. M., Seager, S., et al. 2008, ApJ, 689, 1345

Santos, N. C., Israelian, G., & Mayor, M. 2004, A&A, 415, 1153

Santos, N. C., Israelian, G., Mayor, M., et al. 2005, A&A, 437, 1127

Schrijver, C. J. & Zwaan, C. 2000, Solar and Stellar Magnetic Activity

Seager, S., Kuchner, M., Hier-Majumder, C. A., & Militzer, B. 2007, ApJ, 669, 1279

Seager, S. & Mallén-Ornelas, G. 2003, ApJ, 585, 1038

Siess, L., Dufour, E., & Forestini, M. 2000, A&A, 358, 593

Sing, D. K. 2010, A&A, 510, A21+

Sing, D. K. & López-Morales, M. 2009, A&A, 493, L31

Snellen, I. A. G., de Mooij, E. J. W., & Albrecht, S. 2009a, Nature, 459, 543

Snellen, I. A. G., de Mooij, E. J. W., & Burrows, A. 2009b, ArXiv e-prints arXiv:astro-ph/0909.4080

Sousa, S. G., Alapini, A., Israelian, G., & Santos, N. C. 2009, ArXiv e-prints arXiv:astro-ph/0912.2651

Sousa, S. G., Santos, N. C., Israelian, G., Mayor, M., & Monteiro, M. J. P. F. G. 2006, A&A, 458, 873

Sousa, S. G., Santos, N. C., Israelian, G., Mayor, M., & Monteiro, M. J. P. F. G. 2007, A&A, 469, 783

Sousa, S. G., Santos, N. C., Mayor, M., et al. 2008, A&A, 487, 373

Struve, O. 1952, The Observatory, 72, 199

Tamuz, O., Mazeh, T., & Zucker, S. 2005, MNRAS, 356, 1466

Tingley, B. 2004, A&A, 425, 1125

Torres, G., Andersen, J., & Giménez, A. 2009, A&ARv, 13

Triaud, A. H. M. J., Queloz, D., Bouchy, F., et al. 2009, A&A, 506, 377

Winn, J. N. 2010, ArXiv e-prints arXiv:astro-ph/1001.2010

Winn, J. N., Holman, M. J., Bakos, G. Á., Pál, A., & et al. 2007, AJ, 134, 1707

Winn, J. N., Holman, M. J., Torres, G., et al. 2008, ApJ, 683, 1076

Wolszczan, A. & Frail, D. A. 1992, Nature, 355, 145